TECHNISCHE UNIVERSITÄT MÜNCHEN

Lehrstuhl für Methodik der Fernerkundung

High Precision 3D Localization and Motion Analysis of Persistent Scatterers using Meter-Resolution Radar Satellite Data

Stefan Matthias Gernhardt

Vollständiger Abdruck
der von der Fakultät für Bauingenieur- und Vermessungswesen
der Technischen Universität München
zur Erlangung des akademischen Grades eines
Doktor-Ingenieurs (Dr.-Ing.)
genehmigten Dissertation.

Vorsitzender:
   Univ.-Prof. Dr.-Ing. habil. Thomas Wunderlich

Prüfer der Dissertation:
   1. Univ.-Prof. Dr.-Ing. habil. Richard H.G. Bamler
   2. Univ.-Prof. Dr.-Ing. habil. Stefan Hinz
      Karlsruher Institut für Technologie (KIT)
   3. Assistant Research Prof. Dr.-Ing. Franz J. Meyer
      University of Alaska Fairbanks, USA

Die Dissertation wurde am 30.06.2011 bei der Technischen Universität München eingereicht und durch die Fakultät für Bauingenieur- und Vermessungswesen am 15.09.2011 angenommen.

Summary

In this thesis the impact and benefits of high resolution synthetic aperture radar (SAR) data for persistent scatterer interferometry (PSI) is investigated. The data is obtained by the German remote sensing satellite TerraSAR-X. From the high resolution compared to available SAR satellites so far – like ERS or ENVISAT – a large increase in numbers of persistent scatterers (PS) is expected. Therefore, the influence of different acquisition parameters on the appearance of PS is investigated in order to analyze the opportunistic character of these points. It is shown that the geometrical configuration of the sensor with respect to the objects on ground has to be considered prior to the ordering of data, as the local PS densities vary between 40,000 and 100,000 PS/km^2 in the analyzed areas. The different parameters are discussed in order to help with the choice of assumed best configuration, depending on the goal and demands of deformation monitoring for the area of interest.

Several deformation phenomena on single buildings within two test sites of Berlin and Munich, Germany, are presented and discussed. The benefits for single object observation due to the high density of PS is demonstrated and the high precision of linear as well as periodic displacement is revealed. The availability of several stacks of the same area allows for an interpretation of motion directions with respect to horizontal as well as vertical directions. Very interesting seasonal patterns are discovered at Berlin central train station and the origin of the motion is shown to be related to thermal expansion of the steel construction. Ground truth inspections reveal special constructional devices that enable non-destructive motion at the magnitudes of the observed deformation.

Furthermore, the localization precision of point scatterers is investigated by a comparison of theoretical accuracies with real data results of PSI. The regular patterns of PS on facades of modern buildings are used to derive the standard deviations of PS positions, which fit the theoretical assumptions of 2 cm in range, 4 cm in azimuth and 60-140 cm in elevation. By reason of the limited variation of orbital positions the location in elevation direction is available only at a precision by a factor of 20-30 worse than for azimuth or range direction. This is confirmed by the evaluation of PS at several facades of buildings.

Based on the precise 3D localization of PS, a new methodology for a fusion of independently geocoded PS point clouds obtained from stacks of high resolution SAR data is presented. The goal of this approach is a representation of the mapped objects by preferably completed 3D point clouds. It is suitable for a combination of stacks of arbitrary track directions, i.e., especially the gain in information of fusing ascending and descending stacks is accomplished. The unknown relative height offsets of the reference points are solved without the usage of any reference data within the area. The algorithm is based on a least-squares adjustment of selected pairs of PS assumed (but not necessarily) to be identical. After the fusion the majority of buildings are covered by PS on all sides. Hence, single object observation is feasible. The combination of stacks of opposite viewing directions additionally allows for a calculation of motion components in vertical and horizontal directions. A straightforward algorithm is presented and results are provided for one of the test sites. The findings of the initial interpretation of motion directions by a visual comparison of PSI results of different stacks are confirmed and further examples of seasonal displacement in urban areas are provided.

Zusammenfassung

Hochaufgelöste Radardaten, wie sie beispielsweise von dem deutschen Fernerkundungssatellit TerraSAR-X bereitgestellt werden können, eröffnen neue Möglichkeiten für die sogenannte Persistent Scatterer Interferometrie (PSI). Diese ermöglicht v.a. in urbanen Regionen nahezu flächenhafte Messungen der Oberflächendeformation im Bereich von wenigen Millimetern im Jahr. Die Vorteile dieser neuen Klasse von Radardaten für diese Methode werden in der Arbeit untersucht und bewertet. Durch die sehr hohe Auflösung ist – im Vergleich zu Daten bisheriger synthetische Apertur Radar (SAR) Satelliten, wie z.B. ERS oder ENVISAT – ein sehr großer Anstieg der zur Verfügung stehenden Punktstreuer (sog. Persistent Scatterers, PS) zu erwarten. Daher wird zunächst der Einfluss unterschiedlicher Aufnahmeparameter hinsichtlich des Auftretens der PS untersucht. Anhand von mehreren Beispielen wird gezeigt, dass die Geometrie der Aufnahmekonfiguration sowie die Anordnung und Beschaffenheit der Objekte in der Szene vor der Datenbestellung berücksichtigt werden müssen. Diese Parameter beeinflussen die lokalen PS Punktdichten, welche je nach geometrischer Konstellation zwischen 40.000 und 100.000 PS/km^2 variieren. Die Erkenntnisse sind hilfreich für eine optimale Wahl der Aufnahmeparameter bezüglich der Anforderungen der Deformationsmessung.

Im Rahmen der Arbeit werden mehrere Deformationseffekte an Einzelgebäuden in zwei Testgebieten (Berlin und München) untersucht. Des Weiteren wird der Vorteil der hohen PS Flächenabdeckung für eine Einzelobjektüberwachung demonstriert und die hohe Genauigkeit der linearen sowie periodischen Bewegungsschätzung deutlich gemacht. Die Verfügbarkeit von mehreren Datenstapeln des gleichen Gebiets ermöglicht eine Interpretation der Bewegungsrichtungen in horizontaler und vertikaler Richtung. Am Berliner Hauptbahnhof liegen sehr interessante periodische Bewegungsmuster vor, welche auf eine thermische Ausdehnung der Stahlkonstruktion zurückgeführt werden können. Eine Untersuchung der Konstruktion vor Ort zeigt die baulichen Details, die die Bewegung mit den beobachteten Amplituden erklären. Diese erlauben eine thermische Deformation ohne zu einer Zerstörung der Anlage zu führen.

Die theoretische relative Lokalisierungsgenauigkeit der Punktstreuer wird anhand einer Studie von gleichmäßig angeordneten PS an Fassaden überprüft. Diese regelmäßigen Muster entstehen durch die Anordnung von Fensterreihen in den jeweiligen Stockwerken von Gebäuden, welche zu den entsprechenden Signaturen in den Radarbildern führen. Die Standardabweichungen der relativen Positionen solcher Punkte in einer Reihe bestätigen die theoretisch abgeleiteten Werte von 2 cm in Range, 4 cm in Azimuth und 60-140 cm in Elevation. Die Positionen in Elevationsrichtung sind dabei aufgrund der beschränkten Variation der Satellitenbahnen um Faktor 20-30 schlechter bestimmbar als in Azimuth oder Range.

Auf die 3D-Lokalisation aufbauend wird eine neue Methode zur Fusion von PS Punktwolken präsentiert – mit dem Ziel, die abgebildeten Objekte mit möglichst vollständigen 3D Punktwolken zu repräsentieren. Die Ausgangsdaten werden dabei durch unabhängige PSI Prozessierungen inklusive Geokodierung der Punkte von unterschiedlichen Datenstapeln erzeugt. Der Algorithmus erlaubt eine Zusammenführung von Ergebnissen aus Daten, welche aus beliebigen Flugrichtungen aufgenommen sind, d.h. es wird vor allem eine Fusion von PS aus Stapeln von aufsteigenden und absteigenden Bahnen erzielt. Dadurch kann der Informationsgehalt der Ergebnisse deutlich gesteigert werden. Die unbekannten Höhenzuschläge der Referenzpunkte werden dabei ohne zusätzliche Referenzdaten aus dem jeweiligen Gebiet bestimmt. Der Algorithmus basiert auf einer kleinsten-Quadrate Ausgleichung, in der korrespondierende Punktpaare aus beiden Punktwolken zur Minimierung der jeweiligen Distanzen herangezogen werden. Die selektierten PS werden dabei als identisch angenommen. Nach der Fusion sind bei den meisten Gebäuden PS auf allen Flächen vorhanden. Daher ist eine Einzelobjektüberwachung realisierbar. Zusätzlich ermöglicht die Fusion von Stapeln entgegengesetzter Flugrichtung eine Trennung der horizontalen und vertikalen Bewegungsanteile. Ein geeigneter, unkomplizierter Algorithmus sowie Ergebnisse eines Testgebiets werden gezeigt. Die Ergebnisse der Interpretation von Bewegungsschätzungen unterschiedlicher Stapel können dadurch validiert und exakt berechnet werden. Mehrere Beispiele verdeutlichen den Gewinn an Information zu Deformationen in städtischen Gebieten.

Contents

Nomenclature

Abbreviations

APS	Atmospheric Phase Screen
CPT	Coherent Pixels Technique
DEM	Digital Elevation Model
DB	Deutsche Bahn (German railroads company)
dInSAR	differential InSAR
DSM	Digital Surface Model
EEC	Enhanced Ellipsoid Corrected
GEC	Geocoded Ellipsoid Corrected
GPS	Global Positioning System
ILS	Integer Least-Squares
InSAR	Interferometrical SAR
LAMBDA	Least-squares AMBiguity Decorrelation Adjustment
LOS	Line of Sight
meanmap	temporal average image (amplitudes)
MGD	Multilook Ground range Detected
PhU	Phase Unwrapping
PRF	Pulse Repetition Frequency
PS	Persistent Scatterer
PSP	Persistent Scatterer Pairs
PSC	Persistent Scatterer Candidate
PSI	Persistent Scatterer Interferometry
PSI-GENESIS	PSI module of Generic System for Interferometric SAR of DLR
PSIC4	Persistent Scatterer Interferometry Codes Cross-Comparison And Certification
RADAR	Radio Detection and Ranging
RANSAC	Random Sample Consensus
RCS	Radar Cross Section
rms	root mean square
rmse	root mean square error
SA	Synthetic Aperture
SAR	Synthetic Aperture Radar
SBAS	Small Baseline Subsets Algorithm
SCR	Signal-to-Clutter Ratio
SLC	Single Look Complex
SNR	Signal-to-Noise Ratio
SSC	Slant range Single look Complex (equivalent to SLC)
StaMPS	Stanford Method of PS
SVD	Singular Value Decomposition
TSMP	TerraSAR Multimode SAR Processor
UTM	Universal Transverse Mercator (map projection)
UTC	Universal Time Coordinated
WGS84	World Geodetic System 1984 (global reference system)

List of Symbols

V	speed of satellite
H	height of satellite above ground
x, y, z	UTM coordinates
Δxy	2D-distance in the xy-plane
$\Delta x, \Delta y, \Delta z$	difference in UTM coordinates (position x, y and height z)
P_{xyz}	3D position in UTM coordinate system
R, X, S	radar coordinates of range, azimuth and elevation
$\vec{s}$	normalized vector of elevation direction
ΔS	difference in elevation coordinates
P_{RXS}	3D position in radar coordinate system
R_S	slant range distance from satellite to ground
t_{Az}	azimuth heading angle (flight direction) with respect to northing
BW	bandwidth of chirp signal
c	speed of light
f_{DC}	Doppler centroid frequency
L_{SA}	length of synthetic aperture
a_{φ_i}	amplitude of complex-valued SAR data
B	baseline between satellites
$B_\perp$	perpendicular baseline
ΔR_{diff}	difference in range distance due to surface deformation
T	temporal baseline
N	number of acquisitions
N_{IFG}	number of interferograms (equal to N-1 for single master stacks)
D_a	amplitude dispersion
$\bar{a}$	mean amplitude
W	window for estimation of coherence
g	signal of clutter
p	signal of PS including clutter
q	signal of PS
h	DEM refinement with respect to height component
Δh	relative DEM refinement with respect to height component
Δv_{LOS}	relative displacement rate in line of sight (LOS)
$\overline{\sigma}_{\Delta v_{LOS}}$	mean standard deviation of relative displacement rate in LOS
Δ_a	number of errors in estimated ambiguities using LAMBDA
$\overline{\Delta}_a$	mean number of errors in estimated ambiguities
$p(t)$	base functions of displacement
t	acquisition time
t_0	temporal offset of seasonal base function
v_{LOS}	velocity projected onto LOS
v_{vert}	vertical component of velocity
v_{grg}	component of velocity in ground range direction
a	vector of integer parameters
b	vector of float parameters
z^*	vector of transformed integer parameters
z_B^*	vector of transformed integer parameters using bootstrapping

e	vector of measurement noise and/or unmodeled errors
y	vector of observations
u	vector of unknowns
v	vector of refinements on observations
w	vector of discrepancy
k_c	vector of correlates
Ω	objective function of LSA
$q_{.i \cdot i}$	element (i,i) of covariance matrix $Q_{.}$
A_i, B_i	design matrices
$M_{x/y/z}$	rotation matrices with respect to x/y/z-axis
Z_i	transformation matrix
$E\{.\}$	expectation value
$D\{.\}$	dispersion value
$Q_{.}$	covariance matrix
$\tilde{e}$	unconstrained residual vector
$\tilde{a}$	real valued ambiguity vector of float solution
$\tilde{b}$	real valued parameter vector of float solution
$\tilde{z}^{*}$	real valued transformed ambiguity vector of float solution
$\tilde{z}^{*}_{n|N}$	conditioned real valued transformed ambiguity vector of float solution
$\check{a}$	integer ambiguity vector
$\check{b}$	float parameter vector of fixed solution
$\tilde{b}|a$	conditional vector of real valued parameters
L	length of steel girder
ΔL	maximum expansion of steel girder
ΔK	temperature difference
k	temperature coefficient of steel
N_P	number of points
ρ_R	range resolution
ρ_{Az}	azimuth resolution
ρ_z	vertical resolution
ρ_{xy}	horizontal resolution in direction of a facade
θ_{la}	look angle
θ_{inc}	incidence angle
ϑ	complex radar data
$\Delta\theta_{Az}$	azimuth steering angle (spotlight mode)
α	coefficient of base function for modeling displacement
α_z	vertical component of displacement
α_x	component of displacement in direction of x-axis
α_y	component of displacement in direction of y-axis
α_{3D}	3D displacement vector
α_p	amplitude of periodic motion
$\Delta\alpha_p$	amplitude of relative periodic motion
β	local height to phase conversion factor
γ	coherence estimate
ι	rotation angle of facade
κ	slope of terrain
λ	wavelength

σ_a	standard deviation of amplitude
$\sigma^2_{\cdot}$	variance
$\sigma_{\Delta points}$	standard deviation of point scatterer position in pixels
$\hat{\sigma}^2_0$	posterior variance factor
$\hat{\sigma}_\phi$	estimate of phase dispersion
υ	complex interferogram
ϕ	interferometric phase
$\Delta\phi$	phase difference
ϕ_{defo}	phase due to surface deformation
ϕ_{orb}	phase induced by orbital errors
ϕ_{prop}	phase delay due to propagation effects in atmosphere
ϕ_{scatt}	phase induced by different scattering within resolution cell
ϕ_{topo}	phase induced by topography
ϕ_ε	phase due to noise
φ	phase of complex SAR data
$\Delta\Phi$	unwrapped phase difference
χ	constant defining size of search space of LAMBDA
ω	parameter in Z-matrix

1   Introduction

1.1   Motivation

Monitoring surface deformation phenomena is an important task for analyzing, understanding and forecasting geodynamical processes. The results and findings will increase safety for all people; sources of damage can be investigated and potential risks can be evaluated, which is essential information for liability and insurance questions as well. Radar satellites are very important sources of remote sensing data, suitable for the previously mentioned task of deformation monitoring. One of the most advantageous properties of these active sensors is the independence of illumination by the sun and the large coverage. In addition, the sensors do not suffer from cloud cover, as the used electromagnetic waves penetrate clouds up to a certain concentration of water vapor. Therefore, these sensors can operate almost at all times and deliver data for almost any investigation of surface motion. Prominent examples for monitoring natural disasters include tectonics, volcanoes, earthquakes and landslides. In times of discussions about anthropogenic global warming, surveillance of sea ice, glacier flows as well as tidal currents depict further scenarios for which radar remote sensing can provide substantial information. Maps showing location and magnitudes of subsidence, uplift or any other directional movement including velocity estimates represent the results of processing radar data for the mentioned goals. These findings may be the initial point for models of geodynamical processes or for the reconstruction and analysis of the preceding incidents of displacement.

In the late 1990s a special method called Permanent Scatterer Interferometry or Persistent Scatterer Interferometry (PSI) for estimating surface deformation has been developed. It is particularly suitable for monitoring subsidence phenomena in urban areas. Certain signatures in the radar images, namely Persistent Scatterers (PS), show a long-term coherent point-like scattering behavior, and hence are suitable for precise motion analysis by interferometry. These points are evaluated within PSI, capable of measuring displacement rates in the order of 1 mm/y. The PSI methodology is based on a sophisticated evaluation of the temporal evolution of phase values, including the removal of different nuisance signals to the radar signal in order to obtain the desired final parameters of displacement values and 3D positions of the PS. Investigations based on medium resolution data (5 m by 25 m) of the European radar satellites ERS and ENVISAT have been carried out successfully in the last decade, covering phenomena of subsidence or uplift due to oil, gas or water extraction (or storage underground), CO_2 sequestration, mining activities, construction of tunnels or loading of dams and dykes, for example. Therefore, this method has been proven to be very powerful for high precision deformation monitoring in urban areas.

Recently launched radar satellites like Radarsat-2, COSMO-SkyMed or TerraSAR-X (including its twin TanDEM-X) now offer far higher resolutions of up to 1.1 m in azimuth by 0.6 m in range direction. Thus, higher levels of details are preserved in the radar images that may be detected as PS. Furthermore, the revisit times of the aforementioned satellites are shorter than the ones of the former generation, sampling the deformation signal of the points under investigation at a higher frequency. Consequently, a certain displacement function can be estimated earlier and at a higher level of detail. The expected large amount of PS on single objects could now allow to monitor single buildings, which has not been possible using data from the previous generation of radar satellites. In order to determine the suitability and performance of radar data of the meter-resolution class for this special task, the influence of acquisition parameters on the appearance of PS has to be investigated. Moreover, real data experiments have to be carried out for analysis of deformation estimates obtainable from PSI at this resolution, and investigations on the precision of 3D positions of the PS will help to support a better understanding of the nature of these points. At last, only a fusion of results from different acquisition geometries will

provide sufficient information in order to cover whole buildings with estimates of deformation on all sides of the object, mandatory for the task of single object observation. The mentioned necessary analyses are addressed in the work at hand in order to analyze the potential of the meter-resolution class of radar data for PSI. The main questions to be answered by this thesis relate to the major advantages of meter-resolution for PSI and are the following:

⋄ How do acquisition parameters influence the density and location of PS?
⋄ What is the physical nature of PS and how precise can their position be determined in three dimensions?
⋄ Which details in deformation and object information can be retrieved from evaluating stacks of meter-resolution data?
⋄ How can multi-track PS results be fused to support single object observation using this new class of meter-resolution SAR sensors?

1.2   Outline

The thesis unfolds as follows: In Section 2, a brief introduction to the acquisition system of synthetic aperture radar is given. In addition, this section provides a description of the fundamentals of radar interferometry, differential SAR interferometry and PSI. An introduction and comparison of different similar methods of PSI and a discussion of recent developments in PSI can be found in Section 3. Subsequently, PSI is applied to meter-resolution SAR in Section 4. Besides system parameters of TerraSAR-X, an overview of the acquired data as well as of the given test sites is provided. Furthermore, the LAMBDA estimator is introduced and its sensitivity is analyzed, showing the expected precision of PSI estimates. Thereafter, the dependence of the number of PS on different acquisition parameters is evaluated. The findings will allow for an optimized choice of the acquisition configurations prior to data ordering for all future investigations based on PSI. Moreover, results of processing high resolution data are shown and the obtained deformation estimates are discussed in detail, in order to investigate the benefit of meter resolution data for PSI. The subsequent section, Section 5, contains analyses of the PS with respect to their location for a better understanding of the physical nature of these points. Furthermore, a fusion of results from different tracks is presented in this section, which will finally reveal the suitability of PSI for monitoring single buildings. The thesis is concluded with a summary and outlook in Section 6.

2 Synthetic Aperture Radar (SAR) and Interferometric SAR (InSAR)

2.1 SAR Principle

In this section the main principle of acquiring synthetic aperture radar (SAR) data and the SAR image properties are described briefly. Terms and definitions are provided as necessary basic information for the subsequent Sections 2.2 and 2.3, in which the detection of deformation phenomena by evaluation of radar data is shown. At first, details on the acquisition principle and resolution of the obtained data are presented (cf. Section 2.1.1). Afterwards, geometrical and radiometrical properties of SAR images are specified in Section 2.1.2.

2.1.1 Acquisition System Principle
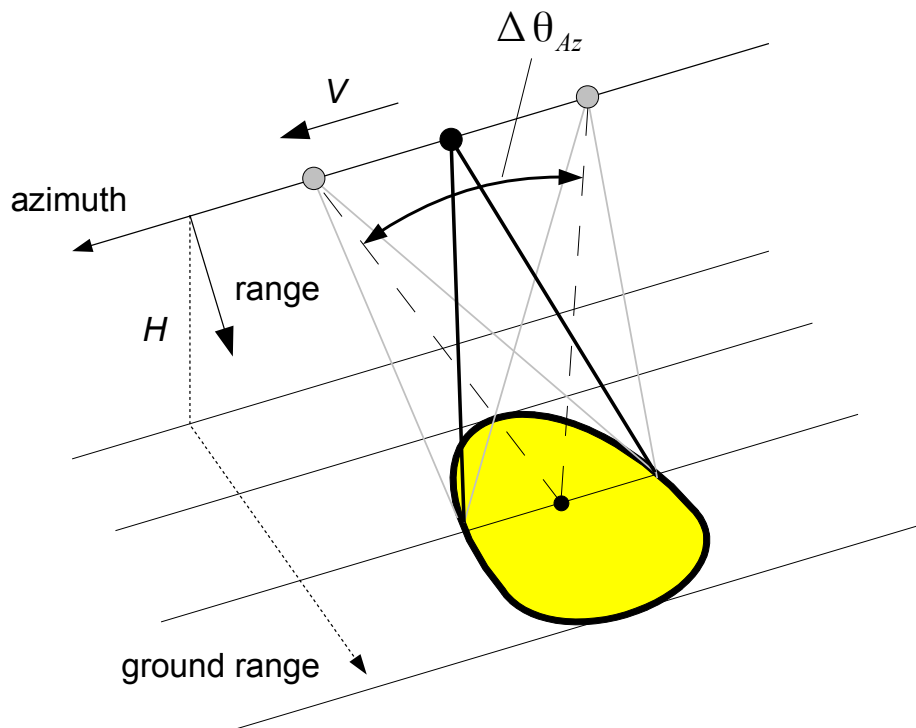
Figure 1. Acquisition geometry of a spotlight SAR system. The side looking sensor (flying at height H with velocity V) illuminates a certain area on ground (yellow part, limited in ground range by its swath width). The scene is mapped to the azimuth - slant range plane (flying direction - look direction). In spotlight mode the resolution is increased by sweeping the azimuth beam backwards (beam steering angle $\Delta\theta_{Az}$) in order to extend illumination time of each scatterer.

Radar (abbreviation: RAdio Detection And Ranging) is an active remote sensing system, which acquires data by sending and receiving microwave signals. The main goal is the detection of targets with their distance or rather range position. In principle any frequency may be used, but microwaves are most common (Skolnik, 1990). For SAR satellite remote sensing, especially L-, C- and X-band radar systems are favored in general. Therefore, the typically used wavelength are 15-30 cm (L-band), 3.8-7.5 cm (C-band) and 2.4-3.8 cm (X-band). The spotlight acquisition geometry is shown in Figure 1. The radar instrument is installed for a side looking geometry in order to prevent range ambiguities and unwanted high level signals from vertical ground reflections. The flight direction of the satellite is defined as azimuth axis X, the looking direction of the instrument is denoted as (slant) range axis R. Signals are transmitted from

the satellite at a certain repetition rate, called pulse repetition frequency (PRF), reflected from ground and received again by the instrument. The signal itself travels close to the speed of light. Slight deviations from the speed of light are due to the refraction properties of the atmosphere. One major advantage of radar systems compared to optical sensors is their penetration of clouds and their independence of ground illumination by the sun, a typical property of active systems. Therefore, data can be acquired at almost any time and during almost any weather conditions.

Figure 2. Temporal mean image of an urban area in Berlin, Germany, generated from several datasets of comparable acquisition geometry. Acquired by TerraSAR-X in high resolution spotlight mode, VV polarization.

A temporal (incoherent) amplitude average SAR image of an urban area in Berlin is shown in Figure 2. It is generated from several datasets of different acquisition times, but of comparable acquisition geometries using TerraSAR-X high resolution spotlight mode. The inherent range resolution ρ_R is 0.6 m, given by the bandwidth BW (300 MHz) of the chirp signal (Cumming and Wong, 2005):

$$\rho_R = \frac{c}{2 \cdot BW} \qquad (1)$$

The azimuth resolution ρ_{Az} is 1.1 m and depends for the (sliding or staring) spotlight mode at hand on the wavelength of the signal λ and the variation of squint angle $\Delta\theta_{Az}$ during the acquisition (Klausing and Holpp, 2000):

$$\rho_{Az} = \frac{\lambda}{2 \cdot \Delta\theta_{Az}} \qquad (2)$$

In the given case of TerraSAR-X, the wavelength is 0.031 m and the beam steering angle range is ±0.75° (Eineder et al., 2009).

The resulting signal that is received after pulse compression is a *sinc*-function. Hence, besides the main lobe of the returned signal side lobes occur in the acquired data. The latter consist of amplitude, as well as phase values of the returned echos, that is measured comparing the received signal to a precise reference signal and timer onboard the satellite (coherent imaging). In general, the amplitude represents the reflectivity of the scene, depending on the roughness and geometry of the targets, and the phase value carries information on the distance of a scatterer to the sensor. Hence, the phase information stored for every pixel is of great importance for any determination of deformation or topography, as will be shown in Sections 2.2 and 2.3.

Detailed information on technical aspects of image formation from raw satellite data can be found in Cumming and Wong (2005), Klausing and Holpp (2000), Henderson and Lewis (1998) and Skolnik (1990).

2.1.2   Geometrical and Radiometrical Effects in SAR Images
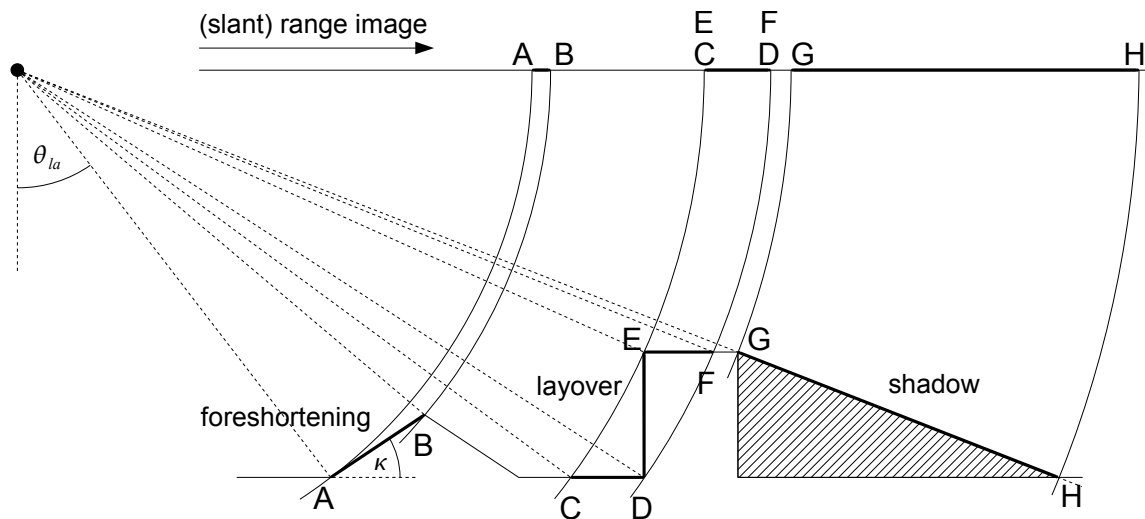
Figure 3. Geometrical effects in SAR images. Distance between A-B is compressed in the slant range image (foreshortening). Areas C-D, D-E and E-F are mapped into the same range cells (layover). None of the surfaces between G and H are illuminated by the sensor, which results in empty range cells in the radar image (radar shadow). Two important parameters are look angle of the sensor θ_{la} and slope of terrain κ.

In a radar image, the 3D objects of the scene are mapped to a 2D image. The radar principle to record objects by distances combined with the side-looking observation geometry of a SAR sensor causes the scene to look different in the resulting images than in pictures obtained by optical sensors. Each azimuth row in the acquired data consists of the signal returns of the objects on ground mapped only by their range distance – the radar sensor is not able to record any information about look angles. In Figure 3 the geometrical effects appearing in SAR images are illustrated. Radar shadow is created by jumps in range distances between objects due to invisible surfaces, dependent on the geometry of the scene and the look angle of the sensor. No data is available for these regions, as no reflections are recorded between the two range distances (cf. area between G and H). This part appears black in the radar amplitude image (with the exception of thermal noise influences). Area A-B in Figure 3 is affected by foreshortening; the distance between two points is shortened due to the projection of the surface onto the slant range direction. This effect occurs for surfaces oriented towards the sensor with a terrain slope κ smaller than the look angle θ_{la} or if the slope of terrain is oriented away from the sensor with an angle smaller than $90° - \theta_{la}$ (otherwise shadow). For larger slopes of terrain oriented towards the sensor ($\kappa > \theta_{la}$), the third effect appears (cf. area C-D-E-F); Several areas are mapped on the same locations in the radar image, e.g., the ground in front of a house (C-D), the facade

(D-E) and parts of the roof (E-F) are overlaid in the slant range image, and consequently this effect is called layover. These parts of the resulting radar image appear relatively bright due to the aggregation of the different contributions. All three effects depend on the look angle of the satellite and the geometry and objects within the scene. For small look angles, i.e., steep look directions, the layover effect dominates, whereas shadow areas are quite limited in dimension. It is the other way around for large look angles, i.e., shallow look directions; layover areas are smaller, while the parts of the data affected by shadow increase.

The brightness of a pixel in the final amplitude image depends on the scattering mechanisms within the scene and within one resolution cell. The radar signal either returns directly after hitting the surface (single bounce) or is reflected a number of times before returning to the sensor. Especially double, triple and multiple bounce effects are dominating visual interpretations of urban scenes, due to their high signal return. Double bounce often occurs between horizontal and vertical planes, a typical structure of urban areas, which results in the presence of many bright double bounce signatures along the base lines of building facades oriented parallel to the sensor heading. The high amplitudes observed are caused by the concentration of the signal return from all specular reflections of the configurations facade-ground and ground-facade at one single range direction – the position of the corner line constructed by the two planes. This effect can be explained by the identical distance of the traversed signals for all these reflections. Therefore, all return signals from facade to ground and back are mapped to one single range cell: at the intersection between both planes. Triple reflections are other prominent examples for scattering mechanisms in cities. Their geometrical configuration corresponds to a corner reflector (trihedral) constructed from three perpendicular aligned planes that give a strong return signal independent of the look direction, comparable to the principle of a retro-reflector. Analog to the description of double bounce signal concentration, any signal hitting the trihedral will cover the same distance. The result is one very bright point scatterer. Examples of the aforementioned scattering mechanisms and their explanation by SAR image simulations are shown in Auer et al. (2010a).

Besides the influence on signal amplitudes due to geometrical scattering effects described above, the intensity of the returned signal shows a granular texture on homogeneous areas. This pattern is often referred to as speckle effect and is the result of random positive and negative interferences within one resolution cell. The final intensity of the signal return depends on the local small scale scattering. The speckle effect can be reduced by spatial filtering methods (see, e.g., Lee (1981)). It also vanishes in general, if temporal mean images are created from several acquisitions of the same area. In high resolution imagery speckle is less severe, because the number of scattering events in a resolution cell is lower. Consequently, the scattered signal is more deterministic.

The radar return of targets therefore is dependent on the acquisition geometry and the properties of the target itself. In addition, strong signal returns are affected by high power side lobes caused by discontinuities at the margins of the signal spectrum. These cause bright pixel patterns along azimuth and range directions. This effect may be reduced by a detection and removal of potential side lobes, called side lobe suppression (see Breit et al. (2008) for more details).

2.2 Deformation Estimation using SAR Interferometry

SAR interferometry can be used for the detection of surface deformation and the generation of digital elevation models (DEMs). In both cases the phase differences between two SAR images are investigated. In Section 2.2.1, the principles of InSAR are briefly explained. The derivation of deformation patterns by applying differential InSAR (dInSAR) and the challenges of this technique are addressed in Section 2.2.2.

2.2.1 SAR Interferometry (InSAR)

In principle, across-track interferometry is based on the exploitation of phase differences of two complex-valued SAR datasets. The latter are acquired from varying positions perpendicular to the flight direction and, in the case of repeat pass interferometry, at different times (cf. Figure 5, left part). Meeting these requirements, differential SAR interferometry (dInSAR) can be applied in order to extract surface deformation, which is addressed in the next section.

Basically, an interferogram contains information about topography and/or movement between two SAR acquisitions covering the same area. It can be applied due to the coherent principle of SAR, i.e., amplitude and phase data is available for every pixel. For PSI, no spectral shift filtering has to be applied, because the phase of exclusively point targets is evaluated. Before interferogram formation, the two datasets have to be co-registered precisely, and one of the datasets (called Slave) has to be resampled to the respective other one (called Master). This step is carried out by using correlation techniques and precise polynomial transformations in order to ensure good quality of the differential phase information. Commonly, one tenth of the resolution cell is the goal to achieve for correlation precision. For meter-resolution datasets of TerraSAR-X topography variations (about 100 m for typical baselines) and even larger displacement (approx. greater than 6 cm) have to be considered in this step to ensure good coherence (Eineder et al., 2008), which is a measure for interferogram quality. With the help of the obtained parameters of co-registration, the Slave data can be transformed to the acquisition geometry of the Master. Finally, the complex interferogram can be calculated from the complex-valued data ϑ_1 and ϑ_2 of the two SAR datasets by a multiplication of one dataset by the complex conjugated of the second one, assuming equal scattering within corresponding resolution cells:

$$v = \vartheta_1 \cdot \vartheta_2^* = a_{\varphi_1} \cdot a_{\varphi_2} \cdot exp(-j\frac{2\pi}{\lambda}\Delta R) \tag{3}$$

The multiplication in Equation (3) corresponds to a convolution in spectral domain. To avoid aliasing effects, both datasets are oversampled prior to this calculation. The interferometric phase of one pixel is dependent on the range distance difference ΔR between the two sensor positions and the surface.

Phase measurements are by definition limited to the interval $[-\pi, \pi[$ (one fringe) and ambiguous to within integer multiples of 2π, hence, a continuous color-wheel is used for visualization purposes, in general. The interferometric phase ϕ is a relative measure, because the absolute range distance is not included. An interferogram can be regarded as an instrument for measuring look angles, as SAR initially does not include this information in the data. Hence, the missing third coordinate besides azimuth and range in order to fix one point in 3D space is available from across track baseline interferograms. These products allow for the derivation of (relative) heights, if the flat earth phase pattern is removed correctly. In general, a reference ellipsoid is used to correct the interferogram for the mentioned flat earth pattern. The resulting fringes now show the local topography of the scene. An example of phase information prior and after

this correction is given in Figures 4a and 4b. The height sensitivity mainly depends on the perpendicular baseline $B_\perp$ for across track constellations (Bamler and Hartl, 1998):

$$\frac{\partial \phi}{\partial z} = \frac{4\pi}{\lambda} \frac{B_\perp}{R_S \sin \theta} \tag{4}$$

The quality of the obtained interferogram can be estimated by the calculation of the coherence, i.e., the local correlation between the two datasets within a small window W (m rows, n columns) around the point of interest. It is calculated for all pixels of the interferogram using the following equation:

$$\gamma = \frac{\sum\limits_{W} y_1[m,n] \, y_2^*[m,n]}{\sqrt{\sum\limits_{W} |y_1[m,n]|^2 \, \sum\limits_{W} |y_2[m,n]|^2}} \tag{5}$$

The results are in the interval $[0,1]$, whereas high values close to 1 denote good phase quality and low values have to be interpreted as loss of coherence; in this case, the phase values are disturbed by different error and noise sources and do not contain any valuable information that could be used for the extraction of local terrain heights. Some examples for these kinds of error sources are the following: receiver noise, propagation effects, temporal and spatial decorrelation or surface deformation. These effects are addressed to in more detail in the next section. In addition, interferograms can be affected by orbital errors, which can be detected by the appearance of residual phase ramps in the obtained interferogram. In general, this effect can be estimated and removed subsequently from the data (Massonnet and Feigl, 1998; Hanssen, 2001).

The corrected interferogram has to be unwrapped and geocoded in a final step to obtain absolute information about the topography of the area. Phase unwrapping (PhU) algorithms are used to unwrap the interferogram, i.e., mapping the phase values of the interval $[-\pi, \pi[$ to relative heights with respect to a reference point in the scene (cf. Figures 4c and 4d). The main difficulties arise from the inherent phase noise, hence, complex and intelligent processing schemes are necessary to solve this task efficiently and accurately. More details on this topic can be found in, e.g., Bamler and Hartl (1998), Hanssen (2001), Eineder and Adam (2005) and Pepe and Lanari (2006). Finally the unwrapped data is geocoded; the obtained topography is transformed into a geodetic reference system, like WGS84. For this task, precise orbit information, the desired reference ellipsoid and the acquisition geometry parameters are used to transform the radar coordinates. Different methods can be found in, e.g., Hellwich and Ebner (2000) and Eineder and Adam (2005).

2.2.2 Differential SAR Interferometry (dInSAR)

Besides the extraction of information about topography SAR interferometry can be used for the detection of surface deformation. From Figure 5 it becomes evident, that any shift of the surface between the acquisitions of the InSAR partners in terms of position will result in a change in range distance. The latter results in the following phase contribution:

$$\phi_{defo} = \frac{4\pi}{\lambda} \Delta R_{diff} \tag{6}$$

If the topographic phase is removed from the interferogram, the phase caused by surface deformation ϕ_{defo} can be obtained. This task can be accomplished either by a two-pass or three-pass method, i.e., either a given DEM is used for this task or the topography is derived using one interferogram of the area (Hanssen, 2001). The geometrical configuration of InSAR restricts
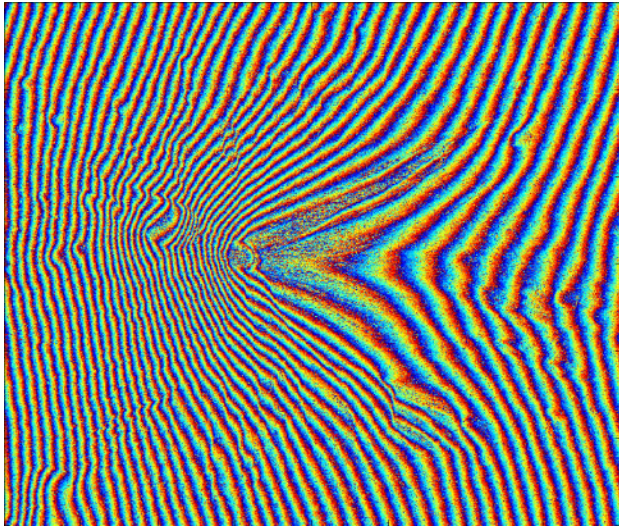
(a) Interferogram of a volcano including flat earth phase.
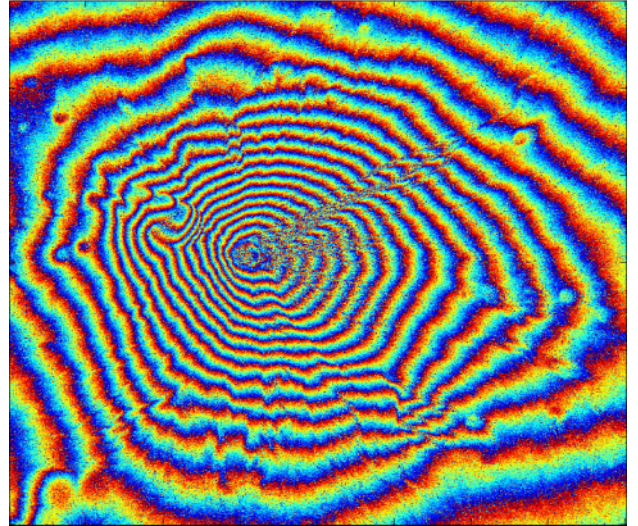
(b) Interferometric phase of the volcano after correction of the phase pattern induced by the reference surface (flat earth phase).
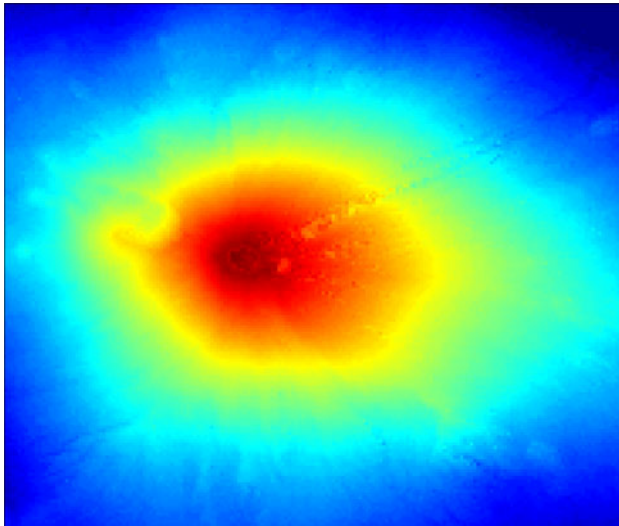
(c) Top view on the DEM of the volcano after phase unwrapping. Colors correspond to relative heights between 0 m (blue) and approximately 2600 m (dark red).
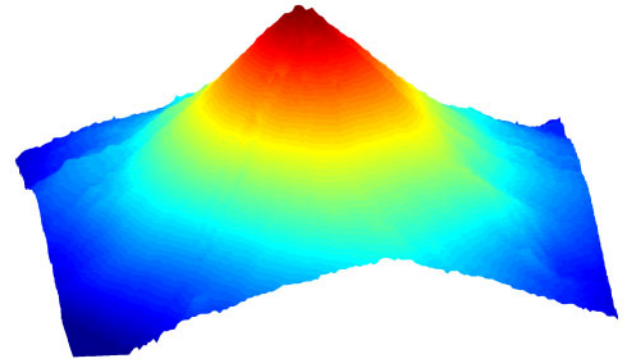
(d) Side view on the DEM of the volcano. Colorcoding of heights like in Figure 4c.

Figure 4. Interferogram before and after removal of the fringe pattern induced by the reference surface (reference ellipsoid in general). Note that only after the subtraction of this pattern the topography becomes evident. In addition, the DEM of the area (calculated by unwrapping the interferogram) is shown in the lower two plots.

the detection of any movements to the component projected in line of sight (LOS), as only changes in range direction will manifest in a change in phase. Hence, from one dInSAR dataset the 3D motion vector cannot be extracted. In general vertical (v_{vert}) or horizontal (v_{grg}, component along ground range direction) motion components are reconstructed from the measured LOS deformation ($v_{LOS} = \Delta R_{diff}/\Delta t$), according to a priori information about the underlying movements and the assumed major direction of deformation:

$$v_{vert} = \frac{v_{LOS}}{\cos \theta} \tag{7}$$

$$v_{grg} = \frac{v_{LOS}}{\sin \theta} \tag{8}$$

Changes in phase can be detected very precisely using interferometry, thus, deformation can be measured as a fraction of the wavelength. But there are additional error sources that have to be considered and eliminated, if feasible. For repeat-pass interferometry, i.e., data acquired at different times, the interferometric phase ϕ is composed of the following terms:

$$\phi = \phi_{topo} + \phi_{defo} + \phi_{prop} + \phi_{orb} + \phi_{scatt} + \phi_{\varepsilon} \tag{9}$$

ϕ_{topo} and ϕ_{defo} represent phase contributions of topography and ground motion respectively and ϕ_{ε} corresponds to phase noise. ϕ_{prop} is an additional phase term originating from differences in propagation delays between the times of acquisitions; ionospheric phase delays are dependent on the wavelength of the signal and the total electron content (TEC) at the time of acquisition. The distribution of this effect is quite homogeneous and changes little on large areas, thus, the delay allows for stochastic modeling, if necessary (Hanssen, 2001). Tropospheric delays vary at higher frequency within one scene (turbulent mixing; correlation length about 1 km). In sum, propagation effects are frequently observed to be in the order of about a quarter of a wavelength delay in ERS interferograms (Bamler and Hartl, 1998).

ϕ_{orb} includes errors due to deviations from the used orbital positions, which can be removed almost completely by a utilization of precise orbit information or by a detrending procedure (Hanssen, 2001). In addition, variations in the scattering mechanisms ϕ_{scatt} within the resolution cell affect dInSAR analyses and even may disable any investigation based on phase information. The effects can be separated into temporal and geometrical decorrelation. Especially in vegetated areas, temporal changes of the objects participating in the scattering within the resolution cell occur within short time intervals, hence, lead to decorrelation and loss of usable information. Furthermore, different orbital positions also may evoke loss of coherence, because of changing acquisition geometry and therefore possibly different scattering processes. The effect of geometrical decorrelation is related to the spatial baseline between the acquisitions. To overcome these limitations a new method has been proposed, called permanent scatterer interferometry, which will be introduced in the next section.
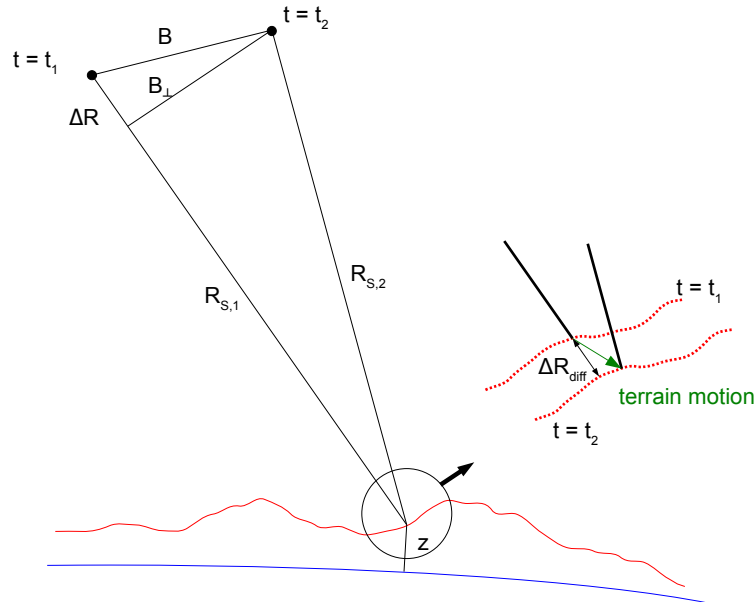
Figure 5. Influence of surface deformation on the interferometric phase. Change in range ΔR_{diff} due to terrain motion between acquisitions at times t_1 and t_2

2.3   Deformation Estimation using Persistent Scatterer Interferometry (PSI)

In the late 1990s, Ferretti, Prati and Rocca developed a new technique at the Politecnico di Milano, Italy, in order to overcome the limitations of deformation monitoring using dInSAR. In the following years, different scientists developed several comparable approaches, based on the same idea; the analysis is carried out only on a subset of pixels, the so called permanent or persistent scatterers (PS), assumed to feature stable phase values throughout the whole time series of datasets. Consequently, the deformation history is likely to be extractable due to the absence of decorrelation noise. The analysis may cover several years and even exhibit large geometrical baselines. In the following section, the basic idea of this method will be presented. Details on the processing chain, as implemented at the German Aerospace Center (DLR), are shown in Section 2.3.2, because all the investigations presented in the context of this work are based on results created from this particular processing system.

2.3.1   Original Implementation and Estimation Principle

Temporal and geometrical decorrelation limit the operational usage of InSAR to short baselines in time and space. In addition, interferograms suffer from atmospheric disturbances (mainly of tropospheric origin), which distort the deformation estimates or even turn the analyses to become useless. To overcome these limitations, the method of persistent scatterer interferometry (PSI) has been introduced by Alessandro Ferretti and his colleagues (Ferretti et al., 2000, 2001). This method is based on a whole stack of SAR data of the same area, typically consisting of tens of datasets. From this stack one single master acquisition is selected, considering baselines in time and space in a way to ensure high coherence in all interferograms formed over the stack. Additionally, the estimation is carried out on a reduced set of pixels in order to minimize temporal and geometrical decorrelation effects. The temporal sampling of the data should be regular to some degree, but at least should not suffer from larger gaps and may cover several years. In addition, a DEM of the area is needed, that can either be generated from one suitable interferogram available from the data, or an external data source may be used. The DEM is needed for the removal of topography-induced phase terms prior to PS processing. An accuracy of about 20 m of the DEM is mentioned to be sufficient (Ferretti et al., 2001), but even a horizontal plane can be used (Colesanti et al., 2003), as the DEM is refined at PS positions during the estimation procedure. The remaining interferometric phase is modeled as the sum of possible target motion in line of sight ϕ_{defo}, residual topographic phase contribution ϕ_{topo} due to height variations not represented within the DEM used (e.g., buildings), atmospheric phase contributions ϕ_{prop} and decorrelation noise ϕ_{ε}:

$$\phi = \phi_{topo} + \phi_{prop} + \phi_{defo} + \phi_{\varepsilon} \tag{10}$$

Previous to the estimation procedure, the subset of pixels - the PS - has to be selected. In the original implementation the amplitude dispersion index D_a is used as a criterion for the selection of appropriate pixels, as it is an estimate of the phase dispersion $\hat{\sigma}_\phi$ as follows (Ferretti et al., 2001):

$$D_a = \frac{\sigma_a}{\bar{a}} = \hat{\sigma}_\phi \tag{11}$$

Hence, with the help of the standard deviation σ_a of the amplitude a and its mean value $\bar{a}$, the index can be calculated and pixels below a certain threshold ($D_a < 0.25$, see Ferretti et al. (2001)) are selected as PS candidates for the first iteration. These pixels are assumed

to feature stable phase values in time due to one dominant scatterer within the resolution cell, whose deformation time series can be determined. On this very sparse distribution of points, the atmospheric phase contributions are estimated for every interferogram. The interpolated map of ϕ_{prop} for the whole area is called atmospheric phase screen (APS). The mean value of these results hold the atmospheric phase contributions relative to the master acquisition. This is based on the assumption of zero mean APS for large stacks of SAR data. Hence, the quality of the calculated master APS depends on the number of available images and the validity of random atmospheric phase contributions in time. The APS of every single dataset can be calculated by simple subtraction of the master atmospheric phase contributions from the estimated ones of each interferogram, in order to remove these disturbing effects from all datasets. For a proper estimation and removal of these effects, at least 25 images are needed in addition to a PS density of about 5-10 PS/km^2 (Colesanti et al., 2003). Prior to the motion estimation a deformation model has to be introduced. Very often, it is modeled as a linear function of time, but also seasonal or progressive motion (Colesanti et al., 2003), or even any other non-linear motion (Ferretti et al., 2000) may be introduced, whereas more complex models will increase the computational effort. For this chapter a linear model is assumed to be sufficient, later on seasonal motion will be used in addition. Finally, the DEM refinement h (often also called DEM error) and the target velocity v can be estimated. This is accomplished by a maximization of the ensemble phase coherence γ of each pixel for all k interferograms:

$$\arg\max\left\{|\gamma| = \left|\frac{1}{K}\sum_{k=1}^{K} e^{j\phi_k} \cdot e^{-j(-\beta \cdot h + \frac{4\pi}{\lambda} T_k \cdot v_{LOS})}\right|\right\} \tag{12}$$

Equation (12) represents a periodogram, solved simply by a comparison of the measured phase ϕ_k in each interferogram to a sampled solution space of the unknown parameters and the detection of the best fit. The height-to-phase conversion factor is given by $\beta = -4\pi B_\perp/(\lambda R \sin\theta)$ and T_k is the temporal baseline. The calculation is carried out on a pixel by pixel basis and all points showing small residual phases with respect to the selected deformation model are included in the final results as additional PS. One major restriction of the initially proposed method arises from the assumption for an estimation of atmospheric phase contributions as a linear function in space, which is only valid for small areas (approx. 5 km x 5 km). To avoid this limitation, relative motion and relative DEM refinements are calculated in a first step between short range pairs of PS in later implementations of the PS technique (Ferretti et al., 2000). Therefore, the phase residuals have to be unwrapped using a weighted least square integration approach in order to subsequently isolate the atmospheric phase contributions by a filtering process (the effect is assumed to be correlated in space but uncorrelated in time). Finally, the estimated contributions are removed as mentioned before and the final estimation of motion and DEM refinements can be carried out following the initial approach. Analytically and experimentally the accuracy of the average deformation rate has been proven to be in the sub-millimeter/year domain (Colesanti et al., 2003). As consequence of the method for PS selection, especially bright pixels in the temporal mean image of the amplitudes represent potential PS candidates. These appear most likely in cities, as many manmade structures provide scattering signatures stable over time and are additionally less sensitive to acquisition geometry changes (variation of the baseline). Therefore, the method of persistent scatterers is especially applicable for urban areas.

2.3.2 Processing Scheme using ERS Data

All results presented in the context of this study have been created by using the PSI module of the GENEric System for Interferometric SAR (PSI-GENESIS) of DLR, introduced by Adam et al. (2003). The system has been proven to be free of systematic errors. Thus, it has been chosen as reference processing system for the product validation of different operational service

providers, which offer PS processing for end users (Adam et al., 2009). A detailed comprehensive description of the processing system can be found in Kampes (2006). In the following section, a brief overview on the single working steps by means of an example PSI processing is given. The area of interest has been restricted to the urban area of Munich, Germany (approx. 25 km x 20 km). Altogether 68 data takes have been used in this example, acquired by the European remote sensing satellites ERS-1 and ERS-2 and covering a time interval between April 1995 and January 2001. The work flow of the processing chain can be seen in Figure 6 and will be described in more detail in the following.
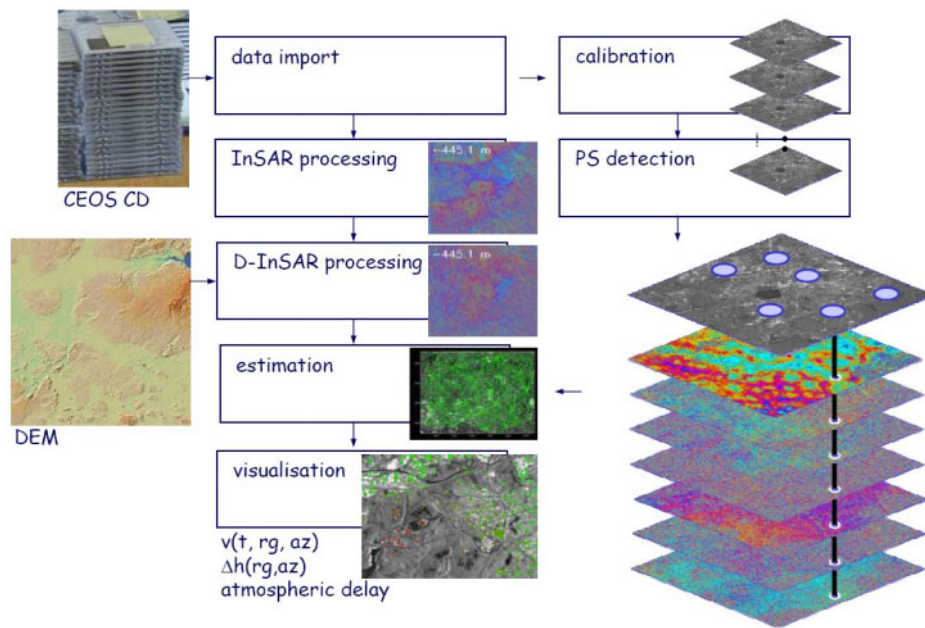
Figure 6. Flow chart of PSI estimation, proposed by Adam et al. (2003).

InSAR Stacking and Detection of Persistent Scatterers (PS)

At first, all desired single look complex (SLC) SAR data have to be prepared. It is provided on media (CD-ROM/DVD) or via download link by the corresponding processing facility of the satellite data. Typically, the size of one complex-valued dataset is about 500 MB, hence, a stack of 50 scenes occupies about 25 GB of disk space. If the investigation will be conducted only on parts of the whole scene, the import to the processing system will allow the area of interest to be defined. At the same time, a reference DEM of the scene is necessary in order to properly remove (approximately) any topography-induced phase components. As already mentioned, there exist three different alternatives; either calculate a DEM from two given scenes, or use an available DEM from different data sources. From shuttle radar topography mission (SRTM), e.g., there exist DEMs of sufficient accuracy for arbitrary areas between -56° and +60° of latitude. The third possibility is the usage of a horizontal plane at the elevation of, e.g., ground position, as for every PS position a DEM refinement is estimated additionally. Even highly accurate DEMs do not allow for a complete removal of phase values created by topography, as the phase centers of the PS are not known in advance. For the test site at hand, a height model obtained from the SRTM mission is used. In a next step, the master scene has to be chosen considering the distribution of temporal and spatial baselines. In Figure 7, the baseline plot of the given data for the Munich test site can be seen with the master selected in March 1998, indicated by a circle. The master is selected in a way to ensure a high stack coherence, which is achieved for a dataset selected approximately centrally within the distribution of the temporal baseline, and essentially in the center of the perpendicular

and Doppler baseline (Kampes, 2006). As soon as the master has been chosen, the interfero-metric processing can be performed. In addition, the data is oversampled by a factor of two prior to interferogram formation. The co-registration of the slave images to the master one is accomplished by a combination of retrieving the necessary transformation parameters from precise orbit and DEM data and a point scatterer matching procedure between master and slave acquisitions (Adam et al., 2003). Subsequently, a polynomial based transformation of all slave images to the acquisition geometry of the master is performed (including a resampling of the slave images) before the generation of all interferograms with respect to one identical master is initiated. Afterwards, a simulated interferogram based on orbit information and the available DEM is generated and used to remove the topography induced phase. Some resulting differential interferograms and their corresponding estimated coherence can be seen in Figure 8. Decorrelation effects increase more rapidly for interferograms of larger perpendicular baselines than for increasing temporal baselines. This effect shows the high dependence of scattering mechanisms on geometry, rather than on temporal influences for urban areas with a low degree of vegetation. Nevertheless, analyses of single point phases even from images of large perpen-dicular baselines can be performed using PSI, as the phases of isolated points are evaluable, if a single strong and stable scatterer is present within the resolution cell.
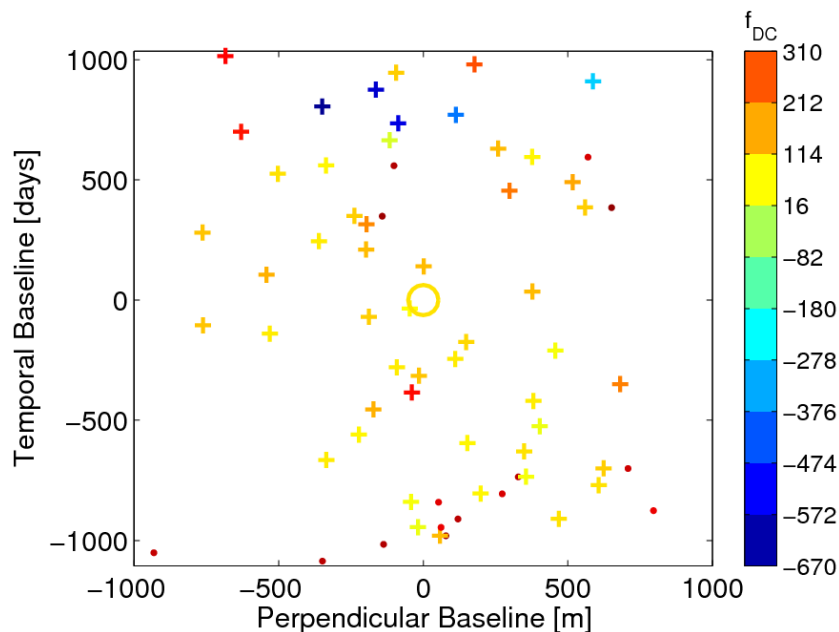
Figure 7. Plot of the distribution of the acquisitions in time and perpendicular baseline space with respect to the selected master scene (circle). Dots and crosses represent data of ERS-1 and ERS-2 respectively. Colors indicate Dopper centriod frequencies (squint angles).

In order to remove most of any remaining phase contributions due to orbital errors, precise orbit information provided by Geoforschungszentrum Potsdam (GFZ) is used. The residual phases caused by limited precision of these orbits are assumed to be negligible (Kampes, 2006).

Within PSI-GENESIS the PS can be detected by thresholding the amplitude dispersion index (cf. Equation (11)) or by evaluating the signal to clutter ratio (SCR) of pixels in the temporal mean image. Both methods are estimators for the phase error of point scatterers. The SCR method has been proven to be more robust (Adam et al., 2004), and hence, the latter is used in most of the cases, which estimates the clutter from neighboring pixels using a certain (spatial) estimation window. It is assumed, that the influence of clutter surrounding dominating scatterers within a resolution cell is comparable to nearby pixels consisting of clutter only, hence, the intensity of clutter for a PS can be estimated from pixels enclosing the scatterer. The observed data of a pixel therefore consists of the signal of a strong scatterer present in a resolution cell superimposed by clutter enclosing the point scatterer. In Figure 9 the signal model for a point scatterer can be seen. The observed signal p consists of the signal of the
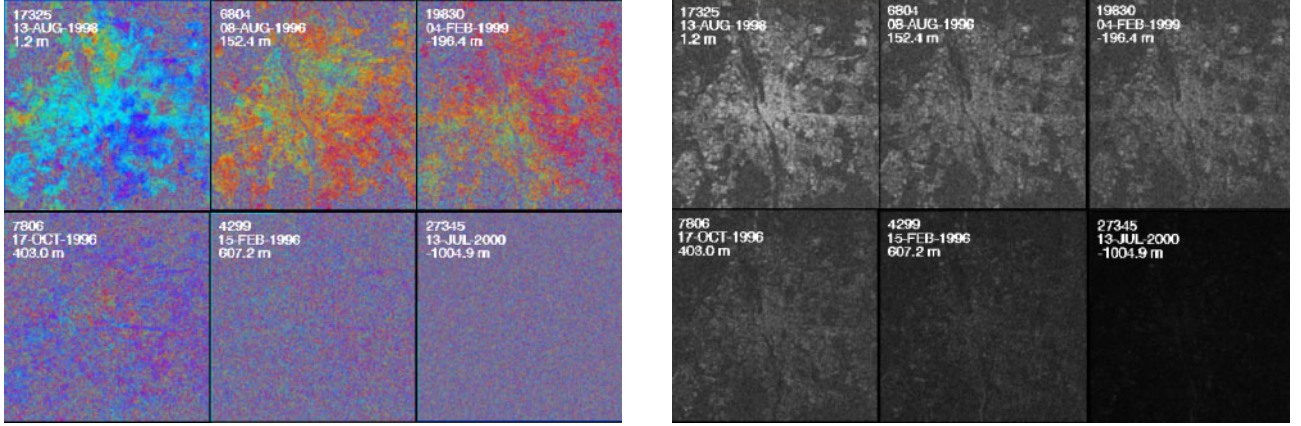
(a) Some examples of differential interferometric SAR images (dInSAR) sorted by perpendicular baseline. No spectral shift filtering is applied for PSI. Consequently, large baselines (lower right) show a high level of decorrelation, i.e., phase noise affects visual interpretation. Nevertheless, single point targets feature stable phase values, which are investigated in the framework of PSI.

(b) Coherence estimates of dInSAR results, sorted by perpendicular baseline. Decorrelation effects increase faster for larger perpendicular baselines than for larger temporal differences between the acquisitions.

Figure 8. Differential InSAR images and corresponding coherence for the test site of Munich.

dominant scatterer q and the sum of contributions of clutter g, resulting in a phase error σ_ϕ and an amplitude error σ_a. A SCR of 2 is a reasonable threshold for the selection of PS candidates, including points with a phase standard deviation of $\sigma_\phi < 0.5$ rad, as a result of the relation of the SCR to the phase error of (Adam et al., 2004):

$$\hat{\sigma}_\phi \simeq \frac{1}{\sqrt{2 \cdot SCR}} \tag{13}$$
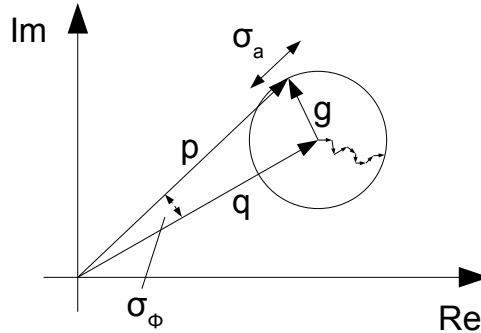
Figure 9. Observed signal p of a dominant scatterer q in clutter g within the resolution cell.

Dominating scatterers especially appear in SAR images of urban areas, as many manmade structures act as stable reflectors, which are only slightly affected by geometrical or temporal decorrelation. In particular double and triple bounce effects at urban structures will produce potential PS signatures in SAR images, because of the high signal return and the stable reflection geometry. As already mentioned in Section 2.1.2, double bounce effects often occur between ground and facade of buildings and triple bounce at all corners of a certain size. Kampes (2006) shows, that square trihedral corner reflectors of at least 0.28 m side length are most likely to be detected as PS using ERS data, i.e., at a ground resolution area of 5 m in azimuth and 25 m in range and a wavelength λ of 0.056 m. For TerraSAR-X (σ_{Az} =1.1 m, σ_R =0.6 m, λ =0.031 m) it follows, that the side length of the corner reflector to be detected as PS has to be at least 0.06 m. Consequently, much smaller constructional details very likely provide sufficient signal strength for acting as PS.

If signatures showing high amplitudes are of main interest for the selection of potential dominant scatterers, especially the effects of layover and side lobes affect the detection of PS. Within PSI-GENESIS, side lobes can be detected and removed by a further analysis of the signal in range and azimuth with respect to the PS candidate positions. Layover areas depict difficult regions for the selection of single scatterers. If two scatterers overlap in one resolution cell, they may either be discarded from PSI in a subsequent step of quality checks (most likely the deformation model does not fit the combined phase history of the double scatterers), or the estimated location and deformation will be wrong due to the superimposed phase values of both PS. In order to avoid such error sources layover areas could either be excluded from PS processing or more complex algorithms could be used for a separation of two scatterers based on the baseline dependency of the radar return (Adam et al., 2005). Fortunately, experience from different test sites show that single scatterers dominate even urban areas affected by heavy layover, hence, a single scatterer case can be assumed in general.

For the given test site of Munich the detected PS (SCR of ≥ 2.0) can be seen in Figure 10, in which the temporal mean intensity image is overlaid by all detected PS candidates. The selection has been limited to PS within the city boundaries (green area), including 84,200 PS candidates. The corresponding density of PS is approximately 220 points per square kilometer. For all PS, the phase and amplitude values of each interferogram, the position in azimuth range plane and different geometrical parameters are provided for the subsequent processing steps.

Reference Network Estimation

In contrast to the original implementation, it is not necessary to estimate and remove the APS in the next step. Instead, the functional model includes phase observations of adjacent pixels only, in order to eliminate atmospheric phase contributions for these double differences between nearby PS (Adam et al., 2003). This assumption holds for differences between points (called arcs) at small distances (in general the distances between neighboring points is chosen to be between 250 m and 500 m), because the correlation length of atmospheric disturbances is expected to be about 1 km. The unwrapped phase difference $\Delta\Phi$ between two points is now given by (Kampes, 2006):

$$\Delta\Phi = \Delta\phi_{topo} + \Delta\phi_{defo} + \Delta\phi_{noise} \tag{14}$$

The functional model for the topographic induced phase residuals now includes a differential DEM refinement (or DEM error) Δh. Phase changes due to differential displacement are modeled as a linear combination of deformation base functions $p(t)$ (dependent on time t), for which the amplitude α_d is estimated. The slant range distance R^m and local incidence angle θ_{inc}^m of the master position m are necessary for the calculation for the local height to phase conversion factor β. The differential phase components of topography and deformation can now be written as follows:

$$\Delta\phi_{topo} = -\frac{4\pi}{\lambda}\frac{B_{\perp}}{R_s{}^m \sin\theta_{inc}^m} \cdot \Delta h = \beta \cdot \Delta h \tag{15}$$

$$\Delta\phi_{defo} = -\frac{4\pi}{\lambda}\Delta R_{diff} \tag{16}$$

with

$$\Delta R_{diff} = \sum_{d=1}^{D} \Delta\alpha_d \cdot p_d(t) \tag{17}$$
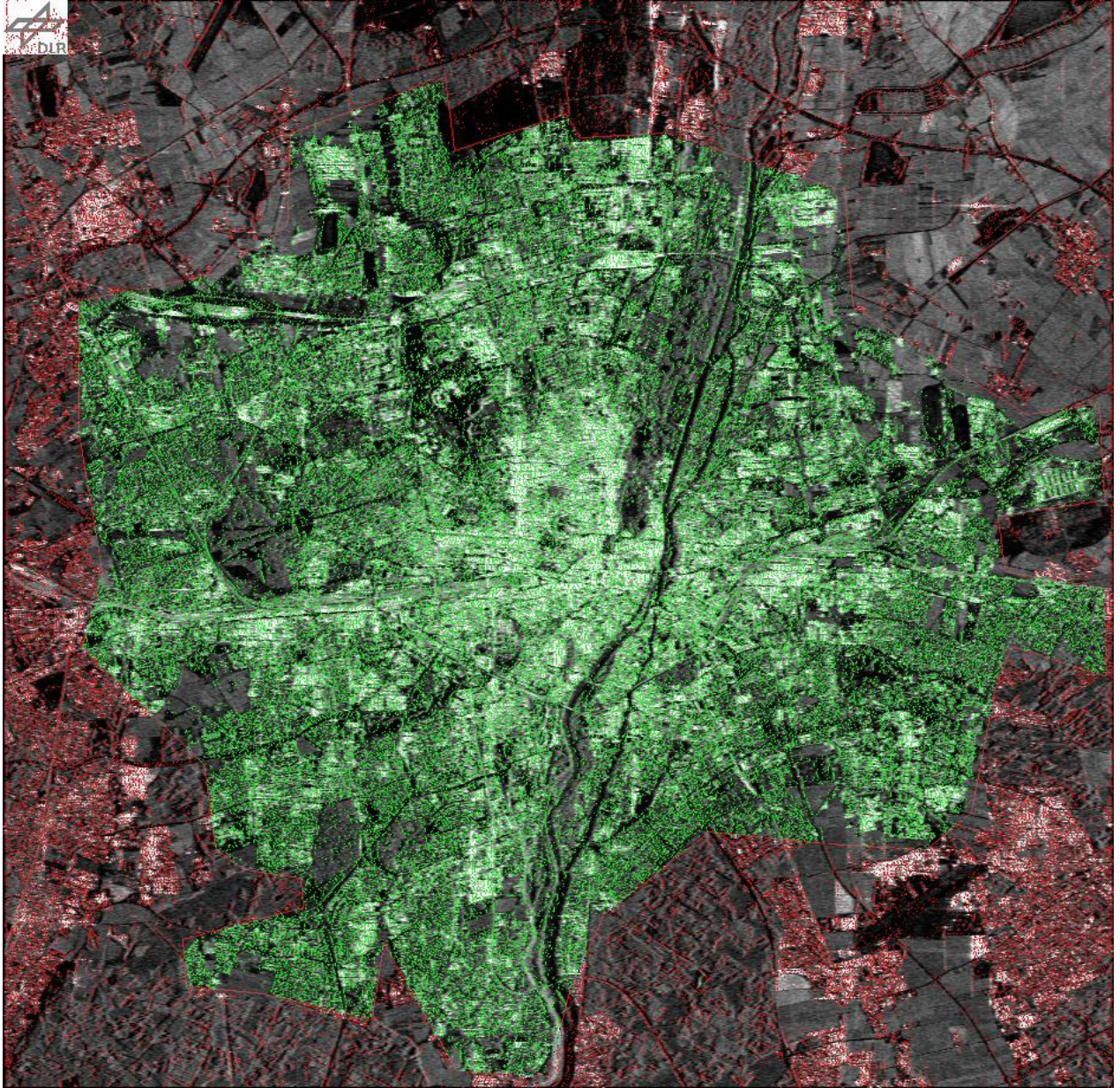
Figure 10. All PS candidates detected for the test site of Munich. The estimation is restricted to the selection of green points, covering the complete city center. Due to the selection criteria, especially bright points are identified as PS.

In principle any combination of base functions may be used for modeling the displacement, but in general the linear deformation model is used initially, equal to the original PS algorithm, given by the temporal baseline T:

$$p_1 = T \qquad \Leftrightarrow \qquad \Delta R_{diff} = \Delta\alpha_1 \cdot T = \Delta v_{LOS} \cdot T \qquad (18)$$

A second important base function for an estimation of seasonal deformation with a period of one year can be introduced by the following equation:

$$d(t) = \Delta\alpha_p \cdot \sin(2\pi(t - t_0)) + \Delta\alpha_p \cdot \sin(2\pi t_0) \qquad (19)$$

The second term has to be introduced by definition, as the displacement at the time of the master acquisition $t = 0$ is zero. Accordingly, the DEM refinements are also estimated for the time of the master acquisition. The amplitude $\Delta\alpha_p$ and offset t_0 in equation (19) can be

estimated by introducing the following two base functions, which can be used as extension to a linear displacement rate, or exclusively, if no constant movement is present:

$$p_1(t) = \sin(2\pi t) \tag{20}$$
$$p_2(t) = \cos(2\pi t) - 1 \tag{21}$$

Since Equation (19) can be expanded to

$$d(t) = \Delta\alpha_p \cdot \cos(2\pi t_0)\sin(2\pi t) - \Delta\alpha_p \cdot \sin(2\pi t_0)[\cos(2\pi t) - 1] \tag{22}$$

the unknown parameters $\Delta\alpha_p, t_0$ are calculated from the estimations $\Delta\alpha_1$ and $\Delta\alpha_2$ (related to p_1 and p_2) as follows:

$$\Delta\alpha_1 = \Delta\alpha_p \cdot \cos(2\pi t_0), \quad \Delta\alpha_2 = -\Delta\alpha_p \cdot \sin(2\pi t_0) \tag{23}$$

$$t_0 = \arctan(-\Delta\alpha_2/\Delta\alpha_1)/2\pi \tag{24}$$
$$\Delta\alpha_p = \Delta\alpha_1/\cos(2\pi t_0) \tag{25}$$

Like in the original implementation, the initial estimation is carried out on a subset of the best PS, i.e., points with a high SCR. These points are used to build a reference network, considering the distance between the points in order to cope for the correlation length of atmospheric phase contributions. For the given test site 476 points in the reference network have been selected, which are indicated by red dots, connected by blue arcs in Figure 11. Note that the network is set up in a redundant manner, connecting each PS to as many other PS as possible. The displacement model has been fixed to a linear base function for the given test site of Munich.

The estimation of the unknown parameters of DEM refinement and displacement rate for every arc is accomplished by the LAMBDA (Least-squares AMBiguity Decorrelation Adjustment) estimator, which is able to estimate the desired parameters for wrapped phase differences superimposed by phase noise of up to approximately 50° (Gernhardt et al., 2007). Details on this estimation procedure are presented in Section 4.2. One of the major advantages of LAMBDA is the possibility to introduce a full variance-covariance matrix of the observations and the propagation of these weights to the estimated parameters (Kampes, 2006). Hence, quality control of the estimated parameters is assured.

Due to the wrapped nature of the observed signal, the displacement signal can be reconstructed unambiguously only, if the sampling theorem given by the Nyquist sampling rate (or Shannon sampling frequency, Shannon (1949)) is met, i.e., the sampling frequency must be higher than twice the highest frequency of the present signal to be reconstructed. As shown in Kampes (2006), using equidistant sampled wrapped phase data of N_{IFG} interferograms in a time span of ΔT years, the maximum displacement rate $\Delta\alpha^{\mathrm{max}}$ and DEM refinement Δh^{max} respectively that can be reconstructed are given by:

$$\Delta\alpha^{\mathrm{max}} = \frac{\lambda}{4} \cdot \frac{N_{IFG}}{\Delta T} \tag{26}$$

$$\Delta h^{\mathrm{max}} = \frac{\lambda}{4} \cdot \frac{R_S \sin\theta}{\Delta B_\perp} \cdot N_{IFG} \tag{27}$$

For ERS parameters (λ=0.0566 m, R_S=850 km, θ=23°, $\Delta B\perp$=2,000 m) the maximum displacement rate is approximately 14 mm/y for one acquisition per year and 150 mm/y for the
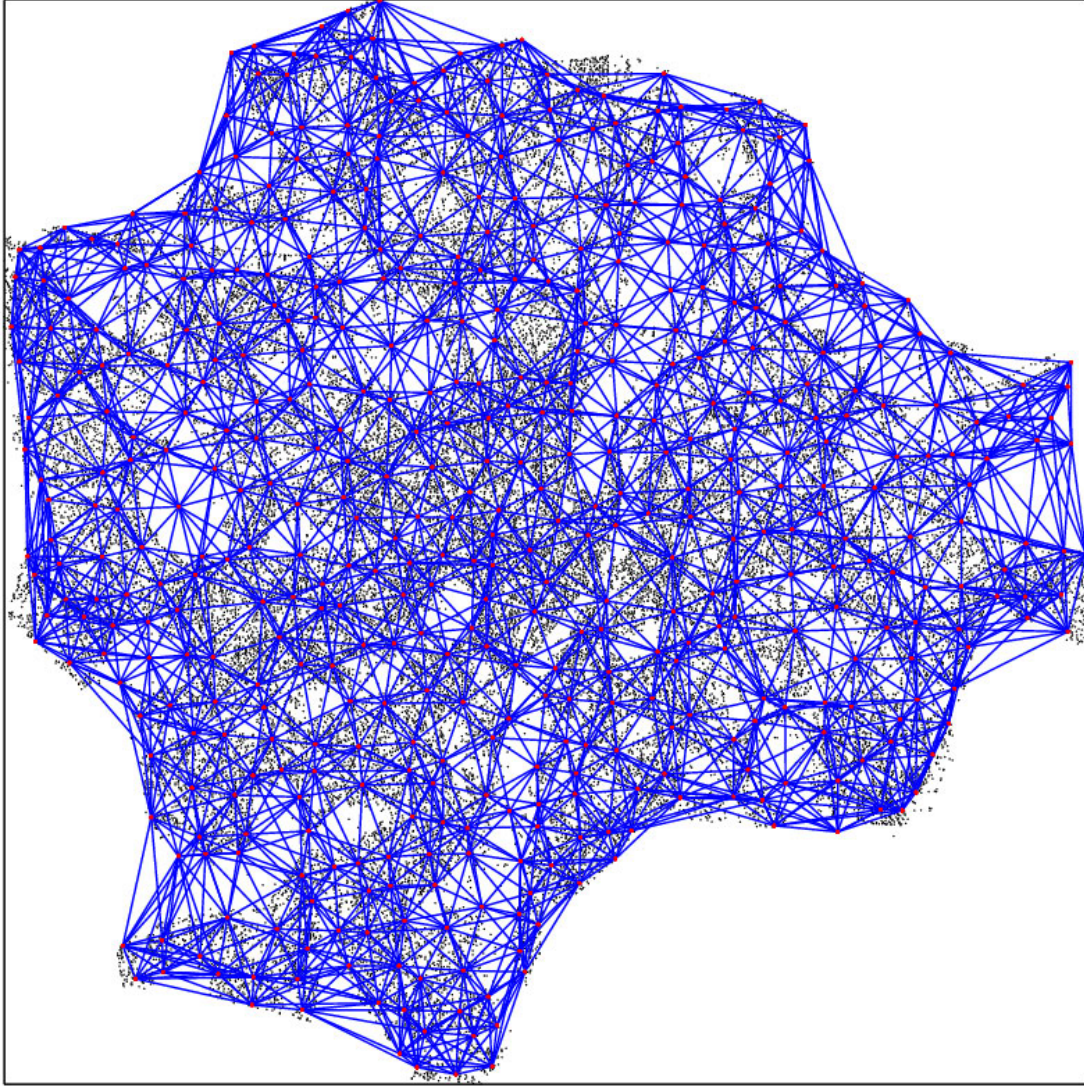
Figure 11. Reference network for the test site of Munich. Red dots represent PS of the reference network, black dots all remaining PS. For all arcs indicated in blue the parameters of deformation and DEM refinement are estimated separately.

maximum acquisition rate of one dataset every 35 days. In comparison, one acquisition per year of TerraSAR-X (λ=0.0311 m, R_S=700 km, θ=23°, $\Delta B\perp$=400 m) may allow for a deformation rate reconstruction of only 8 mm/y, but the availability of one dataset every 11 days increases the maximum displacement rate to 260 mm/y. The utilization of a data stack constructed from, e.g., 35 interferograms acquired within two years (like available at the test sites presented in this thesis) will result in an ambiguity of DEM refinements of 186 m and of deformation estimates of 136 mm/y for TerraSAR-X.

The estimation of the unknown parameters of DEM refinement and amplitudes of deformation is based on relative phase observations between nearby PS, therefore, a robust numerical integration is necessary in order to obtain absolute values at all PS positions. Consequently, a reference point has to be chosen from the reference network as a starting point for the integration procedure. This reference PS has to be selected very carefully, because an undesirable choice may result in biased parameters for all PS. It has to be assumed that the deformation rate is zero for the reference point in order to accurately integrate the displacement rate and DEM refinement gradients. A deviation of the reference PS height from the used DEM will affect all final geocoded PS positions due to a residual height offset. Certainly, a deviation from non-zero movement of the reference point will bias all estimates of the deformation rate equally. A stable and reliable PS can be chosen using a priori knowledge of stable regions within the area of interest and is selected from the reference network in general. In the previous implementation of the

integration within PSI-GENESIS, a least squares estimation has been applied to the redundant reference network in addition to alternative hypothesis testing in order to find outliers, caused by erroneous arcs or incorrect points (Kampes, 2006). The main problem of this algorithm is the enormous computational effort, because the whole system of equations has to be set up and inverted again for each iteration due to the removal of an arc or point. In the meantime a fast and robust integration technique including a multithreaded singular value decomposition has been successfully introduced and verified (Liebhart et al., 2010). In a preprocessing step, the relative estimations of LAMBDA are evaluated along arcs and points in order to find any inconsistencies. In a conservative field of the arcs, the integration result does not depend on the integration path. For each cycle (consisting of three connected arcs in a triangle) the residuals of an integration are evaluated. Erroneous arcs can be identified from the redundant network by evaluating the ratio of accepted and rejected cycle residuals (by means of a threshold) for all triangles including the arc under investigation. Hence, errors can be detected and removed prior to the integration of the whole redundant network. This approach will limit the number of necessary iterations of the subsequent integration to a minimum. As soon as the residuals are below a chosen threshold, the linear system of equations (including redundant network information) solving the integration can be set up. The latter is calculated by applying a singular value decomposition. Finally, the absolute values of deformation rate and DEM refinement are obtained at all PS positions, including variance-covariance information. The latter is used for discarding further single points, which are assumed to be unreliable. The speed-up compared to the formerly used algorithm originates from the severe reduction of iterations by reason of an extended outliers removal prior to the integration and a multi-threaded implementation of the latter. The size of the established linear system of equations depends on the redundancy of the reference network and on the number of PS included and may result in up to 30,000 single equations for large scenes.

Final Estimation and Geocoding

In a final step of the estimation process, all remaining PS candidates are included. For these points the absolute values of deformation rate and DEM refinement are obtained from an estimation relative to the closest PS of the reference network. This is accomplished comparably to the estimation of single arcs described previously using LAMBDA. Thus, the PS are appended to the adjusted network by single arcs, originating from PS of the reference network. Finally, all PS showing a DEM refinement or displacement larger than a chosen threshold are discarded (depending on the decision of realistic parameters for the given scene) and an overall model test is evaluated, removing all points with larger deviations from the assumed displacement model. From the residual phase components, atmospheric phase contributions, phase components of unmodeled deformation and noise can be separated by a spatial low-pass and temporal high-pass filtering procedure, because atmospheric effects are assumed to be correlated in space and uncorrelated in time, whereas remaining deformation signals are expected to be correlated spatially and temporally and noise is considered white in time and space. These two residual fields can be easily unwrapped for each interferogram, because no large gradients are expected. In order to obtain the final unwrapped phases at the positions of the PS the calculated atmospheric phase contributions and noise phase values are added to the estimated model phase (DEM refinement + displacement). These unwrapped phases may be used to estimate the parameters again applying more complex displacement models. Alternatively, the same model can be used again to estimate the parameters more easily due to the absence of phase ambiguities (Kampes, 2006).

For the given test site approximately 46,900 PS have been selected after final outliers removal. The results show spatially uncorrelated DEM refinements. Some larger deviations with respect to the given DEM are present, which can be explained by the low precision of the DEM in urban areas, as surface heights change rapidly in cities. Jumps in height between street level and roof
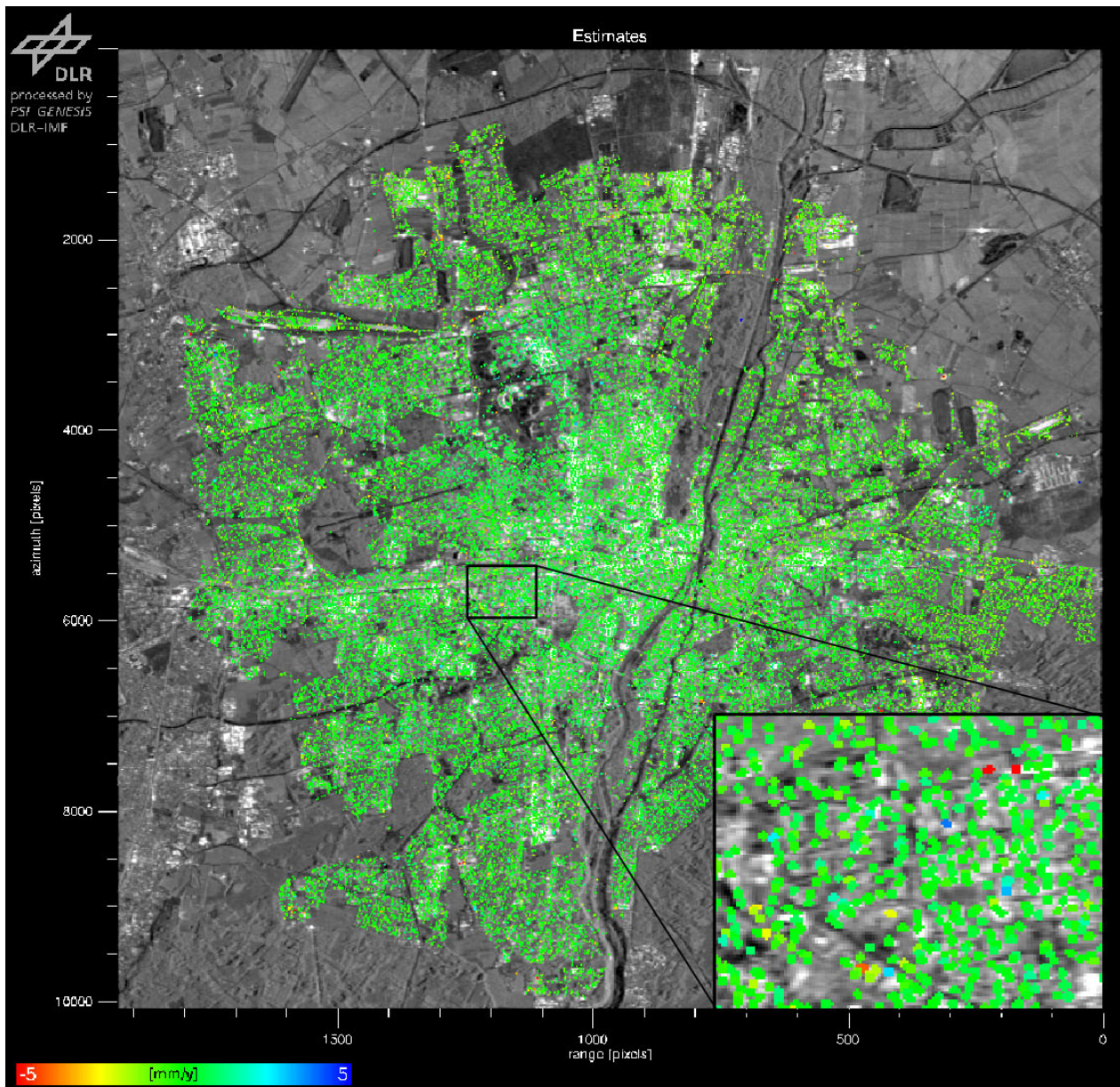
Figure 12. Linear deformation estimated for the test site of Munich in the interval [-5,5], units: mm/y. Green color indicates stable points. Blue colors shows LOS deformation towards the sensor, red colors imply motion in the opposite direction (subsidence). No large area deformation pattern is present; only a few single points are affected by significant deformation (see zoom of area highlighted by black rectangle on bottom right).

areas can be up to 100 m in Munich, and even more in other cities with skyscrapers. In Figure 12 the estimated linear displacement is plotted. Green colors indicate the absence of any linear deformation, hence, no large area deformation pattern is present within the area of Munich. Two examples of isolated relative displacement are given in Figures 13 and 14. The former shows a linear displacement rate of -7 mm/y between two points of a building. Unfortunately, the origin of this large displacement is not known in this case. In the second plot, a remaining seasonal motion can be seen on top of an estimated linear trend. The motion can be explained by the seasonal temperature differences within one year and the related movement of the ground. The stable (green) point is situated at a church, built on a solid basement made of concrete, while the second PS (red) is situated at a garden cottage. The latter is directly connected to the ground, hence, it moves up and down due to the expansion evoked by temperature differences between summer and winter. The period is one year, the amplitude about 5.5 mm. Hence, PSI can be used for the detection of large area deformation patterns, as well as for analyzing displacement at small scales between single points.
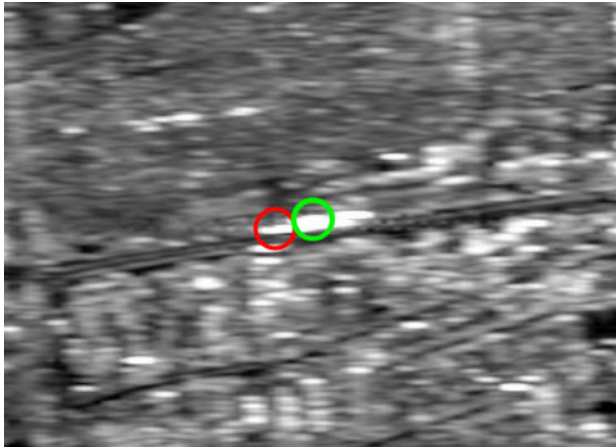
(a) Zoom into the temporal mean image of Munich. Circles indicate the two PS between which the deformation is analyzed. In this case the PS are situated at different parts of one large building. Green circle indicates stable PS; red circle marks position of subsiding point.
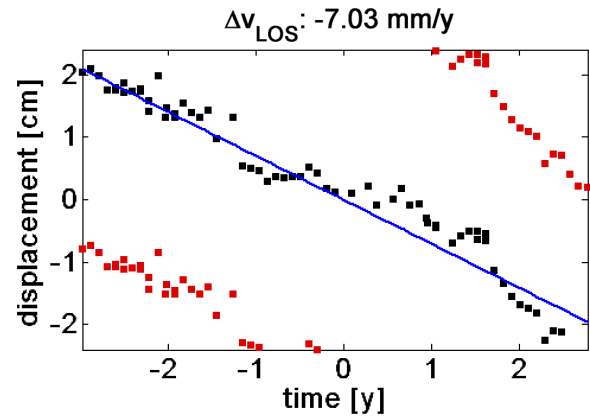
(b) Phase history between two PS given by relative motion after the removal of estimated relative height offset. Phase distribution ($\pm 2\pi$ ambiguities in red) is overlaid by the estimated linear trend (solid line). The displacement rate has been estimated to be approximately 7 mm/y.

Figure 13. Mean temporal SAR image and phase history showing linear displacement between two PS.
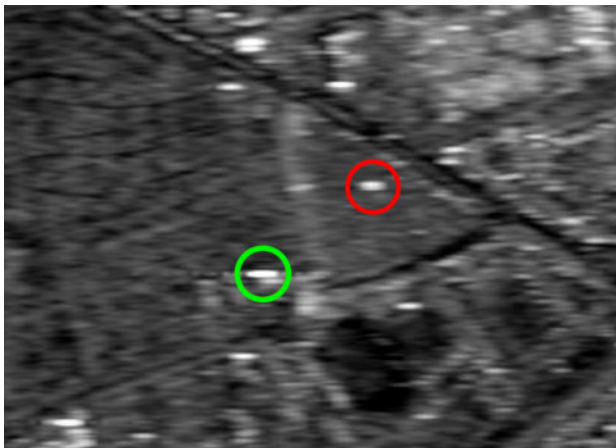
(a) Zoom into the temporal mean image of Munich. Circles indicate the two PS between which the deformation is analyzed. The green circle indicates the PS at the church (stable basement), while the red marker shows the position of the PS at the garden cottage (directly connected to ground) affected by seasonal motion.
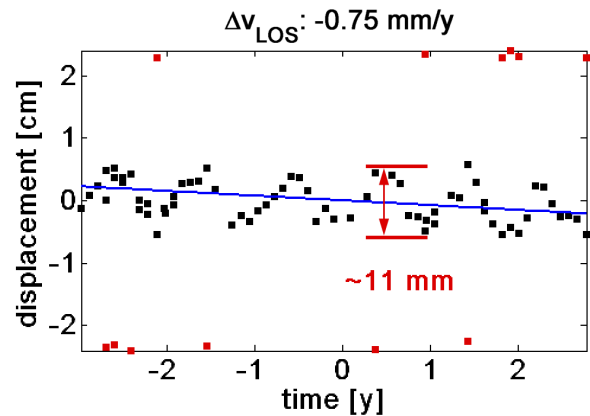
(b) Phase history between two PS given by relative motion after the removal of estimated relative height offset. Phase distribution ($\pm 2\pi$ ambiguities in red) is overlaid by the estimated linear trend (solid line). Remaining residual phase shows seasonal motion with a period of one year and an amplitude of approximately 5.5 mm, originating from thermal dilation effects during one year.

Figure 14. Mean temporal SAR image and phase history showing residual seasonal displacement between two PS.

The final PS coordinates can be transformed from the two-dimensional azimuth-range plane to a three dimensional global coordinate system (like UTM), with the help of precise orbit, range and azimuth timing information and the estimated height of the PS. In principle, the 3D location of each PS is obtained by a circle, given by its center – the precise orbital position at the time of the master acquisition – and its radius – the slant range distance of the PS –, intersected with the surface defined by the ellipsoidal height of each PS (cf. Figure 15). The latter is calculated from the used DEM and the estimated refinement at each PS position. The accuracy of the obtained coordinates depends on the precision of the orbits and range information, as well as on the estimated DEM refinements. But in addition, one critical parameter is the height of the reference point chosen during PSI processing. If this parameter is biased, e.g., by reason of a deviance of the reference point height of the used DEM, which has to be assumed zero for PSI,

this offset directly propagates to all final heights of the PS. The offset will result not only in a different height of the geocoded PS, but in an additional horizontal offset caused by the fixed slant range position. Hence, geocoded PS may differ from precise surface information available from other data sources, if no other reference data is used to correct any height error of the reference point. As soon as an ellipsoidal height of a single PS is known, e.g., by a calibrated corner reflector, the error in geocoded PS position can be compensated.
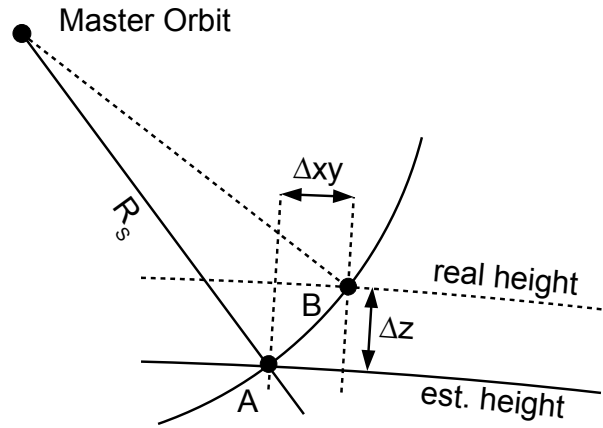
Figure 15. Principle of geocoding PS. The location of the point A in 3D can be obtained from an intersection of a circle, given by the orbital position of the master and precise range distance R_S, with the ellipsoidal height of each PS, given by the DEM and the estimated refinement. By reason of inaccurate DEM information for the reference PS, the point A may deviate from the real location B. In addition the the height offset Δz, a difference in horizontal positions Δxy is present.

3 Recent Developements in PSI and Objectives for Meter-Resolution SAR

In the meantime PSI matured to an operational tool for deformation monitoring of large areas as well as for detecting locally isolated deformation phenomena. Several companies offer deformation analyses using PSI processing methods, like Altamira Information (Spain), Gamma RS (Switzerland), Fugro-NPA (UK) or Tele-Rilevamento Europa (Italy). The performance of the products of these companies has been validated within the Terrafirma project of ESA. As already mentioned in Section 2.3.2, the processing system of DLR has been used as reference for this validation. The accuracies between two different estimations turned out to be $2.16/\sqrt{N}$ mm/y for PS showing a coherence of at least 0.95, depending on the square root number of interferograms $\sqrt{N}$ of the stack (Adam et al., 2009). Hence, for the best PS a precision of the estimated deformation rates in the sub-millimeter domain can be achieved for typical stack sizes, consisting of several tens of datasets. Another performance study, which documents absolute accuracies for the estimated deformation in the sub-millimeter domain has been carried out by Ferretti et al. (2007). They present the results of a blind experiment using RADARSAT-1 and ENVISAT data to estimate the movement of two pairs of dihedral reflectors. The latter have been moved artificially, hence, a comparison to precise ground truth data is feasible. However, the results are based on some pre-conditions, which will never be valid for natural PS detectable in SAR datasets; the positions of the reflectors acting as PS are known very precisely in advance (GPS measurements) and the distance between the two scatterers has been chosen to be at close range (50 m apart). Therefore, there exist no phase components due to APS and the phase contributions of topography could be completely removed. Nevertheless, the achievable accuracy of deformation monitoring by applying PSI has been shown to be smaller than 1 mm/y for point targets showing a high SCR.

Since the introduction of PSI several comparable methods for measuring ground deformation have been proposed, based on the framework of the original implementation. Some important methodologies – besides the already presented PSI-GENESIS system of DLR – and improvements for PSI proposed in the past years will be described briefly in the following section. Afterwards, the objectives for this work will be given.

3.1 Methods and Improvements of Persistent Scatterer (PS) Deformation Estimation

3.1.1 Small Baseline Subset Technique (SBAS)

In contrast to the original implementation, this methodology is based on the evaluation of exclusively small baseline differential SAR interferograms and, thus, is called small baseline subset technique, or shortened SBAS (Berardino et al., 2002). The deformation time series is obtained in this case by an appropriate combination of motion fractions obtained from small (spatial) baseline interferograms, which are created using all available datasets. Hence, no single master scene is used. A second major difference stems from the necessity of unwrapped phase values for a correct estimation (i.e. linking of deformation signal between the interferograms), calculated for each interferogram separately in an initial step. However, comparable to the original implementation, the estimation is based on a subset of pixels showing a higher coherence than an assumed threshold. The temporal low-pass component of the motion and the DEM refinements are estimated using a least-squares adjustment, accomplished by singular value decomposition (SVD) linking different subsets of interferograms. As usual, a linear deformation model is introduced for simplification purposes. But the estimation procedure is iterated once

more in order to enhance unwrapping results; the original (wrapped) phases are reduced by the estimated deformation and DEM refinements, the residuals are unwrapped one more time and the estimated phase components of deformation are added back. Finally, the SVD approach is applied again in order to obtain final deformation values. Atmospheric phase contributions are removed in addition, like proposed in the original PSI approach; spatial low-pass and temporal high-pass is applied to the phase residuals after removing phase components of DEM refinement and deformation signals.

Altogether, the algorithm is suitable for large area deformation monitoring only (extraction of low pass deformation signals) and the correct linking of the subsets of the interferograms virtually is the main challenge. The latter has to be solved very carefully in order to avoid errors in the final displacement time series. In addition, the spatial resolution of the results is very limited, because a multi-looking procedure is applied in order to reduce decorrelation phenomena.

In Lanari et al. (2004) the SBAS method is extended for the usage on full resolution interferograms. To this end, the conventional SBAS approach is used to estimate large-scale deformation patterns, DEM refinements and the APS. These phase components are removed from the full-resolution interferograms and structures highly coherent over time are identified by the investigation of the residual phases for local topography and mean velocity. This is carried out using a periodogram, like proposed in the original implementation of PSI. The final DEM refinement is obtained by the sum of low-pass and high-pass components estimated from the two resolution branches of the data. The non-linear displacement estimates are obtained via the SVD technique from the residual phases calculated by subtracting the estimated high-pass as well as low-pass deformation and DEM refinement from the initial full-resolution interferogram. Consequently, the time-series of the deformation is the sum of the three contributions: high-pass (linear), low-pass (linear) and non-linear motion. Examples of the SBAS technique applied to several different test sites can be found in, e.g., Berardino et al. (2003) and Berardino et al. (2007).

In general, the extensions are reasonable in order to investigate local deformation on small scales, but the challenge to correctly link the subsets of interferograms still remains. Hence, the extension can be regarded as refinement of the SBAS algorithm. In addition, the precision of geocoded pixels is limited due to the usage of pixel center coordinates. The precise source of scattering may be hard to discover in detail.

3.1.2 Coherent Pixels Technique (CPT)

Coherent pixels technique (CPT) is related closely to the SBAS method since the formation of several interferograms using preferably small spatial baselines without the selection of a single master image comprises its basis (Mora et al., 2003). But the authors especially stress the robustness within their implementation in comparison to SBAS. The selection of an appropriate minimum number of best interferograms is accomplished by the use of a Delaunay triangulation of the datasets in the baseline-time-Doppler space, considering the theoretically calculated phase coherence (Blanco-Sanchez et al., 2008). Like in other PSI algorithms, the subsequent estimation of the unknowns is carried out on a subset of pixels only. The selection procedure is based on the stability of the spatial coherence of the points, evaluated for each single dataset. Unfortunately, the usage of a calculation window of certain size, necessary for coherence estimation, results in a reduced resolution of the final products. However, the advantage of this proceeding arises from the reduced set of images the technique can already be applied to in comparison to algorithms using the amplitude dispersion index. The latter is a reliable estimate for phase stability only, if enough data samples of the amplitude are available. Like in the original implementation, linear deformation rates and DEM refinements are calculated between neighboring pixels. The estimation itself is implemented by a conjugate

gradient method, minimizing the difference between the observed phase values and the model, comparable to a periodogram. Another similarity to the initially proposed PSI method is the adding of further pixels to the network of assumed best PS after the integration of relative estimation values using the latter. Hence, pixels with decreasing quality are added in an iterative algorithm (Blanco-Sanchez et al., 2008). Additionally, the non-linear motion is obtained from the remaining phase residues by a filtering process, separating spatial low resolution non-linear deformation and phase components induced by atmospheric effects. As usual, the signal of the latter is considered correlated in space (low frequency) and white in time, whereas the deformation is assumed to be correlated in space and time. However, the different subsets of interferograms still have to be linked correctly again. This is performed (again) by a SVD method, comparable to the SBAS approach. But after the removal of all estimated phase contributions from the original phases, the residuals are unwrapped and the spatial high resolution non-linear deformation is estimated the same way like for low resolution fractions (including SVD method and temporal filtering). The final value for deformation estimates follows from the sum of all estimated fractions. Examples of this technique can be found in, e.g., Blanco et al. (2006) and Duque et al. (2007).

The method of CPT maximizes the number of usable pixels for non-urban areas by the selection criterion of the coherence at the cost of a lower resolution of the final results. But it can already be applied to just a few datasets, which is an advantage in comparison to other methods. Certainly, the nature of scatterers is hard to investigate due to the limited localization precision, comparable to the SBAS method. A comparison between the CPT method and the methodology of stable point network (SPN) in addition to ground measurements can be found in Herrera et al. (2009). Unfortunately, algorithmic details of the SPN cannot be found in the literature, obviously due to the keeping of the corporate secret of Altamira Information. However, the comparison reveals similar performance of the different methods and a precision of the best scatterers in the sub-millimeter domain.

3.1.3   Stanford Method for PS (StaMPS)

Hooper et al. (2004) present another method (Stanford method for PS, StaMPS), suitable for non-urban areas, because the main limitation in natural terrain is the lack of PS detectable by investigating the amplitude dispersion. Hence, standard PSI would fail as PS are too far apart (reliable unwrapping is not possible). In addition, especially geophysical deformation patterns are likely to be different from linear or seasonal motion patters. Like in the original implementation, one single master is selected in order to form the interferograms. However, the selection of suitable PS is quite different; all pixels showing small phase noise in time are assumed to be dedicated PS, for which the deformation phase can be extracted. Hence, the PS are detected from evaluating variations of underlying noise estimated in a first step. This can only be accomplished by making several assumptions; the phase contributions due to deformation, atmospheric effects and orbital errors are considered correlated in space up to a certain distance, whereas fractions induced by residual topography and noise are assumed to be uncorrelated spatially with zero mean with respect to the same distance as previously mentioned. In principle, the residual topographic phase and noise can be separated from the other mentioned parts by a subtraction of appropriate mean values calculated from local patched including some PS. In contrast to this simple low-pass filtering in the spatial domain Hooper et al. (2007) proposes a better approach, implemented by a band-pass filter for the estimation of the spatially correlated parts, allowing for steeper deformation gradients than the initial method. After the separation, remaining fractions of atmospheric phase components, deformation and orbital errors are assumed to be small and can be neglected furthermore. Subsequently, any remaining topographic residual fractions can be estimated from their dependence on the perpendicular baseline. Finally, a measure for phase stability is obtained by the temporal coherence calculated from the initial phase reduced by the mean values (patches) and the estimated phases of

topographic fractions. High coherence indicates small noise, which is the requirement for PS pixels. The mentioned algorithm requires an initial set of PS, generated by using the dispersion index (cf. Ferretti et al. (2001)). But in this case, the PS are refined iteratively by the above mentioned algorithm. The final selection of PS is based on statistical tests, checking the probability of a pixel to be a PS. The latter also includes evaluations of the variation of the residual phases and the amplitude dispersion index.

As already mentioned, no deformation model is used for the estimation of motion. The latter is obtained, in contrast to the original implementation, by an unwrapping algorithm including temporal integration using the phases of the PS, corrected for the estimated DEM refinement. However, the deformation time series is still masked by residual error terms of atmospheric phase components, orbits, residual DEM refinements and noise. Hence, further assumptions are made in order to obtain motion time series; in contrast to the deformation signal, the spatially correlated parts are assumed to be uncorrelated in time, thus, a high-pass filtering in time followed by a low-pass filtering in space reveals the spatially correlated error terms. The latter are subtracted from the unwrapped phases, finally revealing the deformation time series, including only spatially uncorrelated errors (modeled as noise).

A comparable strategy has been proposed by Zebker et al. (2007), with the attempt to increase the PS density in vegetated areas as well. This is achieved by a statistical modeling of the phase values of each pixel in combination to a maximum likelihood test, selecting pixels following the expected phase distribution. However, robust phase unwrapping algorithms are required using this additional selection strategy.

Both methods are suitable for the investigation of deformation patters in non-urban areas, but will not be applicable in cities, as the assumption of correlated deformation and uncorrelated DEM refinements will not be valid in general. The different selection of PS certainly is an interesting alternative, which should be investigated in terms of suitability for urban PSI, because there may be PS discarded within the algorithms of present PSI methodologies for sure holding useful information. However, the deformation time series is obtained by applying quite extensive filtering operations based on many assumptions. There arises the question whether an introduction of certain deformation models and a subsequent analysis of phase residuals would not be the better choice.

3.1.4   Persistent Scatterer Pairs (PSP)

A relatively new method (persistent scatterer pairs, PSP) has been proposed by Costantini et al. (2008) and Costantini et al. (2009). Like the original methodology, it is based on the usage of one single master dataset, albeit the selection of appropriate PS is different. The method does not depend on the initial selection of PS by the dispersion of the amplitude or by any other method, thus, no calibration of the data is needed. The points are added successively during the estimation process, based on an initial choice of points. This seed of PSP can be generated by connecting each pixel to its neighbors. Another difference to the original implementation is mentioned to be the abandonment of deformation models. The main idea consists of the assumption, that spatially correlated phase contributions can be neglected for close range points, comparable to Adam et al. (2003) and Kampes (2006). Despite the statement about deformations models mentioned above, the unknowns of DEM refinement and velocity of an arc, created by two points, is estimated by maximizing the (eventually weighted) multi-acquisition coherence identically to the original implementation. Hence, a linear deformation between PS is assumed. In contrast to the original algorithm, the coherence calculated is used additionally for the selection of PS; a good coherence indicates low level noise, hence, the arc is treated as a PSP. Subsequently, the number of PSP is increased by iterative connections of further points to existing graphs of point pairs, evaluating the coherence function. As usual, an integration finally yields the absolute values of motion and DEM refinements. The residual

phase can be unwrapped after the removal of the estimated parameters, in order to obtain the non-linear time series of deformation. Atmospheric artifacts have to be removed, which is accomplished comparable to the original implementation of PSI.

To a certain extent, this method can be interpreted as a mixture of previously developed algorithms, because the estimation is carried out on arcs only (cf. Adam et al. (2003)), no deformation model is stated to be used and non-linear time series can be obtained (cf. Hooper et al. (2004) or SBAS methods) and the parameters are estimated maximizing the ensemble coherence (cf. Ferretti et al. (2001)). However, the evaluation of the periodogram proposed does imply the use of a linear deformation rate on each arc. The non-uniform motion is obtained like presented in the original implementation of PSI. Certainly, the abnegation of preselecting points prior to the estimation comprises an innovative way for the detection of point holding useful phase information. But the computational effort seems very high. Unfortunately, there exists no information on the integration procedure, as there could arise the need of a robust adjustment summing up linear increments between points (cf. Liebhart et al. (2010)).

3.1.5 Potential Improvements for PSI

In the following, improvements proposed by different scientists for existing methods of PSI are summarized:

Marinkovic et al. (2005) show a method to include new datasets to existing stacks of SAR data, evaluated by PSI, without the need to reprocess the whole stack. Instead, the parameters of deformation and height update of each PS are estimated sequentially using the results and variance-covariance matrix of the previous step. This is accomplished by recursive estimation techniques and multi-modal adaptive estimation. Within the framework, a belief network is constructed, used for statistically comparing the different "most-likely" solutions of the LAMBDA estimator for each arc. Subsequently adding new acquisitions, branches of the belief network are rejected that show a low probability of correct results for more than a specific number of successive periods, until a high probability of one correct solution is obtained. A recommended number of samples, the rejection should be performed in, is proposed to be 5-10 (Marinkovic and Hanssen, 2007). One disadvantage of this approach could arise from the selection of the master acquisition, which has to be selected within the first samples used for initialization. Hence, temporal decorrelation will increase successively with each recursively added dataset. In addition, no hint is given on the selection of the PS - whether any recursively refinement should be applied or how the initial set is obtained. Especially partly coherent points could also distort the results.

Ketelaar et al. (2007) show a method to combine several independent estimation results from different tracks in order to evaluate the reliability of different results, to enlarge the area under investigation using several overlapping datasets or to decompose horizontal and vertical components of the underlying deformation signal. The challenge is considered as datum connection problem, in order to transform all results to one common radar datum and to connect the estimated parameters. The linking is carried out before the geocoding procedure resulting in only one range and azimuth timing error and one uncertainty in reference point height, which affects the final geocoded position (cf. Section 2.3.2). An initial transformation between master and slave tracks is estimated from the precise orbit information available for each stack. The results are refined by a comparison of the PS point fields, to cope for relative azimuth and range timing errors between the tracks. Additionally, the refinement can be calculated from cross-correlation of distributed reflectivity patches (matching of simple features) between different tracks. Subsequently, all PS are transformed to one common radar datum and common PS, or PS related to the same deformation regime can be detected. The deformation estimates are linked based on hypothesis testing, assuming a common deformation time series for corresponding targets or clusters. Hence, PS may be excluded that cannot be treated reliable with respect

to the estimated motion. However, the problem of the height uncertainty of the reference PS still remains, which will influence the final geocoded positions. In addition, matching features between SAR images especially in urban areas is a very challenging task due to highly variable viewing geometries from cross-heading tracks, i.e., comparing ascending and descending image features. In summary, the method seems to be only feasible for areas without elevated PS, i.e., it is not applicable to urban areas using meter-resolution SAR data, because most of the PS are situated at facades of buildings hampering a linking of deformation fields. Other methods for a combination of different tracks are, e.g., using a cross-correlation of binary images created from geocoded PS maps (Colesanti et al., 2002) or the usage of a common PS with ground truth information (height) visible in all tracks, in order to geocode the different tracks with respect to the common ground control point (Perissin and Rocca, 2006). By far, the latter mentioned methods are very rudimentary approaches or do need additional reference information.

In Hooper (2007) and Hooper (2008) a combination of SBAS and PS approaches is shown. The main idea consists of a combination of points detected by the two approaches in order to increase spatial coverage of pixels with useful phase information. The PS selection scheme corresponds to the one described in Hooper et al. (2007). Additional pixels are selected from the SBAS processing branch. An initial set of points is obtained by thresholding the amplitude difference dispersion, given by the standard deviation of the difference in amplitudes of master and slave divided by the mean amplitude (similar to the amplitude dispersion index). The further selection algorithm of appropriate points within the initial choice is the same as for PS selection. In order to combine both datasets, the small baseline phase is calculated for the PS pixels from a recombination of single master interferograms. If one pixel contains phase values from PS and SBAS, a weighted mean is calculated. Finally, an increased number of pixels can be used for estimating the deformation time series, similar to SBAS algorithms. One advantage arises from the fact, that no isolated clusters of interferograms are present, because all datasets are connected for SBAS processing. In addition, phase unwrapping is simplified by reason of the higher point density. On the other hand, this method seems to be useful only in non-urban areas by means of the assumed spatial correlation of deformation and uncorrelated DEM refinements.

The increase in number of PS is desired in general for a more robust estimation and extended coverage. One possibility is the implementation of an automatic selection of a suitable deformation model from different global deformation classes or an introduction of adaptive deformation models (van Leijen and Hanssen, 2007). The former includes alternative hypothesis testing procedures in order to find a model that fits the data best. The latter requires an iterative calculation, which removes the phase of the used deformation model in each iteration. Hence, additional points may be included successively, because the deviations of the time series to the used deformation model are dropping below the selection threshold. From results of the Persistent Scatterer Interferometry Codes Cross-Comparison And Certification (PSIC4) study Esfahany et al. (2007) analyze the resulting PS densities and show some ideas to raise point densities. New algorithms for the interpolation of APS, modelling of the deformation signal and the inclusion of azimuthal sub-pixel positions of the scatterers and the influence on the number of PS are discussed. Further approaches to increase the number of pixels from which deformation can be extracted are proposed by Perissin et al. (2007) and Ferretti et al. (2008). The ideas are based on the detection of only partly coherent targets with respect to the temporal baseline. In the latter a maximum likelihood estimator and the coherence matrix (considering all interferograms) are used for an estimation of deformation and height update of PS that exist only for certain temporal episodes. The former method uses multi-interferograms (cf. SBAS method) and selects appropriate subsets of short temporal or geometrical baselines in order to estimate deformation rates and height updates of PS. The spatial coherence is used as weighting factor to restrict the extraction of information to coherent interferograms only. As a result, the unknowns are obtained from a subset of the data – a critial choice for both parameters; if the geometrical baseline distribution is small, the accuracy of the estimates turns low. Addition-

ally, the deformation rate is estimated only from a short period and different results may be obtained even for nearby pixels in later epochs. Therefore, if the results of different epochs are combined in one common image the information can be misleading, because the displacement estimates originate from different epochs and may not be valid for the whole time series of available data. It is still an open question, how such information can be used, especially when short temporal baselines are used. However, motion of distributed scatterers can be extracted by a grouping of pixels showing similar scattering mechanisms (Ferretti et al., 2010). The adaptive multi-looking approach allows to estimate the coherence matrix more precisely, which is finally used to estimate the displacement for the whole patch. Results based on a maximum likelihood estimator applied to high resolution TerraSAR-X data is shown in Wang et al. (2011).

Furthermore, the separation of multiple PS within one resolution cell has been addressed to in the past years. Adam et al. (2005) proposes a method to detect the appearance of two scatterers from amplitude only data. The baseline dependent reflectivity is investigated and the decision for one or two PS is supported by Bayesian theory. In addition, the relative height between the scatterers can be estimated along elevation direction. 15% of the PS are reported to be composed of two dominant scatterers. Higher order models corresponding to three or more scatterers are not considered. Ferretti et al. (2005) shows a possible extension of the original PSI approach for the separation of scatterers. A second order model is introduced, which can be extended to multi-scatterer cases. However, the number of scatterers is not detected directly, but a hypothesis testing procedure has to be used in order to find the model that fits the underlying data best. This implies an increase in calculation times for each scattering model used. For typical urban areas up to 20% of PS may be detected in addition using second order models, but at higher computational costs. An initial use of first order models is proposed, because these are regarded to be sufficient as long as the highest possible number of PS is not needed. By reason of the increased complexity, these approaches have to be carefully balanced in terms of necessity for the given investigation. Fore sure, an increased number of PS is always desirable, but only inevitable for areas suffering from a sufficient number of points in order to analyze the expected deformation phenomenon or provide a good coverage of PS within the area of interest. However, the separation of multiple scatterers within one resolution cell can be achieved by recently developed tomographic methods (Lombardini, 2003; Fornaro and Serafino, 2006), which are capable of resolving layover. It is applied to ERS data by Fornaro et al. (2005) and for the first time to high resolution SAR data of TerraSAR-X by Zhu et al. (2008) (see also Zhu and Bamler (2010c)). An increase in number of PS up to 30% is reported in Zhu and Bamler (2010a), especially due to the separation of many double scatterers at low heights with respect to ground surface.

For a better understanding of the nature of PS, Perissin and Ferretti (2007) analyze the point targets by means of polarization, target position, target RCS, phase values from autointerferograms, amplitudes and geometrical baseline dependence. From the investigations it is possible to distinguish between ground level single bounce, roof level single bounce, dihedrals, resonating dihedrals, poles and trihedrals. Hence, different urban targets can be separated from the selection of PS. Unfortunately, this classification is restricted to the availability of alternating polarization data in order to distinguish between different scattering mechanisms and the evaluation of local temperatures at the times of acquisitions has to be considered carefully, as these will most likely vary significantly between different locations within one scene and even locally at diverse heights.

A very important step towards the understanding of the scattering mechanisms providing bright signatures in SAR data has been accomplished by SAR simulation. For this task ray tracing software has been modified to simulate SAR images using models of urban objects. Several interesting phenomenon of real SAR data can be explained by using this method of SAR simulation. Auer et al. (2009) show, that double bounce lines may be present on facades and are not necessarily situated on ground, as one would expect from double bounce between ground

and walls. In addition, the location of PS within building complexes could be demonstrated as a result of complex scattering mechanisms. The details and geometrical quality of the reflectivity map depend on the precision of the models used, but the interpretation of SAR images is feasible, anyway. Auer et al. (2010a) present the existence of "ghost corners", which stem from triple reflections of not connected walls. Additionally, many triple bounce effects have been proven to originate from windows at facades. The occurrence of even fourfold and fivefold bounce is explained in Auer et al. (2010b), potentially leading to PS geocoded underground. Altogether, SAR simulation enables the precise 3D identification and localization of PS detected from stacks of SAR images and helps investigating the nature of these signatures and provides explanations for inconvenient geocoded PS positions.

First PSI results using meter-resolution data of TerraSAR-X are presented by Adam et al. (2008b). The density of PS is reported to be incredibly high and structural stress investigations on buildings are mentioned to become feasible. In addition, thermal expansion of one large building could be monitored using a similar method to PSI. Furthermore, Adam et al. (2008a) shows, that stable phases are available mainly at man-made features and the height of buildings even can be extracted simply from counting the fringes. In addition, deformation may be evaluated using interferograms only due to high coherence. Altogether, the SCR increased providing much more PS and the coherence at buildings stays high even for larger temporal baselines. However, there exist areas heavily affected by layover affecting PSI analysis, which could be resolved by tomographic approaches. High resolution SAR therefore shows new potentials for PSI, but SAR data of urban areas present a new challenge due to the high complexity of the scenes. Hence, further investigations on the nature of PS and the potential of PSI using high resolution SAR data have to be performed.

The complexity and computational costs of many of the mentioned methods for an improvement of PSI at challenging conditions are relatively high. One major goal is to increase the number of PS that allows for a more reliable and detailed analysis of the underlying motion. A second direction of research is a refinement of strategies for an integration and verification of appropriate deformation models. However, the main goals of this thesis are different; the potentials of the new class of meter-resolution SAR data are analyzed with respect to the feasibility of a geodetic monitoring of single buildings. Therefore, the PS are investigated with respect to their precise 3D localization and a fusion of PS point clouds is developed in order to allow for an object specific deformation analysis.

3.2 Objectives for PSI Using Meter-Resolution Data

The prospective advantages of PSI using the new class of meter-resolution SAR data are evident. Above all, the number of potential scatterers will be extremely high. By reason of the opportunistic character of PS, one of the main questions for PSI using meter-resolution data is the suitability of this method for precise geodetic observations of single objects in urban areas. Medium resolution SAR sensors do not provide the necessary detailed information needed for a good coverage of buildings by PS. Only isolated buildings, constructed from steel and holding large footprints, have been shown to be reasonably sampled by PS using ERS or ENVISAT data (Perissin and Rocca, 2006). This thesis will show, how such a task of single object observation can be accomplished by combining different estimation results from independent data stacks acquired at the highest resolution available from TerraSAR-X. Presumably, the mentioned methods in the previous section for a combination of different tracks will have to be extended for an application on meter-resolution data due to the different distribution of PS. The precision of the detected PS is another important issue, which has not been addressed to in detail for high resolution data. Meter-resolution data will allow for a much more detailed view on the nature of PS that the few investigations (with respect to localization precision) on

previous available SAR sensors cannot provide. Therefore, meter-resolution data is processed and the derived PS locations will be investigated on their localization precision. The findings will help – in combination with SAR simulation – to investigate the origin of the scattering and to find corresponding real world objects the PS can be related with. In addition, PSI applied to meter-resolution data will show the potentials of deformation monitoring concerning motion details and phenomenon in urban areas. Besides the location of PS, the appearance of these points has not been investigated with respect to acquisition parameters. Therefore, this thesis will show how polarization, track type and varying incidence angles affect the occurrence of PS. In combination to analyses on the nature of the PS, this will give insight to the opportunistic character of these points. Finally, a comparison of two conventional estimators used in PSI – namely LAMBDA and periodogram – will show the stability and performance of these methods. In contrast to previous studies, the two estimators are compared directly within the same PSI processing system.

Altogether, the objectives of this work can be summarized as follows:

⋄ Sensitivity of the LAMBDA estimator and its performance compared to a periodogram.
⋄ Impact of different acquisition parameters on the appearance of PS.
⋄ Performance of PSI using meter-resolution data of TerraSAR-X.
⋄ 3D localization precision of PS in urban areas.
⋄ Geodetic utilization of PSI for monitoring of single objects by fusing results of different stacks.

4 PSI with Meter-Resolution SAR

4.1 The TerraSAR-X Satellite System and Test Sites

The German remote sensing satellite TerraSAR-X has been launched on June 15th 2007. This marked the first German space project in a public private partnership, a cooperation agreement between DLR and EADS Astrium GmbH. It is one of three satellite systems of the new meter-resolution class besides RADARSAT-2 and COSMO-SkyMed. All investigations in context of this thesis are based on data of TerraSAR-X. In the following sections a brief overview on this satellite system will be given, including system parameters and acquisition modes. In addition the two test sites will be introduced, whereas details on locations, available SAR data and reference data are presented.

4.1.1 System Parameters
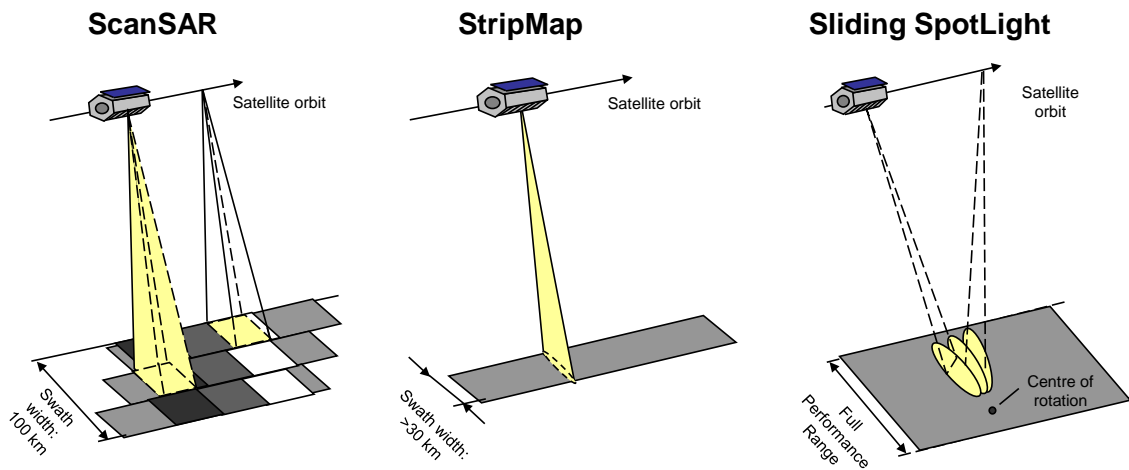
Figure 16. TerraSAR-X acquisition modes (left to right): ScanSAR, StripMap and Spotlight. Each mode differs in coverage and resolution.

The TerraSAR-X satellite is in a sun-synchronous orbit 514 km above the earth's surface (altitude at equator) at an inclination of 97.44°. The repeat period is 11 days, implying a very fast build-up of stacks for PSI processing compared to ERS' or ENVISAT's 35 days repeat rate. The dimensions of TerraSAR-X are 4.88 m in height and 2.4 m in width. It is designed for a lifetime of approximately 5 years and operates in X-band at 9.65 GHz ($\lambda = 31.07$ mm), offering a transmission bandwidth up to 300 MHz and polarization types HH, VV, HV and VH (Werninghaus and Buckreuss, 2010). The satellite offers 3 different acquisition modes – ScanSAR, StripMap and Spotlight – pictured in Figure 16 for incidence angles between 20° and 45°, whereas spotlight operates up to 55° (Pitz and Miller, 2010). ScanSAR offers the largest coverage of up to 100 km of swath width at a ground resolution of approximately 16 m by a repeated switch between three sub-swaths on ground, which are merged to one dataset by the TerraSAR multimode SAR processor (TSMP) described in Breit et al. (2010). Stripmap offers a higher resolution of 3 m at an extent of the scene of 30 km in ground range and up to 1500 km in azimuth direction. The highest possible resolution has been implemented by a sliding spotlight mode. The antenna is electronically steered in order to increase illumination time on ground, hence, the synthetic aperture is increased. As a result, the coverage is limited to 10 km (spotlight) or 5 km (high resolution spotlight) in azimuth and 10 km in range. For high resolution spotlight mode a bandwidth of 300 MHz is used instead of 150 MHz for regular spotlight, resulting in a resolution of up to 1.1 m in azimuth and 0.6 m in range (Breit et al.,

2010). In Table 1 the different coverages and resolutions are summarized for the different acquisition modes. Basic product types of TSMP are slant range single look complex (SSC) data, which will be used for PSI, multilook ground range detected (MGD), or geocoded products like geocoded ellipsoid corrected (GEC) and enhanced ellipsoid corrected (EEC) data. Further details on the different products, focusing and calibration can be found in Breit et al. (2010).

Orbit accuracies and orbit distribution are further very important system parameters. Both influence substantially the precision of geocoding (cf. Section 2.3.2) and the elevation resolution of PS (cf. Section 5.1.1). Yoon et al. (2009) show the high precision of science orbit solutions, which are obtained from comparisons to satellite laser ranging measurements. DLR and Geoforschungszentrum Potsdam (GFZ) provide ten-day orbit solutions showing average daily rms biases of better than 3 cm. Even long term assessments reveal an average rmse of only 4 cm at maximum. From the 1D evaluations using satellite laser ranging, an absolute 3D rms accuracy of the precise orbit product better than 10 cm is concluded. Ground control keeps the orbit tube tight at a radius of approximately 250 m, hence, the distribution of baselines is also restricted within a few hundreds of meters (Eineder et al., 2009).

	ScanSAR	StripMap	High Resolution Spotlight
Ground Resolution	16 m	3 m	1 m
Coverage	<1500 km x 100 km	<1500 km x 30 km	5 km x 10 km

Table 1. Ground resolution and coverage of different TerraSAR-X products (Pitz and Miller, 2010).

High resolution spotlight data of TerraSAR-X provide the basis for all investigations within this thesis. This implies some peculiarities during interferogram formation. Eineder et al. (2008) illustrate the critical requirements for successful repeat-pass spotlight interferometry using data of TerraSAR-X, like identical along-track orbit positions for subsequent acquisitions and the same squint angles. In addition, precise co-registration algorithms have to be adapted to the high resolution, because a precision of 1/10 of a resolution cell has to be achieved, i.e., a deviation of 6 cm at maximum at highest available resolution. An essential adjustment for the generation of interferograms comprises the common band filtering, which has to be applied also in azimuth direction for a provision of a common frequency band, by reason of the linear varying Doppler centroid (Adam et al., 2008b; Eineder et al., 2009). However, this adjustment has to be considered only, if distributed scatterers are investigated. In general the coherence in urban areas is reported to be very good (Adam et al., 2008a; Eineder et al., 2009).

4.1.2 Test Sites and Available Datasets

The test sites used for this thesis cover the central city areas of Berlin and Munich, Germany. The center of the scenes is chosen at the central train station in Berlin and at the Frauenkirche in Munich. The stacks consist of high resolution spotlight data, acquired by TerraSAR-X using a bandwidth of 300 MHz. In all following sections of this thesis a shortcut for each stack will be used, given by the label in Table 2 and 3. This allows for an easy association with the underlying acquisition geometry, as it is composed by track type (A = ascending, D = descending) followed by the approximate incidence angle number.

For the intended systematic investigations several different stacks are prepared for cross-comparisons in Berlin: 3 ascending stacks and 3 descending stacks are available, acquired at different orbital positions using VV polarization. Table 2 shows details on the system parameters and stack properties. Ascending data is acquired around 16:50 (UTC) in the afternoon, descending data approximately at 5:15 (UTC) in the morning. The incidence angles in the middle of the scenes vary between approximately 30° and 55°, whereas shallow angles reduce the observable area in range direction. Each stack consists of 25 to 35 scenes, acquired between

February 2008 and December 2009 (cf. Figure 18). By reason of conflicting order requests, stack A30 is lost since spring 2009 and other single orders have been canceled, leading to gaps in the theoretically regular temporal baseline sampling. In addition, a few datasets are available in HH polarization, which are not mentioned in the table but have been acquired using comparable acquisition geometries as the VV counterparts. These are needed only for a cross-comparison of PS densities between polarizations and are not used for an entire PSI processing (cf. Section 4.3). The coverage of the different stacks can be seen in Figure 17 from a composition of an aerial image and the colored rectangles, corresponding to each stack. In the center of the common area visible from each of the stacks (indicated by the white polygon), central train station of Berlin can be seen.

In Munich, there exist only three stacks due to heavy ordering conflicts in south Bavaria. At least one ascending and two descending stacks are available. They consist of 27 to 35 datasets, acquired between February 2008 and December 2010. The incidence angles are steep for stacks A23 and D25 and in the mid range for stack D39 leading to coverages of approximately 30 km^2 to 59 km^2 (cf. Table 3). Figure 20 shows that two stacks already end in spring 2009, and one large gap is present in the remaining stack, disadvantageous for continuous deformation monitoring. The ground coverage is pictured in Figure 19. Again, the common area is sketched as white polygon, with the Frauenkirche in its center. By reason of a dense arrangement of buildings throughout the whole city only few distinctive formations can be seen in the overview, for example the oval shape of Theresienwiese (famous location of the Oktoberfest), a little down and to the left of the center.

For both test sites, the master datasets are chosen at the beginning of 2009 in order to minimize atmospheric effects, which are assumed to be heavily present during summer periods affected by high percentages of water vapor in the troposphere. All stacks are processed separately using PSI-GENESIS software of DLR (cf. Section 2.3.2). The selection of appropriate reference points during PSI processing is critical for both test sites, because in both areas stable ground may be present only for small fractions within the city. In Berlin, the ground water level is just a few centimeters below the surface, resulting in possible fluctuations due to varying water-levels and temperature dependencies. However, these deformation regimes are assumed to show effects on large scales and the points may be chosen at central locations on ground. In Munich, an area of reliable stable ground is only known to be at the church "Alter Peter" (a little south-east of the center), approved by Geologists to be located on solid rock. Hence, a reference PS is chosen within this part of the test site.

Orbit	Beam	Inc.Angle	Head.angle	Track Type	Area [km^2]	# Datasets	Label
146	28	30.0°	348.6°	Ascending	50.00	25	A30
55	57	41.9°	350.3°	Ascending	40.94	25	A42
131	85	51.1°	352.0°	Ascending	32.90	29	A51
2	42	36.1°	190.6°	Descending	42.52	35	D36
93	70	46.6°	188.9°	Descending	34.96	33	D47
17	99	54.7°	187.2°	Descending	33.46	34	D55

Table 2. Stack acquisition parameters of Berlin test site including orbit number, beam number, incidence angle, heading angle (flight direction), track type, covered area and number of datasets included in the stack. The shortcut (label) is chosen in order to indicate track type (A = ascending, D = descending) followed by the approximate incidence angle number in order to facilitate an association with the underlying acquisition geometry.

In addition, point cloud data of aerial LASER scanning is available for both test sites, which can be used as reference data for accuracy analysis of PS positions. This data is generously provided by Land Berlin (EU EFRE project) and Landesamt für Vermessung und Geoinformation, Bayern. The two point clouds consist of unfiltered and pre-classified points in the UTM
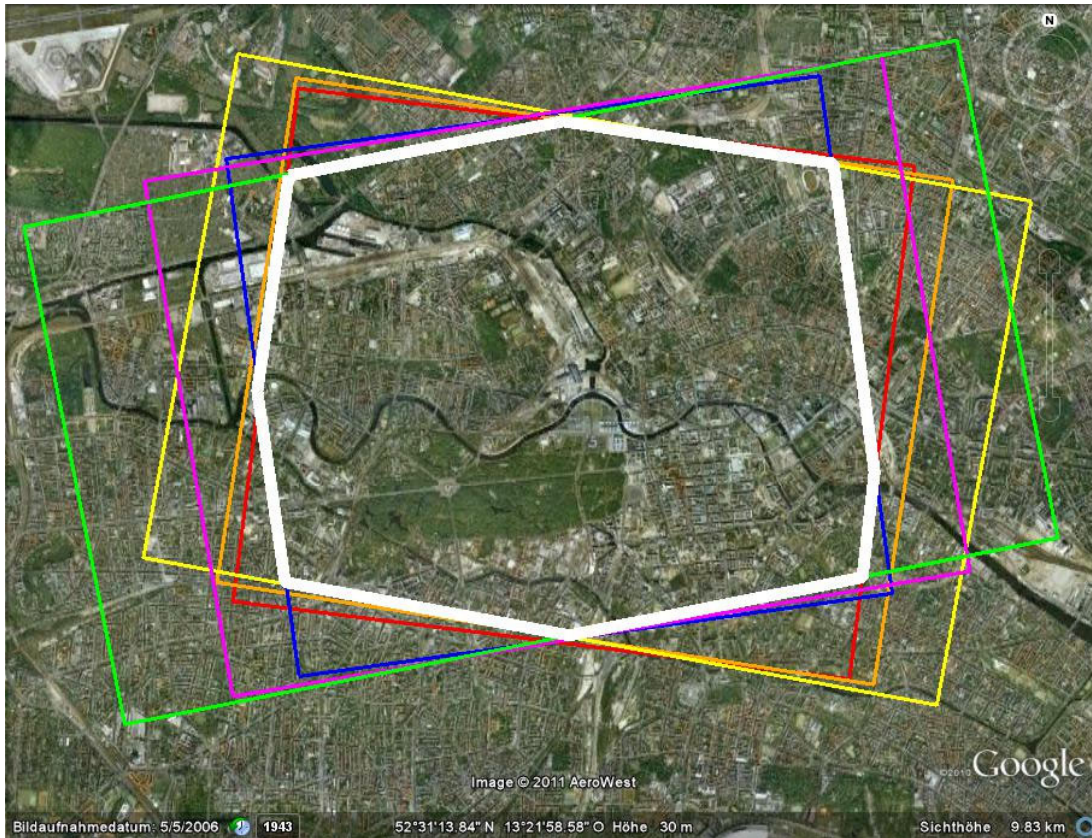
Figure 17. Test Site Berlin. Rectangles indicate different stacks, separated by color: Ascending stacks A30 (green), A42 (purple) and A51 (blue); descending stacks D36 (yellow), D47 (orange) and D55 (red). Layover generated in Google Earth$^{\text{TM}}$. White polygon indicates area covered by all stacks.
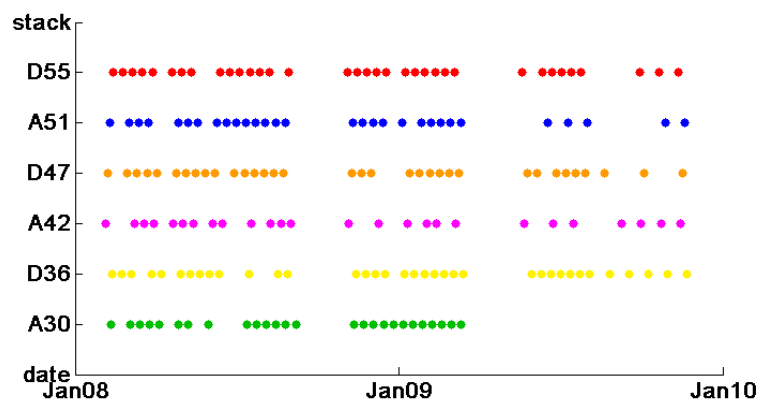
Figure 18. Acquisition time plot for Berlin test site showing temporal distribution of datasets.

coordinate system, including points from vegetation. A triangulation delivers a simple DSM that may be used for visual interpretation and analysis. The construction of a complex 3D city model is not intended to be part of this work. Thus, precise comparisons are carried out using the originally available point clouds. The density of points differ for the two datasets. In Munich there are about 113 million points available, i.e., approximately 1.69 points per square meter. The amount of data for Berlin is four times larger, i.e., 444 million points providing approximately 5.6 points per square meter. The higher density of points reveals even small structural details and improves the analysis on the nature of PS. Since a point cloud depicts a sampled version of reality, it may provide only limited support for this kind of analysis. Precise 3D models are preferable, but are not (yet) available.
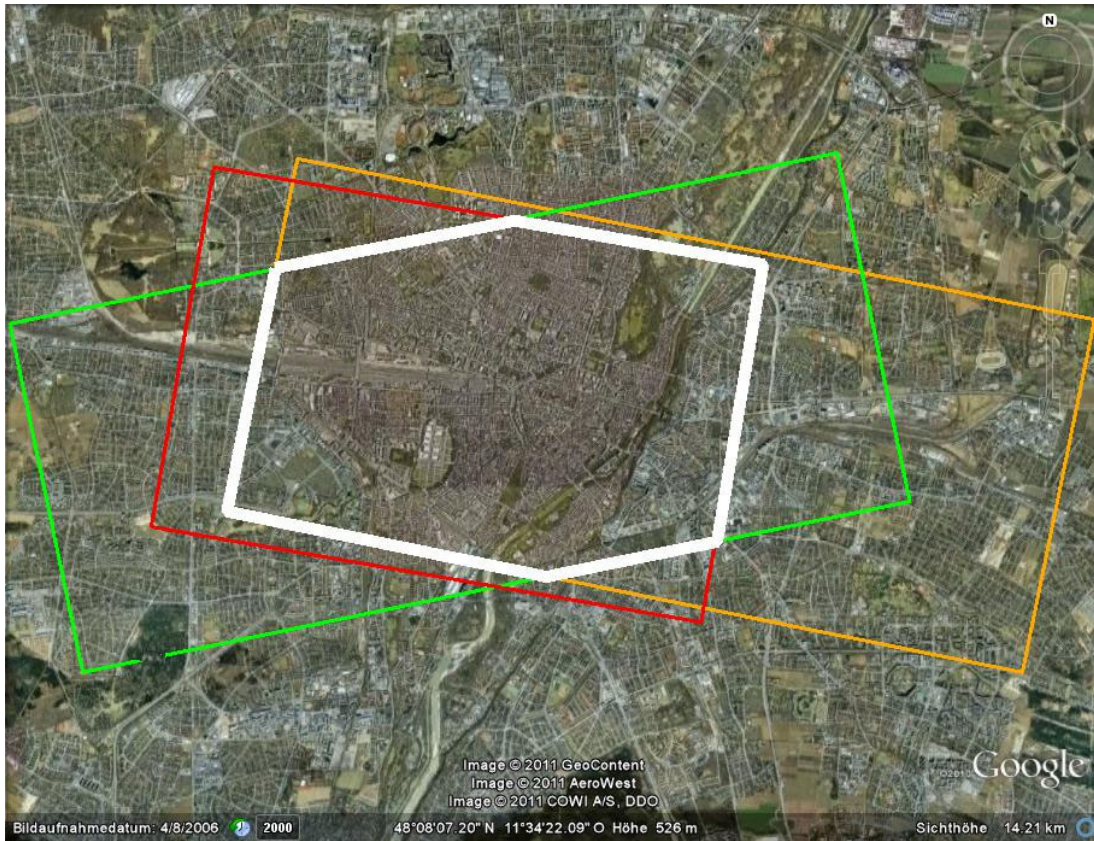
Figure 19. Test Site Munich. Rectangles indicate different stacks, separated by color: Ascending stack A23 (green); descending stacks D25 (orange) and D39 (red). Layover generated in Google Earth™. White polygon indicates area covered by all stacks.

Orbit	Beam	Inc.Angle	Head.angle	Track Type	Area $[km^2]$	# Datasets	Label
55	14	22.8°	347.8°	Ascending	45.05	30	A23
78	19	25.2°	191.7°	Descending	59.03	35	D25
2	50	39.4°	190.0°	Descending	29.65	27	D39

Table 3. Stack acquisition parameters of Munich test site including orbit number, beam number, incidence angle, heading angle (flight direction), track type, covered area and number of datasets included in the stack. The shortcut (label) is chosen in order to indicate track type (A = ascending, D = descending) followed by the approximate incidence angle number in order to facilitate an association with the underlying acquisition geometry.
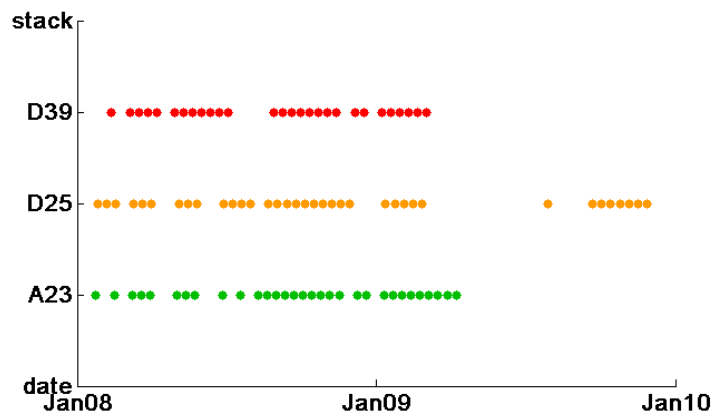
Figure 20. Acquisition time plot for Munich test site showing temporal distribution of datasets.

4.2 The LAMBDA Estimator Applied to PSI

Originally, the LAMBDA method was developed for the global positioning system (GPS) in order to solve double difference integer ambiguity problems efficiently. The underlying measurements are ambiguous by an unknown integer number of cycles, which have to be resolved. The main objectives of LAMBDA are the decorrelation of the ambiguities and a sequential conditional search for the integer number of cycles in the resulting reduced solution space. Within PSI processing, the LAMBDA method is used during the estimation of the topographic height refinement and the deformation rate of each arc, i.e., between pairs of PS. Similar to the unknown integer number of cycles in GPS, the wrapped phase values are ambiguous to multiples of 2π. Hence, an integer estimation method is necessary to cope with this problem.

In the following sections, the basic principle of LAMBDA and its appliance to PSI will be presented, because of the fundamental importance for PS deformation analysis. In addition, the stability and robustness of LAMBDA will be analyzed and a comparison between results of PS deformation estimates obtained by LAMBDA and a periodogram (the second conventional method) will be shown and discussed.

4.2.1 Algorithmic Details

In Teunissen (1995) and Teunissen et al. (1995) a detailed description of LAMBDA is given, which is stated to be fast and to provide the highest probability of correct integer estimation for multivariate normal distributed problems. In the following a brief description on the basic idea and the computational steps is given.

Initially, the ambiguity problem can be formulated as a linear system of equations:

$$y = A_1 a + B_1 b + e \tag{28}$$

where a denotes the unknown integer ambiguity vector, b the vector of any other unknown real-valued parameters and e represents measurement noise and unmodeled errors. A_1, B_1 are design matrices of the system of equations and y contains the values of observed measurements. The bias-terms in e are assumed to either be correctable or small, hence, they are neglected in the following. Now, the least-squares criterion with an integer constraint can be written as:

$$\min_{a,b} \|y - A_1 a - B_1 b\|_{Q_y}^2 \quad \text{with} \quad a \in \mathbb{Z}^n, b \in \mathbb{R}^m \tag{29}$$

Q_y is the variance-covariance matrix of the observations, $\mathbb{Z}^n$ and $\mathbb{R}^m$ denote the spaces of integers and reals respectively.

There exist no methods for a direct inversion of the problem at hand due to the integer constraint on the ambiguities. However, it can be solved in a three step procedure (Teunissen, 1995). At first the integer nature of the ambiguities is discarded and an ordinary LSA is calculated, minimizing the unconstrained residual vector $\tilde{e}$. The result is referred to as the "float" solution. In a second step the integer nature of the ambiguities is taken into account, looking for a solution $\check{a}$ that minimizes the differences between estimated float $\tilde{a}$ and unknown integer ambiguities a. The calculated covariance matrix $Q_{\tilde{a}}$ of the float ambiguities comprises the necessary information for a correct solution that fits the initial mathematical model, as it is calculated from the design matrices A_1 and B_1. If LAMBDA is applied to PSI for example, this matrix includes the relations between the observed phase values with respect to baselines and times of acquisition as well as used deformation model(s). Consequently, the ambiguities can be resolved by a search in the solution space. Finally, the float parameters of the initial

estimation are adjusted using the obtained integer estimates. The final result is called "fixed" solution. Therefore, the objective function of the three step procedure can be written as:

$$\|y - A_1 a - B_1 b\|^2_{Q_y} = \|\tilde{e}\|^2_{Q_y} + \|\tilde{a} - a\|^2_{Q_{\tilde{a}}} + \left\|\tilde{b}|a - b\right\|^2_{Q_{\tilde{b}|a}} \tag{30}$$

with the unconstrained residual vector $\tilde{e}$, the unconstrained, but real-valued, ambiguity vector $\tilde{a}$ (including $Q_{\tilde{a}}$) and the conditional vector of real valued parameters $\tilde{b}|a$ (including the covariance-matrix $Q_{\tilde{b}|a}$). In equation 30 the last two terms would vanish identical, if a real-valued solution in a and b was allowed. However, after resolving the integer ambiguities, the last term vanishes identical and the minimization problem is solved.

An example of a successful integer estimation procedure is shown in Figure 21. The observations y are phase values related to deformation only, which are ambiguous by multiples of 2π. The unknown float parameter b is the slope of the line, that can be derived after resolving the unknown integer phase ambiguities a. In this special case of PSI the float solution corresponds to a horizontal line, i.e., the float ambiguities are obtained simply by (Kampes, 2006):

$$\tilde{a} = \frac{y}{-2\pi} \tag{31}$$

Nevertheless, the correct integer ambiguities can be obtained on basis of $Q_{\tilde{a}}$, including the necessary correlations for a reconstruction of the unwrapped phases. The resulting best and second best solutions are provided in the figure, differing in only one single integer estimation. The difference in this case is only one cycle, i.e., the difference in integer numbers is one.

In the following some more details are provided on the integer estimation procedure. For the sake of completeness all three mentioned steps are included. In general, the first step is straightforward; the integer constraint is removed and an ordinary least-squares solution is calculated providing the "float" solution:

$$\begin{pmatrix} \tilde{a} \\ \tilde{b} \end{pmatrix}, \begin{pmatrix} Q_{\tilde{a}} & Q_{\tilde{a}\tilde{b}} \\ Q_{\tilde{b}\tilde{a}} & Q_{\tilde{b}} \end{pmatrix} \tag{32}$$

The second step consists of the integer least-squares (ILS) estimation procedure to find $\check{a}$, whereas the obtained results of the float solution are used as basis:

$$\min_a (\tilde{a} - a) Q_{\tilde{a}}^{-1} (\tilde{a} - a) \tag{33}$$

However, there exists no standard technique for solving equation 33, because of the integer constraint in a. One straightforward solution is obtained by a simple rounding of the real-valued solution of the first step to the nearest integer. This approach will often deliver non-satisfactory results, by reason of a more or less intense correlation between the unknown ambiguities, i.e., the fixing of one ambiguity will directly affect all remaining unknowns. However, if the ambiguities were not correlated, this simple rounding scheme applied on the float solution would deliver the correct result (Teunissen, 1995). An improved solution is derived from a sequential integer rounding method, which accounts for some correlation between the ambiguities. This method is called integer bootstrapping and results from a sequential least-squares adjustment. The conditioning on the integer ambiguities is based on the integer values of the respective previous step. The initial value is obtained from an integer rounding of the assumed best float ambiguity (Verhagen, 2005). In principle, the calculation chain consists of rounding one float solution to the nearest integer and correcting the remaining float ambiguities on basis of their correlations to the previous one (Kampes and Hanssen, 2004). A third method is LAMBDA,
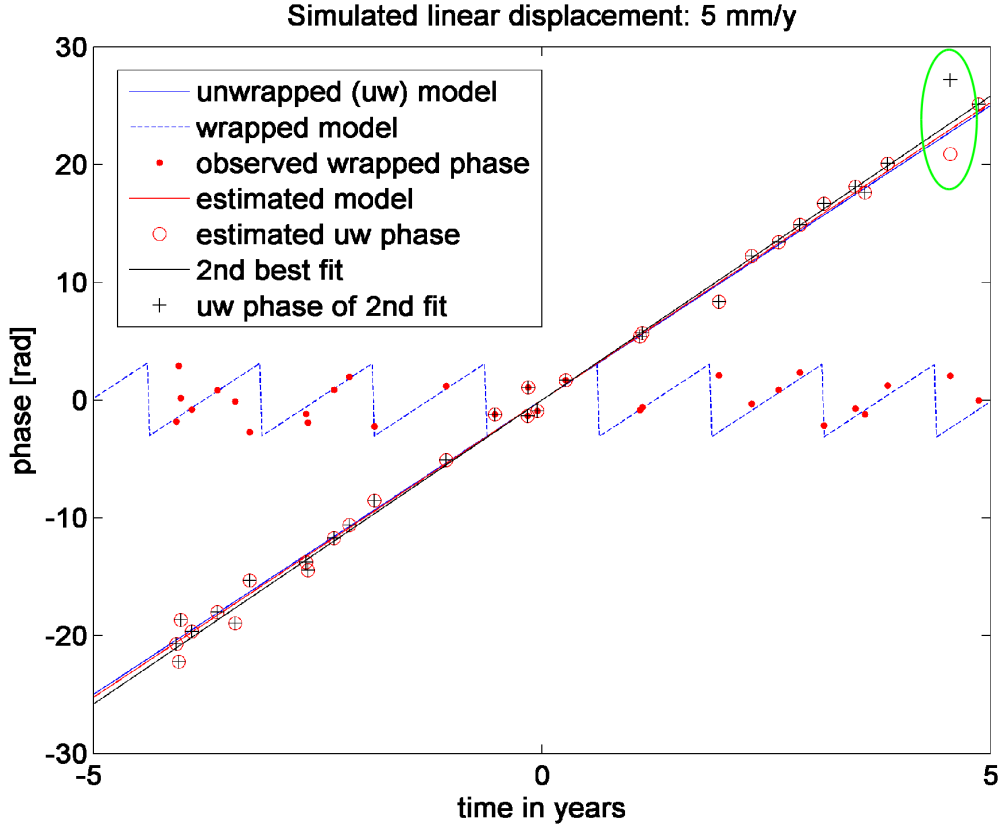
Figure 21. Example for integer ambiguity estimation taken from PSI. The linear slope is estimated from the initial distribution of wrapped phase observations (red dots), simulated from a deformation model and noise. The unwrapped true model is plotted as blue line, the estimated best and second best solutions are indicated by red and black lines. The corresponding unwrapped phase values are shown as red circles and black crosses. The second best solution differs in one single ambiguity (area highlighted by green ellipse), which is at a distance of one cycle (2π) in comparison to the best solution.

which shows a larger computational cost at the benefit of higher probabilities for the correct solution. In principle, the integer ambiguities can always be found by a search in the solution space. However, if the ambiguities are correlated, the ellipsoid containing the solutions can be extremely elongated. Hence, the integer search space is very large and the search will take a long time. Therefore, in a first step of LAMBDA the ambiguities are transformed in order to minimize the degree of correlation:

$$z^* = Z \cdot a, \qquad \tilde{z}^* = Z^T \cdot \tilde{a}, \qquad Q_{\tilde{z}^*} = Z^T Q_{\tilde{a}} Z \qquad (34)$$

As a result, the confidence ellipse shows a more circular shape and a faster search for the solution is facilitated (cf. Figure 22). However, the transformation must satisfy the conditions of being volume preserving (no exclusion of solutions), including only integer values in the transformation matrix (integer nature must be preserved) and reducing the product of variances on the main diagonal (scaling down the search space). One possible candidate is a Gauss transformation. It is implemented by a repeated use on pairs of equations (2D cases) for an extension to the n-dimensional case. In a 2D case, the transformation matrix Z is given by Z_1 or Z_2, depending on the smallest variance of the two parameters:

$$Z_1 = \begin{pmatrix} 1 & 0 \\ \omega_1 & 1 \end{pmatrix} \qquad or \qquad Z_2 = \begin{pmatrix} 1 & \omega_2 \\ 0 & 1 \end{pmatrix} \qquad (35)$$
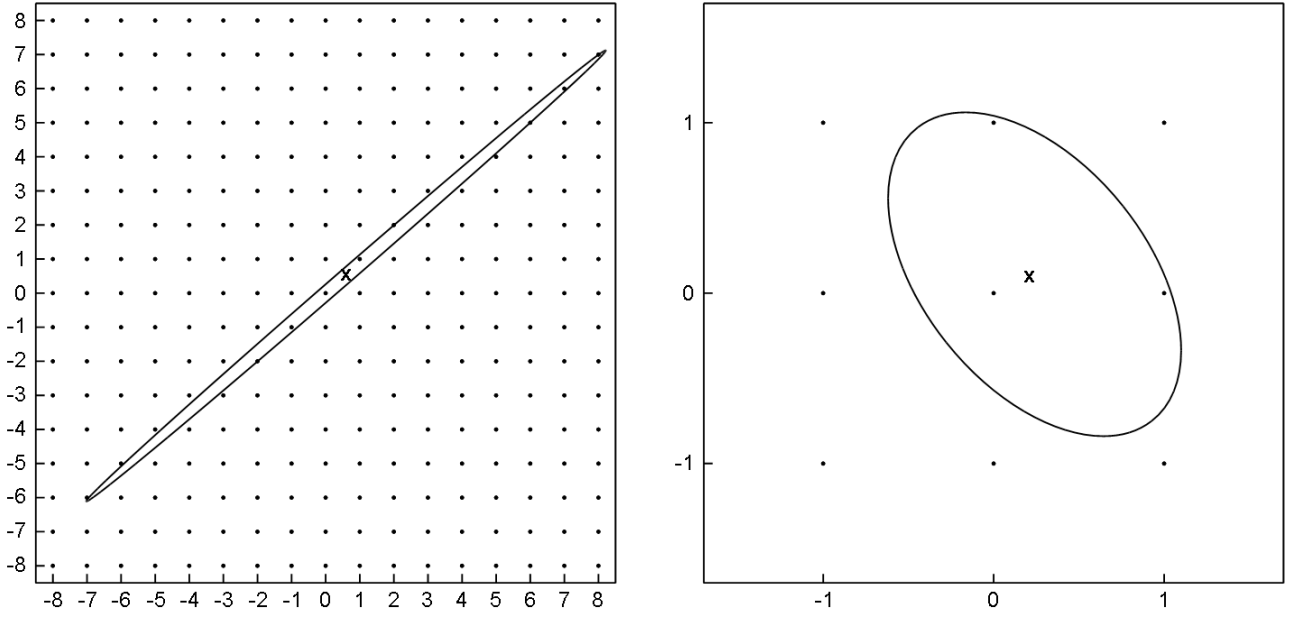
Figure 22. Example for a 2D search space before (left) and after (right) the decorrelation of the ambiguities by applying the transformation matrix Z. The size of the integer search grid is significantly reduced. The float ambiguity vector is indicated by a cross.

Applying the transformation to a given cofactor matrix $Q_{\tilde{a}}$ yields:

$$Q_{\tilde{z}^*} = Z^T Q_{\tilde{a}} Z = \begin{pmatrix} q_{a_1 a_1} & \omega_1 q_{a_1 a_1} + q_{a_1 a_2} \\ \omega_1 q_{a_1 a_1} + q_{a_1 a_2} & \omega_1^2 q_{a_1 a_1} + 2\omega_1 q_{a_1 a_2} + q_{a_2 a_2} \end{pmatrix} \tag{36}$$

A diagonal structure of the result is obtained, if ω_1 is chosen as follows:

$$\omega_1 = -\frac{q_{a_1 a_2}}{q_{a_1 a_1}} \tag{37}$$

A closer look on the elements of the resulting matrix yields a decorrelation of both parameters, because off-diagonal elements are equal to zero. Additionally the product of the variances is reduced, i.e., the search space is shrunk, because element (2,2) of $Q_{\tilde{z}^*}$ is smaller than before:

$$Q_{\tilde{z}^*}(2,2) = -\frac{q_{a_1 a_2}^2}{q_{a_1 a_1}} + q_{a_2 a_2} < q_{a_2 a_2} = Q_{\tilde{a}}(2,2) \tag{38}$$

In order to preserve the integer nature of the transformation ω_1 has to be rounded to the nearest integer. The procedure is repeated until the identity matrix remains. The final transformation matrix Z is created from the product of all derived matrices. As a result, the search space is much smaller and a high decorrelation of the ambiguities is achieved.

In a second step of LAMBDA, individual search boundaries have to be created in order to solve for each integer ambiguity separately. To this end, the objective function is rearranged to a sum of individual squares using a LDL^T decomposition of $Q_{\tilde{z}^*}$ (Teunissen, 1995), which corresponds to a conditional least-squares decomposition of the ambiguities. L represents a unit lower triangular matrix and D is a diagonal matrix, whereas D^{-1} is composed of conditioned variances $\sigma_{\tilde{z}^*_{i|I}}^2$ with the ith element conditioned on the previous one. If the ambiguities were fully decorrelated, L would be the identity matrix and n independent equations could be formulated, including the variance $\sigma_{\tilde{z}^*_i}^2$ of the least-squares ambiguities:

$$\min_{z^*} (\tilde{z}^* - z^*) Q_{\tilde{z}^*}^{-1} (\tilde{z}^* - z^*) = \min_{z^*} \sum_{i=1}^{n} \frac{(\tilde{z}_i^* - z_i^*)^2}{\sigma_{\tilde{z}_i^*}^2} \tag{39}$$

In this special case, the solution of the minimization problem could be derived by a simple rounding of each float ambiguity. Nevertheless, using the above mentioned matrix decomposition of $Q_{\tilde{z}^*}$, a sum of conditional squares can be formulated, using the conditional variances $\sigma_{\tilde{z}_{i|I}^*}^2$ of matrix D^{-1}. The solution of the minimization problem is obtained by a search based on a set of bounds:

$$\sum_{i=1}^{n} \frac{(\tilde{z}_{i|I}^* - z_i^*)^2}{\sigma_{\tilde{z}_{i|I}^*}^2} \leq \chi^2 \tag{40}$$

The parameter χ^2 controls the size of the solution (search) space and has to be chosen in a way to include at least one solution. From equation 40 the n individual intervals for the search space are created (Teunissen, 1993). This is accomplished simply by reformulating the inequality, omitting all summands of index i larger than the actual number of ambiguity. Consequently, the individual boundaries are calculated from the integer result z_j^* of the previous step:

$$
\begin{aligned}
(\tilde{z}_1^* - z_1^*)^2 &\leq \sigma_{\tilde{z}_1^*}^2 \chi^2 \\
(\tilde{z}_{2|1}^* - z_2^*)^2 &\leq \sigma_{\tilde{z}_{2|1}^*}^2 (\chi^2 - (\tilde{z}_1^* - z_1^*)^2 / \sigma_{\tilde{z}_1^*}^2) \\
&\vdots \\
(\tilde{z}_{n|N}^* - z_n^*)^2 &\leq \sigma_{\tilde{z}_{n|N}^*}^2 (\chi^2 - \sum_{j=1}^{n-1} (\tilde{z}_{j|J}^* - z_j^*)^2 / \sigma_{\tilde{z}_{j|J}^*}^2)
\end{aligned}
\tag{41}
$$

A good choice for χ^2 can be obtained from integer bootstrapping (yielding z_B^*), because this solution gives a good approximation for the ILS estimator and is easy to compute (Verhagen, 2005):

$$\chi^2 = (\tilde{z}^* - z_B^*) Q_{\tilde{z}^*}^{-1} (\tilde{z}^* - z_B^*) \tag{42}$$

The solution space constructed in this way is larger or equal the search space needed for the final step of LAMBDA. An alternative method for a definition of the search space is shown in de Jonge and Tiberius (1996) and Teunissen et al. (1996); the number of included solutions in the ellipsoidal search space can be approximated from its volume, that can be derived using $Q_{\tilde{a}}$. The search itself is performed by trying all possible combinations within the solution space until one valid integer vector is found. Subsequently, χ^2 is decreased until no further solutions can be derived. The last integer vector obtained represents the final and optimum solution $\check{a}$.

Finally, the residual $(\tilde{a} - \check{a})$ is used to adjust the unconstrained solution $\tilde{b}$ in order to obtain the final solution for the float parameters. A straightforward approach is a simplification of equation 28 by using the estimated integer ambiguities in order to unwrap the initial observations y:

$$\check{y} = y - A\check{a} \tag{43}$$

The float parameters can now be obtained from solving an ordinary LS problem:

$$\check{y} = B_1 b + e \tag{44}$$

Further details on implementational and computational aspects can be found in de Jonge and Tiberius (1996) and de Jonge et al. (1996).

4.2.2   Application to PSI

Within PSI, the LAMBDA approach offers the ability to estimate the topographic height residuals and deformation rate on basis of the used DEM and deformation model. Following equations 15 and 16, the phase difference between two PS is given by:

$$E\{\Delta\Phi\} = \beta \cdot \Delta h - \frac{4\pi}{\lambda} \sum_{d=1}^{D} \Delta\alpha_d \cdot p_d(t) \tag{45}$$

Assuming linear deformation, k different equations for one arc can be set up:

$$E\{\Delta\Phi^k\} = \beta^k \cdot \Delta h - \frac{4\pi}{\lambda}\Delta\alpha \cdot T^k \tag{46}$$

However, the phase difference $\Delta\Phi^k$ is ambiguous by multiples of 2π, but can be unwrapped by the correct integer ambiguity a^k:

$$\Delta\Phi^k = \Delta\phi^k + 2\pi \cdot a^k \tag{47}$$

In matrix notation the system of equations can now be written as follows:

$$E\left\{\begin{bmatrix} \Delta\phi^1 \\ \vdots \\ \Delta\phi^k \end{bmatrix}\right\} = \begin{bmatrix} -2\pi & & \\ & \ddots & \\ & & -2\pi \end{bmatrix}\begin{bmatrix} a^1 \\ \vdots \\ a^k \end{bmatrix} + \begin{bmatrix} \beta^1 & -\frac{4\pi}{\lambda} \cdot T^1 \\ \vdots & \vdots \\ \beta^k & -\frac{4\pi}{\lambda} \cdot T^k \end{bmatrix} \cdot \begin{bmatrix} \Delta h \\ \Delta\alpha \end{bmatrix} \tag{48}$$

which corresponds to a linear system of equations with unknown integer ambiguities a and float parameters b (cf. equation 28):

$$E\{y\} = A_1 a + B_1 b \tag{49}$$

The solution can only be obtained, if additional constraints are introduced, because the system of equations holds $k + 2$ unknown parameters (k integer ambiguities a^k, Δh, $\Delta\alpha$) but only k different equations are available. Therefore, pseudo-observations are used, one for each unknown float parameter in order to remove the datum deficiency. As shown in Kampes and Hanssen (2004), pseudo-observations of the DEM refinement and each displacement parameters are introduced, regularizing the system of equations:

$$E\left\{\begin{matrix} y_1 \\ y_2 \end{matrix}\right\} = \begin{bmatrix} A_1 \\ A_2 \end{bmatrix} a + \begin{bmatrix} B_1 \\ B_2 \end{bmatrix} b, \qquad D\left\{\begin{matrix} y_1 \\ y_2 \end{matrix}\right\} = \begin{bmatrix} Q_{y_1} & 0 \\ 0 & Q_{y_2} \end{bmatrix} \tag{50}$$

In general, the values of the pseudo-observations are chosen as $y_2 = 0$, hence, matrix A_2 is a zero matrix and B_2 is an identity matrix. The dispersion D of the observations is obtained from the propagation of the covariance matrix of the original phase observations (see Kampes (2006) for details), summarized in Q_{y_1}, and for Q_{y_2} pessimistically chosen a priori standard deviations are used. After the regularization LAMBDA can be applied to the given equations following the steps mentioned in the previous section, i.e., calculation of the float solutions and determination of the integer ambiguities. Unfortunately, the introduction of pseudo-observations extremely biases the float solution parameters (Kampes and Hanssen, 2004). However, if the correct ambiguities are estimated the observed phases can be unwrapped (ϕ_{uw}). This task can be

accomplished by using equation 47 and the float parameters can be obtained from a ordinary unconstrained least-squares adjustment (Kampes, 2006), leaving k equations and 2 unknowns:

$$
E\left\{\begin{bmatrix} \Delta\phi_{uw}^1 \\ \vdots \\ \Delta\phi_{uw}^k \end{bmatrix}\right\} = \begin{bmatrix} \beta^1 & -\frac{4\pi}{\lambda}\cdot T^1 \\ \vdots & \vdots \\ \beta^k & -\frac{4\pi}{\lambda}\cdot T^k \end{bmatrix} \cdot \begin{bmatrix} \Delta h \\ \Delta\alpha \end{bmatrix} \tag{51}
$$

The resulting system of equations for the unknown float parameters $\check{b}$ represents an ordinary least-squares problem:

$$
E\{\tilde{y}_1\} = B_1 b, \quad D\{\tilde{y}_1\} = Q_{y_1} \tag{52}
$$

The solution can be obtained using the estimated integer ambiguities $\check{a}$:

$$
\check{b} = (B_1^T Q_{y_1}^{-1} B_1)^{-1} B_1^T Q_{y_1}^{-1}(y_1 - A_1\check{a}) \tag{53}
$$

In summary, the parameters are estimated from an initial calculation of the float solution. Subsequently, the integer values of the ambiguities are derived from the transformed solution space. Finally, the refined float parameters are calculated from the unwrapped phase, obtained from the retransformed integer ambiguities. The advantage and acceleration of LAMBDA stems from the decorrelation of the ambiguities and the involved reduction of the search space.

4.2.3 Sensitivity Analysis

In principle, comparisons exist between PSI results applying the LAMBDA method or a periodogram (Kampes, 2006). Both algorithms are used to estimate deformation and height residuals within a network of PS. But these investigations are based on completely different processing chains. Therefore, in this thesis the robustness of LAMBDA and its performance in comparison to a periodogram are investigated using one single PSI processing system. This approach allows for a direct inspection of the estimation results between equal pairs of PS within the same selection of PS candidates. For these analyses, a reference PSI processing is performed using ERS data of the urban area of Munich, already presented in Section 2.3.2. The results are used as reference for a comparison to different tests; the influence on results obtained using LAMBDA at a reduced number of acquisitions and varying reference points, as well as in direct comparison to the estimation results using a periodogram. In addition, the stability of LAMBDA is investigated on basis of simulated data.

Dependence on Number of Acquisitions

In a first step, the stack is divided into two different subsets with one single common scene, used as master in both cases. The latter prevents a bias originating from different master APS. For the split-up of the reference dataset, the temporal and geometrical baselines are considered to ensure a comparable distribution and reduce any bias due to seasonal effects (e.g., water vapor, temperature, backscattering). An identical initial state for both subsets is achieved by the usage of PS locations detected in the reference stack, i.e., all PS candidates are pre-selected equally for both stacks, at the locations detected in the reference processing. All subsequent steps that follow the selection of PS candidates are performed separately in each of the subsets using equal processing parameters.

The final results are compared between the subsets and in addition to the reference stack. Only a few single PS exist that show significant differences to the reference processing. Approximately

79% of the ($\sim$10,000) PS are selected identically as final PS within the two subsets, whereas the percentage is increased to 84% and 87%, if the selections of final PS of the subsets are compared to the reference stack. The varying selections originate from slightly differing phase histories and an exclusion of PS due to deviations from the selected deformation model. However, the large majority of final PS are available from all stacks. Certainly, the estimated parameters will show variations as well. Overall, the standard deviations of the differences for deformation estimates are between 0.24 mm/y and 0.45 mm/y at a mean value of -0.19 mm/y to 0.13 mm/y. The differences in DEM refinements show standard deviations between 0.32 m and 0.64 m at a mean of -0.14 m to 0.36 m. In both cases, the differences between the two subsets are larger than any comparison to the reference stack. The non-identical PS (locations) are mainly present in the subsets and only few in the reference stack. This effect can be explained by the removal of PS that are affected by model mismatches as soon as the temporal sampling is increased, thus are rated unreliable. For the same reason, other PS are included in the reference stack but not available in the subsets, because the increase in number of available datasets results in an acceptance of some PS due to lower deviations from the deformation model or due to falling below thresholds of reliability tests. Consequently, as many acquisitions as possible should be used for the estimation. In general, about 50 scenes are necessary for a reliable processing using regularly acquired medium resolution SAR data.

It has to be mentioned, that the choice of the reference point indeed is a critical issue concerning final absolute values of displacement and height refinements, but it does not affect the adjustment of the reference network. A disadvantageous choice will result only in a common offset in deformation amplitudes and absolute height for all PS, because the integration is based on a least-squares adjustment without any constraints on the inner geometry of the network. The reference point is needed only to fix the datum deficiency. However, the variances of the estimated and integrated unknowns are dependent on the location of the reference point. A choice close to the border of any side of the reference network will result in high standard deviations for the estimated PS at the opposite borders. For this reason, the reference point should be chosen in the center of the network in order to minimize error propagation within the area under investigation. However, relative estimates show a high precision due to the quite equal distribution of errors throughout the reference network, whereas absolute values have to be treated carefully at larger distances to the reference point due to the mentioned increase of variances.

Influence of Phase Noise

The statistical analysis of LAMBDA is based on simulations of linear deformation superimposed by noise of different levels. To this end, the LAMBDA toolbox available for MATLAB (Kampes, 2006) is used. The configuration is chosen to be comparable to the PSI estimation procedure. For each estimation a linear deformation is randomly selected between -5 mm/y and +5 mm/y. The temporal baselines cover approximately 10 years and include between 50 and 100 data samples. The wrapped phase values that represent observed phase differences between two PS additionally contain phase noise between 20° and 80° in order to simulate real circumstances for deformation estimation in PSI. Altogether, 2000 loops are evaluated, and the results are summarized in Table 4. From the statistics, it becomes evident that all ambiguities (except 5) can be estimated correctly for phase noise up to 40° providing perfect results of the deformation rates. Between 50° and 60° of phase noise the number of errors in estimated ambiguities Δ_a increases dramatically and the mean standard deviation of the estimated deformation rate $\overline{\sigma}_{\Delta v_{LOS}}$ raises to 10.1 mm/y. In addition, there already appear a few large deviations from the real displacement values in some of the single estimations (cf. maximum error of deformation $max|\Delta v_{LOS}|$) at a phase noise of 50°. In summary of this configuration, the LAMBDA estimator provides almost perfect estimates up to 40° of phase noise. Starting from approximately 50° of phase noise, the number of wrongly resolved ambiguities increases very fast and the estimation

results must be treated with care. However, there exist control parameters for LAMBDA that limit the search space in order to suppress unrealistic values for the estimated parameters, but this is based on a priori knowledge that has to be introduced prior to the estimation procedure.

Noise level [°]	20	30	40	50	60	70	80
$\overline{\sigma}_{\Delta v_{LOS}}$ $[mm/y]$	0.05	0.09	0.14	1.85	10.1	19.1	35.0
$max|\Delta v_{LOS}|$ $[mm/y]$	0.23	0.36	0.45	80.2	156	211	213
Δ_a	0	0	5	860	15269	54637	160979
$\overline{\Delta}_a$	0	0	0	0.43	7.6	27.3	80.5

Table 4. Statistical analysis of LAMBDA including different noise levels: Mean standard deviation ($\overline{\sigma}_{\Delta v_{LOS}}$) and maximum error ($max|\Delta v_{LOS}|$) of the estimated deformation rate. Number of erroneously estimated ambiguities and the respective mean are given by Δ_a and $\overline{\Delta}_a$.

Performance in Comparison to a Periodogram

The comparison of estimation results between LAMBDA and a periodogram – implemented by a maximization of the ensemble phase coherence (cf. Section 2.3.1) – is split into two parts. First, the unknowns of deformation and height residuals are estimated apart from each other for one common reference network and the obtained results are compared directly. Subsequently, the PSI processing is continued for both results separately to investigate the impact of differences on the final results of deformation estimates and height residuals, including all PS available. For this analysis the reference stack of the test site of Munich is used again. The PS processing is split into two different lines at the step of reference network estimations, whereas the subsequent steps are the same again for both processing lines. By reason of the availability of LAMBDA in PSI-GENESIS, only the periodogram has to be inserted into the processing chain, replacing the standard approach. Only a simple estimator is used, i.e., no further statistical analysis for a detection of outliers is applied. The ensemble phase coherence is calculated as follows:

$$|\widehat{\gamma}_{x,y}| = \left| \frac{1}{K} \sum_{k=1}^{K} \exp\left\{ j\Delta\phi_{x,y}^k \right\} \cdot \exp\left\{ -j\left(\beta_x^k \cdot \Delta h_{x,y} - \frac{4\pi}{\lambda} T^k \cdot \Delta v_{LOS}(x,y) \right) \right\} \right| \quad (54)$$

$\Delta\phi_{x,y}^k$ represents the observed phase difference between points x and y in the interferogram k. The evaluation of a periodogram can be considered "brute force", because all pairs of potential values of $\Delta h, \Delta v_{LOS}$ at every single arc have to be calculated using the given formula. The maximum within the result denotes the estimated solution for each arc. Therefore, the solution space has to be quantized and boundaries have to be fixed prior to the calculations. Certainly, the size of the solution space has to be chosen appropriately to cover all reasonable results, but this choice directly affects calculation times. In addition, too generously chosen borders may give an increased number of incorrect results. On the other hand, a too small search space will always lead to an increasing number of incorrect estimates. The sampling distance of the solution space is another critical issue of an estimation using a periodogram. The solution space must be sampled appropriately in order to avoid aliasing, that would lead to incorrect results due to emerging ambiguities for the unknowns to be estimated. Summarizing, it is important to consider the range of the solution space as well as its sampling with respect to the expected values of the unknowns. In comparison to LAMBDA these prerequisites are major disadvantages for this kind of estimation procedure.

A comparison of the results from the arcs of the reference network obtained from both estimators shows larger differences in a few arcs, depending on the threshold of coherence. As can be seen from Figure 23 some differences are quite large, thus, can be regarded as wrong estimations of

one of both estimators. But in most of the cases, these erroneous arcs originate from single PS, that are the source of errors in these cases and should be removed. The number of potential outliers can be reduced significantly, if the threshold on coherence is increased to 0.5. However, this parameter should not be used exclusively for outliers removal, because a further increase would also remove many of the correctly estimated arcs. The difference between both estimators finally show a mean of -2.0·10^{-3} m ($\sigma_{\Delta h}$ = 0.16 m) for residual heights and a mean of 0.01 mm/y ($\sigma_{\Delta v_{LOS}}$ = 0.12 mm/y), mainly originating from residual deviations between a few single arcs. In general, faulty arcs show large deviations in DEM refinements as well as in displacement rate estimates, as can be seen in the plot of low coherence arcs in Figure 23. The deformation phase histories and estimated linear trends obtained by both estimators for one arc showing a larger residual deviation is given in Figure 24. In this case, the result of LAMBDA seems to fit better. However, there also exist some arcs for which the periodogram (most likely) performs better.

Furthermore, the results are integrated using confidence values from each corresponding estimator and final deformation values and height residuals are calculated for all PS. In addition, statistical tests for the detection of outliers within the obtained results are applied, based on the same thresholds for both cases. The results shown in Figure 25 are almost identical, only isolated points show larger local differences. Obviously, some of the outliers could not be removed from each of the two final estimates. This could be refined by tuning the statistical test parameters, but by reason of the local limitation to single isolated points, this is not necessary for the performance comparison of both estimators. The final results hold a mean difference in height residuals of -0.05 m ($\sigma_{\Delta h}$ = 3.58 m) and in displacement estimates of 0.001 mm/y ($\sigma_{\Delta v_{LOS}}$ = 1, 53 mm/y). These relatively large numbers mainly originate from the mentioned remaining outliers. The majority of estimated parameters are identical, as derived from the scatterplots provided in Figure 25.

This analysis concludes that LAMBDA is a robust way of estimation and an intelligent way of optimizing the search space. Hence, it decreases the computational costs. Nevertheless, both methods deliver comparable results except for some local isolated discrepancies, which could be removed, e.g., by further restrictive outliers detection. The run-time between both estimators cannot be compared easily, because it depends on a variety of initial parameters and the implementations of the algorithms. Both estimators may be optimized in terms of assumed best size of the search space and how the search is performed. Consequently, the comparison of calculation times between LAMBDA and the used (simple) implementation of a periodogram does not provide useful information.
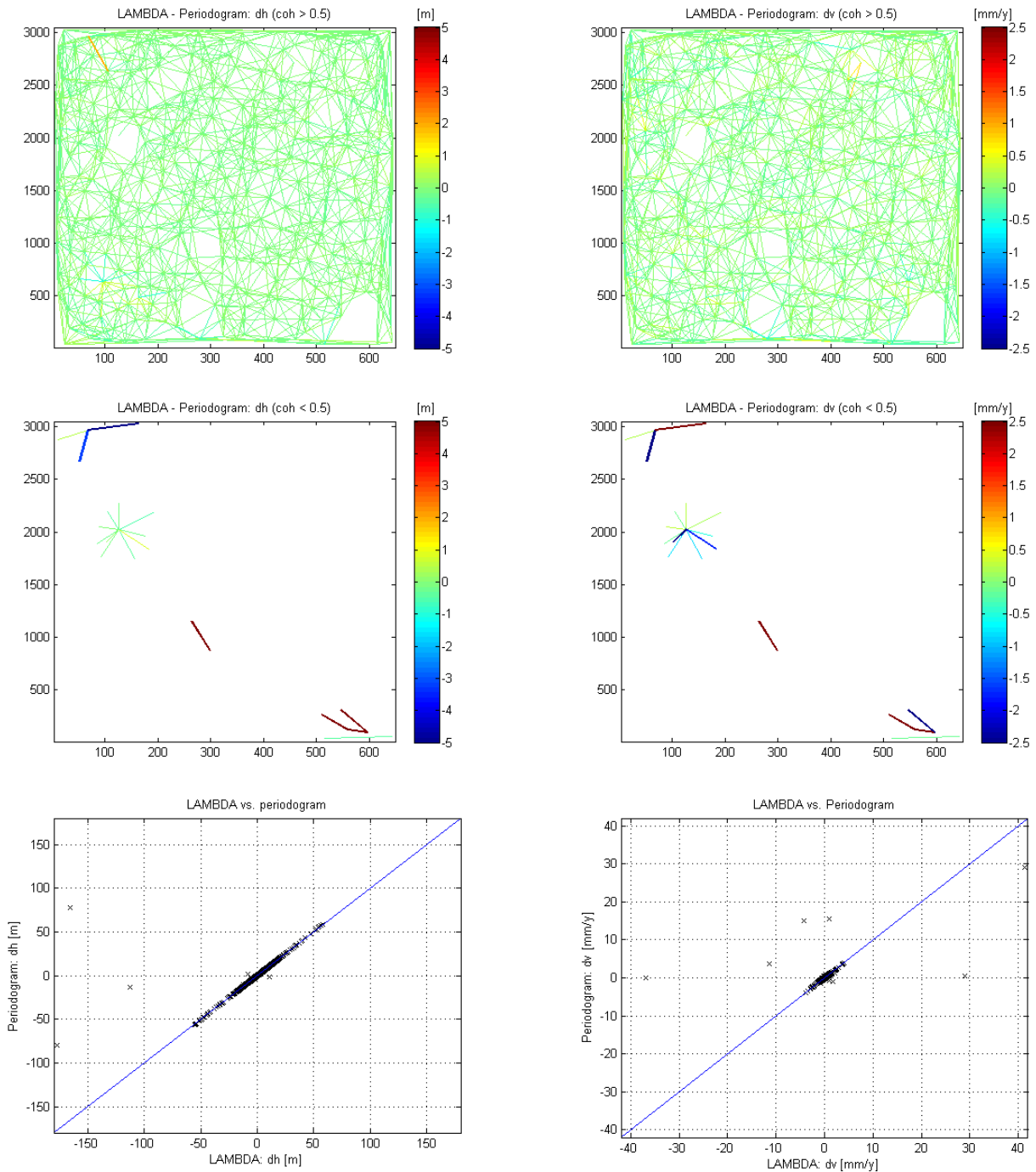
Figure 23. Differences in height (left) and displacement (right) estimation of the reference network between LAMBDA and the periodogram. Top: A threshold in coherence of 0.6 significantly reduces the number of obvious outliers based on wrong estimates of the periodogram. Middle: Bad arcs (low coherence) in general radiate from single points, hence the sources of the errors mainly are these single PS. Bottom: Scatterplot of results from both estimators, restricted to coherence values above 0.6. Only a few estimated arcs still show differences, but the majority of estimations are identical, as can be seen in the scatterplots.
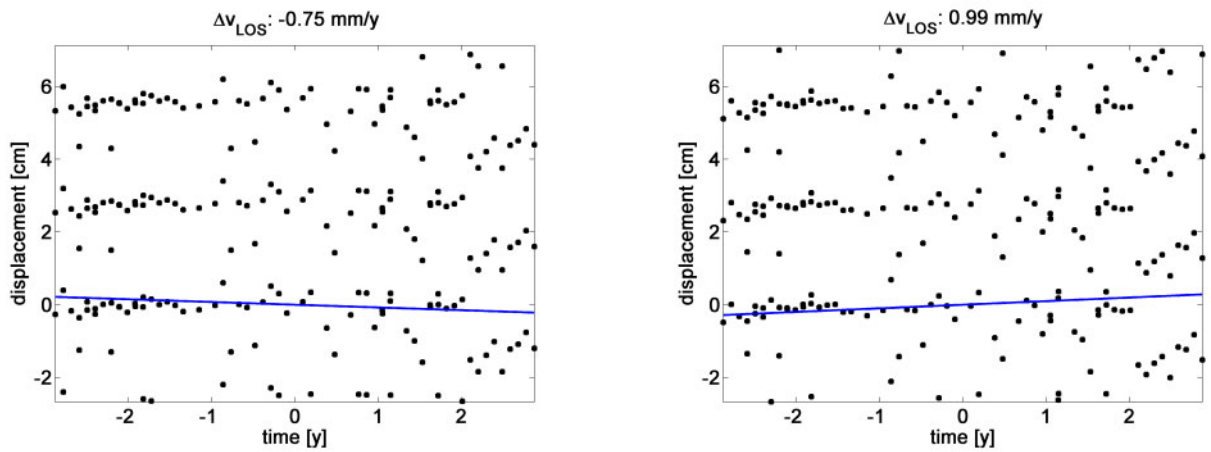
Figure 24. Comparison of deformation phase histories of one arc between both estimators. The estimated linear trend differs by 1.74 mm/y. The result of the periodogram (left) maximizes the ensemble coherence. However, the result of LAMBDA (right) seems to fit better. Black dots represent deformation phase (including $\pm 2\pi$ ambiguities) after the removal of estimated relative height offset. Solid blue line indicates the estimated linear deformation.
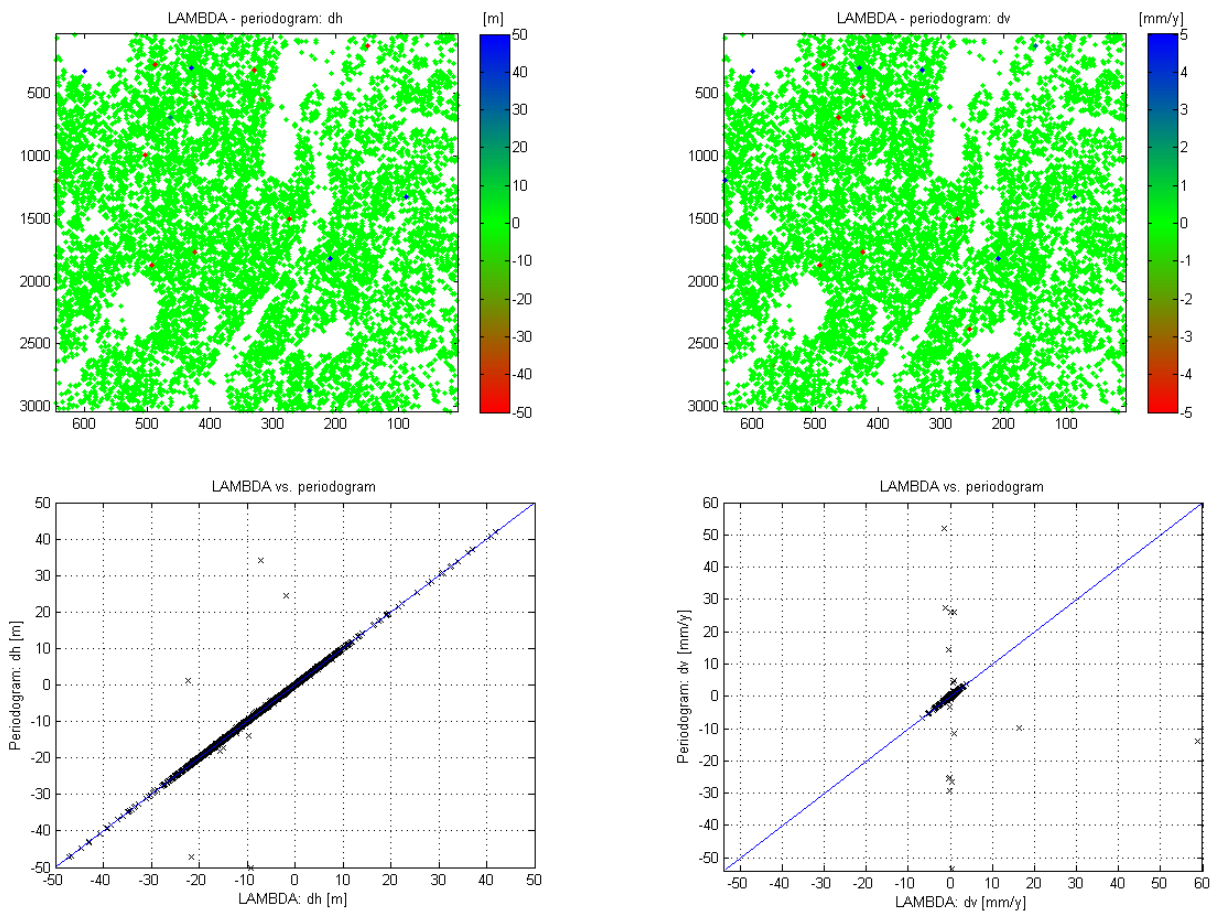
Figure 25. Top: Comparison between final results using the two different estimates of the reference network. Only a few single PS show larger deviations. Bottom: Scatterplot of both results show only a few discrepancies between the two final results for both parameters.

4.3   PS Densities

The success of PSI is directly connected to the amount of suitable scatterers available in the area of interest. Especially for medium resolution data, the opportunistic character of PSI does not allow for any predictions on the availability and/or density of PS on certain objects of interest. Typical numbers are several hundred PS per square kilometer. For meter-resolution SAR, many more PS are reported in urban areas (Adam et al., 2008a). Figure 26 gives an impression on the large difference in numbers of PS between medium and high resolution SAR. The density of PS increased by factor of 100 - 200 in comparison to medium resolution SAR (Bamler et al., 2009), mainly due to the increased resolution and the small required corner size of only 6 cm side length (cf. Section 2.3.2) in order to be selected as PS. But the number of signatures which act as PS certainly depends on acquisition parameters, besides the structure and material of the objects within the scene. Hence, the variation in densities of potential PS candidates with respect to polarization, incidence angle and track direction is investigated in the following section, in order to better understand the appearance of these points. To this end, several areas of different size are analyzed within the test site of Berlin due to the availability of several different acquisition geometries. The findings can help with the decision of orbit and track type useful for the desired application within the area of interest.
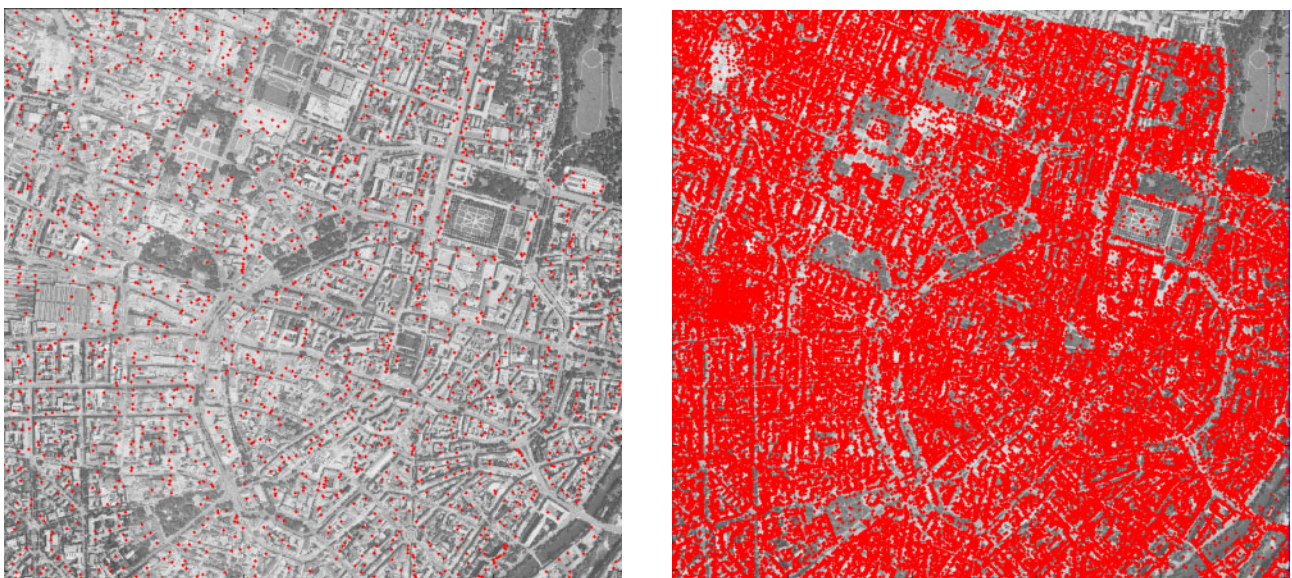
Figure 26. Visual comparison of PS detectable from stacks of medium (left) and high resolution (right) SAR data of Munich. The geocoded PS (red dots) are overlaid on an aerial image. The results are based on stacks of ERS and TerraSAR-X high resolution spotlight data.

4.3.1   Derivation of a PS Local Density Map

The stacks used for this investigation are based on the data of Berlin test site already presented in Section 4.1.2 but are limited to only 6 datasets each, because HH-polarized stacks of the same acquisition geometry are available only at this low number of datasets. Larger stacks of HH data would have limited the data continuity and dense temporal sampling of already ordered stacks of VV polarization, because TerraSAR-X cannot acquire high resolution spotlight data in HH and VV polarization at the same time. The temporal baselines of the selected VV data are chosen preferably equal to the available HH stacks. In sum, 12 small stacks have been processed until the step of PS selection following the presented chain (cf. Section 2.3.2), providing 6 stacks in HH and VV data each. Half the amount of stacks of each polarization is obtained from descending tracks, the other half from ascending tracks.

Within ascending and descending tracks, the stacks differ in incidence angles, i.e., one steep, one mid range and one shallow incidence angle are available (cf. incidence angles in Table 2, page 45). These small stacks are not suitable for a reliable estimation of any deformation signal; hence, the comparison does not include PS fitting a deformation model. Nevertheless, the data is sufficient for an analysis based on PS candidates selected by a threshold on the SCR of 3.0 in this case, accounting for the low number of acquisitions. The latter is calculated from a temporal average image, called *meanmap* in the following. The comparison of differences in numbers of PS at later processing steps may even bias the results of the intended analysis, as points would be discarded by reason of deviations from the assumed deformation model. Hence, PS could be lost that follow a different type of deformation. The detection of local differences in number of PS between the different stacks is supported by a calculation of local PS densities. To this end, the number of neighboring PS is counted in a small window (side length of 15 m) around each scatterer and the obtained numbers are normalized by the window area. For a fast and easy comparison, the ordinate of all meanmaps and density maps, as well as PS position maps shown in the following are rotated in a northward direction. In addition, a scaling to one meter pixel size is applied.

4.3.2   Dependence on Polarization

The first sample area is chosen south-east of Berlin central train station and includes several large blocks of houses of medium height. The meanmap is shown in Figure 27a including red arrows that indicate azimuth directions. The left arrow shows the approximate flight direction of the satellite for ascending tracks, the right arrow for descending tracks respectively. The directions are valid for all subsequent meanmaps within this section. Note that the alignment of bright facades is approximately in parallel to the flight direction of ascending tracks. This particular configuration results in an almost linear increase of point densities up to 100,000 PS/km^2 for this track type (cf. Figure 27b). Facades aligned towards the sensor obviously produce a large amount of PS, possibly by reason of increased occurrence of double and triple bounce effects, that result in bright signatures to a greater extent. In addition, HH polarized data allows for an even larger number of PS to be extracted of up to 20% compared to VV stacks in this case. The numbers of PS for descending stacks are slightly lower, and the difference between HH and VV data is less distinctive. Consequently, the alignment of facades is an important parameter, which will be discussed later on again.

The second sample area includes a sports stadium. This object allows for a more detailed view on the change of PS densities between stacks of different polarization. From Figures 28 and 29, the changes in intensity between the meanmaps and the corresponding changes in density maps can be seen. For stack D36, up to 12% more PS can be extracted at this location if HH data is used, whereas the increase is even 21% for stack A51. A closer look on the density maps of Figures 28 and 29 reveals that densities vary most intensively especially at locations of features most presumably aligned perpendicular to ground range direction. This is the case at 4 positions within the stadium, at northern and southern seats (in these cases possibly the sides of the seats are incorporated into the reflection process), as well as at seats a little down of the grandstand (located east) and the north-western corner for descending stack D36 (cf. Figures 28a and 28b). Accordingly, the locations of largest variations change for ascending stacks, represented by stack A51, to the following positions: at the grandstand, at the top of the opposite stand, at the northern and southern seats (cf. Figures 29a and 29b). Also note that for this shallow angle the opposite stand is not visible due to radar shadow.

The third example covers a larger region in the north-west with respect to central train station (cf. Figure 30). It is a typical urban area of residential buildings constructed to both sides of the road network. The houses are directly connected to each other forming elongated, continuous facades showing an average of approximately 7 floors. In this area, the facades are oriented towards the sensor for descending stacks, resulting again in a high number of PS for these

(a) Meanmap of the selected area.

(b) Distribution of PS densities.
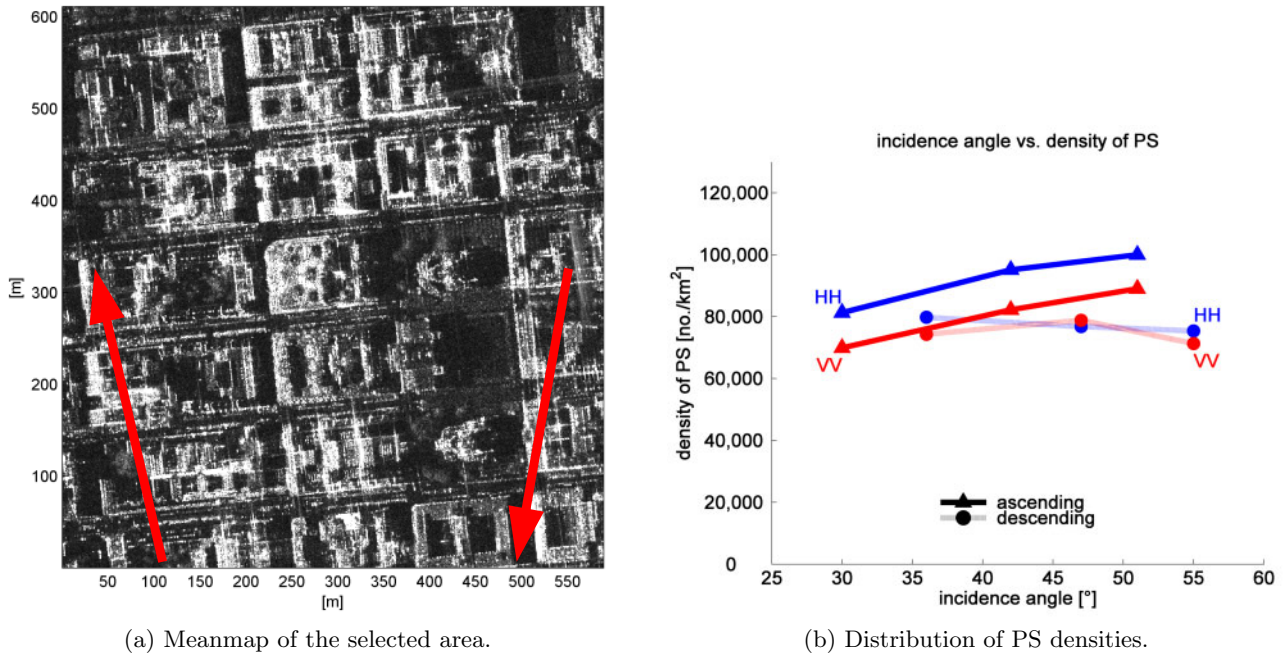
Figure 27. Left: Meanmap of first sample area used for analysis on polarization (stack A51 VV shown here). Red arrows indicate azimuth directions for ascending (left arrow) and descending (right arrow) stacks. Right: Distribution of PS densities with increasing incidence angle. Different polarization indicated by different colors and by HH/VV signatures. Solid lines including triangular markers indicate ascending tracks. Diffuse lines including round markers indicate descending tracks. PS selection requirement: SCR ≥ 3.0

datasets. The increase between VV and HH cases is up to 30% for descending and 20% for ascending cases, at least for steep incidence angles (cf. Figure 31). In general, data using HH polarization mode will most likely produce more PS than VV data of the same scene using the same acquisition geometry. Altogether, the variation in PS densities in this special area is very large: 39,000 PS/km^2 for stack A30, VV and 89,000 PS/km^2 for stack D47, HH, which corresponds to an increase of almost 130% mainly due to the alignment of facades to the sensor for descending tracks. As shown previously, the additional plots of the local densities facilitate a localization of PS density deviations.

4.3.3 Dependence on Heading Angle

The variation in number of signatures selected in PSI between ascending and descending tracks is clearly visible from the distribution already shown in Figure 31. None of the facades in the meanmaps of ascending stacks feature such bright signatures as for descending cases. The difference between the two track types is 60% - 70% for both polarizations due to strong dependencies of PS appearance on the track or rather heading direction relative to facades: an angle close to the perpendicular is beneficial for the number of PS that will be available. Although heading angles between stacks of equal track direction only differ slightly (in general below 2 - 4°), these changes may influence the scattering within the scene, too. In Figure 32 one example is pictured, in which most likely the change in brightness – and consequently the number of PS – changes between stack A42 and A51. The intensity of the left facades is reduced significantly, whereas it is the other way round for parts of the facade on the right hand side. Consequently, there is an increase and decrease in number of PS within parts of one small area. Between the two stacks also incidence angles change, but the present alternation of intensities of the return signals is – by experience – most unlikely induced by the latter. In general, the number of PS will be much higher for facades aligned towards the sensor. Furthermore, the separability of columns of windows of facades has to be considered, because a look on facades different from the perpendicular will affect PS (of neighboring columns, but different floors) to move together in azimuth direction. Assuming two PS to be separable if the two dominating
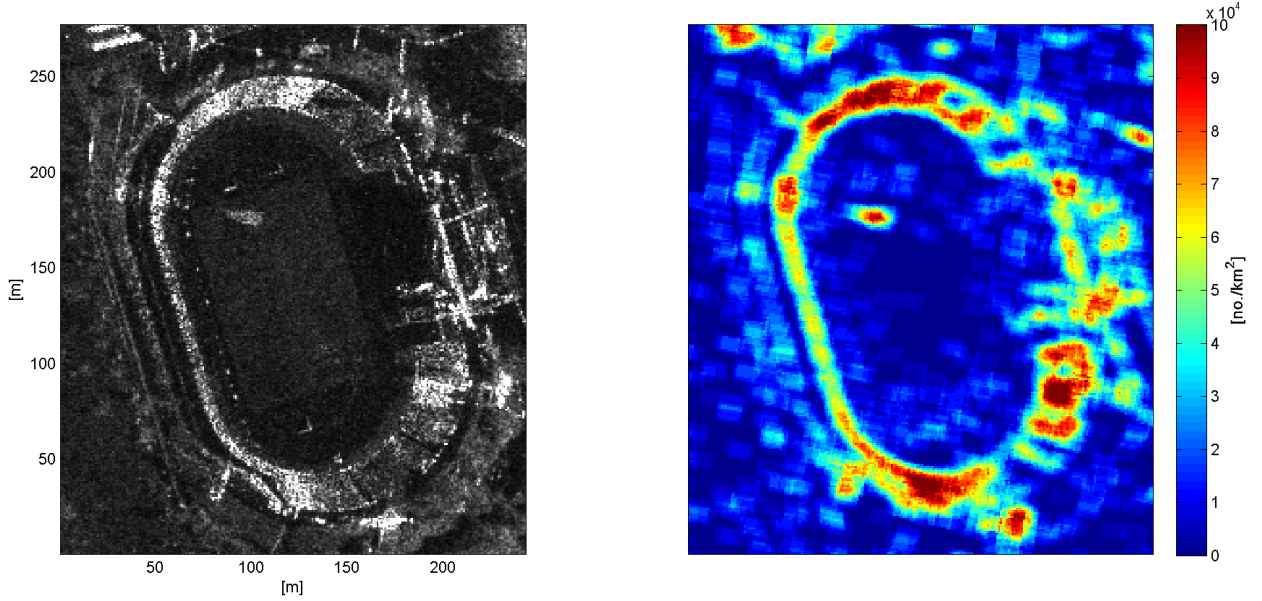
(a) Meanmap and density map of stack D36, HH.
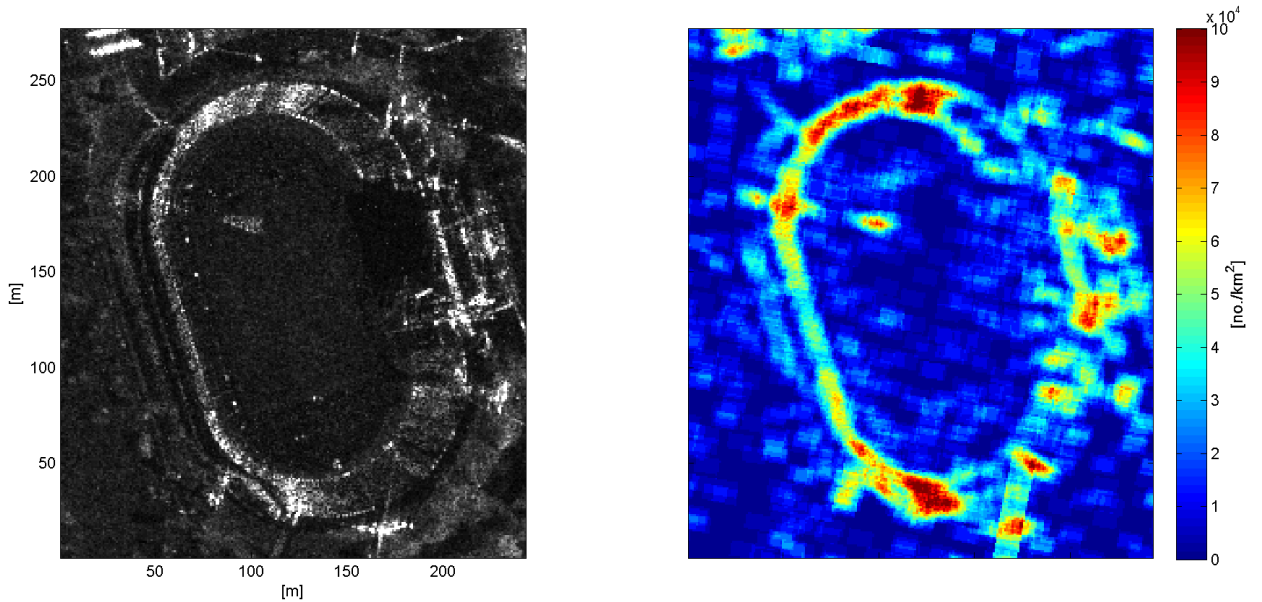
(b) Meanmap and density map of stack D36, VV.

Figure 28. Meanmaps of one descending stack of HH and VV polarized data of second sample area used for analysis on polarization. Right of each plot the density maps are shown for a better visualization of PS changes between HH and VV stacks. Colors indicate local densities up to 100,000 PS/km^2 (in red).

scatterers are located within different resolution cells, their distance must be larger than the given resolution of the radar instrument. The horizontal resolution in direction of a facade ρ_{xy} can be expressed by the azimuth resolution ρ_{Az} of the SAR system and the angle of rotation ι with respect to an alignment perpendicular to ground range direction:

$$\rho_{xy} = \frac{\rho_{Az}}{\cos \iota} \tag{55}$$

Given ρ_{Az} of TerraSAR-X (1.1 m) and a horizontal distance between windows of 2.7 m, the maximum rotation angle ι of facades still allowing for a separation of neighboring PS is approximately 66°. This effect can be validated experimentally by using SAR simulation. In Figure 33 two simulated radar images are shown, including different angles of rotation of a facade.
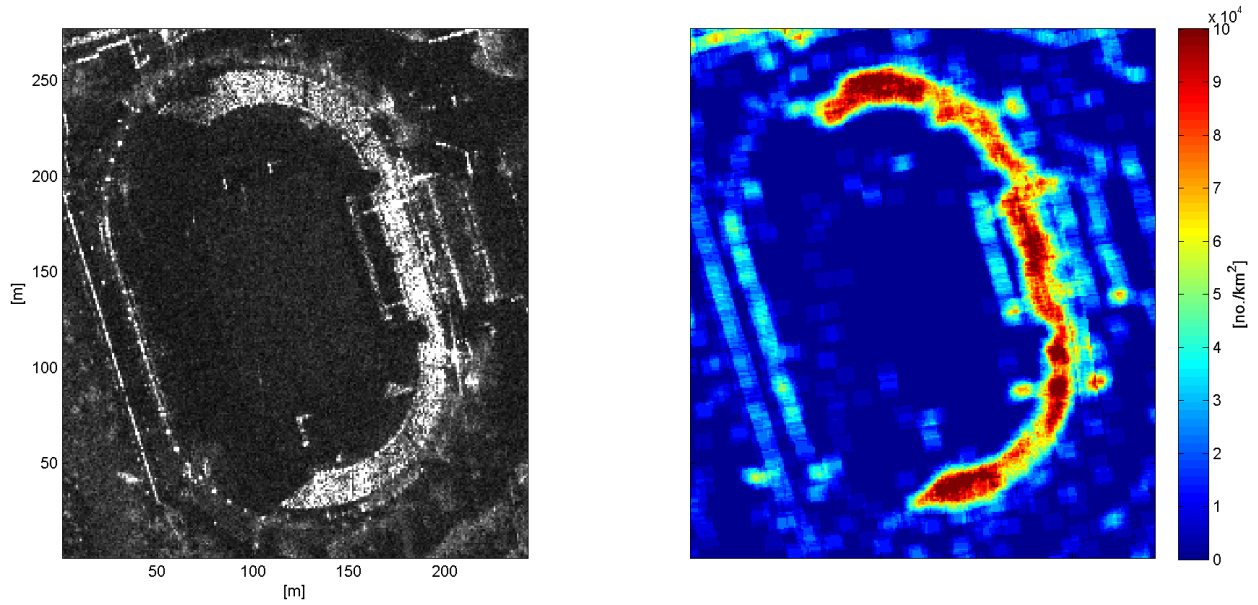
(a) Meanmap and density map of stack A51, HH.
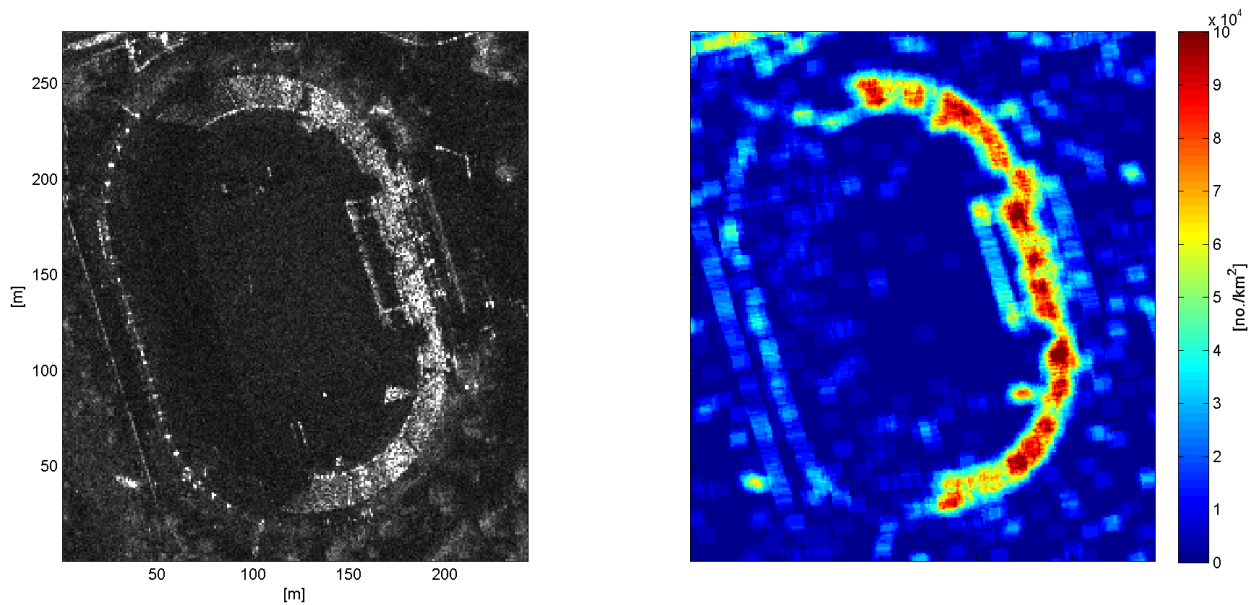
(b) Meanmap and density map of stack A51, VV.

Figure 29. Meanmaps of one ascending stack of HH and VV polarized data of second sample area used for analysis on polarization. Right of each plot the density maps are shown for a better visualization of PS changes between HH and VV stacks. Colors indicate local densities up to 100,000 PS/km² (in red).

Obviously, the PS of different floors but neighboring columns of windows cannot be separated any more in the second case of 75° of rotation. Consequently, this also will affect the number of PS available at facades, depending on the alignment of the latter with respect to the looking direction of the sensor. However, PS may be lost for smaller angles of rotation, because the corner responsible for the intense signal return is already hidden by reason of the inherent local building structures.

4.3.4 Dependence on Incidence Angle

Besides heading direction and polarization, incidence angles have an effect on PS densities. In the first example shown in Figure 34, the number of PS increases significantly (+45%) from steep to mid range incidence angles. Indeed, some structures at building facades (bal-
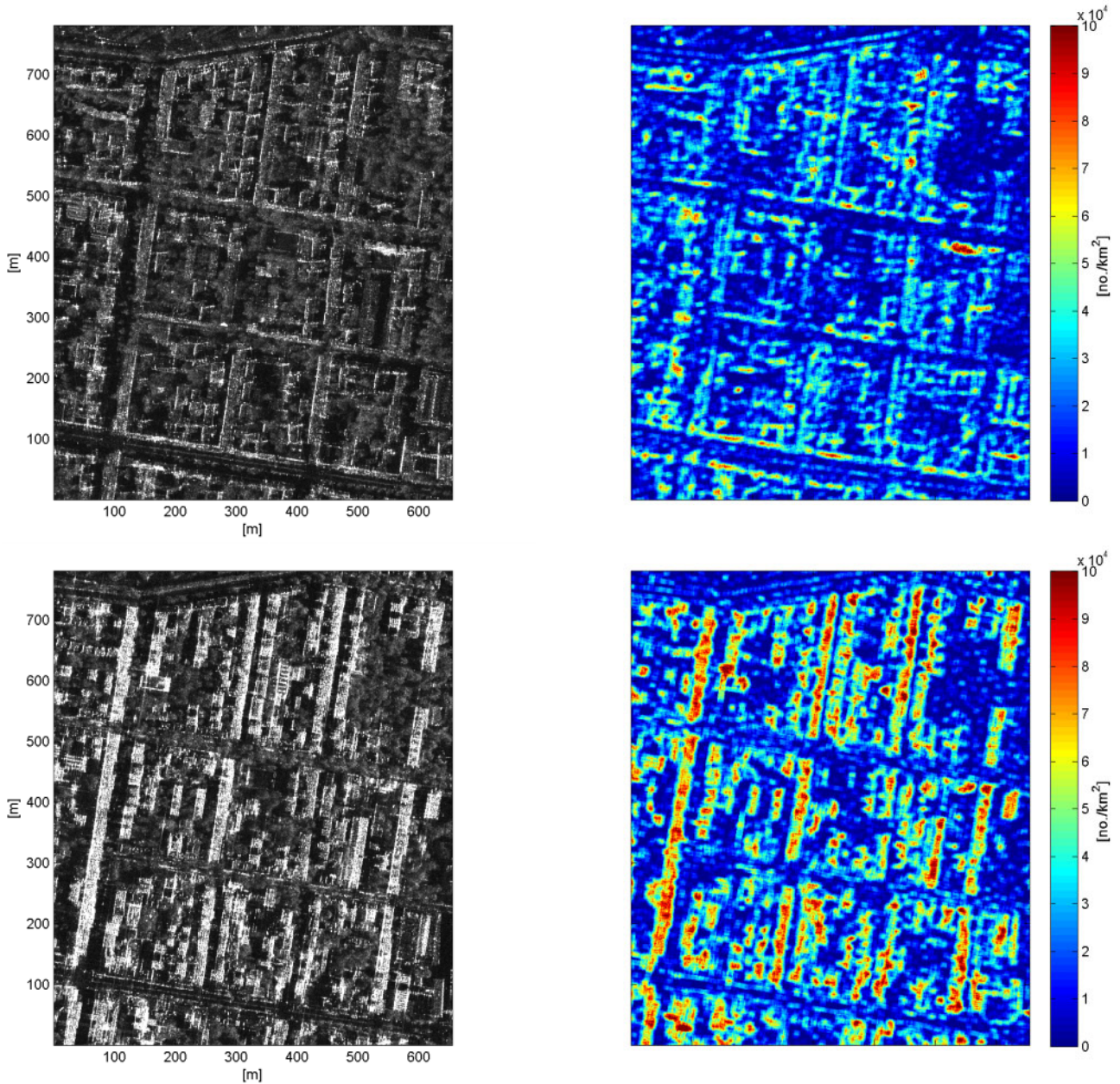
Figure 30. Meanmaps and density maps of sample area 3. Top: Meanmap and density map of stack A42, VV; bottom: Meanmap and density map of stack D47, VV. Colors indicate local densities up to 100,000 PS/km^2 (in red).

conies/window frames) only produce potential PS starting at mid range incidence angles, but no further increase is observed at the largest incidence angles, i.e., shallow looking directions. Note that especially rows and columns of windows at facades of houses will generate regular patterns of PS.

The second effect of increasing incidence angles on the number of PS can be seen in Figures 35 and 36; radar shadow induced by nearby buildings or building parts prevent lower floors from being illuminated by the sensor. Hence, the number of PS decreases. In the first example, the number of visible floors (lines of regular patterns at constant offsets) is reduced from 7 to 4, when moving from the stack of mid range to the one of largest incidence angle. In the second example of an extinction of PS due to shadow, the number of PS changes by almost 50% between steep and shallow looking directions. In the meanmaps of Figure 36 the loss of the first floors at mid range incidence angles is easy to observe, by reason of the vanishing bright double bounce line left of the center of the image. The large height and short distance of the opposing building is responsible for the large shadow effect and the loss of half the building for PSI. In general, the
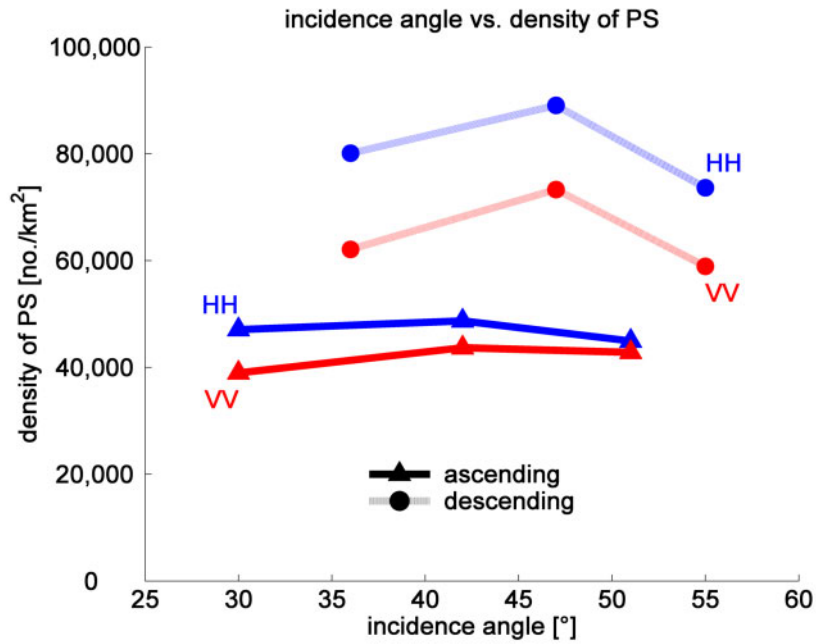
Figure 31. Distribution of PS densities with increasing incidence angle for sample area 3 shown in Figure 30. Different polarization indicated by different colors and by HH/VV signatures. Solid lines including triangular markers indicate ascending tracks. Diffuse lines including round markers indicate descending tracks. PS selection requirement: SCR $\geq$ 3.0
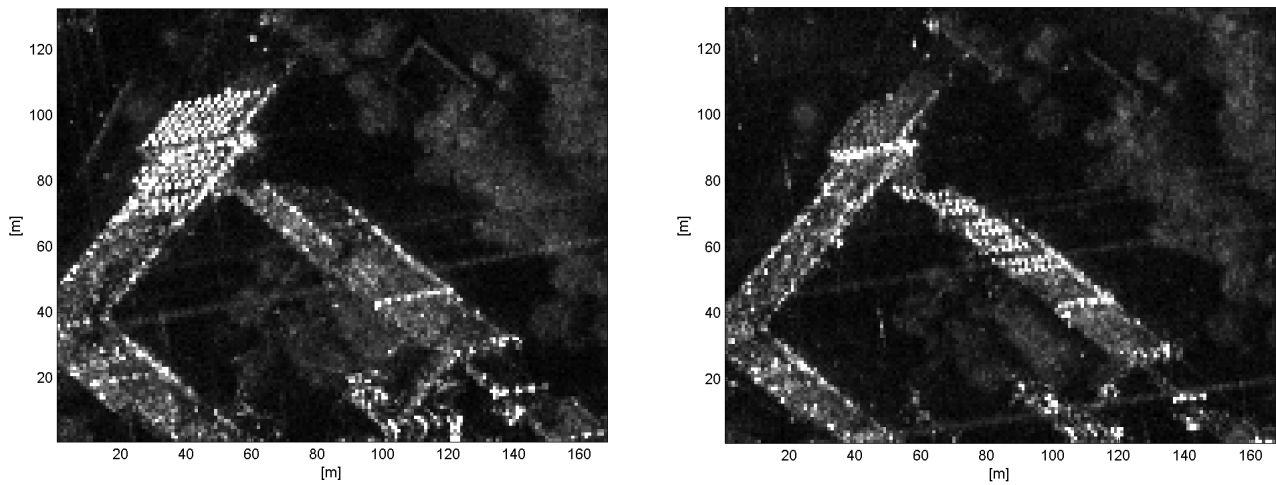
Figure 32. Sample area used for analysis on track direction. Left: Meanmap of stack A42. Right: Meanmap of stack A51.

appearance or disappearance of PS are related to the geometrical configuration of the satellite and objects within the scene, but in the case of shadow, an interaction of nearby objects is included. Large incidence angles may prevent the detection of PS at ground locations and first floors of buildings, especially in urban areas of high rise buildings at short distances. The maximum incidence angle $\theta_{inc,max}$ for which ground floor is still visible (assuming a horizontal ground plane) can be calculated from the distance of two buildings Δxy and the height Δz of the front building, inducing radar shadow:

$$\theta_{inc,max} \leq \arctan \frac{\Delta xy}{\Delta z} \tag{56}$$
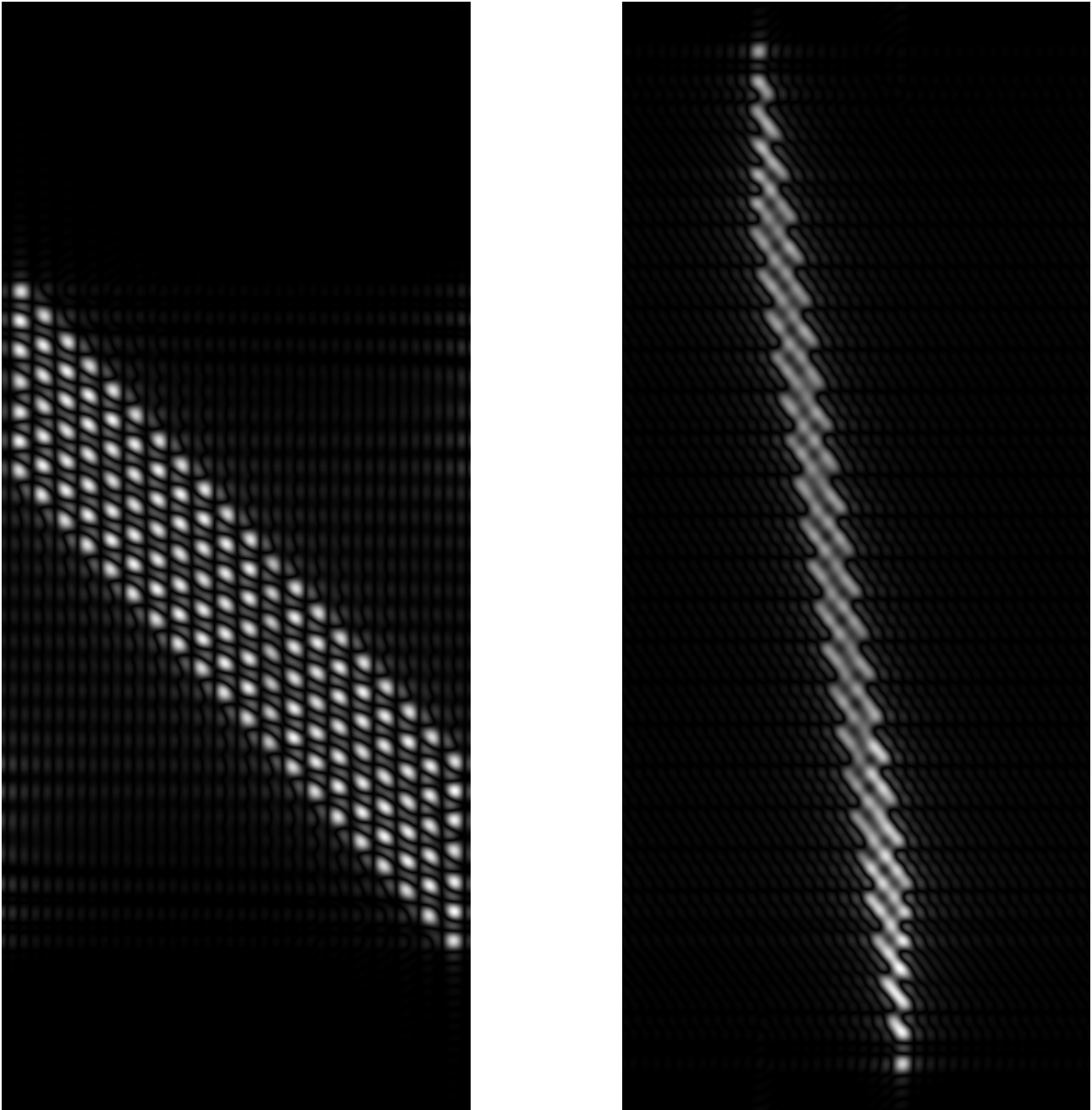
Figure 33. Simulated SAR images of a facade consisting of 21 windows in each row of 7 floors. The spacing between equal corners of the windows is set to 2.7 m. The radar resolution of TerraSAR-X is used for the simulation, whereas the images are oversampled by a factor of 8 for better visualization purposes. The incidence angle is set to 55°. In the left image, the facade is rotated by 35° with respect to an alignment perpendicular to ground range direction. The signatures corresponding to trihedral reflections at the windows can be separated easily, i.e., one PS per window is available. In the right image, the rotation angle is 75°. In this case, the separation of all signatures is not possible any more. SAR images are generated using RaySAR. See Auer (2011) for more details on this simulation software.

In Figure 37, this dependency is plotted, dependent on the two aforementioned parameters of height and distance, allowing for a fast assessment of shadow occurrence given a certain geometrical configuration. In addition, the isolines of exemplary maximum incidence angles are overlaid. As an example, the ground floor of one building is still visible at an incidence angle of 25° given a front building of 50 m extension in height, which is horizontally located at least 25 m away. If the incidence angle changes to 55°, the buildings have to be about 70 m apart, in order to allow PS to appear at ground and first floors of the building behind the one inducing shadow.
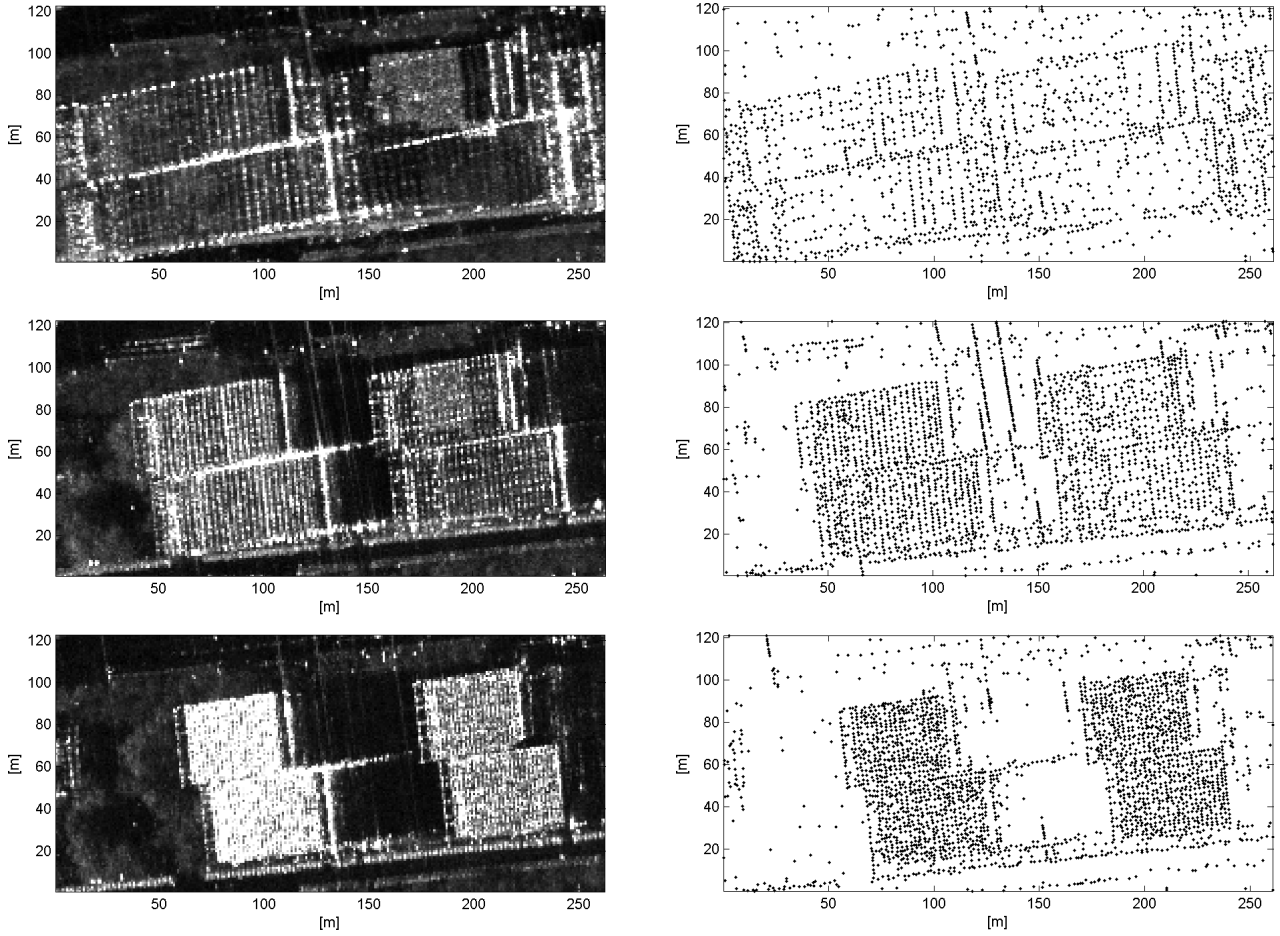
Figure 34. First sample area for analysis on incidence angle influence. Left: Meanmaps of skyscrapers at increasing incidence angles; top to bottom: Stack A30, A42, A51, all VV); right: plot of detected PS positions (black dots). Note the major change in number of PS switching from steep to mid range incidence angles (top to mid figures). Also note the regular patterns that are induced by rows of windows on the facade of the building.

Additionally, the variation of incidence angles evokes another effect on facades; the vertical resolution ρ_z changes, responsible for the separability of different floors. It can simply be derived from the current range resolution ρ_R and incidence angle θ_{inc}:

$$\rho_z = \frac{\rho_R}{\cos\theta_{inc}} = \frac{c}{2 \cdot BW \cdot \cos\theta_{inc}} \tag{57}$$

The limit for a separability of two PS is given by the range resolution of the SAR system in this case. Hence, the lower bandwidth limits for windows 2.7 m apart are approximately 60 MHz and 95 MHz of system bandwidth for incidence angles of 25° and 55° respectively. Consequently, spotlight (150 MHz) and high resolution spotlight (300 MHz) modes of TerraSAR-X do not limit the separation of rows of windows for any incidence angle within the operational range at facades aligned approximately perpendicular to ground range direction. Certainly, rotated facades will have major influence on the necessary range resolution in order to separate PS from facades, because vertical aligned patterns of PS may also be influenced by a decreasing separability in azimuth direction (cf. equation 55 and Figure 33). However, the aforementioned configuration is given as an example for an ideal case of facade orientation and is valid for a quite a large variety of facade orientations below the critical rotations angle of $\iota_{max} = 66°$. As soon as the geometrical configuration would prevent every second facade PS from being separated from another, already 25% of all available PS are lost, because statistical analysis show an origin of PS of 50% from facades within urban areas.
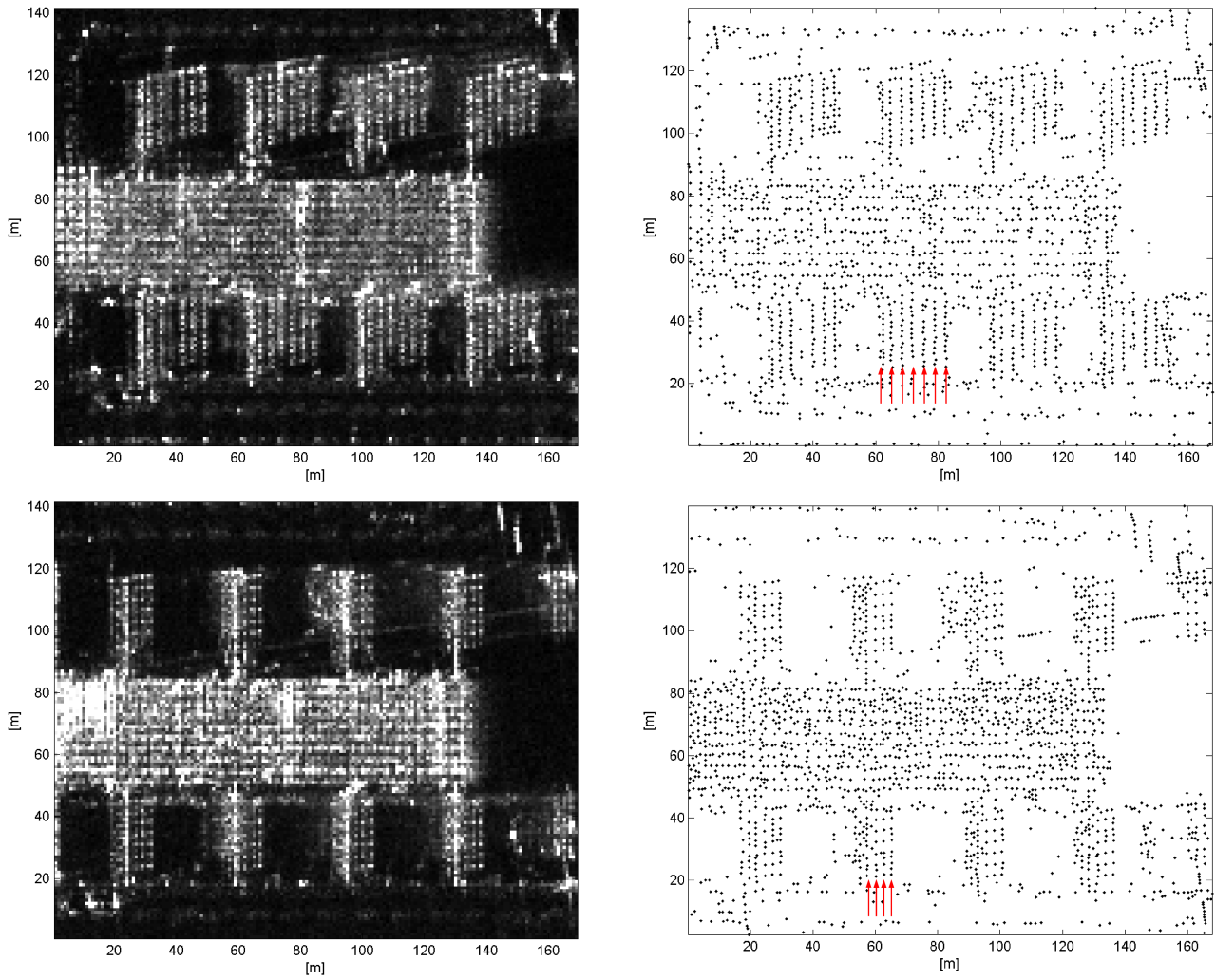
Figure 35. Second sample area for analysis on incidence angle influence. Left: Meanmaps of building at increasing incidence angles; top to bottom: Stack A42, A51, all VV); right: plot of detected PS positions (black dots). Note the loss of PS due to shadow effects, i.e., the reduction of 7 visible floors to 4 visible floors, indicated by red arrows.
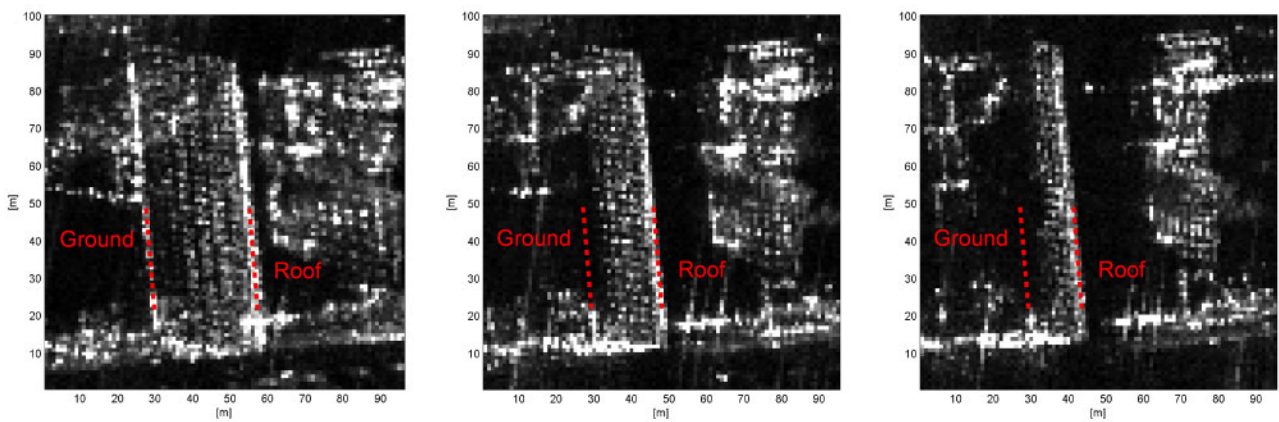
Figure 36. Third sample area for analysis on incidence angle influence. From left to right: Meanmaps of building at increasing incidence angles (Stack D36, D47, D55, all VV) heavily affected by shadow of the front building (situated to the right). Approximate location of ground and roof indicated by dashed red lines.
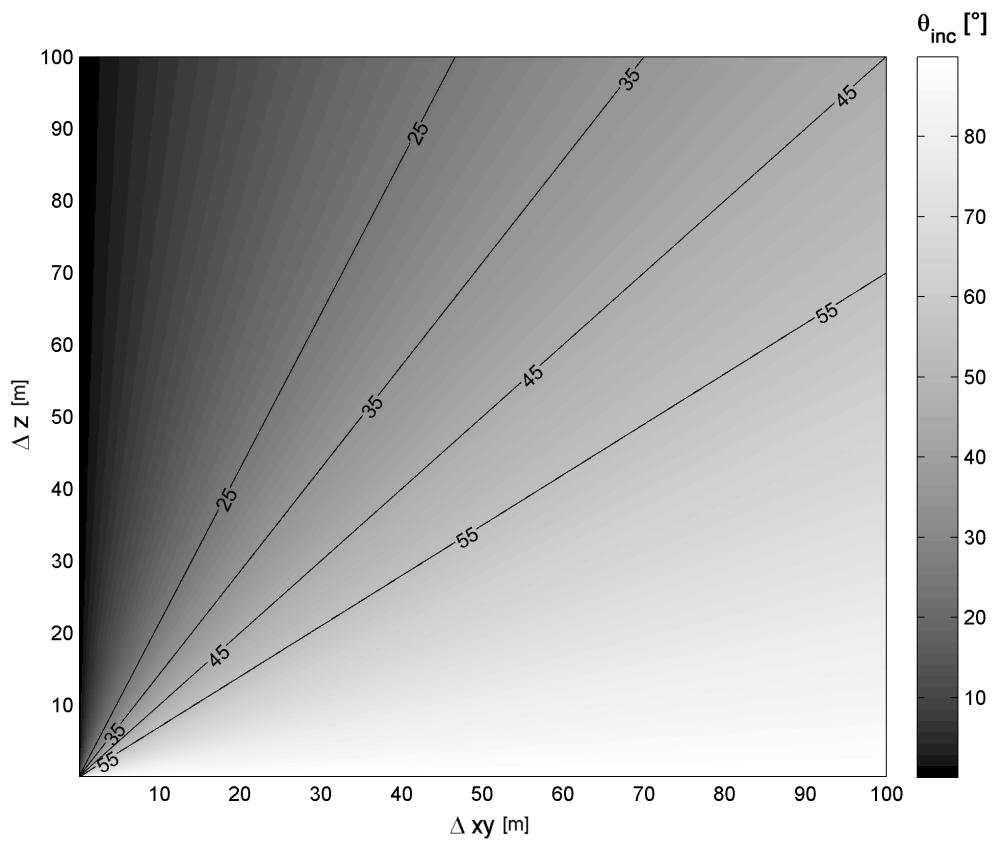
Figure 37. Plot of maximum incidence angles in order to allow an extraction of potential PS from ground floor. Geometry given by distance Δxy between two buildings and height Δz of the front building inducing shadow on the other one. Isolines of different incidence angles are overlaid on top.

4.3.5 Concluding Suggestions for Acquisition Parameters

In summary, the following conclusions can be drawn; in most of the cases stacks of HH data will provide slightly more PS than stacks of VV data. This fits expectations, because most likely the majority of PS originate from dihedral/trihedral scattering mechanisms and the amplitudes of the signal responses for these kinds of reflections are lower in the case of VV in comparison to HH at given incidence angles between 25° and 55° (Hajnsek, 2006). The largest differences occur at building facades aligned perpendicularly to ground range direction. However, the difference between HH and VV is small, especially within large areas, and PSI can be applied successfully using both types of polarization. In Figure 38 approximately half of the test site of Berlin is included in a density analysis, omitting the large vegetated area south-west of the center. From the distribution of PS density a difference of only 10% to 15% at maximum between VV and HH polarized data remains. Moving from steep to mid range incidence angles an increase of approximately 5% to 10% can be observed and the change from mid range to shallow incidence angles in turn removes approximately 5% to 10% of the available PS. Hence, mid range incidence angles are best, if the maximum number of PS is desired. In the cases of Berlin and Munich test sites, mid range incidence angles also hold a high probability to include PS from all floors of buildings, limiting the loss due to shadow effects. Certainly, this depends on the local geometry of the city, whereas steep look angles have to be preferred if many skyscrapers at close range are available in the scene. Finally, if there exists a certain major orientation of facades within the area of interest, the orbit of the satellite should be chosen in a way to ensure a view on facades closest to the perpendicular in order to increase the number of PS. In general, the acquisition geometry and the distribution and height of buildings should be taken into account for PSI stack acquisition planning.
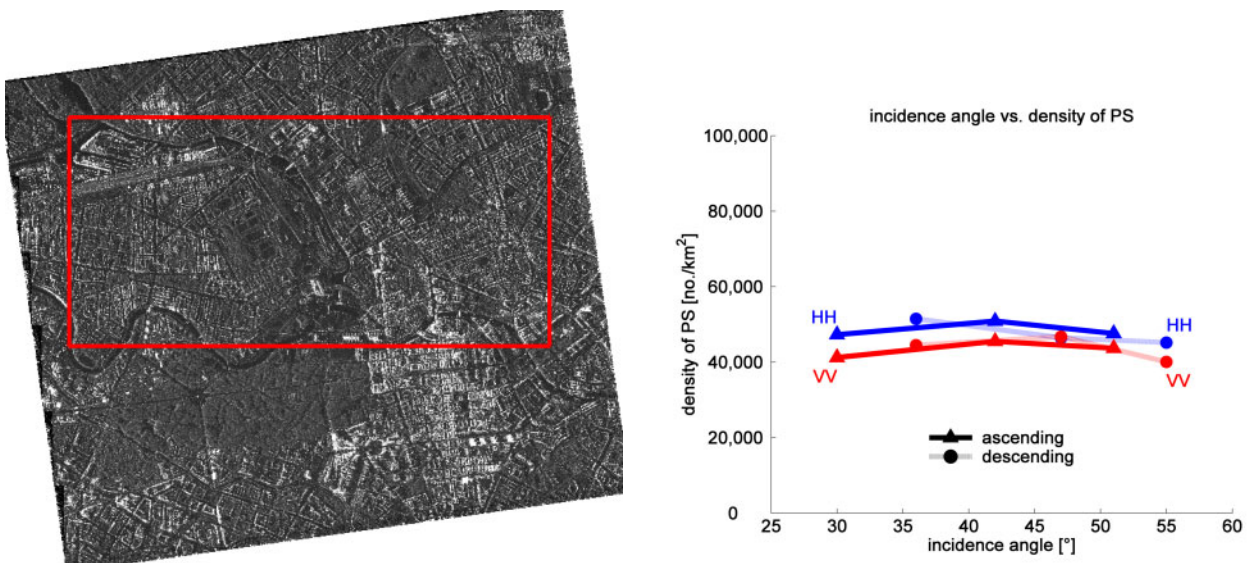
Figure 38. Large sample area for the analysis of PS densities (red rectangle). Left: Meanmap of stack A42. Right: Distribution of PS densities with increasing incidence angle. Different polarization indicated by different colors and by HH/VV signatures. Solid lines including triangular markers indicate ascending tracks. Diffuse lines including round markers indicate descending tracks. PS selection requirement: SCR $\geq$ 3.0

4.4 Deformation Estimation

The enormous amount of PS available from stacks of meter-resolution SAR data obviously weakens the opportunistic character of PSI, because now many point scatterers appear on almost any single building. One may also state that for this resolution class it is now very unlikely to discover buildings, which are not covered by at least some tens of PS in urban areas. Deformation monitoring by means of PSI therefore benefits from this large amount of scatterers as will be demonstrated in the following section. To this end, all stacks of meter-resolution SAR data obtained by TerraSAR-X mentioned in Section 4.1.2 have been processed independently. No specific DSM data is used. Instead, a horizontal plane of mean terrain height is introduced – one for each of the two test sites. This choice is sufficient, because the offset between the surface and the phase center of each PS is estimated anyway (DEM refinements), as already mentioned. Furthermore, the same processing parameters are used for all stacks, assuring comparability of the results. The master acquisitions are chosen in winter seasons, as described in Section 4.1.2, and the SCR for PS selection is set to 2.0 in all cases providing between 1.5 and 2.2 million initial candidates. The threshold for maximum arc length is set to 150 m - 250 m for the reference network, assuring virtually identical atmospheric delays between neighboring points. Further details on the processing are given in the following two sections.

4.4.1 Test Area Munich

Unfortunately, the data of the three stacks either only cover about one year or show a larger gap in the temporal baseline (stack D25). Consequently, an estimation of both seasonal as well as linear amplitudes of deformation rates cannot be obtained reliably, hence, only a linear base function is introduced as deformation model. At first the reference network is set up and the relative deformation rates and DEM refinements are calculated and integrated based on the reference point chosen. The position of the reference point affects variance propagation of the errors within the network (cf. Section 4.2.3). Hence, the reference points are chosen near the center of the scenes (considering stable areas) in order to assure a balanced distribution of increasing variances to the borders of the scene. The mean standard deviations of the estimated parameters for the reference network are summarized in Table 5. The accuracy is between 0.5 mm/y and 1.1 mm/y for relative deformation estimates and between 0.6 m and 1.6 m for relative DEM refinements. The precisions are related to the number of available datasets: The larger the stack, the lower the standard deviations of the estimates. The number of PS selected in the reference network is about 0.3 to 0.5 percent of the total number of PS candidates selected. The final numbers of PS depend (amongst others) on the restrictive choice of the maximum posterior variance factor $\hat{\sigma}_0^2$ acceptable, which can be treated as quality criterion for final PS selection, and vary between 500,000 and 1.1 million PS (cf. table 6).

Stack	A23	D25	D39
mean $\sigma_{\Delta v_{LOS}}$ (linear) [mm/y]	0.92	0.53	1.06
mean $\sigma_{\Delta h}$ [m]	0.75	0.61	1.58

Table 5. Estimated mean values of standard deviations concerning relative linear displacement rate Δv_{LOS} and relative DEM refinement Δh. Stack D25 includes the best precisions, possibly due to the largest amount of available datasets (35 acquisitions in comparison to 30 and 27 for stacks A23 and D39 respectively).
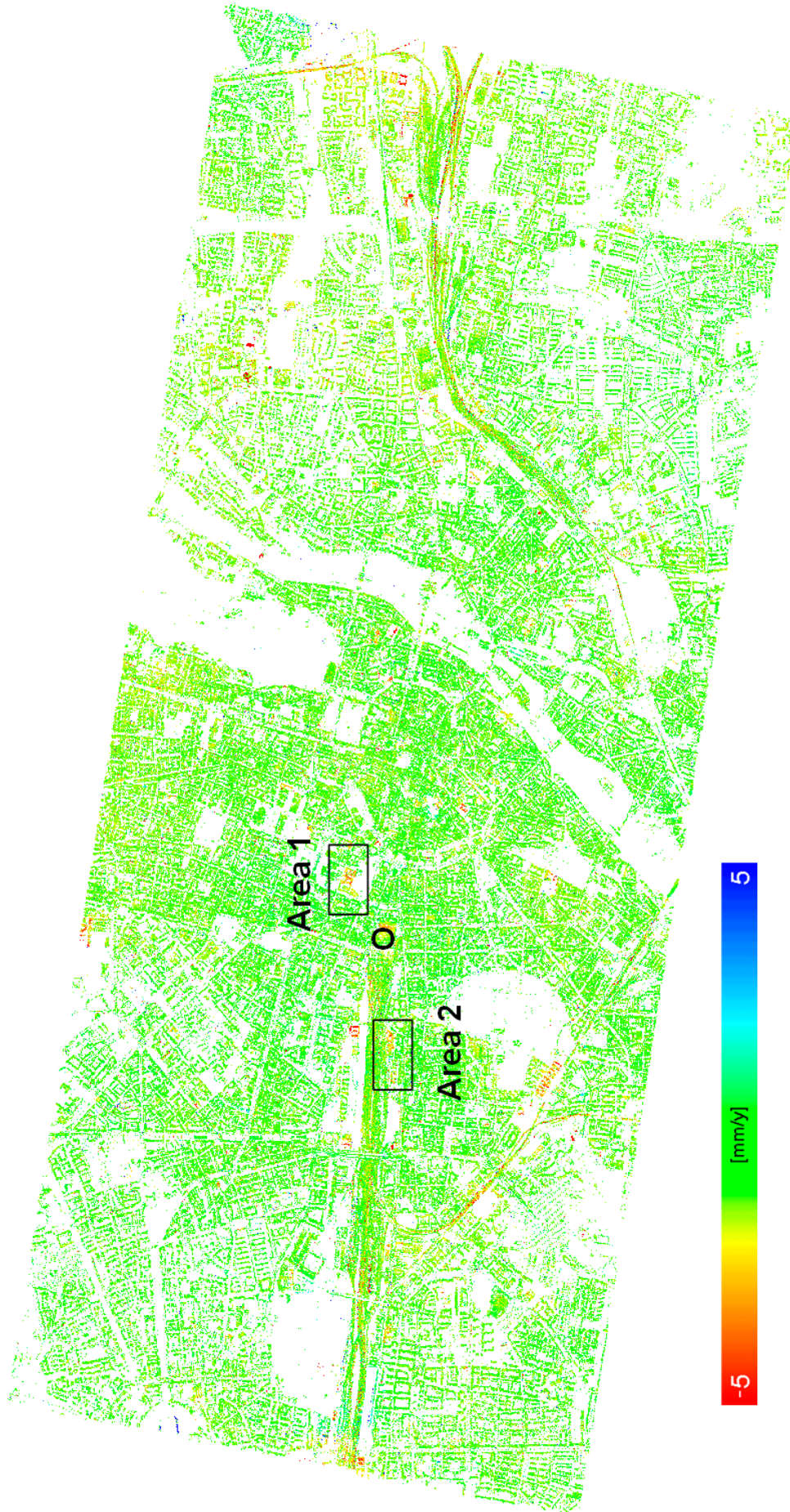
Figure 39: Results of linear deformation estimation for stack D25 in Munich: Geocoded PS colorcoded by their amplitudes of motion between -5 mm/y (red) and +5 mm/y (blue) are shown. Green colors indicate no deformation. Several groups of PS can be identified showing significant linear displacement. Central train station is marked by circle. Areas 1 and 2 are investigated in more detail in this section.

Stack	A23	D25	D39
Initial PSC	1,218,258	1,730,054	1,229,715
PS in RefNet	6,454 (0.5%)	4,853 (0.3%)	4,267 (0.4%)
$\hat{\sigma}_0^2 \leq 1.5$	887,855 (73%)	1,152,997 (67%)	889,008 (72%)
$\hat{\sigma}_0^2 \leq 1.0$	758,551 (62%)	929,014 (54%)	765,991 (62%)
$\hat{\sigma}_0^2 \leq 0.5$	530,656 (44%)	567,724 (33%)	526,971 (43%)

Table 6. Number of initial PS candidates, points in reference network and final PS selected using different thresholds on the posterior variance factor $\hat{\sigma}_0^2$.
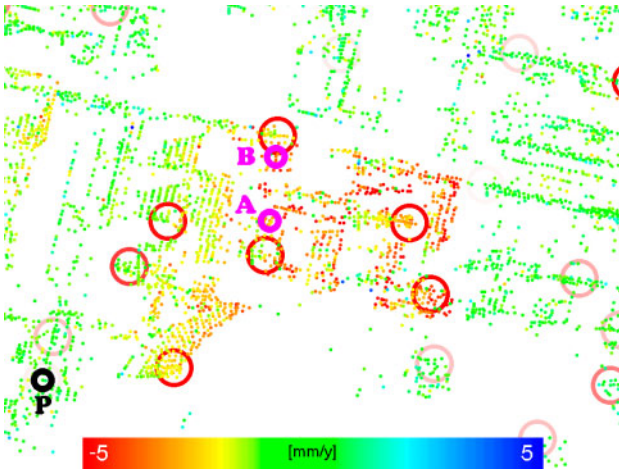
(a) Area 1 north-east of central train station in Munich (Sophienstrasse).
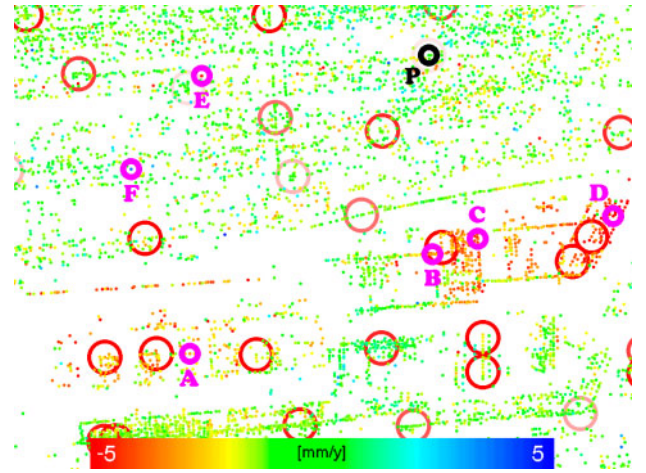
(b) Area 2 west of central train station in Munich (west of Hackerbrücke).

Figure 40. Sample locations showing larger deformation signals at final PS in Munich. Circles indicate points of reference network, intensity of circle color shows deformation rate between 0 and 1 mm/y (intense red color) of linear deformation. Colors of points represent estimated linear amplitudes of deformation signal between -5 mm/y (red = subsidence) and +5 mm/y (blue = uplift) in LOS. Relative displacement in subsequent phase history plots between PS indicated by black (P) and each magenta (A-F) circle. Points are plotted in the azimuth-range plane.
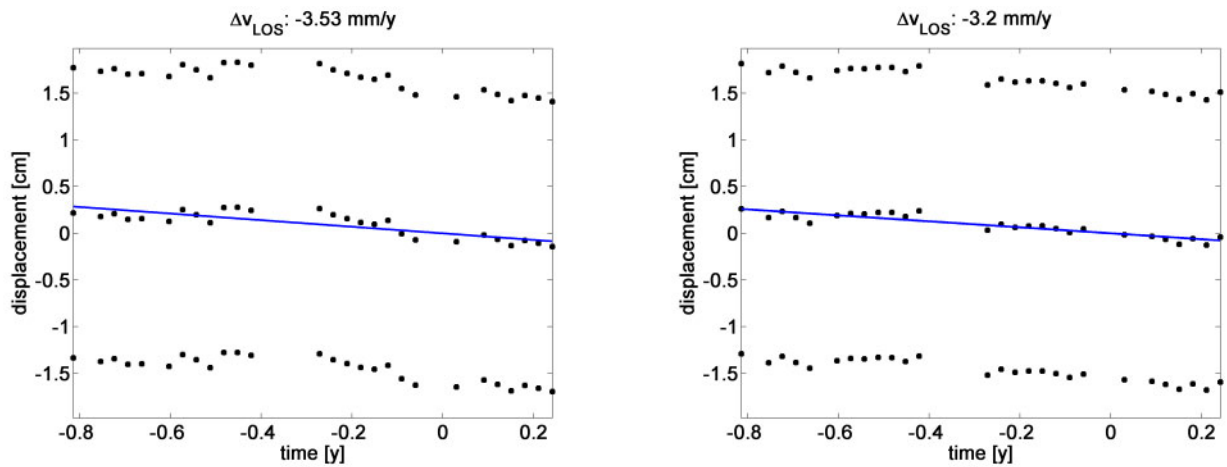
Figure 41. Phase history (including $\pm 2\pi$ ambiguities) showing relative deformation rate between two PS of area 1. Black dots represent relative deformation signal. Blue line indicates estimated deformation. Left: -3.53 mm/y of subsidence (selection P-A). Right: -3.2 mm/y of subsidence (selection P-B).
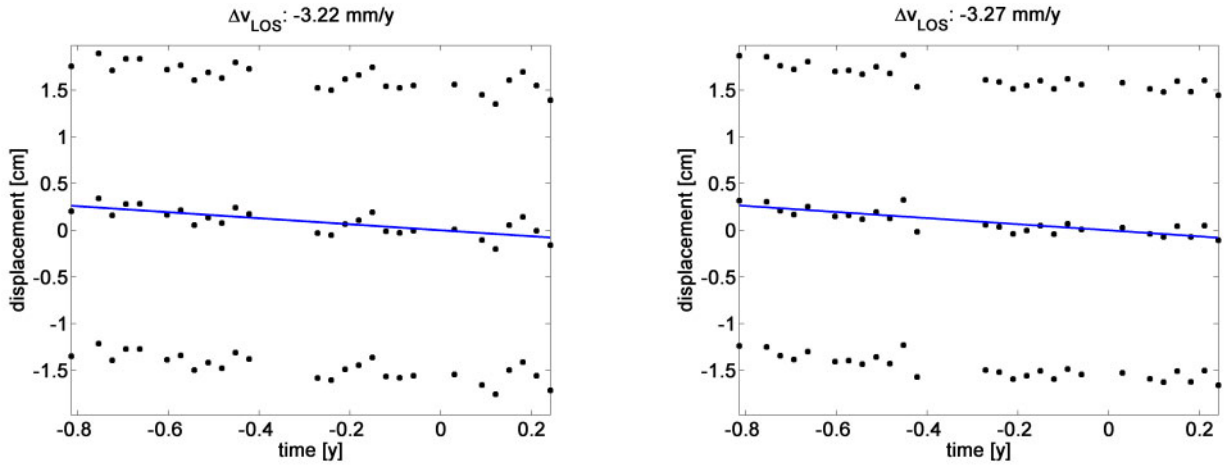
Figure 42. Phase history (including $\pm 2\pi$ ambiguities) showing relative deformation rate between two PS of area 2. Black dots represent relative deformation signal. Blue line indicates estimated deformation. Left: -3.22 mm/y of subsidence (selection P-A). Right: -3.27 mm/y of subsidence (selection P-B).
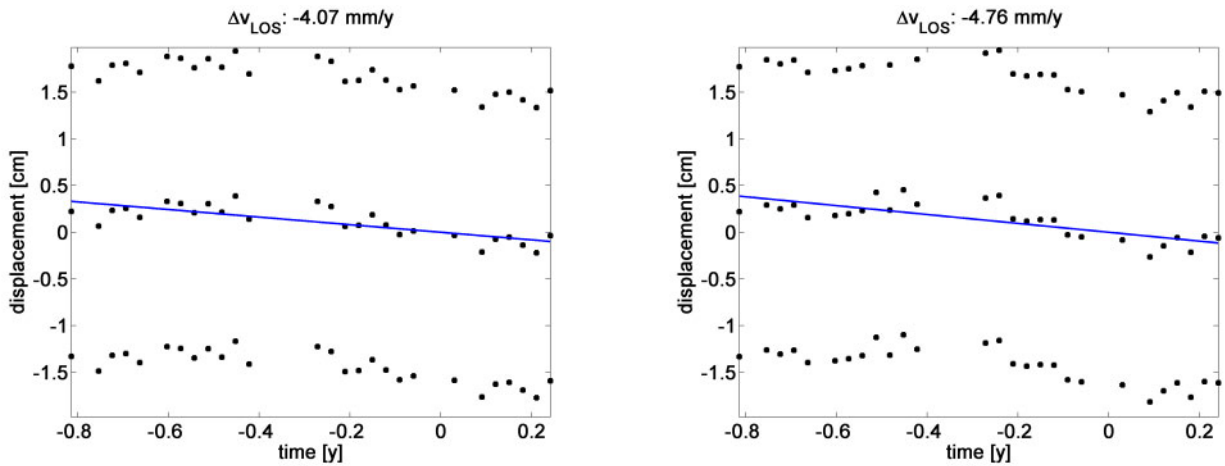
Figure 43. Phase history (including $\pm 2\pi$ ambiguities) showing relative deformation rate between two PS of area 2. Black dots represent relative deformation signal. Blue line indicates estimated deformation. Left: -4.07 mm/y of subsidence (selection P-C). Right: -4.76 mm/y of subsidence (selection P-D).
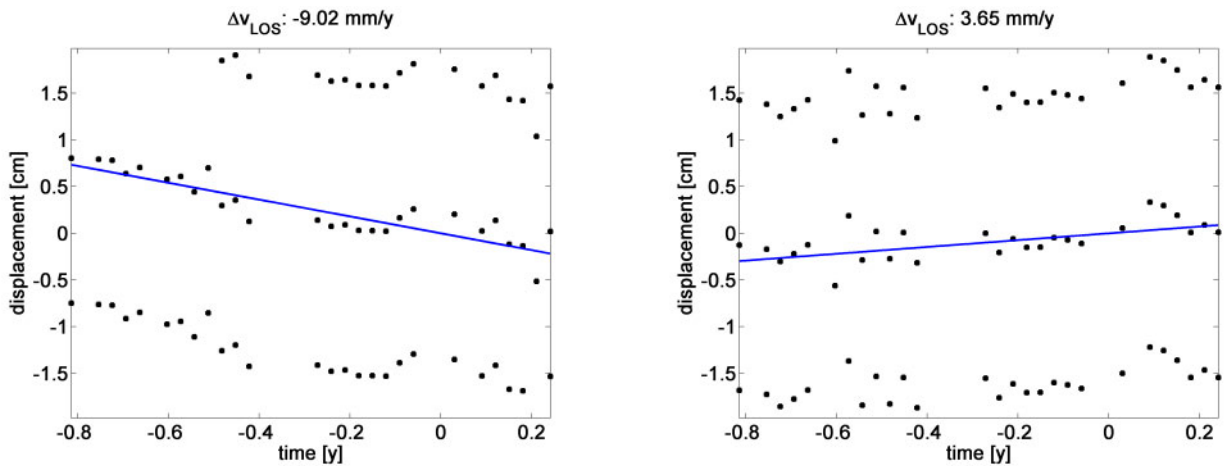
Figure 44. Phase history (including $\pm 2\pi$ ambiguities) showing relative deformation rate between two PS of area 2. Black dots represent relative deformation signal. Blue line indicates estimated deformation. Left: -9.02 mm/y of subsidence (selection P-E). Right: +3.65 mm/y of uplift (selection P-F).

The city structure of Munich differs from the one of Berlin, as all constructions within the city center are lower than 100 m besides the presence of several historic buildings. The latter are built of different material than modern buildings, which may influence the presence of PS. Hence, the applicability of PSI to this type of urbanization is shown. In addition, ground truth information about stable areas as well as potential subsiding buildings is already available that is beneficial for the choice of the reference point and for validation purposes. In the following, examples of linear deformation estimates are shown.

Compared to medium resolution results using ERS data – and also due to recent building activity – there appear several accumulations of PS affected by motion in Munich. An overview on the deformation results of one descending stack is given in Figure 39. Two locations will be investigated in more detail in the following. The first area is located north-east of central train station, including several buildings north of *Sophienstrasse*. In Figure 40a the estimated amplitudes of linear deformation are shown for all final PS in the azimuth-range plane as an overview and in Figure 41 the phase histories between two selected pairs of PS are plotted. The latter are obtained from the phase differences between two selected (nearby) points after subtraction of the estimated differential phase of relative DEM refinements, caused by unequal heights between the two phase centers of the two PS. In all plots of phase histories the $\pm 2\pi$ ambiguities are included, appearing as copies shifted in displacement axis direction. The graphs show the temporal evolution of the deformation signal and includes the estimated linear motion, which fits the phase history very well. Most likely, the apparent motion in this area is caused by recent building constructions and a mass induced subsidence of the whole building complex of approximately 3-4 mm/y.

Another comparable area can be found west of central train station, south of the rail tracks near *Hackerbrücke* (area 2). From the plot of the PS colorcoded by the estimated amplitude (cf. Figure 40b) several buildings seem to be affected by linear motion. Again, the phase histories (cf. Figure 42) show a subsidence of the recently built houses of approximately 3-4 mm/y. In addition, the deformation history presented in Figure 43 includes a slight seasonal signal superimposed on the linear motion. In these two cases, the points are selected at the upper floors of the buildings, therefore, a thermal dilation of the houses could be the origin of this periodic motion. Further details on seasonal motion are presented in Section 4.4.3.

As already mentioned, periodic deformation cannot be estimated reliably for the given stacks in Munich due to the short temporal baseline. Certainly, estimates of linear motion may be biased by periodic fractions in these cases, but the availability of data from at least one year – like in this case – already allows for an estimation of the linear fraction of the underlying deformation signal. Accuracies of estimates will be decreased for PS showing additional periodic movement, but a trend can still be discovered, if present. The standard deviations of the presented relative linear deformation rates are below 1 mm/y for all estimates, assuming a reference network estimation free from errors.

Besides building complexes, also isolated points are affected by high amplitudes of subsidence or uplift (cf. Figure 44). Unfortunately, it is hard to give a reasonable explanation for the observed motion prior to precise geocoding and a comparison of the location to real world objects. Nevertheless, the estimation can be considered reliable by reason of the clear trend of the deformation history, which fits the linear displacement model. Further examples will be given from the second test site in Berlin.

4.4.2   Test Area Berlin

The continuous distribution of acquisition times within almost two years allows for an estimation of both seasonal (period of one year) and linear deformation rates simultaneously. Appropriate base functions are introduced as deformation model. The seasonal amplitudes as well as the offset of the periodic deformation model are obtained by estimating the amplitudes of a sine

and a cosine function (cf. Section 2.3.2). The reference network consists of 1,800 to 2,800 points (approximately 0.2% of PSC) and the accuracies of reference network estimation can be seen in Table 7.

Stack	A30	A42	A51	D36	D47	D55
σ_{t_0} median [y]	0.01	0.01	0.01	0.01	0.01	0.01
σ_{t_0} max [y]	0.54	0.41	0.93	0.22	0.08	0.13
$\sigma_{\Delta\alpha_p}$ (periodic) median [mm]	0.05	0.06	0.03	0.03	0.02	0.03
$\sigma_{\Delta\alpha_p}$ (periodic) max [mm]	0.36	0.23	0.05	0.19	0.09	0.04
$\sigma_{\Delta v_{LOS}}$ (linear) median [mm/y]	0.36	0.22	0.06	0.03	0.04	0.02
$\sigma_{\Delta v_{LOS}}$ (linear) max [mm/y]	2.43	1.01	0.07	0.23	0.16	0.03
$\sigma_{\Delta h}$ median [m]	0.51	0.13	0.04	0.06	0.22	0.19
$\sigma_{\Delta h}$ max [m]	23.3	0.59	0.05	0.51	1.03	0.26

Table 7. Estimated maximum and median values of standard deviations concerning offset of periodic function t_0 and its amplitude $\Delta\alpha_p$, as well as relative linear displacement rate Δv_{LOS} and relative DEM refinement Δh. Stack A30 includes large values, besides the seemingly random nature of t_0 for the reference network.

Stack A30 shows some larger variances, especially for the height estimations, that stem from the low number of acquisitions compared to the other stacks. In addition the short temporal baseline of this stack is not beneficial for a combined estimation of seasonal and linear deformation rates. Furthermore, some stacks show large maximum variations in the estimated offset of the periodic displacement function, which certainly originate from points not affected by significant periodic movement. Therefore, the offset can be considered random. As soon as all PS are included a dominant offset of oscillating deformation signals can be investigated.

Ascending Stack	A30	A42	A51
Initial PSC	1,935,247	1,618,381	1,089,153
PS in RefNet	2,825 (0.2%)	2,396 (0.2%)	1,795 (0.2%)
$\hat{\sigma}_0^2 \leq 1.5$	1,497,590 (77%)	1,313,357 (81%)	831,208 (76%)
$\hat{\sigma}_0^2 \leq 1.0$	1,132,899 (59%)	1,027,090 (63%)	692,132 (64%)
$\hat{\sigma}_0^2 \leq 0.5$	773,587 (40%)	744,156 (46%)	478,335 (44%)

Table 8. Statistics for ascending stacks: Number of initial PS candidates, points in reference network and final PS selected using different thresholds on the posterior variance factor $\hat{\sigma}_0^2$.

Descending Stack	D36	D47	D55
Initial PSC	1,494,975	1,254,044	1,050,444
PS in RefNet	2,405 (0.2%)	1,967 (0.2%)	1,851 (0.2%)
$\hat{\sigma}_0^2 \leq 1.5$	1,119,787 (75%)	947,793 (76%)	804,240 (77%)
$\hat{\sigma}_0^2 \leq 1.0$	962,469 (64%)	826,250 (66%)	699,896 (67%)
$\hat{\sigma}_0^2 \leq 0.5$	659,944 (44%)	615,085 (49%)	501,786 (48%)

Table 9. Statistics for descending stacks: Number of initial PS candidates, points in reference network and final PS selected using different thresholds on the posterior variance factor $\hat{\sigma}_0^2$.

Variance propagation shows comparable characteristics to the Munich test site, because the reference points are similarly chosen; they are located near the center of the scene, hence, the variances rise at increasing distances to the reference point of each stack and show the largest values at the border of the area. In Tables 8 and 9 the numbers of PS candidates, PS of the reference network and final PS are summarized. In total, between 500,000 and 1.5 million final PS are available (up to 75%-81% of the PS candidates), depending on the restrictive choice of the threshold on the posterior variance factor.

After the estimation of the unknown parameters for all PS, i.e., connecting the remaining PS candidates to the closest PS of the reference network, localized deformation on single buildings can be investigated. The estimation results of seasonal motion of one descending stack can be seen in Figure 45. Several spots showing large amplitudes of periodic motion can be identified. In the following, two sample areas will be investigated in more detail.
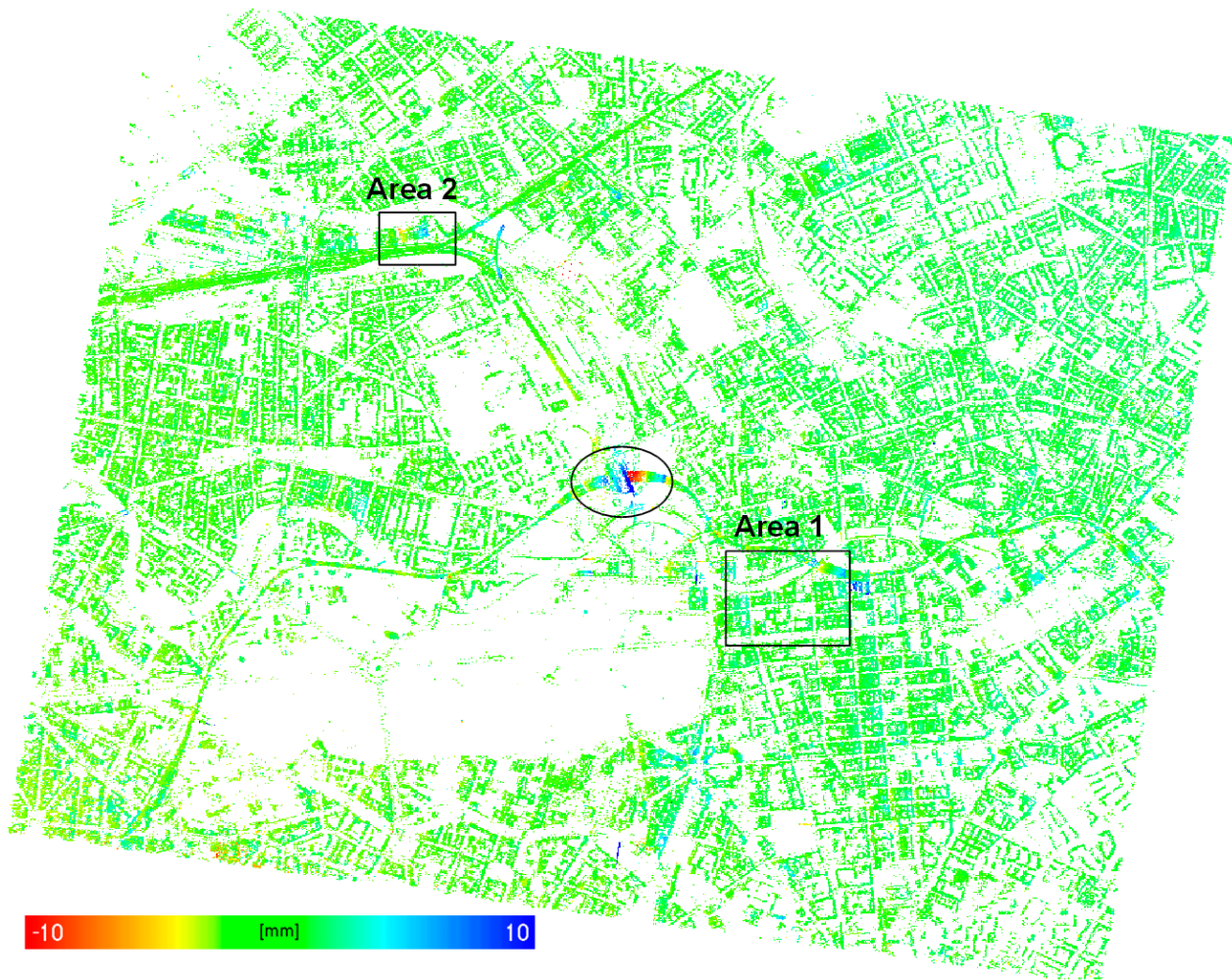
Figure 45. Results of seasonal deformation estimation for stack D55 in Berlin: Geocoded PS colorcoded by their amplitudes of motion between -10 mm (red) and +10 mm (blue) are shown. Green colors indicate no deformation. Several groups of PS can be identified showing significant seasonal displacement. Central train station is marked by circle. Areas 1 and 2 are investigated in more detail in this section.

The first area is situated south east of central train station and includes houses of medium height showing several floors and a train station next to a bridge across the river *Spree*. A more detailed view on the deformation estimates is given in Figure 46. The phase histories reveal the precise deformation regimes; the houses close to P1 are affected by seasonal motion of amplitudes approximately between 2.7 mm and 3.8 mm, i.e., between summer and winter times the building roof is moving up to 7.6 mm (cf. Figure 47). In addition, there exists a slight subsidence in the area; an amplitude between -0.8 mm/y and -1.5 mm/y is estimated for the selected PS. The seasonal motion certainly originates from thermal dilation effects, because

the maximum expansion can be observed during summer times. An explanation on the linear subsidence cannot be given at this point.
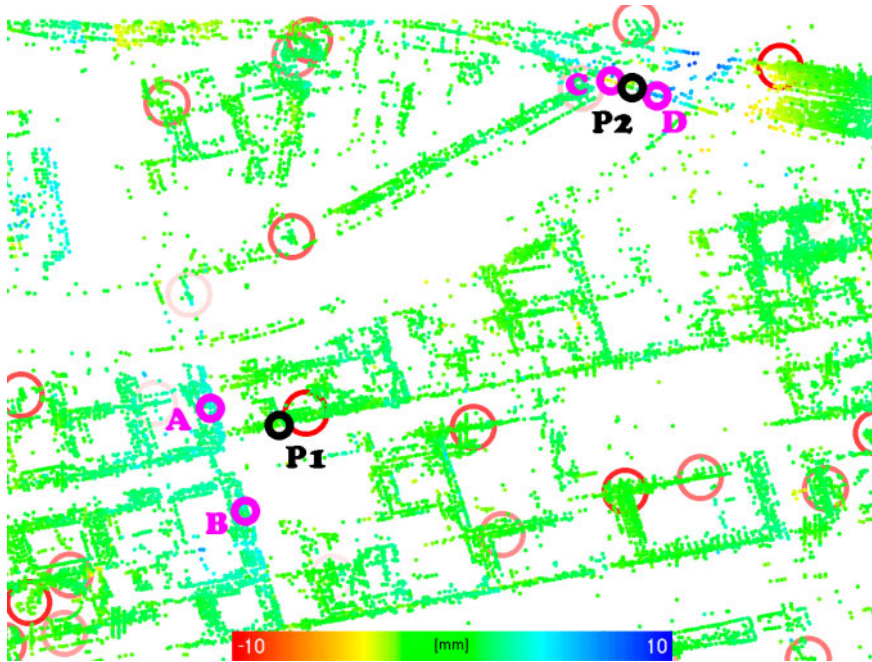
Figure 46. Sample location (area 1) 1.25 km south-east of central train station (between *Brandenburger Tor* and train station *Berlin-Friedrichsstraße*) showing larger deformation signals at final PS in Berlin. Circles indicate points of reference network, intensity of circle color shows deformation rate between 0 and 1 mm (intense red color) of periodic motion. Colors of points represent estimated seasonal amplitudes of deformation signal between -10 mm (red = subsidence in summer) and +10 mm (blue = uplift in summer) in LOS. Relative displacement in subsequent phase history plots between PS indicated by black (P1 and P2) and each magenta (A-D) circle. Points are plotted in the azimuth-range plane.

Another interesting periodic deformation can be seen in Figure 48, which corresponds to the deformation signal of the bridge, situated in the top-right of the area. Interestingly, the two relative deformation patterns show inverse amplitudes of magnitudes -3.9 mm for PS pair P2-C and +5.9 mm for PS pair P2-D. All PS are situated along one side of the bridge, hence, vertical periodic motion cannot be assumed in this case. Most likely, horizontal deformation of two constructional separated parts may evoke the observed motion. This assumption can be verified by a combination or comparison of results from different looking directions, more precisely, from a combination of ascending with descending results (see Section 4.4.4).

4.4.3 Origin of Periodic Motion

Seasonal motion on medium resolution data is shown in, e.g., Perissin and Rocca (2006). The origin of periodic deformation is related to thermal expansion of large steel constructions. The high resolution of TerraSAR-X now reveals a large number of buildings that are – in all probability – affected by seasonal temperature differences between summer and winter times. The main component of thermal dilation may be observed in horizontal as well as vertical directions. Two prominent examples are given in this section.

The first object of interest is situated north-west of central train station in Berlin (cf. area 2 in Figure 45). It represents a hall of large horizontal extent. Several relative deformation histories from the roof of the building are selected with respect to one stable point next to the building, indicated by a black circle in Figure 49. Slightly east of the center, no deformation is present (cf. phase history in Figure 50), whereas the amplitudes of periodic motion increase up to 9.1 mm to the west (see selections P-B, P-C and P-D). The PS pairs to the east show inverse amplitudes (up to -6.6 mm) compared to the previously mentioned ones, but they again increase with larger distances to the non-moving part at point A (cf. Figure 51). The largest amplitudes
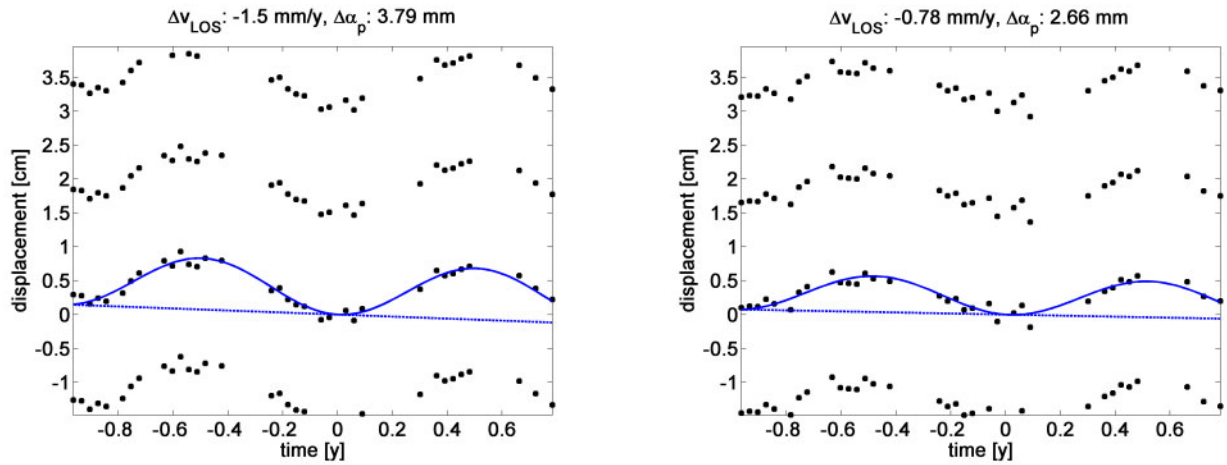
Figure 47. Phase history (including $\pm 2\pi$ ambiguities) showing relative deformation rate between two PS of area 1. Black dots represent relative deformation signal. Blue line indicates estimated deformation. First number in title corresponds to estimated linear, second to amplitude of periodic deformation. Left: Dominating seasonal amplitudes of +3.79 mm (selection P1-A) and slight subsidence of -1.5 mm/y. Right: Dominating seasonal amplitudes of +2.66 mm (selection P1-B) and slight subsidence of -0.78 mm/y.
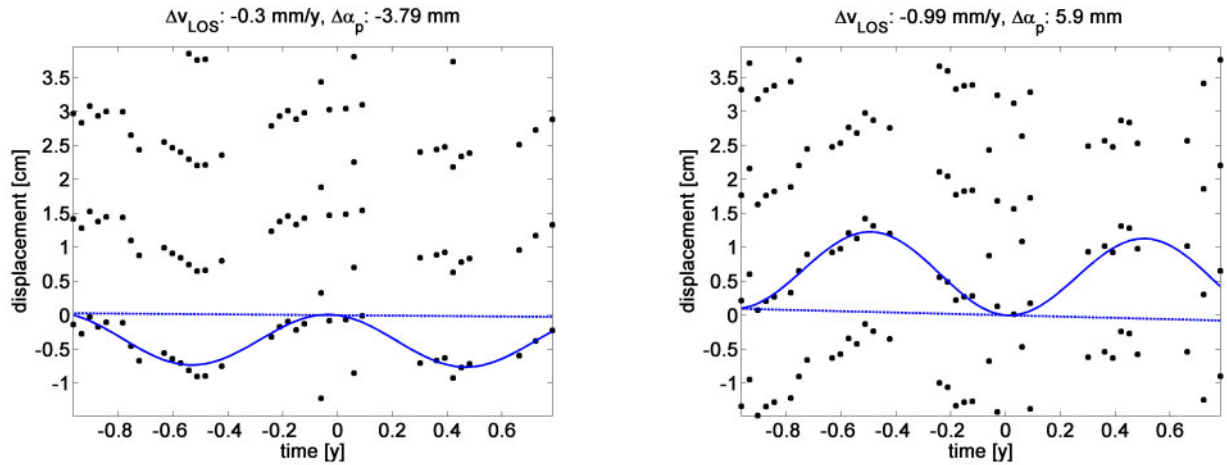
Figure 48. Phase history (including $\pm 2\pi$ ambiguities) showing relative deformation rate between two PS of area 1. Black dots represent relative deformation signal. Blue line indicates estimated deformation. First number in title corresponds to estimated linear, second to amplitude of periodic deformation. Left: Dominating seasonal amplitudes of -3.79 mm (selection P2-C). Right: Dominating seasonal amplitudes of +5.9 mm (selection P2-D).

are observed during summer times and the period of one year emphasized a thermal dilation as origin of deformation. From the phase histories showing large amplitudes it is evident, that a reliable estimation becomes more and more difficult. Especially phase noise may prevent a successful resolution of the underlying deformation signal.

The second large object most likely affected by thermal dilation is central train station, located at the center of the scene. From the photograph shown in Figure 52 the structure of the construction is visible; two main buildings are built across the rail tracks, which are aligned approximately in west-eastern direction. Left and right to the center, the rail tracks are covered by halls up to a certain extent. In addition, on the right hand side, the rail tracks cross an expanse of water via a bridge. Left to the main buildings a tower of triangular profile is constructed, showing the company logo of the railway company *Deutsche Bahn* (DB). Large parts of the whole building complex is made of steel and glass, hence, thermal expansion is most likely to be expected. The meanmap of one stack reveals all the mentioned constructional details, as can be seen in Figure 53. By reason of the steel girders many bright signatures appear in the amplitude image, which act as PS. The amplitudes of periodic deformation can be seen in Figure 55 for all 6 different stacks.
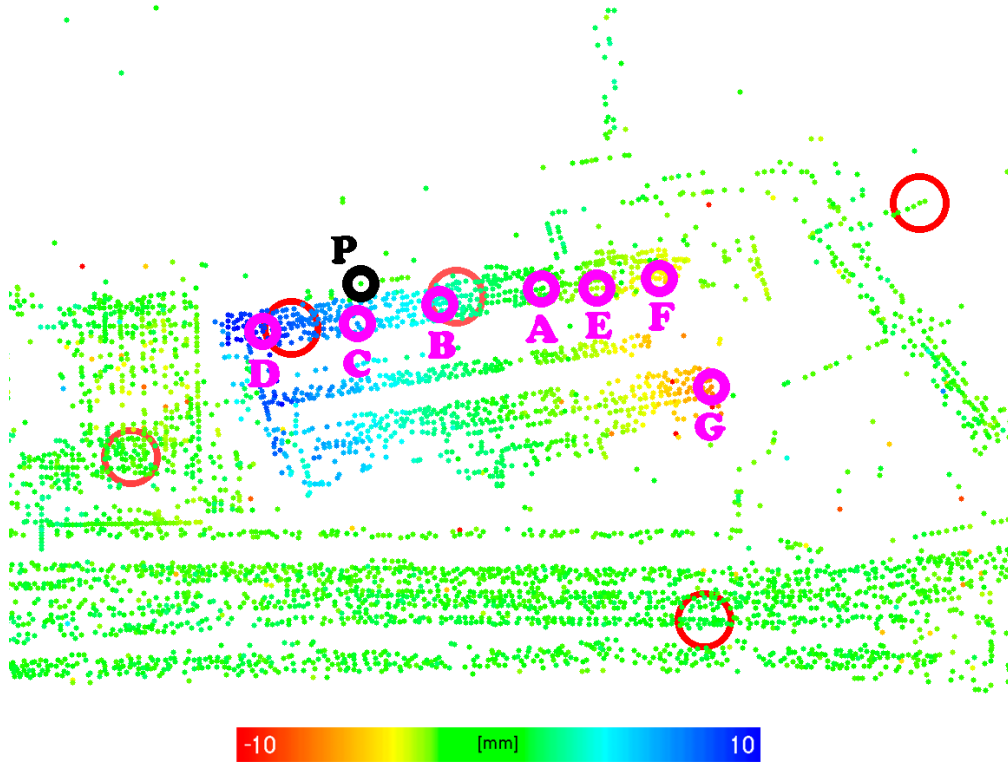
Figure 49. Sample location (area 2) 1̃.5 km north-west of central train station in Berlin (Friedrich-Krause-Ufer) showing larger deformation signals at final PS in Berlin. Circles indicate points of reference network, intensity of circle color shows deformation rate between 0 and 1 mm (intense red color) of periodic motion. Colors of points represent estimated seasonal amplitudes of deformation signal between -10 mm (red = subsidence in summer) and +10 mm (blue = uplift in summer) in LOS. Relative displacement in subsequent phase history plots between PS indicated by black (P) and each magenta (A-G) circle. Points are plotted in the azimuth-range plane.
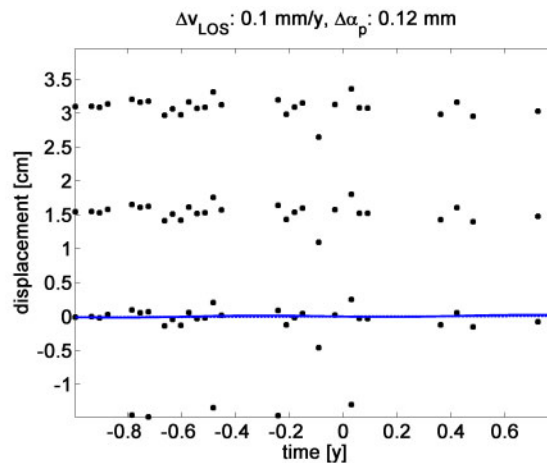
Figure 50. Phase history (including $\pm 2\pi$ ambiguities) showing relative deformation rate between two PS of area 2. Black dots represent relative deformation signal. Blue line indicates estimated deformation. First number in title corresponds to estimated linear, second to amplitude of periodic deformation. No significant motion present, neither linear nor seasonal (selection P-A).

The two main buildings show an interesting pattern, suitable for validation of thermal dilation; the amplitudes of estimated motion increase with height of the building. A linear dependency is validated easily from the PS heights obtained from the DEM refinements (with respect to the horizontal plane used for PSI) and the inherent amplitudes. The maximum vertical expansion ΔL at the top of the building is 16 mm between winter and summer. Including the height L of approximately 45 m, the temperature difference ΔK (in degree Kelvin) needed for the apparent expansion of steel can be calculated using the temperature coefficient of steel k:
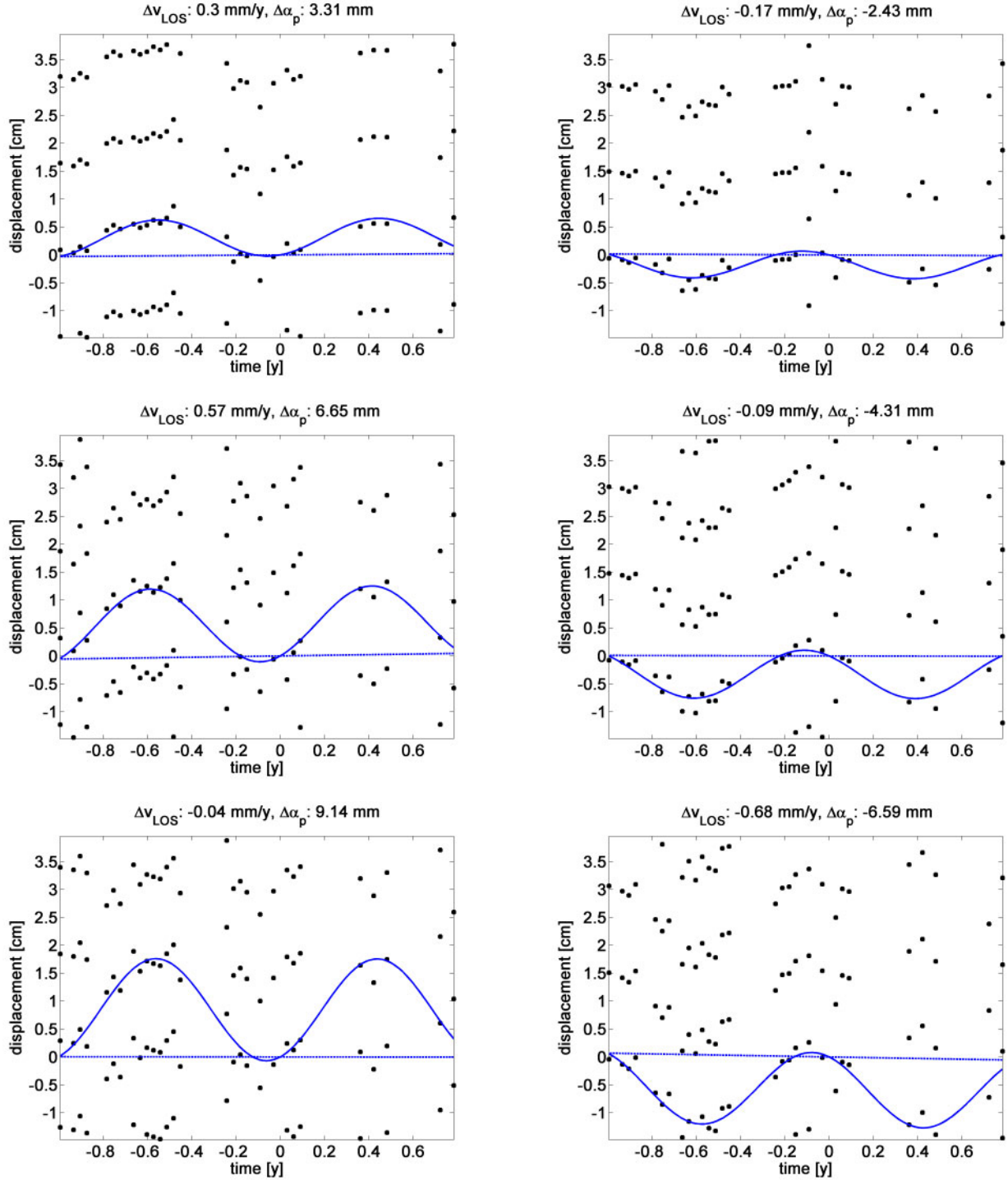
Figure 51. Phase histories (including $\pm 2\pi$ ambiguities) showing relative deformation rate between two PS of area 1. Black dots represent relative deformation signal. Blue line indicates estimated deformation. First number in title corresponds to estimated linear, second to amplitude of periodic deformation. Left, top to bottom: Increasing positive amplitudes of seasonal motion of selection P-B, P-C and P-D up to +9.1 mm. Right, top to bottom: Increasing negative amplitudes of seasonal motion of selection P-E, P-F and P-G up to -6.6 mm.

$$\Delta K = \frac{\Delta L}{kL} = \frac{0.016 \; m}{12.2e^{-6}K^{-1} \cdot 45 \; m} = 29.1 \; K \tag{58}$$

Temperatures histories of the area under investigation of the same period like the acquired datasets confirm the assumption of thermal dilation. The differences between winter and summer are 33 K and 29 K for mean high and mean low temperatures respectively. In addition, the

Figure 52. Optical image of central train station in Berlin. Building consists of two main parts, which are constructed across the rail tracks and of two halls covering the rail tracks to the left and right. Nearby a tower can be seen with the DB sign of the *Deutsche Bahn* on top. Large parts are constructed from glass and steel.

Figure 53. SAR image of central train station. The main parts can easily be identified: The two main building parts across the rail tracks, the two halls covering the tracks (to the left and right) and the tower, partly overlaid by one of the main building parts to the left. Azimuth: bottom-up, range: left-right.

temporal offset t_0 can be determined from the dense distribution of temperatures. The fitting of a sine function holds the date of April 14th as origin for a sine function. This result can be compared to a median offset obtainable from the estimation results of all PS of each stack. To this end, the median of all offsets from assumed highly reliable PS is calculated. The threshold on the posterior variance factor $\hat{\sigma}_0^2$ is selected to be 0.5 and all PS showing an amplitude of at least 4 mm have been selected for this approximation. The resulting offsets deviate about 11 to 15 days from the value calculated from the temperature history. Furthermore, the distribution of t_0 within each stack shows larger deviations from the median.
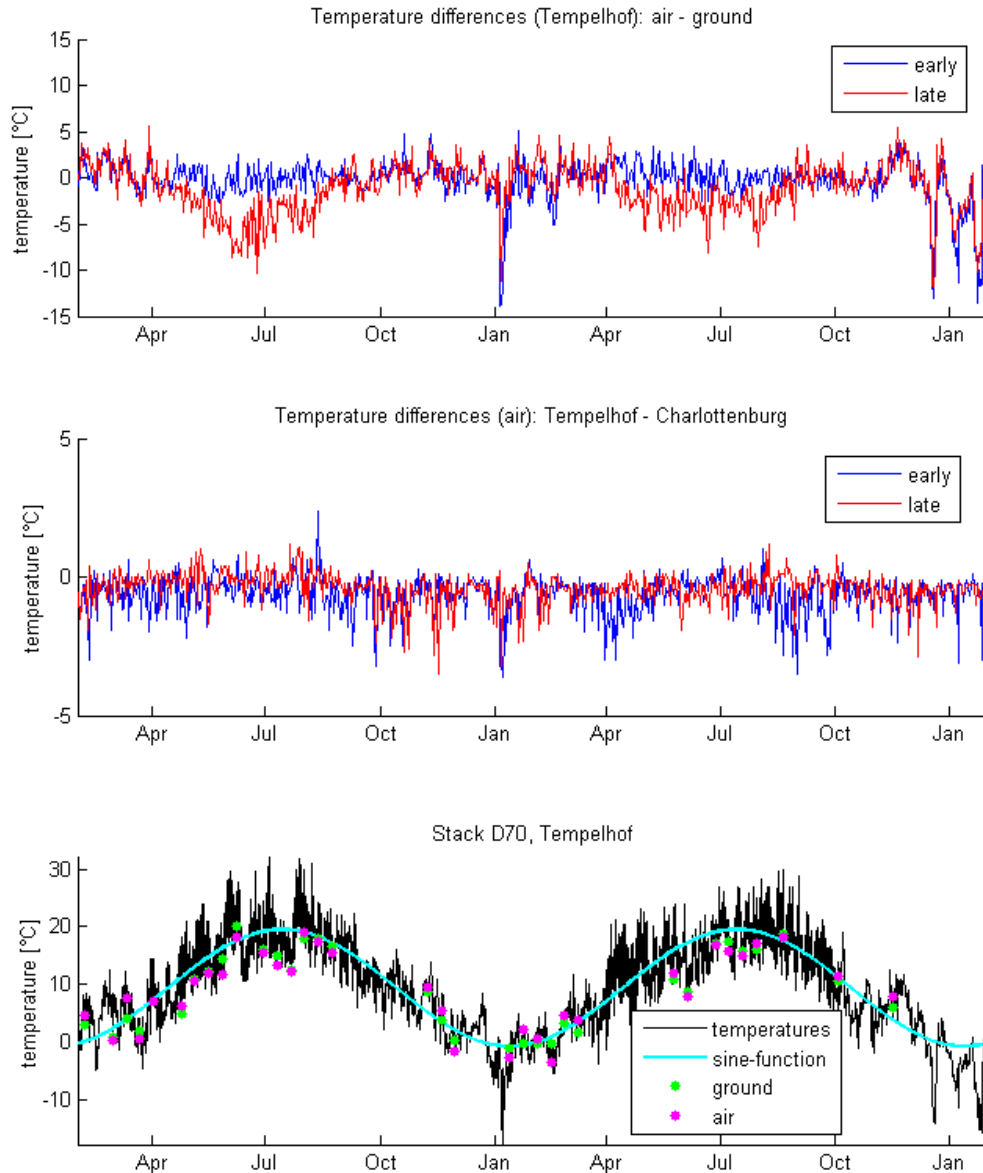
Figure 54. Top: Morning (early) and late afternoon (late) temperature differences between solid ground and air in 2 m above ground at measurement station Tempelhof. Middle: Morning (early) and late afternoon (late) temperature differences between two different locations within Berlin test site. One station is located in Charlottenburg, the other in Tempelhof. Bottom: Temperature history for station Tempelhof superimposed by a sine function fitted to the distribution. In addition, the temperatures of ground and air are indicated at the exact times of acquisitions for stack D70 by green and purple dots. Temperature data covering two years (starting January 2008) provided by FU-Berlin, Institut für Meteorologie.

Obviously, the relationship between local temperatures and thermal expansion cannot be considered to fit precisely the given temperature distribution. But the correlation certainly cannot be derived simply from one temperature history obtained at one limited location, horizontally as well as vertically, as the local differences between all PS will show larger deviations from this special temperature history. Even at one and the same location, but vertically 2 m apart, the temperatures between solid ground and air vary up to 15 K (cf. Figure 54). The variations between two stations within the city at 2 m above ground reveals local differences of up to 4 K (see also Figure 54). Variations due to the exposure to direct sunlight or shadow may be even higher, affecting the actual thermal dilation. This mis-fit to one common temperature history can be proven by the extraction of temperatures at the exact time of acquisitions and the usage of these temperatures as base function in PSI. The availability of dense sampling of the temperatures at two different locations in Berlin allows for this experiment. Exemplary, the temperature history of one measurement station is shown at the bottom of Figure 54, includ-

ing a sine fitted to the distribution of measurements and the temperatures. In addition, the temperatures at the exact acquisition times of every single dataset of stack D70 are highlighted by green and purple dots representing ground and air temperatures respectively.

The results are double edged; on the one hand the deformation of some PS perfectly fit the deformation model given by the distribution of temperatures, while on the other hand some PS (formerly treated reliable with respect to the underlying deformation model) are completely discarded from the results. The latter are missing by reason of larger deviations from the deformation model. Consequently, single temperature histories cannot be used as precise information for the derivation of periodic amplitudes for all PS within an urban area. Certainly, mean temperatures or rather a mean offset derived by fitting a sine to the temperatures could be used in PSI for setting up the base functions of the deformation model, if the estimation of individual offsets is not applicable. However, the latter will be the best choice in most of the cases in order to include as many PS as possible in the final selection. Experiences from the test site of Berlin show, that there does not exist one single temporal offset t_0 that will be valid for the large majority of PS affected by seasonal motion.

4.4.4   Decomposition of Motion and Cross-Validation

The availability of 6 different stacks enables a comparison and interpretation of the estimated LOS motion. In Figure 55 the final results of seasonal amplitudes in the area of central train station are illustrated, in the left column for all 3 ascending and in the right column for all 3 descending stacks. The respective azimuth directions are indicated by the larger purple arrow at the lower left and upper right (bottom up for ascending and top down for descending stacks), while the short one indicates range direction. In addition, the schematics to the right of each picture show an approximate geometrical configuration of a side view on central train station (illustrated by the symbol of a house) and the satellite LOS direction, given by the incidence angle (slope of the arrows with respect to the vertical). The colors of the two-headed arrows facilitate the interpretation of the estimated motion directions. Red colors indicate a movement of the PS away from the sensor, while motion towards the sensor is illustrated by blue colors. In the case of periodic deformation at hand, the maximum amplitudes towards the sensor (blue colors) occur during summer times.

A visual comparison of the estimated amplitudes holds a good agreement within ascending or descending stack results by reason of similar color distribution in general. However, there exist some slightly visible differences within the results of each triplet, i.e., within exclusively ascending or descending stacks. A closer look especially on the left main building (aligned approximately top-down) or the tower reveals that for steep look angles (small incidence angles) the intensity of blue colors is larger than for shallow angles. This is an indication for mainly vertical motion components at these locations, because the projection of vertical motion to LOS will confirm a decreasing intensity at increasing incidence angles. A contrary behavior can be observed for most parts of the rail tracks to both sides of central train station. The yellow and light blue colors show an increased intensity for shallow looking directions compared to steep ones. Consequently, a main component of motion in horizontal directions is expected.

In addition, two sections can be identified located near the left and right border of the images at the rail tracks, that show a sudden jump in colors, i.e., from yellow to blue. The position can be precisely located due to the defined change forming a linear feature perpendicular to the rail track directions. The latter is visible in almost the same manner from the descending triplet. However, the differences between ascending and descending stack results are clearly visible from large changes in colors, whereas the color order is reversed; at the horizontally aligned rail tracks and halls to both sides of the main buildings, the colors are changed from blue-to-green-to-red (left to right) to the inverse. In addition, the increase of color intensities for shallow looking directions is comparable to the ascending cases. Only the two main buildings show the
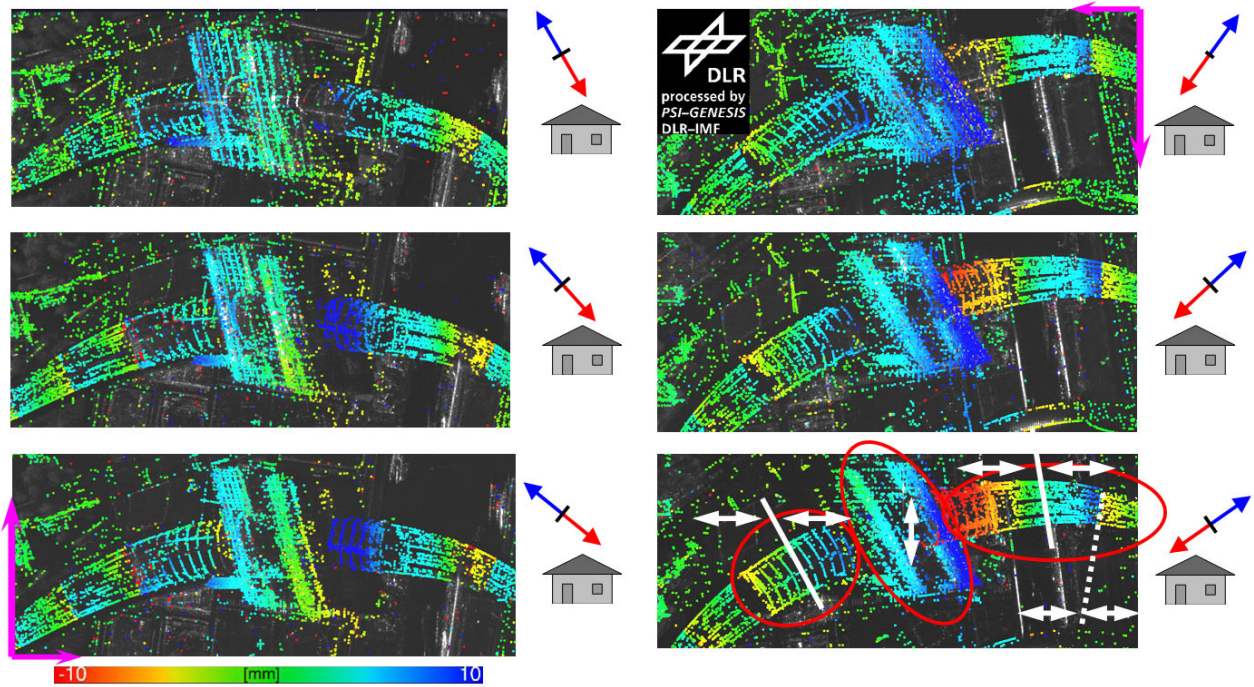
Figure 55. Estimated seasonal amplitudes at central train station obtained from each of the 6 stacks of Berlin. Left, top to bottom: Ascending stacks A30, A42 and A51. Right: Descending stacks D36, D47 and D55. Colors indicate amplitudes between -10 mm (red) and +10 mm (blue). Azimuth and range directions given by long and respectively short purple arrows at bottom left and top right. Houses and red-blue colored arrows indicate direction of motion with respect to LOS (side view on train station). White arrows show parts of dominating horizontal (left-right) and vertical (up-down) motion. White solid bars mark stable part, possibly fixed to ground. Dashed bar indicates position of rail tracks that are moving towards each other during summer times.

same colors for all 6 cases. Summarizing the observations and taking the LOS directions into account, that correspond to the colors shown in the image, the following conclusions can be drawn:

◇ Thermal expansion can be verified due to the consistently increasing amplitudes from bottom to top of the tower and the two main building parts.
◇ Estimated motion is consistent and verified from the cross comparison of 6 independently processed stacks.
◇ The two main buildings as well as the tower are mainly affected by vertical seasonal motion.
◇ The halls covering the rail tracks and the tracks themselves are mainly oscillating in horizontal directions.
◇ There have to be constructional gaps at the positions of rail track parts moving towards each other in summer times in order to prevent damage induced by that kind of motion.

Ground truth inspections reveal several constructional details, that allow for the observed motion. At first, the halls are separated from the main building and mounted on horizontally movable devices and the rail tracks are disconnected from the parts inside the central area by a special rail track construction in order to enable large horizontal movements without risk of damage (cf. Figure 56). Secondly, the piles of the bridges to both sides of the central part show particular mounts that enable horizontal shifts (see Figure 57a). Finally, constructional gaps – like shown in Figure 57b – at the positions of rail tracks moving towards each other are validated.

Unfortunately, an automatic decomposition of horizontal and vertical motion components cannot be carried out at this stage, because the geocoded PS point clouds show different residual offsets due to the unknown heights of the reference points (cf. Section 2.3.2). To this end, a methodology for a combination of all stacks will be developed in Section 5.2, which finally

enables the decomposition of motion components. Nevertheless, a visual interpretation of deformation estimates obtained from *cross heading* tracks (i.e. ascending and descending track directions) already allows for an assessment of main components of the apparent motion. Consequently, by reason of a dense coverage of buildings with PS and the incorporation of cross heading tracks, precise deformation data of buildings can be derived with the help of PSI. Hence, single object observation becomes already feasible, although a fusion of stacks is not achieved, yet.
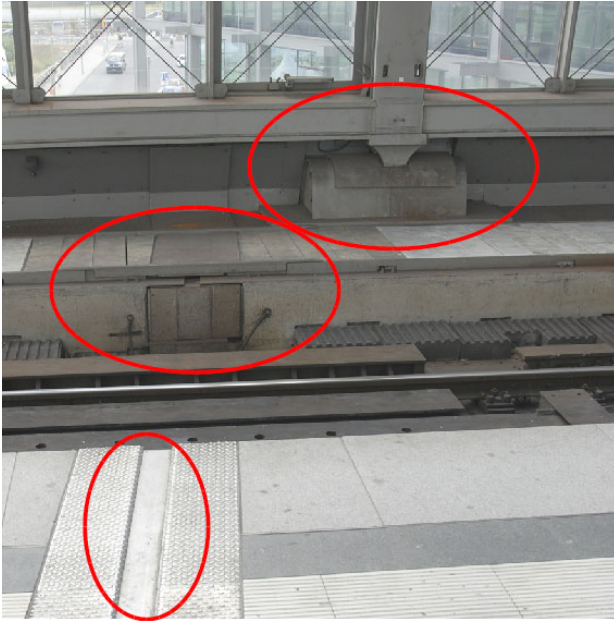
(a) Three special constructions, enabling horizontal movement for the halls and both sides of the station platform. Locations highlighted by red ellipses.

(b) View on the separation of the rail tracks. The detached parts along direction of train allow for large horizontal movements.

Figure 56. Constructional separation of the halls and rail tracks between different parts of Berlin central train station.

(a) Special mounting of piles enabling horizontal movement in any direction.

(b) Constructional gap at bridge that allows for different motion directions of bridge segments, i.e., observed movement towards each other during summer times.

Figure 57. Constructional details at bridges near Berlin central train station.

5 3D Point Localization and Multi-Track PS Fusion

5.1 Localization of PS

The detailed analysis on deformation estimates presented in the previous section already revealed some details on the localization of PS in general and more specifically on single buildings. Scatterers from different floors actually can be separated visually from the deformation plots presented in Section 4.4 showing different amplitudes of deformation at increasing heights due to thermal expansion. In the following section the precision of localization of these points is investigated. The theoretical limit for localizing PS is shown and a validation is carried out on basis of PS detected at facades of different buildings. The findings hold the accuracy of PS positions derived from real data processing, hence, the possibility to detect the origin of these signatures is evaluated.

5.1.1 Theoretical Localization Precision

The position of a point scatterer in uncorrelated clutter is detected in SAR images by a correlation of a sinc-function (the impulse response function of an ideal point scatterer) with the complex image data. The estimated error between two detected maxima (i.e., the assumed coordinates of the point scatterers) is a function of the signal-to-noise ratio (SNR) (Bamler and Eineder, 2005):

$$\sigma_{\Delta points} = \frac{\sqrt{3}}{\pi} \frac{1}{\sqrt{\text{SNR}}} \approx \frac{0.55}{\sqrt{\text{SNR}}} \tag{59}$$

The detection of the PS is carried out on the basis of the meanmap, i.e., the temporal average of N images of the whole stack is calculated. Hence, the error is divided by $\sqrt{N}$. In addition, it is transformed from pixels to meters considering the inherent azimuth and range resolution ρ_{Az} and ρ_R of the SAR data. Consequently, the previous formula is adapted, yielding the relative localization precision of PS in azimuth σ_X and range σ_R:

$$\sigma_X \approx \frac{0.55}{\sqrt{\text{SNR} \cdot \text{N}}} \cdot \rho_{Az} \tag{60}$$

$$\sigma_R \approx \frac{0.55}{\sqrt{\text{SNR} \cdot \text{N}}} \cdot \rho_R \tag{61}$$

The standard deviation $\sigma_{\hat{S}}$ of the elevation estimates (elevation S correspond to the DEM refinements: $S = h/\sin\theta_{inc}$) can be approximated by (Bamler et al., 2009):

$$\sigma_{\hat{S}} \approx \frac{\lambda R_S}{4\pi\sqrt{N} \cdot \sqrt{2 \cdot \text{SNR}} \cdot \sigma_{B_\perp}} \tag{62}$$

It depends on the SNR and standard deviation of the baseline distribution $\sigma_{B_\perp}$. The approximation is based on the linear dependency of the phase contributions due to residual topography on the perpendicular baseline. Hence, the DEM refinements correspond to the slope of a line estimated from the distribution of measurements in the coordinate system of $B_\perp$ and ϕ_{topo}. In case of TerraSAR-X the influence of orbit errors is negligible, because the rmse is in the range of centimeters and the distribution of perpendicular baselines in comparison is within

some hundreds of meters. An approximation of the additional elevation error by orbit errors yields values smaller than 4 cm, assuming relative DEM refinements to be 50 m at maximum. However, most of the relative DEM refinements are actually smaller in typical PS networks, hence, errors in the perpendicular baseline can be neglected.

For many bright points a SNR of 10dB can be assumed. If TerraSAR-X high resolution spotlight images are used and typical stack parameters are given, like presented in Section 4.1.2 ($\sigma_{B_\perp} = 56 - 122$ m, $R_S = 555 - 833$ km), the theoretical localization precision of PS is approximately within the following ranges:

◇ $\sigma_R = 1.7$ to 2.1 cm
◇ $\sigma_X = 3.2$ to 3.8 cm
◇ $\sigma_S = 62$ to 139 cm

The relations between range and azimuth accuracies are about 1:2, i.e., azimuth precision is about 2 times worse than range precision. The relations between azimuth and range in comparison to elevation precisions are roughly 1:20 to 1:30 (azimuth:elevation) and 1:30 to 1:50 (range:elevation).

5.1.2 Relative Localization Accuracy

Many geometrical details are expected to show up in geocoded PS point clouds that can be derived from the distribution of points in 3D space. This is facilitated by the large amount of PS in combination with the high precision of localization of these points presented in the last section. A top view on two of these point clouds obtained from two stacks of the test sites Berlin and Munich is presented in Figures 58 and 59 in the UTM coordinate system. The points are colorcoded by their height deviations from the chosen reference surface (defined by the horizontal plane used in PSI), whereas the difference between lower and upper limits (blue and red colors) is 35 m and 30 m in the case of Berlin and Munich respectively. The images already give an impression on the structural details available from the spatial distribution of PS using meter-resolution SAR data; individual buildings and bridges can be identified, as well as rail tracks, which interestingly show a high density of point scatterers. In principle, the structure of the city can be derived, because the PS are mainly situated at building facades, roofs and most likely at the intersection between vertical and horizontal structures aligned towards the sensor creating double bounce lines. At a few spatially limited locations no PS are available due to the absence of dihedral or trihedral structures, or simply as an effect of viewing geometry (e.g., not all facades of each building can be seen). The areas of low PS densities can be assigned to, e.g., vegetated or unused areas, like the large part in Berlin south-west of central train station (*Großer Tiergarten*) or north and south-west of Munich city center (*Englischer Garten* and *Theresienwiese*), water surfaces (Berlin: river *Spree*; Munich: river *Isar*) and areas under (de)construction affected by fast structural changes.

In order to give a hint on the affiliation of PS to facades, roofs and most likely to ground height, a simple filtering is applied. To this end, at each location of the geocoded PS, a small patch is centered on the point under investigation. The horizontal extent is chosen 4 m by 4 m (no limitation in z) and the variance in height of all PS within this elongated cuboid is calculated. If the variance in z is larger than a threshold, the PS is assumed to be part of a facade, because the height variations of vertically aligned points (a simple indicator for facades) are most likely to be large. A threshold of 1.5 m^2 on the vertical variance turned out to be suitable for the given test sites. Figure 60 shows the histograms of the PS heights of stack D36 and A42 of the Berlin test site. The graphs in the left column represent the distribution of PS classified as points on facades, whereas the plots on the right hand side show the histograms of the remaining points after removal of the former. Two peaks can be identified in the histogram of non-facade PS. The almost horizontal ground surface in Berlin facilitates the interpretation,
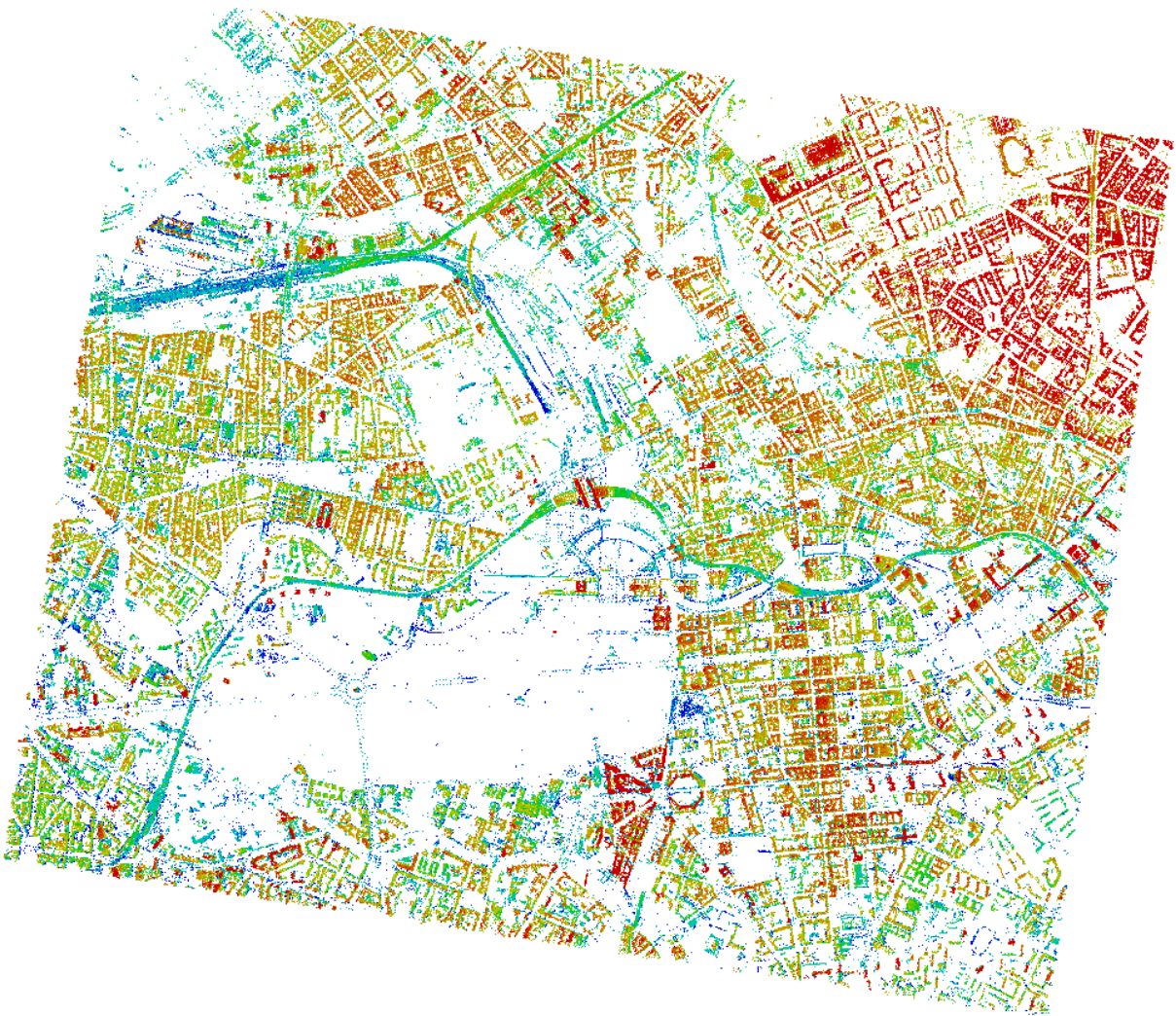
Figure 58. Top view on geocoded PS of stack D55, Berlin. Colors indicate relative height deviations from the chosen reference surface. Lower points in blue colors, higher points in red colors. Difference in height between limits is 35 m.

because the location of many houses at the same height will most likely lead to a large number of PS at the same height due to double bounce lines appearing at the intersections between ground surface and facades. Hence, the largest gradient of increasing number of points can be determined easily in this case by the location of the first peak. The second peak indicates the presence of a large number of roofs at the same height, certainly a unique feature of the given test site. The shape of the histogram at further increasing heights depends on the amount of skyscrapers within the scene. However, the special geometrical configuration of the Berlin test site allows for a very rough approximation of the location of scatterers. About 50% of the PS can be assigned to facades, most likely less than 25% are situated at low heights and at the ground, and the remaining points are situated at elevated locations, possibly on roofs.

A closer look on the distribution of PS on facades reveals the presence of regular patterns. In Figure 61 two examples can be seen, showing two interesting features. At first, the PS on many building facades are aligned in rows and columns, hence, originate from windows at facades. However, this regular grid will be visible only, if the viewing direction is parallel to the elevation direction. Using this special viewing geometry, the uncertainties in elevation estimates simply disappear and the high precision of azimuth and range localization are reflected in the regular pattern of rows and columns of windows. This kind of appearance of PS can be observed
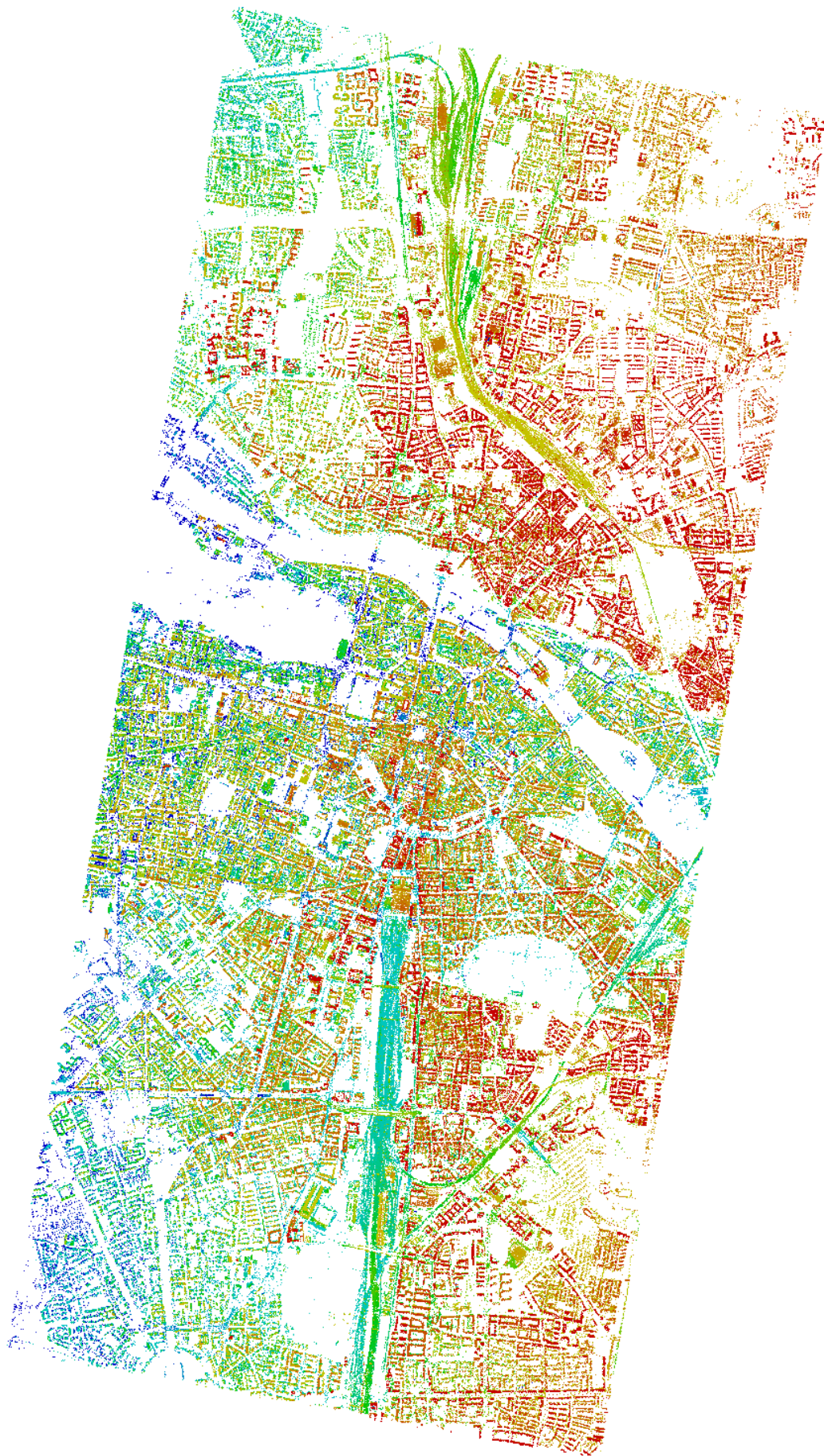
Figure 59: Top view on geocoded PS of stack D25, Munich. Colors indicate relative height deviations from the chosen reference surface. Lower points in blue colors, higher points in red colors. Difference in height between limits is 30 m.
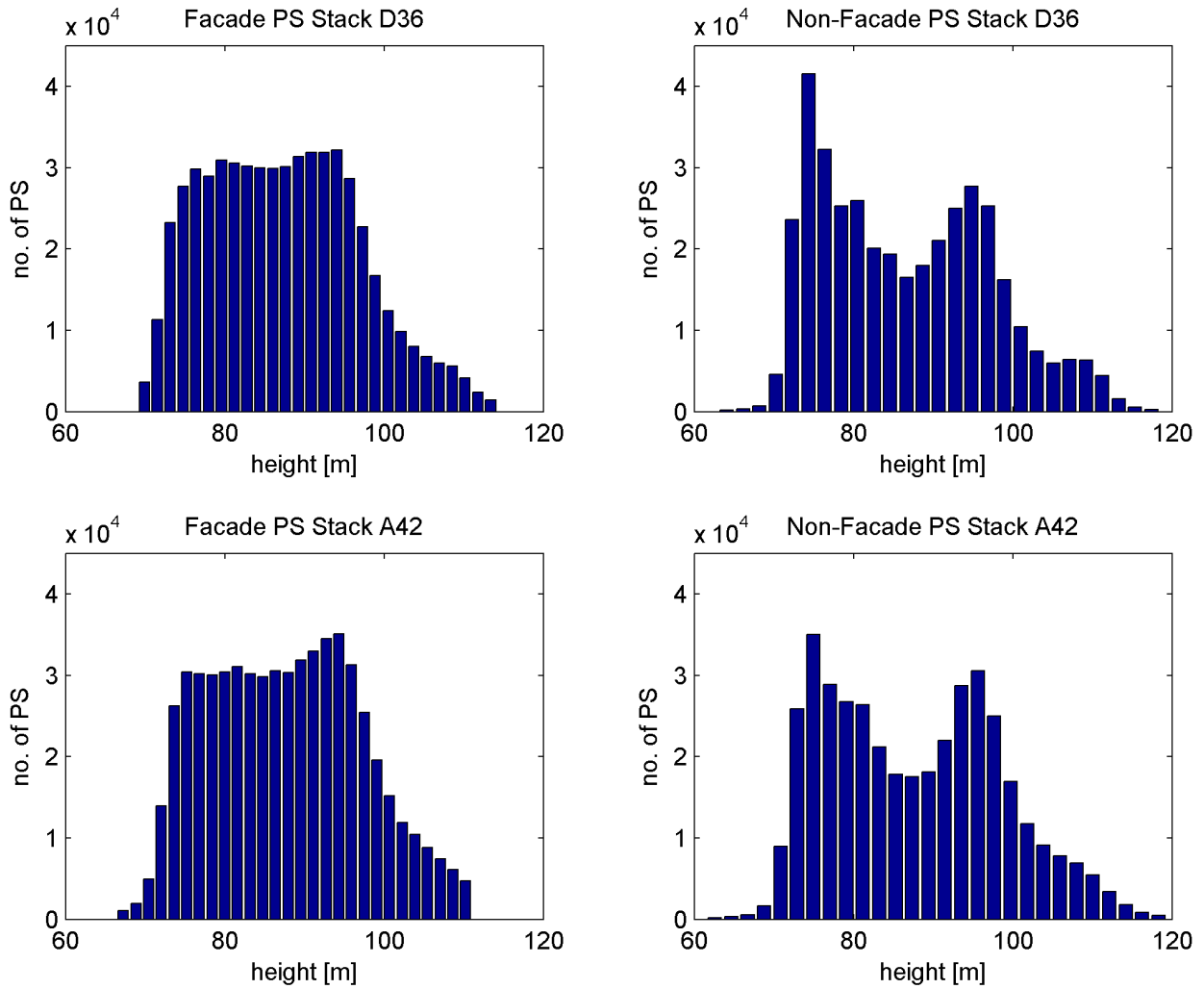
Figure 60. Histograms of PS absolute heights, geocoded to the UTM coordinate system of stacks D36 and A42. The unknown height offsets are already fixed (see Section 5.2). The left column shows the graphs of potential facade PS. On the right hand side the distribution of the remaining PS heights is plotted. The two peaks indicate approximately the heights of ground surface (first peak) and the roofs of a majority of houses (second peak). This interpretation is facilitated by the almost horizontal ground surface in Berlin.

at a majority of facades, however at different distinctive formations by reason of different alignment, visibility and local geometry of windows at facades. Certainly, the PS originate from reflections at the window frames and/or ledges, as glass is penetrable for radar. The second interesting feature is the appearance of subsurface PS, which follow the direction of the facade perpendicular into ground. The occurrence of these "ghost" points can be explained by fivefold reflections including the ground in front of the building twice. However, an investigation on the nature of these points is not intended to be part of this thesis. Detailed analyses on the origin of these "ghost" PS can be found in Auer et al. (2011c), Auer et al. (2011a) and Auer et al. (2011b).

The observed regular appearance of PS, i.e., the alignment of points along horizontal lines, is used for an experimental validation of the relative precision of geocoded PS positions. The SNR for the selection of points is chosen comparable to the one used for theoretical localization evaluations. For the investigation, several single rows of PS are extracted from different facades within the point clouds obtained from stacks of Berlin test site. Figures 62 and 63 show two areas that are included in this analysis. In the optical images the regular spacing of windows in horizontal and vertical directions can be seen, that is also visible from the geocoded PS.
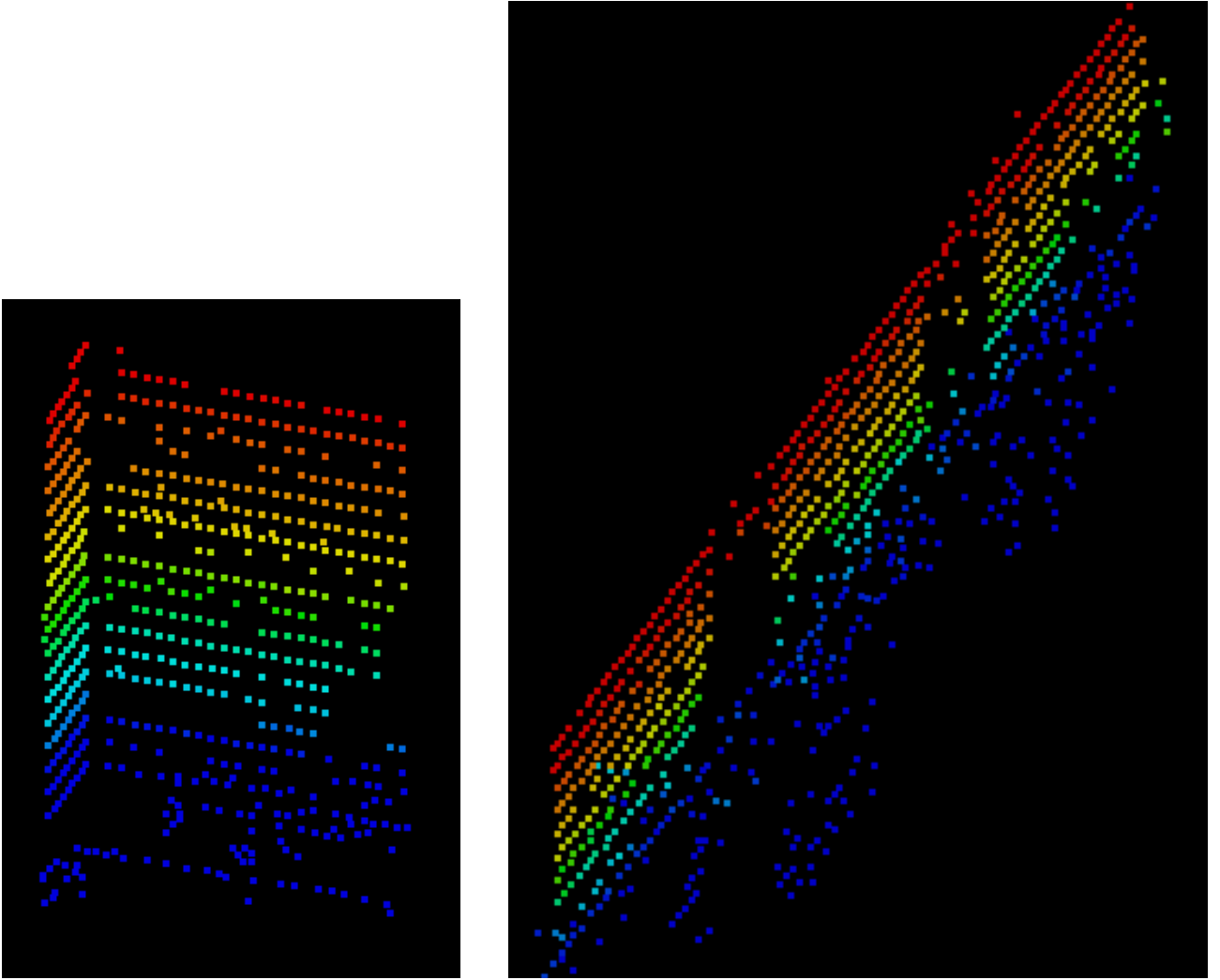
(a) PS originating from two facades of a skyscraper.

(b) PS originating from facades of three houses. Additionally, "ghost" PS below the surface are visible (dark blue points).

Figure 61. Clipping of point cloud to PS originating from several building facades. Almost all floors show linearly aligned PS at a regular spacing, most likely originating from rows of regularly spaced windows. Viewing direction on the PS is opposite to elevation direction. The points are colorcoded by their relative height.

If the PS originate from certain repeating structures at the rows and columns of windows on the facade, the points should be aligned horizontally at a regular distance to each other. The correctness of this special geometrical configuration is tested using a least-squares adjustment (LSA) of the observations (PS positions) to fit a straight line. The adjusted coordinates $\hat{x}_i, \hat{y}_i, \hat{z}_i$, that are the sum of initial observations x, y and z and the respective adjusted refinements $\hat{v}_x$, $\hat{v}_y$ and $\hat{v}_z$, have to fulfill the following equations for $i \in [1, ..., N_P - 2]$:

$$[(\hat{v}_{x_{i+1}} + x_{i+1}) - (\hat{v}_{x_i} + x_i)] - [(\hat{v}_{x_{i+2}} + x_{i+2}) - (\hat{v}_{x_{i+1}} + x_{i+1})] =$$
$$(\hat{x}_{i+1} - \hat{x}_i) - (\hat{x}_{i+2} - \hat{x}_{i+1}) = 0 \qquad (63)$$

$$[(\hat{v}_{y_{i+1}} + y_{i+1}) - (\hat{v}_{y_i} + y_i)] - [(\hat{v}_{y_{i+2}} + y_{i+2}) - (\hat{v}_{y_{i+1}} + y_{i+1})] =$$
$$(\hat{y}_{i+1} - \hat{y}_i) - (\hat{y}_{i+2} - \hat{y}_{i+1}) = 0 \qquad (64)$$

The equations for z-coordinates deviate slightly in order to include the horizontal alignment (i.e., all differences in height have to be zero), besides equal spacing:

$$[(\hat{v}_{z_{i+1}} + z_{i+1}) - (\hat{v}_{z_i} + z_i)] = \\ (\hat{z}_{i+1} - \hat{z}_i) = 0 \tag{65}$$

On basis of the mathematical model given by the last three equations the sum of the squared adjusted refinements on the observations is minimized in the LSA:

$$\hat{v}^T \hat{v} \rightarrow \min. \tag{66}$$

Altogether, $3 \cdot N_P - 5$ linear independent equations can be set up for each line consisting of N_P PS. No unknowns are introduced, hence, the spacing is calculated from the adjusted coordinates after the LSA. The observations are weighted equally within the adjustment and the relative precisions are obtained from the deviations of the observations from the adjusted coordinates. Figure 64 shows two different views on the PS positions (shifted to the balance point of the selected PS) previous and after the LSA; geocoded PS are plotted as black dots, the adjusted positions are shown in red and the horizontal line is accentuated by a blue line connecting all adjusted coordinates. The PS are extracted from one row of points of the facade shown in Figure 62. As in the previous figures of geocoded PS of facades, the viewing direction is set in parallel to elevation direction in Figure 64a. Hence, the deviations in elevation disappear and only small differences remain. In a rotated view (Figure 64b) the 3D deviations can be seen, indicated by the thin blue arrows pointing from the PS (black dots) to the adjusted coordinates (red dots) on the horizontal line.
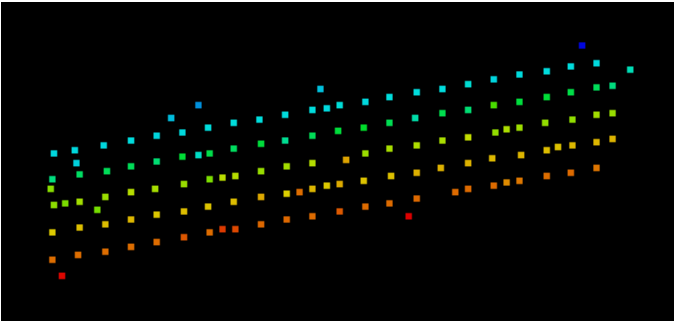
(a) Approximate clipping of point cloud to PS originating from building facade. Upper 5 floors show 22 linearly aligned PS each.

(b) Photograph of the facade under investigation. Windows are aligned in a regular grid of 5 by 22 windows.

Figure 62. Example of building facade that shows regular pattern of PS in geocoded results of stack A30. Viewing direction on the PS is opposite to elevation direction. The points are colorcoded by their relative height. Additionally, an optical image of the facade is provided, showing the alignment of windows.

For validation purposes, both groups of points (adjusted as well as initial) are transformed to a range-azimuth-elevation (RXS) coordinate system using the heading angle t_{Az} (flight direction) and local incidence angle θ_{inc}:

$$\vec{P}_{RXS} = M_y \left(\theta_{inc} - \frac{\pi}{2} \right) \cdot M_z(t_{Az}) \cdot \vec{P}_{xyz} \tag{67}$$

M_y and M_z represent the conventional rotation matrices with respect to y and z axis respectively. Two projections of the transformed points are shown in Figures 65a and 65b in the

range-azimuth plane as well as range-elevation plane. A comparison of these two fits expectations of worse precisions for elevation estimates compared to range or azimuth coordinates of PS, by reason of the good fit of positions to the line in the range-azimuth plot. In contrast, the deviations of PS positions to the line are much larger for elevation directions, as can be seen from the distribution of points in the elevation-range plane.

The results of several rows of windows from different facades are summarized in Table 10 including the theoretical values calculated in the previous section. Furthermore, the results of a LSA omitting the horizontal alignment are provided including the deviation angle from the horizontal direction κ. The results show a consistency between the theoretical approximation of localization precision and the experimental results. The deviations from a horizontal alignment may originate from inaccuracies during the geocoding process, e.g., caused by errors in the satellite heading direction of the master acquisition. However, especially the large difference between the precision in range or azimuth in comparison to elevation is clearly visible.

The obtained geocoded PS cannot be compared to reference data, like a DSM of the area, because of the apparent shift between the point clouds and ground truth data. The reason already has been mentioned in Section 2.3.2; due to uncertainties in the height of the reference point, final geocoded positions will deviate horizontally as well as vertically from the real position. Hence, absolute positions of PS can be investigated only after a correction of the height error of the reference point. One possibility is shown in the next section, without the need for any further reference data. Afterwards, the PS can be compared to ground truth data and the absolute precision may be evaluated.

Line #	1	2	3	4	5	Theory
σ_R [m]	0.08 (0.04)	0.04 (0.03)	0.07 (0.04)	0.15 (0.02)	0.14 (0.04)	0.02
σ_X [m]	0.08	0.13	0.14	0.06	0.05	0.04
σ_S [m]	1.84	0.89	0.78	1.14 (1.13)	1.06 (1.05)	0.6-1.4
σ_R/σ_X [m]	1:1 (1:2)	1:3 (1:4)	1:2 (1:4)	2:1 (1:3)	3:1 (1:2)	1:2
σ_X/σ_S [m]	1:20	1:7	1:5	1:16	1:17	1:20-1:30
σ_R/σ_S [m]	1:21 (1:49)	1:20 (1:27)	1:9 (1:18)	1:6 (1:43)	1:6 (1:27)	1:30-1:50
κ [°]	0.0 (0.45)	0.0 (0.21)	0.0 (0.16)	0.0 (0.52)	0.0 (0.60)	0.0
Δxy [m]	2.45	2.41	3.56	2.81	2.72	n/a

Table 10. Results of a LSA applied to different rows of windows extracted from building facades within geocoded PS point clouds of Berlin and Munich test sites. If the results deviate from a LSA without a restriction of the line to be aligned horizontally, they are given in parentheses. In addition, the estimated slope of the line and the estimated spacing between windows are given by κ and Δxy respectively. Unfortunately, no ground truth data is available at the moment in order to validate the horizontal spacing, i.e., the distance between windows.
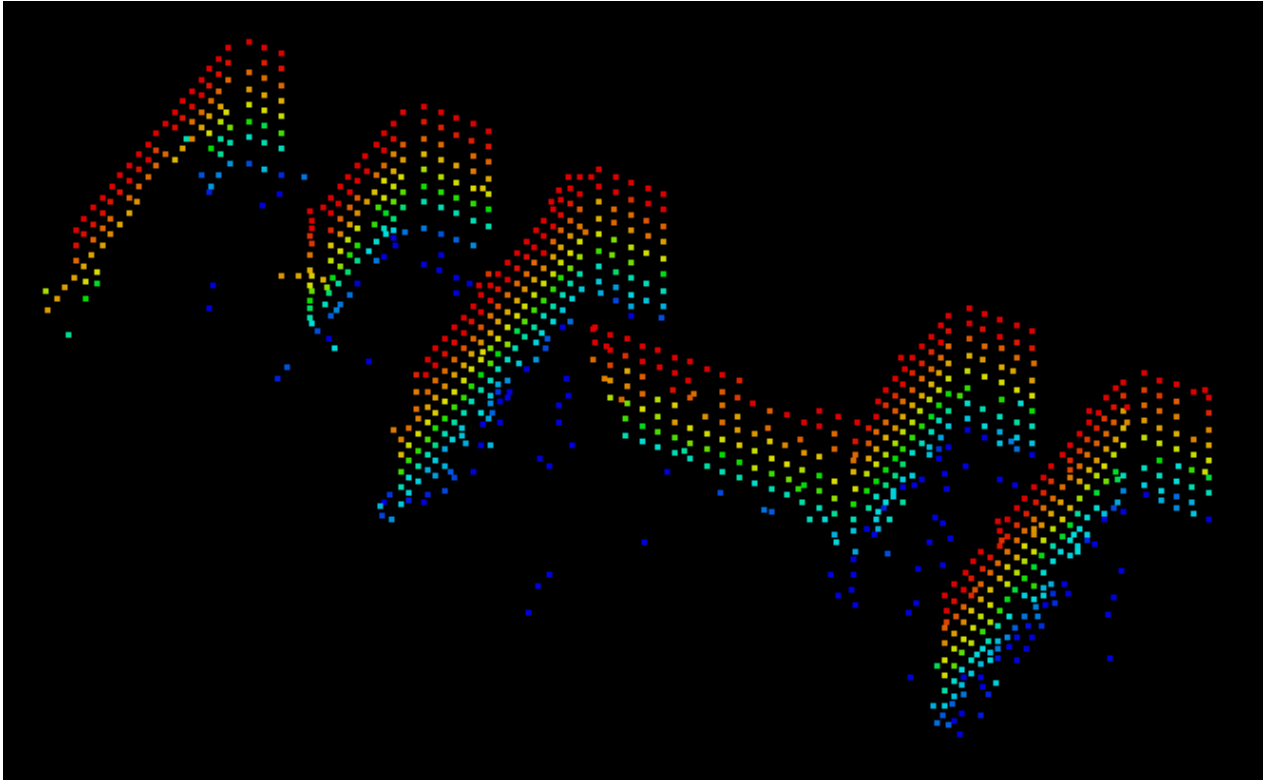
(a) Clipping of point cloud to PS originating from several building facades of identical architecture. 8 floors show linearly aligned PS at a regular spacing, most likely originating from rows of regularly spaced windows.

(b) Photograph of the facades under investigation. Windows are aligned in a regular grid of 8 rows and varying number of columns.

Figure 63. Example of building facade that shows regular pattern of PS in geocoded results of stack A42. Viewing direction on the PS is opposite to elevation direction. The points are colorcoded by their relative height. Additionally, an optical image of the facade is provided, showing the alignment of windows.
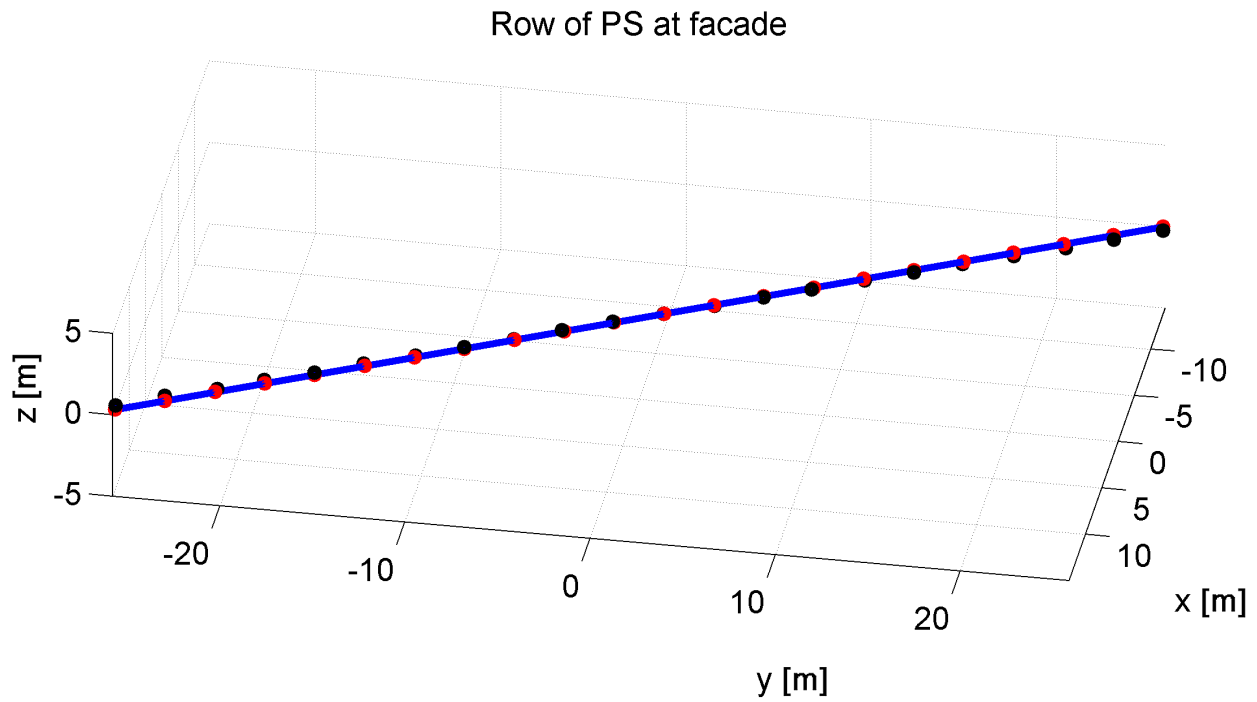
(a) View on PS positions parallel to elevation direction. Consequently, the deviations from the regular spacing is very small.
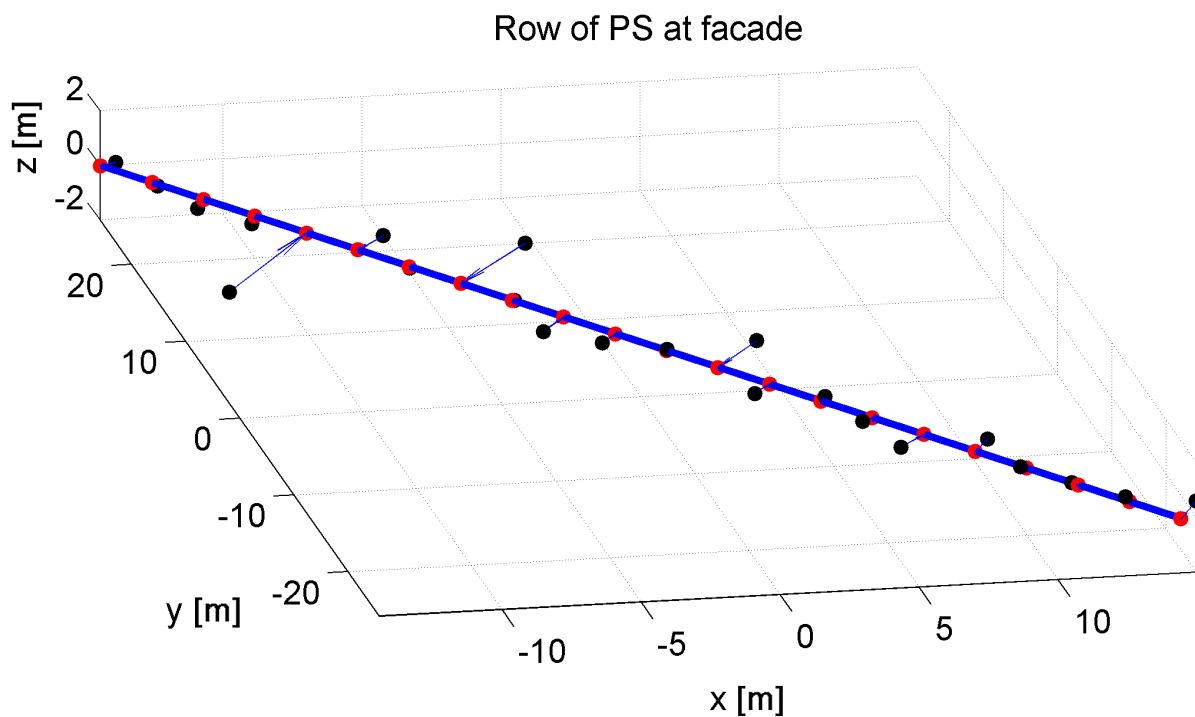
(b) View on PS positions from a different side compared to Figure 64a. The deviations of the geocoded PS in elevation become apparent. Blue arrows indicate necessary adjustments to PS positions in order to fit an equally spaced horizontal alignment.

Figure 64. Different views on geocoded original and adjusted PS positions indicated by black and red dots respectively. Horizontal line shown in blue. Deviations of PS from equally spaced positions indicated by blue arrows. Points are extracted from one row of windows shown in Figure 62.

Row of PS at facade in radar coordinate system

Row of PS at facade in radar coordinate system
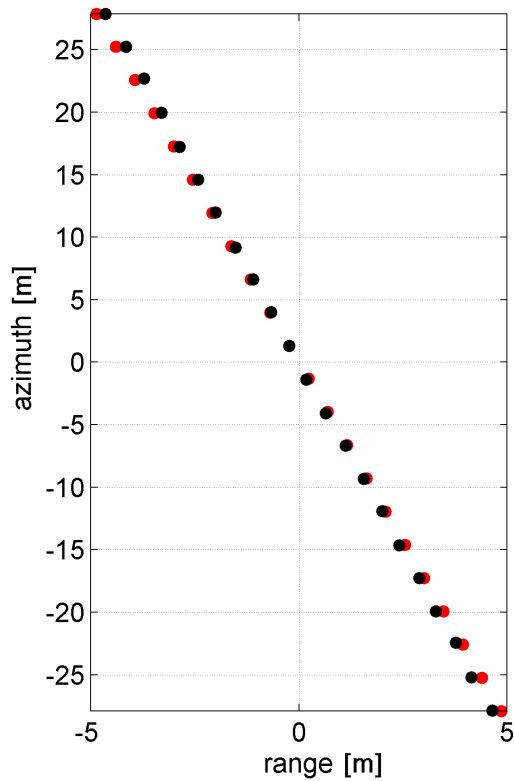
(a) View on PS positions in range-azimuth plane. Differences between adjusted and initial positions are very small.
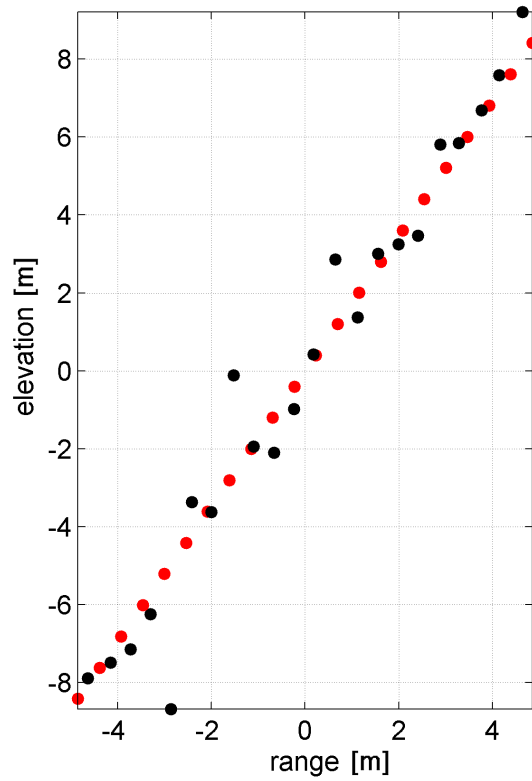
(b) View on PS in range-elevation plane. As expected, deviations in elevation direction are much larger than in azimuth or range.

Figure 65. Different views on geocoded original and adjusted PS positions indicated by black and red dots respectively transformed to the range-azimuth-elevation coordinate system. Selection of points equal to Figure 64.

5.2 Fusion of Multi-Track PS Point Clouds

PSI deformation estimates are available in LOS direction only. However, the combination of PSI results obtained from stacks of different acquisition geometry (i.e., stacks acquired at different incidence angles and/or track directions) offers the possibility to separate motion components to vertical as well as to horizontal directions, if *cross-heading* tracks are combined, i.e., one ascending and one descending stack. Besides advantages for deformation monitoring, the fusion of PS point clouds will provide enhanced 3D information of the structure of buildings, because most likely PS on all sides of the building are available afterwards. However, a special methodology is needed for a successful fusion of PS point clouds in order to compensate the offsets between the geocoded results due to the unknown heights of the reference points.

Colesanti et al. (2002) show a simple solution for a combination of PS based on stacks of ERS data by generating binary images of the geocoded PS positions. The offsets between the datasets are determined from a cross-correlation of these images. However, the precision is low (approximately 5 m to 10 m by reason of medium resolution SAR data of ERS), hence, the methodology is only used to combine the results of ascending and descending stacks, whereas the absolute positions of PS do not seem to be of further interest in their work. Consequently, the final results most likely show large deviations from a reference DSM and the nature of PS may still be unclear.

Ketelaar et al. (2007) propose another approach, which is again based on medium resolution SAR data. In principle the PSI results are linked by a transformation of all detected PS to a common radar datum. Even though the results are very promising, this method cannot be applied to PS positions derived from meter-resolution SAR data. The proposed refinement of transformation parameters based on a cross-correlation of reflectivity patches most likely is a difficult task in urban areas, because layover dominates the images. This approach is suitable only for relatively flat terrain, without the usage of additional a priori data (like a DSM). In addition, the height uncertainty of the reference point of the master track still remains. Hence, the tracks are aligned relative to the master track only. Certainly, the proposed algorithm works very well on medium resolution data and is suitable to connect several tracks for displacement monitoring of huge areas, as shown in the paper.

However, for meter-resolution SAR data a different method is needed that allows for a precise fusion of two tracks without the need for any further reference data, providing final absolute PS positions. One suitable method inspired by the two aforementioned ideas is presented in this section. It is based on the geocoded PS positions and precise orbit data of TerraSAR-X and is capable of combining *adjacent* tracks, i.e., exclusively ascending or descending stacks of data, as well as cross-heading tracks. In the following sections the developed methodology is presented and examples of fusion results are provided. Finally, a decomposition of motion components is applied and the findings are shown for sample areas of the Berlin test site already introduced in Section 4.4.

5.2.1 Methodology

Assuming precise orbit and range information, only the inaccurate knowledge of the heights of the reference points does have major influence on final geocoded PS positions. Indeed, azimuth and range timing errors are limited to the sub-meter domain (Yoon et al., 2009), thanks to the sophisticated radar instrument of TerraSAR-X and highly precise orbit information. As already mentioned, the uncertainty of the reference point will lead to an offset in ground range and height of the whole geocoded PS point cloud of one stack (cf. Section 2.3.2). This offset corresponds to a rotation of each PS with the master scene orbit position as the center of rotation. The unknown rotation angle is related to the unknown height difference between

true and assumed ellipsoidal height of the reference point. However, a simple shift in elevation direction is a sufficient approximation for the necessary rotation, because the range distance is magnitudes larger than the existent offset in elevation. Assuming an incidence angle of 40° and a typical range distance of 670 km, the difference in ground range between a rotation and a shift is only approximately 9 mm, if the vertical shift is set to 60 m. Hence, the transformation of each point cloud can be modeled as a shift in elevation direction. However, if the highest available precision is needed, this difference could be considered easily in the model.
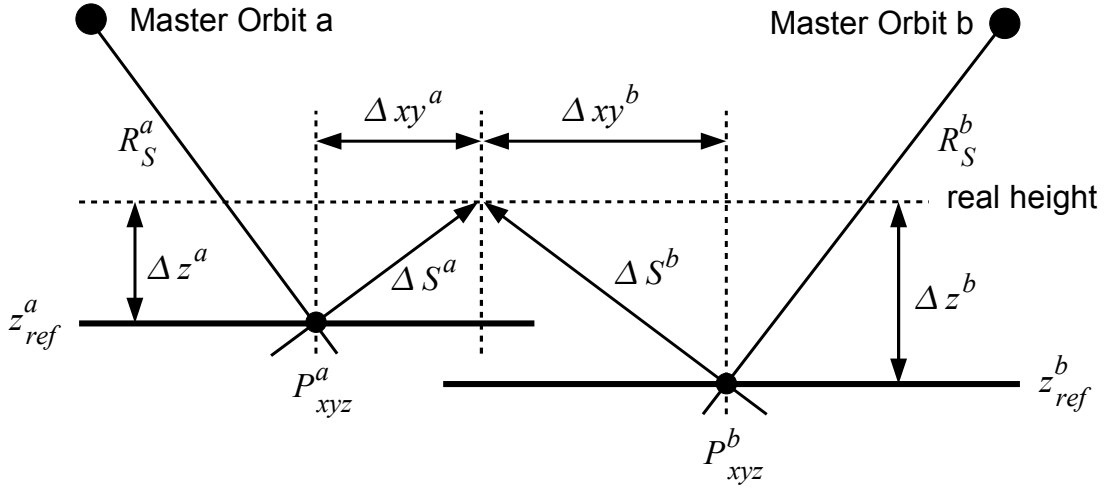
(a) Side view on acquisition geometry of cross-heading tracks. Two identical PS (P_{xyz}^a, P_{xyz}^b) from both point clouds may differ in vertical as well as horizontal positions, indicated by Δz^a, Δz^b and Δxy^a, Δxy^b. These offsets are induced by uncertainties in the height of the reference points z_{ref}^a, z_{ref}^b. A shift by ΔS^a, ΔS^b in elevation directions of the respective points will lead to identical coordinates for both PS in their final absolute positions at the real height. R_S^a, R_S^b indicate range distance between master orbits and PS.
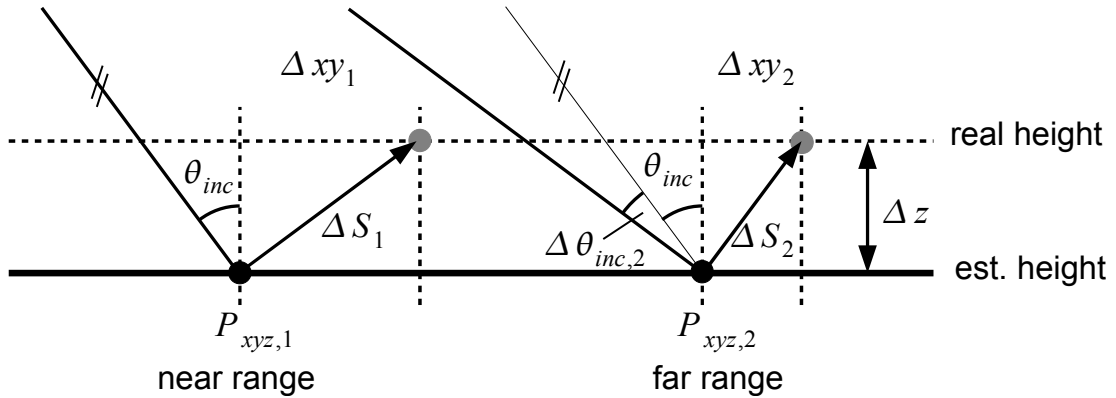
(b) Incidence angles vary between near and far range positions $P_{xyz,1}$ and $P_{xyz,2}$. Therefore, the shifts in elevation directions ΔS_1, ΔS_2 as well as the shifts in horizontal directions Δxy_1, Δxy_2 differ. Consequently, the shift has to be modeled depending on the range coordinate of each PS, implemented by individual shift directions based on the local incidence angle $\theta_{inc} + \Delta \theta_{inc}$. The vertical component of the shift is equal for all points of one stack.

Figure 66. Geometrical configurations that are considered by the mathematical model of the fusion algorithm.

Figure 66a shows the geometrical configuration for a fusion of two cross-heading tracks. Most likely the reference point heights show different offsets Δz^a, Δz^b to the true height. Consequently, the two stacks also hold unequal deviations in horizontal (Δxy^a, Δxy^b) directions compared to the true positions of the PS, due to the mentioned geocoding principle based on precise range information R_S^a, R_S^b. The basic idea of the proposed algorithm consists of a least-squares matching procedure of assumed identical PS. The positions of two corresponding points P_{xyz}^a, P_{xyz}^b of the two stacks have to be shifted in the respective elevation direction by

ΔS^a and ΔS^b in order to be finally located at identical positions. The horizontal shift is a function of the vertical offset Δz and the incidence angle θ_{inc}. In Figure 67a the development of Δxy is pictured assuming four fixed differences in heights of the reference point. Especially for small incidence angles, the horizontal component (in ground range) of the shift in elevation direction is much larger than the vertical component and may exceed 100 m for $\Delta z > 50$ m.

Additionally, the local incidence angle – that depends on the range coordinate of each PS – has to be considered for a precise transformation of PS position. Within one scene the incidence angle increases from near to far range locations (cf. Figure 66b), whereas the difference $\Delta\theta_{inc}$ is about 1° for scene extents of 10 km. The influence of this variation on the difference in horizontal shifts within one scene, depending on the vertical component of the shift, is depicted in Figure 67b. The differences exceed already 1 m for small incidence angles, i.e., steep looking directions, and a vertical offset of approximately 18 m. Therefore, this effect has to be included in the transformation model by individual elevation directions for each PS within one point cloud. In sum, the mathematical model of the fusion can be described by the following equation, with respect to one pair of identical points:

$$\vec{P}^a_{xyz} + \Delta S^a \cdot \vec{s}^a(t^a_{Az}, \theta^a_{inc}) - \vec{P}^b_{xyz} + \Delta S^b \cdot \vec{s}^b(t^b_{Az}, \theta^b_{inc}) = \vec{0} \tag{68}$$

with the respective local incidence angles θ^a_{inc}, θ^b_{inc} and normalized elevation directions $\vec{s}^a$, $\vec{s}^b$ ($|\vec{s}| = 1$). Elevation direction is defined by the heading angle t_{Az} and the incidence angle:

$$\vec{s}(t_{Az}, \theta_{inc}) = \begin{bmatrix} \Delta x \\ \Delta y \\ \Delta z \end{bmatrix} = \begin{bmatrix} \cos t_{Az} \cos\theta_{inc} \\ -\sin t_{Az} \cos\theta_{inc} \\ \sin\theta_{inc} \end{bmatrix} \tag{69}$$
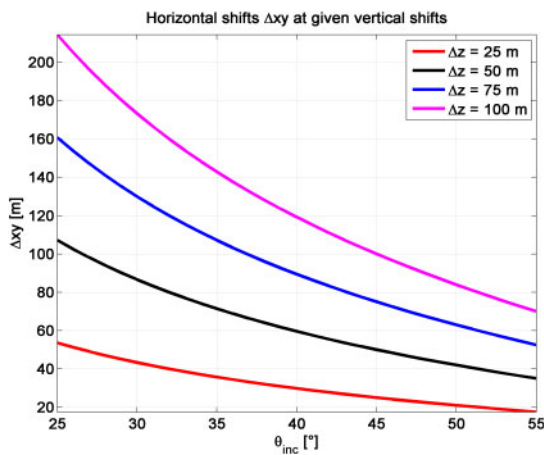
(a) Horizontal shift Δxy at four different fixed vertical offsets Δz, indicated by different colors. Graphs show dependence on incidence angles θ_{inc}.
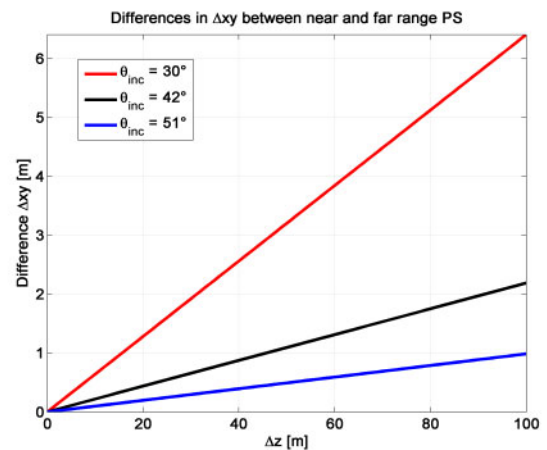
(b) Differences in horizontal shifts within one scene between PS at near and far range locations depending on the vertical offset Δz. Results for three typical stack parameters are given, indicated by different colors of mean incidence angle.

Figure 67. Horizontal shift Δxy in ground range direction depending on vertical offset of reference point, incidence angle and PS position within the scene, i.e., local incidence angle variations.

A successful fusion based on the aforementioned geometrical model can only be achieved, if corresponding pairs of PS are available. This precondition is easily fulfilled using adjacent tracks by reason of similar acquisition geometries, hence, many identical PS should be available. For cross-heading tracks, the requirement is challenging. However, despite the almost opposite viewing directions, the number of assumed identical points turns out to be still sufficient for a successful fusion. E.g., poles (like metallic fence posts), as well as structures on ground and roofs provide PS that can be used for a fusion. Certainly, these close range pairs of PS do not originate from the same physical target, i.e., phase centers are not identical in reality. Consequently, the results of a least-squares matching based on inexact point matches yield a residual bias in the range of some centimeters, depending on the real distance of phase centers. However, this bias is smaller than the localization precision of PS, if the threshold on the distance for the selection of pairs is chosen appropriately low. For the Berlin test site first visual analyses on the sources of scattering of the selected close range points reveal PS positions at poles and other structures of limited extent. Hence, the distance between phase centers should be very small (about 10-20 cm) and the final precision of PS positions is mainly limited by the accuracy of elevation estimates (cf. Section 5.1.2). In addition, a least-squares matching based on inexact point matches can still be carried out successfully, if these selections of points allow for an unbiased estimation of the mean shift.

The entire algorithm can be summarized as follows (cf. Figure 68); at first, the assumed best PS are selected from individual PSI processing results of each stack after the geocoding procedure. The selection is accomplished by a threshold on the variance of the estimated DEM refinements. This pre-selection is necessary in order to avoid a matching of "noisy" PS positions that only fit by chance and consequently would distort the fusion result. Subsequently, facade PS have to be excluded for a fusion of cross-heading tracks, because different facades are visible by the two acquisition configurations. In a next step, corresponding points, i.e., assumed identical PS, are determined prior to a least-squares adjustment. The latter will provide the unknown height offsets for each stack based on the presented mathematical model, minimizing distances between all selected pairs of PS. Finally, the two point clouds can be shifted in the respective elevation direction using the findings of the LSA and the final absolute positions of all PS are obtained. In the following sections, a detailed description of all steps is provided.
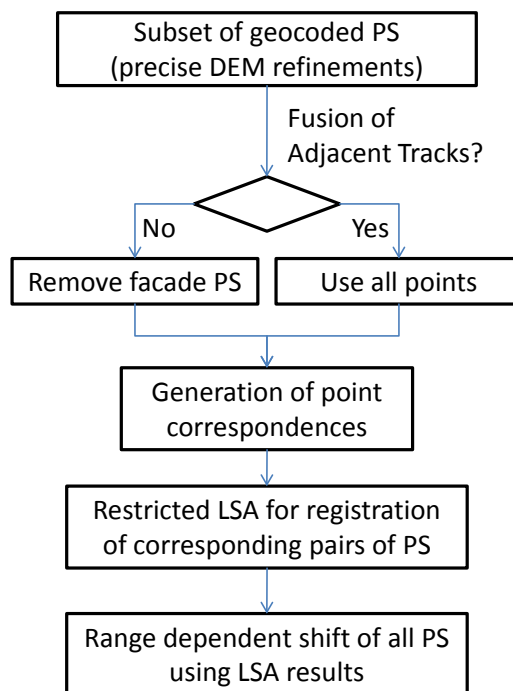
Figure 68. Flowchart of the proposed fusion algorithm.
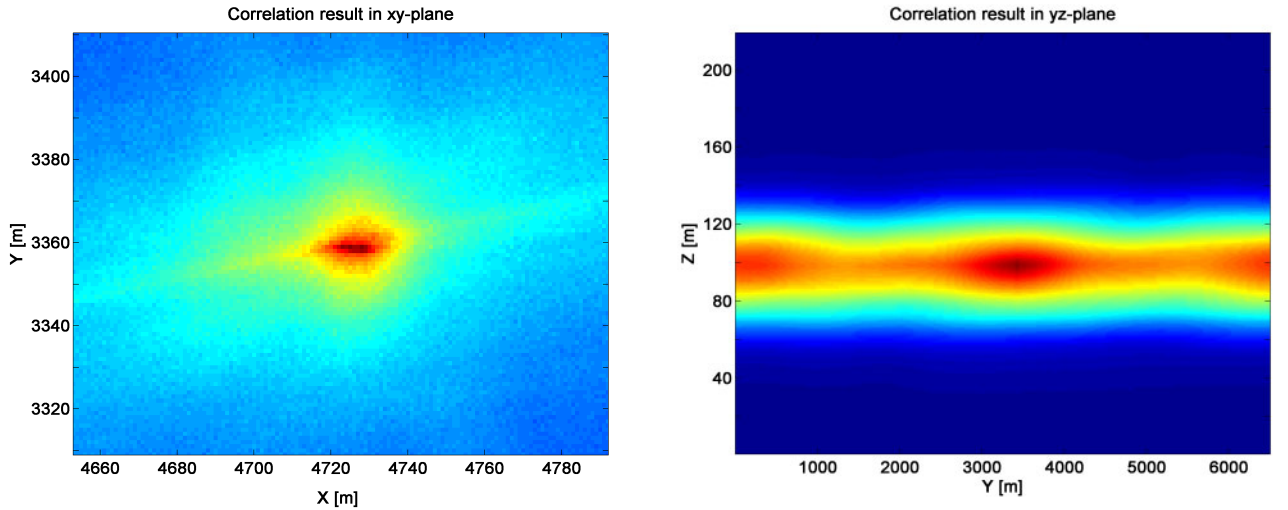
(a) Cross-correlation result of binary images of PS positions projected to the xy-plane. The maximum in the correlation matrix is quite distinctive.

(b) Cross-correlation result of binary images of PS positions projected to the yz-plane. The maximum cannot be determined very precisely in horizontal direction. Nevertheless, a maximum in vertical direction is available using both results of skyline correlations.

Figure 69. 2D Cross-correlation results of binary images created from PS positions projected to the xy- and yz-plane. Highest correlation (i.e., best fit) indicated by red color.

5.2.2 Creation of Point Correspondences

The determination of corresponding pairs of PS is one of the two major parts of the proposed fusion algorithm. It is composed of two steps and makes use of the geometrical distribution of PS. After the initial removal of PS showing larger standard deviations in estimated DEM refinements, the points originating from facades are removed for a fusion of cross-heading tracks. The filtering is accomplished by a threshold on the variance of vertical coordinates of the PS within a certain patch, like described in Section 5.1.2. This preprocessing step is necessary, because the subsequent search for corresponding PS relies on a cross-correlation of binary images created from a projection of the PS on a regular grid in the xy-, xz- and yz-plane. Therefore, these PS would distort the cross-correlation results especially for binary images of the xy-plane. The reason is quite simple; in this case the maximum of the correlation is obtained, if the lines generated by PS of opposing facades are overlaid due to the large amount of these structures in PS point clouds. The parallel alignment of many facades and the high point density on vertical walls are the main reasons for this bias, if these PS are included. This problem does not appear using adjacent tracks, because no opposing facades are present.

In principle, the idea of determining identical PS is based on the geometrical distribution of PS. A top view on a geocoded PS point cloud reveals the structure of the city independent on the track type. Hence, this feature can be used for an initial matching procedure of one stack relative to a second one. To this end, binary images are created by a projection of the initial geocoded PS positions to horizontal and vertical planes using a grid size of 1 m (a pixel size that turned out to be suitable for both test sites). A cross-correlation of the former hold an initial relative shift between the point clouds in horizontal directions. The maximum of the correlation result can be detected very precisely, as can be seen in Figure 69a; the peak is quite distinctive and locally limited. The correlation of the side views (or skylines), i.e., xz- and yz-projections, do not provide such precise results (cf. Figure 69b). Certainly, a matching of the whole skyline projected to a plane is more inaccurate if only few high rise buildings are present, besides the different point distribution for cross-heading tracks. Nevertheless, only the vertical offset is of interest within these results. A maximum can still be detected and the results of both correlations (xz- and yz-plane projections) are averaged in order to strengthen the solution.

(a) Top view on geocoded PS positions (UTM coordinate system) previous to cross-correlation.

(b) Top view on geocoded PS positions (UTM coordinate system) after cross-correlation of binary images.
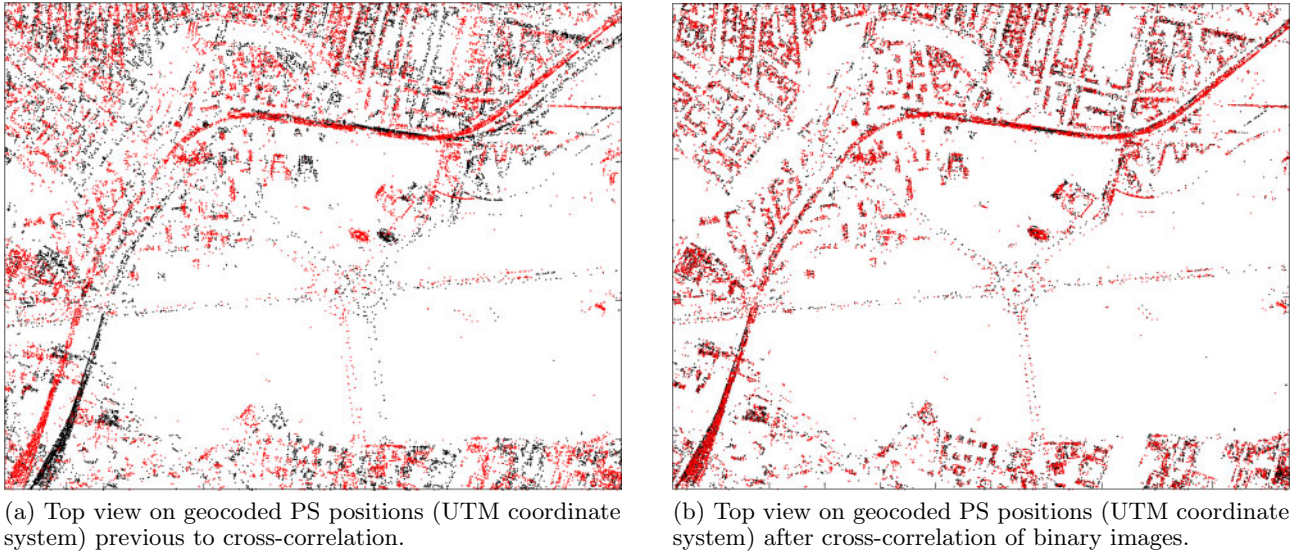
Figure 70. By reason of large vertical offsets the two stacks (one indicated in black, the other in red) show large horizontal separation (left). Point clouds shifted by results of refined cross-correlation show a good fit between both stacks (right). Therefore, corresponding close range pairs can be selected.

The results of the cross-correlation are used to apply a relative shift of one point cloud to the other one. Subsequently, the relative shift between both point clouds is refined, prior to the selection of corresponding pairs of PS. The refinement is accomplished by a statistical search of the best fit between both 3D point clouds. This criterion is assumed to be met, if a large number of close range point pairs is available. To this end, for each PS of one stack all neighboring PS within the other stack are selected. The maximum search radius is set to 2.5 times the diagonal distance of the voxel, defined by the respective pixel dimensions used for creating binary images. Therefore, a bias of the initial shift due to the rasterization and cross-correlation steps is accounted for. Subsequently, the refinement of the shift (i.e., the maximum number of close range pairs) is obtained making use of a random sample consensus (RANSAC) approach (Fischler and Bolles, 1981).

The basic principle of this algorithm is the random selection of a minimum number of samples from the available sample pool to define one specification of a predefined general model. Then, the numbers of inliers from the remaining samples are calculated based on a threshold that has to be fixed in advance. These two steps are repeated many times until a desired maximum number of inliers is found. The choice of samples that show the maximum number of inliers defines the model that fits best. Applied to the problem at hand, the model is defined by one candidate pair, i.e., the shift between these two points in 3D space. Consequently, one random pair is selected within each iteration and the differences in coordinates are used to shift one point cloud relative to the other, i.e., the distance of the selected two PS is achieved to be zero. Afterwards, the distances of all other pairs are calculated and the number of inliers is determined by a threshold on the residuals in coordinate differences of each pair. Suitable thresholds are given by the standard deviations of the PS positions (cf. Section 5.1.1), or may be chosen even more restrictive. The procedure is repeated until the desired maximum number of inliers is obtained. In the current implementation the code of Peter Kovesi is used, freely available online (see Kovesi (2006) for details).

Horizontal differences between the two point clouds previous and after the refined shift are pictured in Figure 70. The large initial offset in horizontal directions is caused by the choice of horizontal planes below mean surface height during PSI processing. Consequently, the vertical offsets will be several tens of meters. Additionally, the positions of appropriate points of close range pairs are shown in Figure 71 for the Munich test site, including two zooms to highlighted areas. The locations are homogeneously distributed, only holding some higher densities along

(a) Overview (top view) on locations of the selected close range pairs in the Munich test site.

(b) Zoom to area 1 highlighted in Figure 71a.
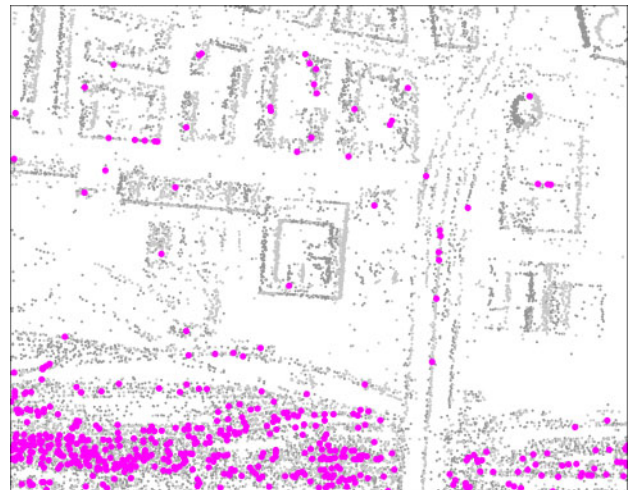
(c) Zoom to area 2 highlighted in Figure 71a.

Figure 71. Locations of the selected close range pairs (purple dots) in the Munich test site available for the subsequent least-squares matching procedure. The selected PS are almost uniformly distributed all over the scene, showing only higher densities along rail tracks. All remaining PS from both stacks are indicated by small gray dots. Below, two zooms to the highlighted areas (black rectangles) are provided, showing details on the locations of the selected pairs. The remaining residual distances between each pair are too small to be visible in these plots.

rail tracks. Approximate numbers for close range pairs are 10,000 for cross-heading and 100,000 for adjacent tracks for both test sites. Hence, a sufficient number of pairs is available, whereas a further reduction based on the distance of the corresponding pairs may be applied. In the cases at hand, 1,000 pairs are selected for the LSA, selected by the smallest distances.

Finally, the estimated refined relative shift is applied to the PS of one point cloud and the nearest neighbor for each PS of one point cloud is determined in the second point cloud. These correspondences are reduced to single ones, i.e., each PS can be related only to one point in the respective other point cloud. In addition, the number of pairs may be reduced based on a more restrictive threshold on the distance between the corresponding PS, if desired. The final selection of pairs is used in the subsequent second major part of the fusion algorithm for the determination of the unknown height offsets of the two point clouds with respect to their final absolute positions, applying a least-squares adjustment.

5.2.3   Least Squares Adjustment

As soon as appropriate pairs of corresponding PS are available from both point clouds, the LSA based on equation 68 can be applied, yielding two estimations of the vertical offsets between initial used reference point heights and real absolute heights of each stack. Assuming identical points, the mathematical model as a function of the observations y and unknowns u is defined by the following equation:

$$f(y,u) = \vec{P}^a_{xyz,n} + \Delta S^a_n \cdot \begin{bmatrix} \cos t^a_{Az} \cos \theta^a_{inc,n} \\ -\sin t^a_{Az} \cos \theta^a_{inc,n} \\ \sin \theta^a_{inc,n} \end{bmatrix} - \vec{P}^b_{xyz,n} + \Delta S^b_n \cdot \begin{bmatrix} \cos t^b_{Az} \cos \theta^b_{inc,n} \\ -\sin t^b_{Az} \cos \theta^b_{inc,n} \\ \sin \theta^b_{inc,n} \end{bmatrix} = \vec{0} \quad (70)$$

The shift in elevation direction ΔS is a function of the local incidence angle $\theta_{inc,n}$ and the unknown vertical offset Δz:

$$\Delta S_n = \frac{\Delta z}{\sin(\theta_{inc,n})} \tag{71}$$

In addition, the local incidence angles are divided into a large constant fraction and an increment, that depends on the position of the PS in range direction:

$$\theta_{inc,n} = \theta_{inc} + \Delta \theta_{inc,n} \tag{72}$$

The advantage of this split-up is the reduction of computational costs of the LSA, if the incremental fractions are treated as constant values that are assumed to be precisely derivable from the differences in range coordinates. Hence, they are introduced as fixed values during the adjustment and no corrections have to be calculated during the LSA. Only one large fraction (per stack) is treated as observation value that is included in the process of least-squares adjustment. A straightforward choice is the usage of near range incidence angles that are available from precise orbit information.

Equation 70 is fulfilled after the least-squares adjustment of the involved observations, which namely are: The initial geocoded PS coordinates of $\vec{P}_{xyz}$, the heading angles t_{Az} and near range incidence angles θ_{inc}. The unknowns to be determined are the two vertical offsets Δz, i.e., one constant offset for all PS within each stack. Three linearly independent equations can be set up for every corresponding pair (based on equation 70), whereas hats indicate adjusted observations and unknowns:

$$\hat{x}^a_n + \frac{\Delta \hat{z}^a}{\tan(\hat{\theta}^a_{inc} + \Delta \theta^a_{inc,n})} \cdot \cos(\hat{t}^a_{Az}) - \hat{x}^b_n - \frac{\Delta \hat{z}^b}{\tan(\hat{\theta}^b_{inc} + \Delta \theta^b_{inc,n})} \cdot \cos(\hat{t}^b_{Az}) = 0 \tag{73}$$

$$\hat{y}^a_n - \frac{\Delta \hat{z}^a}{\tan(\hat{\theta}^a_{inc} + \Delta \theta^a_{inc,n})} \cdot \sin(\hat{t}^a_{Az}) - \hat{y}^b_n + \frac{\Delta \hat{z}^b}{\tan(\hat{\theta}^b_{inc} + \Delta \theta^b_{inc,n})} \cdot \sin(\hat{t}^b_{Az}) = 0 \tag{74}$$

$$\hat{z}^a_n + \Delta \hat{z}^a - \hat{z}^b_n - \Delta \hat{z}^b = 0 \tag{75}$$

Hence, the mathematical model is a function of two parameters: the adjustments on the observations and the unknowns.

$$f(\hat{y}, \hat{u}) = f(y + \hat{v}, \hat{u}) = \psi(\hat{v}, \hat{u}) = 0 \tag{76}$$

In principle, one pair of points would be sufficient for an exact solution. However, a high redundancy obtained from a large number of observations allows for a more robust and more precise result. Especially uncertainties in PS positions as well as the inclusion of possibly inexact point matches request for an adjustment that minimizes the residual errors of mis-matches in a least-squares sense. In Geodesy, a least-squares problem like given by equation 70 is called *Gauß-Helmert* model, because the observations cannot be separated from the unknowns, i.e., the former cannot be written as a function of the latter (Mikhail and Ackermann, 1983; Niemeier, 2002). The solution is calculated iteratively after a linearization of the mathematical model based on a Gauß-Newton iteration scheme, that corresponds to a strict solution of the Gauß-Helmert model (Neitzel and Petrovic, 2008). The linearized equations of conditions are given by a first order Taylor expansion:

$$\psi(\hat{v}, \hat{u}) = \psi(v^0, u^0) + \frac{\partial \psi(v^0, u^0)}{\partial v^0} \cdot (\hat{v} - v^0) + \frac{\partial \psi(v^0, u^0)}{\partial u^0} \cdot (\hat{u} - u^0) = 0 \tag{77}$$

with approximation values v^0 and u^0. In short notation it can be written like follows, using the design matrices A and B that contain the respective partial derivatives:

$$B(\hat{v} - v^0) + A(\hat{u} - u^0) + \psi(v^0, u^0) = B\hat{v} + A\Delta\hat{u} + w = 0 \tag{78}$$

with w called the vector of discrepancy:

$$w = \psi(v^0, u^0) - Bv^0 \tag{79}$$

The estimation principle of a LSA is the minimization of the weighted squared sum of refinements $\hat{v}$, using the weight matrix of the observations P:

$$\sum \hat{v}^T P \hat{v} \rightarrow \min. \tag{80}$$

As a final solution equations 78 and 80 must be fulfilled after the LSA. This corresponds to a minimization of the following objective function (Niemeier, 2002):

$$\Omega = \hat{v}^T P \hat{v} + 2k^T (B\hat{v} + A\Delta\hat{u} + w) \tag{81}$$

Equation 81 contains the correlates k, which correspond to the Lagrange multipliers necessary for solving a minimization problem with constraints. The adjusted refinements of the observations as well as the increments on the unknowns with respect to the approximation values are calculated by (Niemeier, 2002):

$$\Delta\hat{u} = -(A^T (BQB^T)^{-1} A)^{-1} A^T (BQB^T)^{-1} w \tag{82}$$

$$k = -(BQB^T)^{-1} (A\Delta\hat{u}) + w \tag{83}$$

$$\hat{v} = QB^T k \tag{84}$$

The linearization by means of a Taylor expansion requires an iterative calculation of the final solution, using the results of each loop $u^0 + \Delta\hat{u}$ and $\hat{v}$ as approximation values u^0 and v^0 for the next iteration. The method of least-squares at hand allows for an introduction of weights for the observations within the matrix $Q = P^{-1}$. Reasonable values can be obtained, e.g., from the standard deviations of the coordinates of the PS, the heading angle and near range incidence angle for each stack. To this end, the standard deviations of the PS positions in range, azimuth and elevation are propagated to the UTM coordinate system, based on the theoretical

precisions of PS within the RXS coordinate system (cf. Section 5.1.1). The standard deviations of heading and incidence angles are obtained from an approximation based on orbit accuracies and typical range distances. All observations are assumed uncorrelated, hence, Q is of diagonal structure. However, the heading angles of the orbits have to be adapted for a usage in the UTM coordinate system, because these observation values are initially provided in the WGS84 system. Consequently, the map projection to the respective UTM zone also has to be applied to the heading direction. The discrepancy of the angles between the two coordinate systems is about $1.2°$ to $1.3°$ for Berlin and $1.8°$ to $2.0°$ for Munich.

The adjusted values of the unknowns ($\Delta \hat{z}^a$, $\Delta \hat{z}^b$) are finally used to shift all PS of each point cloud by its respective elevation direction to the final absolute positions. Figure 72 shows the results after a successful fusion of one ascending and one descending stack. The corrected PS positions now allow for a comparison of the point clouds to a DSM of the area in order to analyze the precision of the results. Further details on fusion results as well as the findings of the precision analysis are provided in the next section.
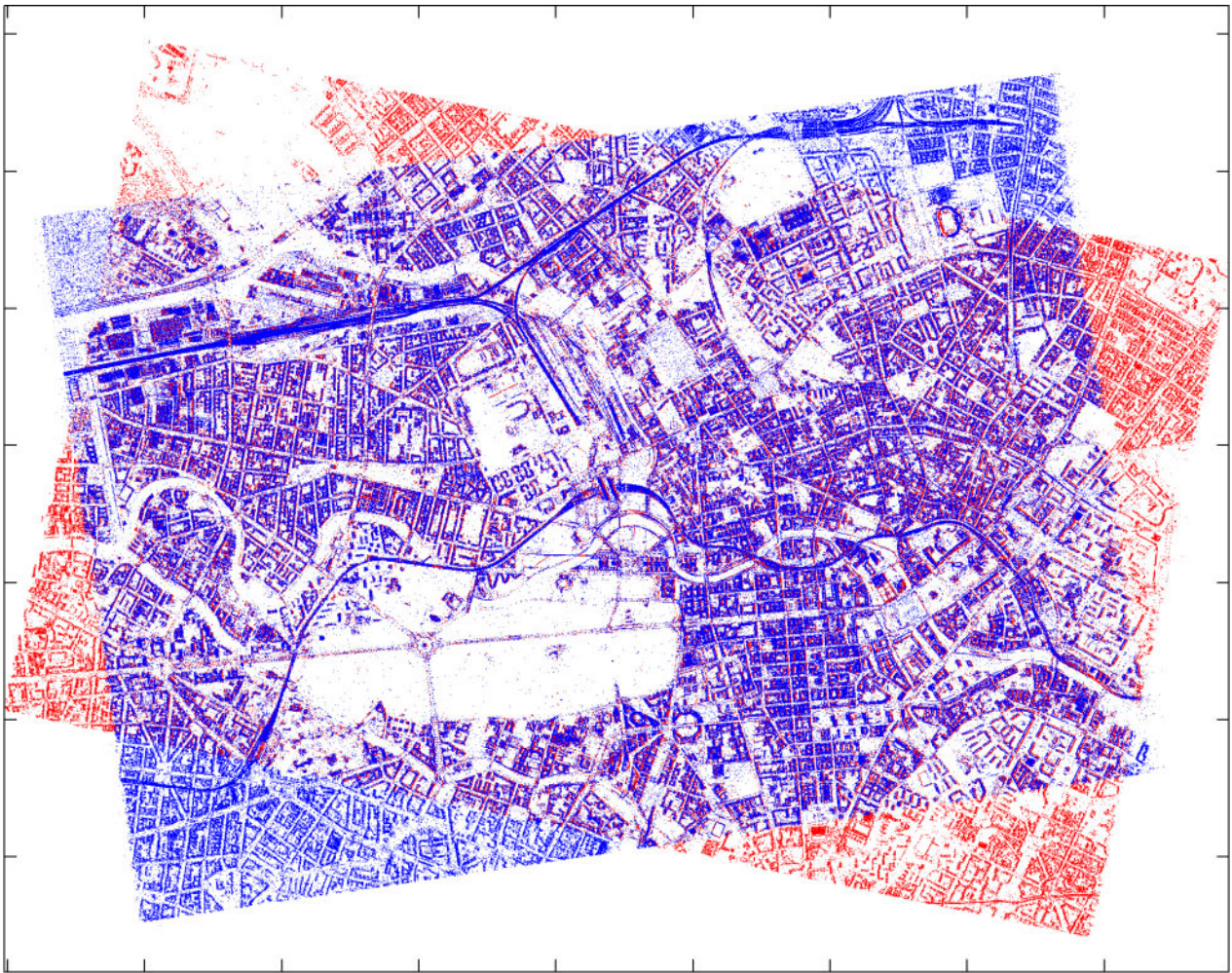
Figure 72. Fusion result of cross-heading tracks of the Berlin test site. PS of ascending track indicated in blue. PS of descending track plotted in red.

5.2.4 Results and Accuracies

The proposed fusion algorithm is suitable for a combination of adjacent as well as cross-heading tracks. After the fusion, the point cloud yields detailed object information, especially if ascending and descending tracks are merged, due to the availability of PS on almost any facade of buildings. The top views on both test sites now show the city structure with completed facade information (cf. Figures 73 and 74). Many details of buildings are available now thanks to the high resolution of the underlying SAR data and the high density of PS. In Table 11 the results are summarized. The estimated vertical offsets are between 40 m and 57 m due to the initial choice of the reference surface. Consequently, the shifts in eastern directions are quite large by reason of the acquisition geometry. The sample shifts in Table 11, indicated by Δx_1 and Δy_1, cannot be compared between the fusion results of cross-heading and adjacent track directions, because the shifts correspond to different points. Certainly, the fusion results deviate in estimates of vertical offsets for equal stacks, if cross-heading track results are compared to a fusion of adjacent tracks. The differences originate from the disparity of corresponding pairs by reason of the underlying acquisition geometries, as already mentioned. However, the differences are below 2 m and if accuracies of elevation estimates are considered, the results satisfy expectations. The adjustments on the heading angles are very small, the ones of the incidence angles can be considered negligible.

Test site	Berlin	Berlin	Munich	Munich
Fusion of	D36 / A42	A42 / A51	A23 / D25	D25 / D39
Δz [m]	39.73 / 44.68	46.80 / 44.99	52.23 / 53.60	52.48 / 57.84
Δx_1 [m]	-53.48 / 49.35	51.82 / 36.24	121.57 / -111.70	-110.28 / -69.93
Δy_1 [m]	11.30 / 7.13	7.78 / 4.12	29.80 / 19.40	18.83 / 9.85
$\hat{t}_{Az} - t_{Az}$[°]	0.12 / 0.11	0.21 / 0.15	0.31 / -0.18	0.23 / 0.15
$\hat{\theta}_{inc} - \theta_{inc}$[°]	$-2.5e^{-4}$ / $2.7e^{-4}$	$2.4e^{-4}$ / $-2.4e^{-4}$	$1.1e^{-3}$ / $-8e^{-4}$	$2.2e^{-5}$ / $-9e^{-6}$

Table 11. Results of fusion for both test sites including one fusion of cross-heading tracks and one fusion of adjacent tracks. Besides the estimated vertical offset Δz, an example of horizontal components of the shift Δx_1, Δy_1 for one arbitrary chosen PS is provided. In addition, the difference between adjusted and initial heading angles as well as incidence angles are listed.

The availability of reference data (point clouds obtained by airborne laserscanning) allows for a comparison of the fit of PS on a DSM of the area. Figures 75 and 76 show two different views on the DSM and the overlaid fused PS point clouds. The PS are colorcoded by their heights, whereas the DSM is plotted in gray for better visualization purposes. From the images, the good fit of the PS after the fusion to the reference surface can be seen. Consequently, the nature of the PS may now be investigated in more detail, as the points are finally located at the assumed absolute positions. Therefore, the uncertainties of the heights of the reference points are solved successfully by the fusion algorithm. After the fusion of cross-heading tracks, PS of further stacks can be added. This is accomplished simply by fixing the available relative height estimation of one point cloud during the fusion algorithm, i.e., the number of unknowns is reduced to one height offset for the point cloud to be added. Another possibility may be the extension of the algorithm to include pairs of additional stacks. However, this procedure increases the size of the matrices and a solution will become very memory-consuming, besides increased computational costs. Therefore, the fixing of the obtained results of a fusion based on one ascending and one descending stack is applied in order to fuse all available datasets of each test site.
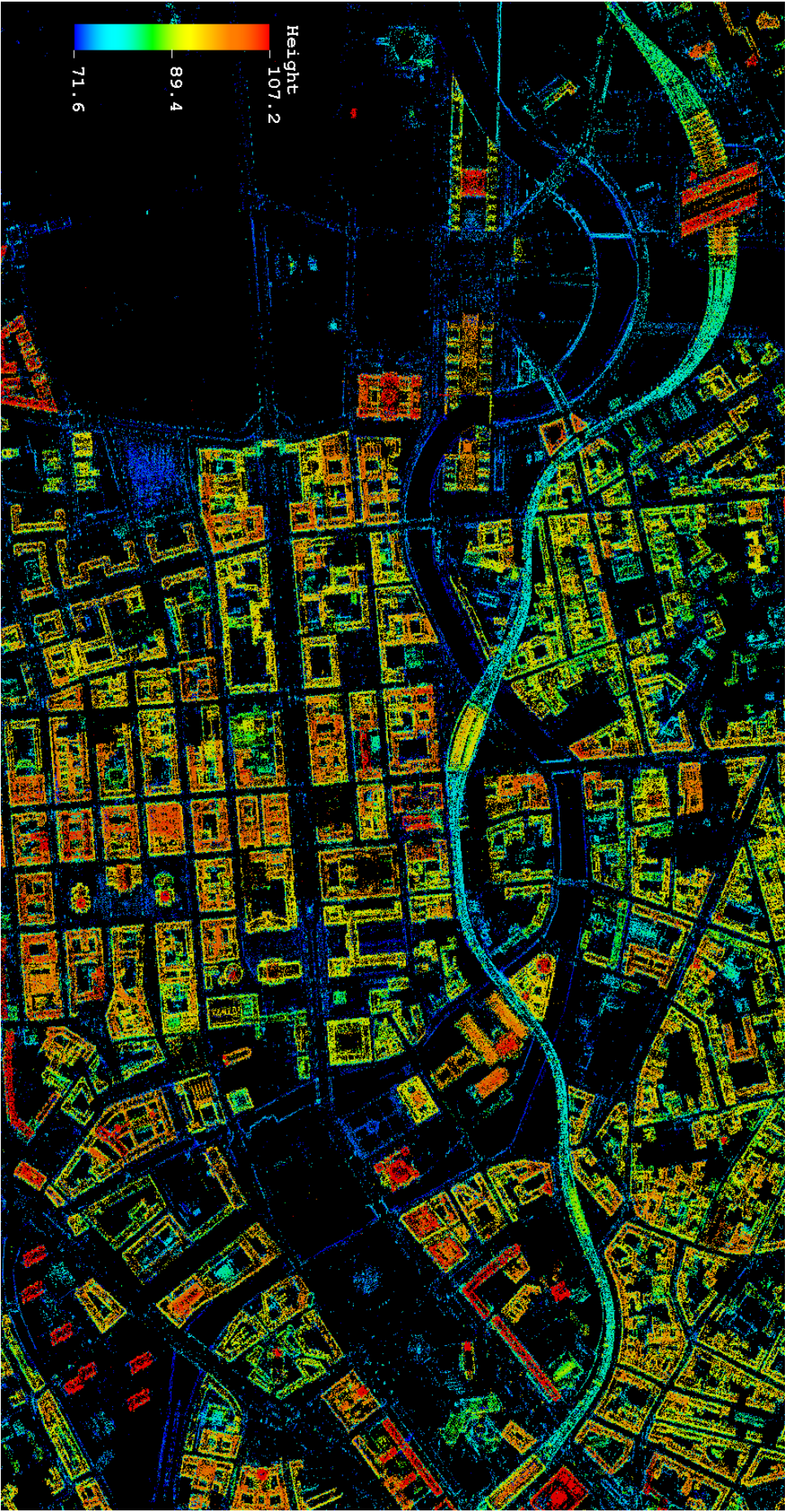
Figure 73: Top view on PS point cloud generated from fusion of 5 stacks of Berlin test site. PS are colorcoded by their height between approximately 72 m and 107 m. The outline of buildings is completed by the combination of ascending and descending stacks. The 3D information from the point cloud on the structure of the city becomes apparent. In addition deformations estimates are available for each single PS.
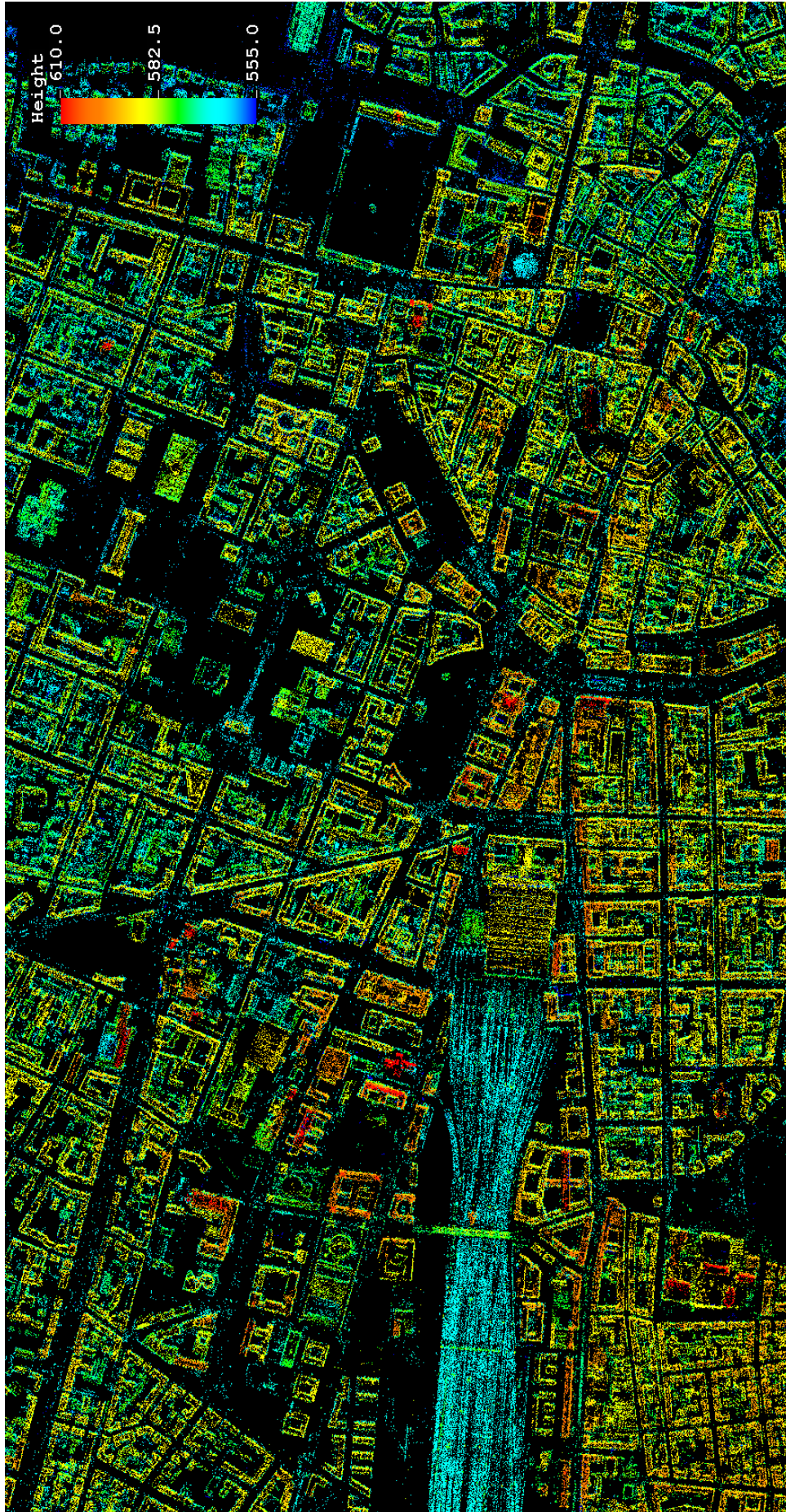
Figure 74: Top view on PS point cloud generated from fusion of 3 stacks of Munich test site. PS are colorcoded by their height between approximately 555 m and 610 m. The outline of buildings is completed by the combination of ascending and descending stacks. The 3D information from the point cloud on the structure of the city becomes apparent. In addition deformations estimates are available for each single PS.
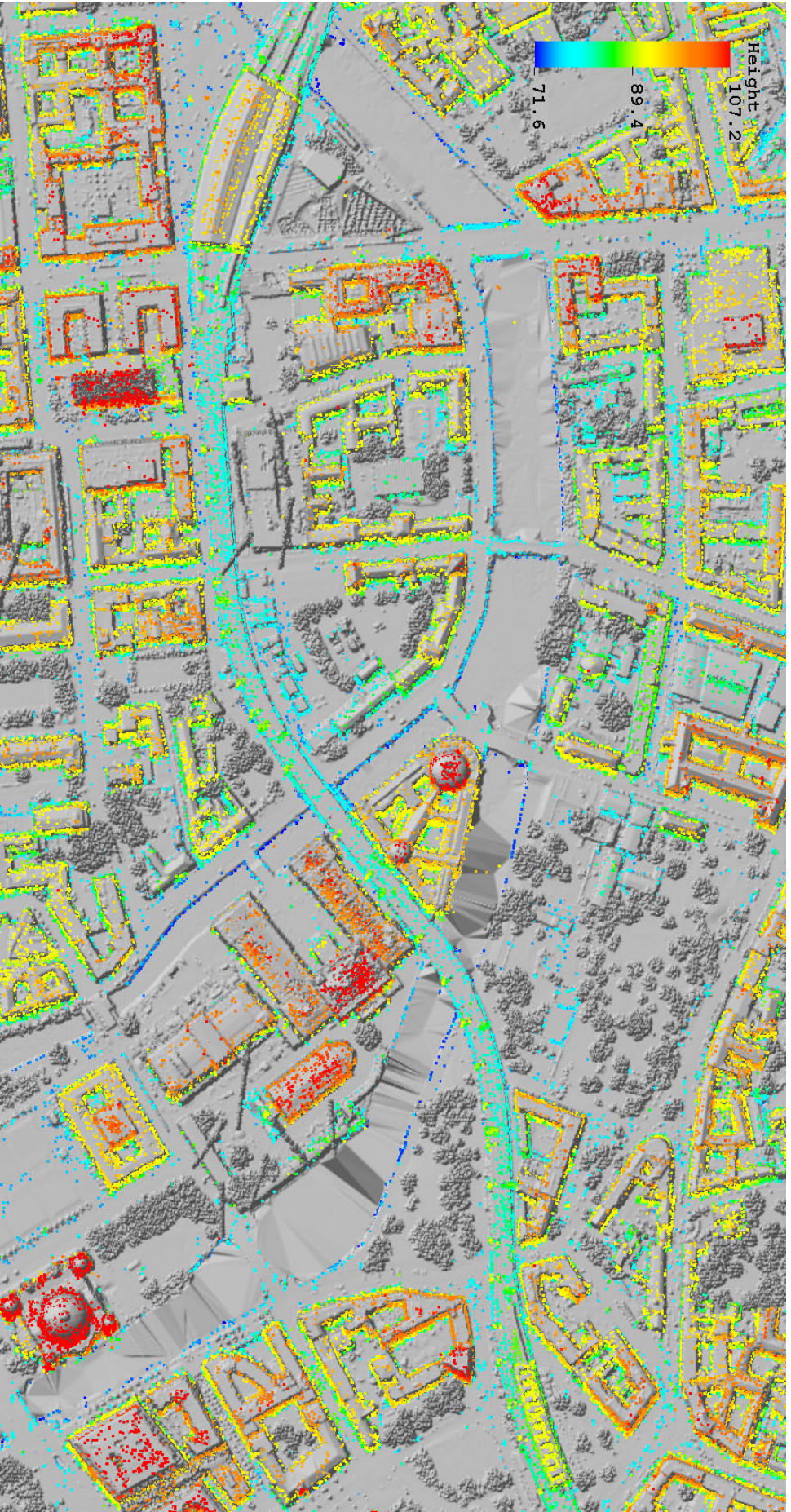
Figure 75: Top view on PS point cloud generated from fusion of 5 stacks of Berlin test site. In addition, a DSM of the area is included in the background. PS are colorcoded by their height between approximately 72 m and 107 m. Visually, the fused PS point clouds already fit the reference surface (DSM) quite well. Hence, absolute positions could be estimated successfully.

Figure 76: Side view on 3D PS point cloud generated from fusion of 5 stacks of Berlin test site. In addition, a DSM of the area is included in the background. PS are colorcoded by their height between approximately 72 m and 107 m. The majority of buildings show a large number of PS on all facades. Some PS are hidden by the inaccuracies of the DSM, because the walls are not represented by vertical planes, but are slightly tilted towards the sides of the roofs.

Certainly, there may occur residual offsets between PS and the reference surface by reason of, e.g., errors in absolute range distances used to geocode the PS or errors in the heading angle of the satellite. In addition, the integration of estimation results with respect to the reference point shows significant impact on the final PS positions after the fusion. Visual inspections of the fit of PS to the DSM at the border of the scene show an increased offset of facades in comparison to positions near the reference point. This effect can be explained by the error propagation effect, as variances of the estimated absolute position in elevation rise for points at increasing distance to the reference point.

The deviations can be approved by a comparison of single facades. To this end, the distribution of PS and laser measurements are investigated (cf. Figure 77). Vertical planes are extracted from the PS point cloud and the reference data and the orientation is corrected to a parallel alignment of both (with respect to the respective balance point) in order to extract the distance between the two planes. Preliminary results yield a mean distance of about 0.64 m for several facades near the reference point and about 1.64 m for locations at the border of the scene. At the current state of the analysis, there seem to be no significant differences with respect to the goodness of fit to the reference data between results obtained from a fusion of adjacent tracks or cross-heading tracks. A comparison of relative accuracies between the point clouds of two fused adjacent tracks fits expectations; the median differences in the range-azimuth-elevation coordinate system correspond to accuracies derived from a relative precision assessment presented in Section 5.1.2. In the UTM system, the deviations are, e.g., below 0.90 m in each direction for the fusion results of stacks D36 and A42 of the Berlin test site.

One major advantage of the fusion of different stacks is the availability of 3D object information provided by the distribution of points in 3D space. In addition, deformation estimates are available for each PS. Hence, a monitoring of single buildings is feasible by evaluating the amplitudes of linear and seasonal motion estimated by PSI. However, the motion parameters are available in LOS and an interpretation is still necessary in order to derive components in vertical as well as horizontal directions. Therefore, the second major advantage of fusing multiple stack results is exploited; after the fusion, an estimation of motion components can be carried out by a reconstruction of the deformation vector from LOS motion estimations of different stacks. The algorithm and results are provided in the next section.

5.2.5 Separation of Motion Vector Components

After a fusion of cross heading tracks there exist most likely several locations including PS from both stacks, i.e., LOS motion vector components are available from different viewing directions. Consequently, the original 3D motion vector may be reconstructed, if the observed signals originate from the same deformation phenomena, as the estimated amplitudes of motion α are a projection of the 3D displacement vector $\vec{\alpha}_{3D}$ to LOS direction:

$$\alpha = \vec{e}_{LOS} \cdot \vec{\alpha}_{3D} \tag{85}$$

with the unity vector of LOS $\vec{e}_{LOS}$ given by:

$$\vec{e}_{LOS} = \begin{bmatrix} \cos(t_{Az}) \cdot \sin(\theta_{inc}) \\ -\sin(t_{Az}) \cdot \sin(\theta_{inc}) \\ -\cos(\theta_{inc}) \end{bmatrix} \tag{86}$$

However, the reconstruction is limited to components in direction of west-east (x-axis) and the vertical (z-axis), because the sensitivity in the direction south-north is too low. The reason for the latter is the orbit configuration of TerraSAR-X that results in a flight direction close to
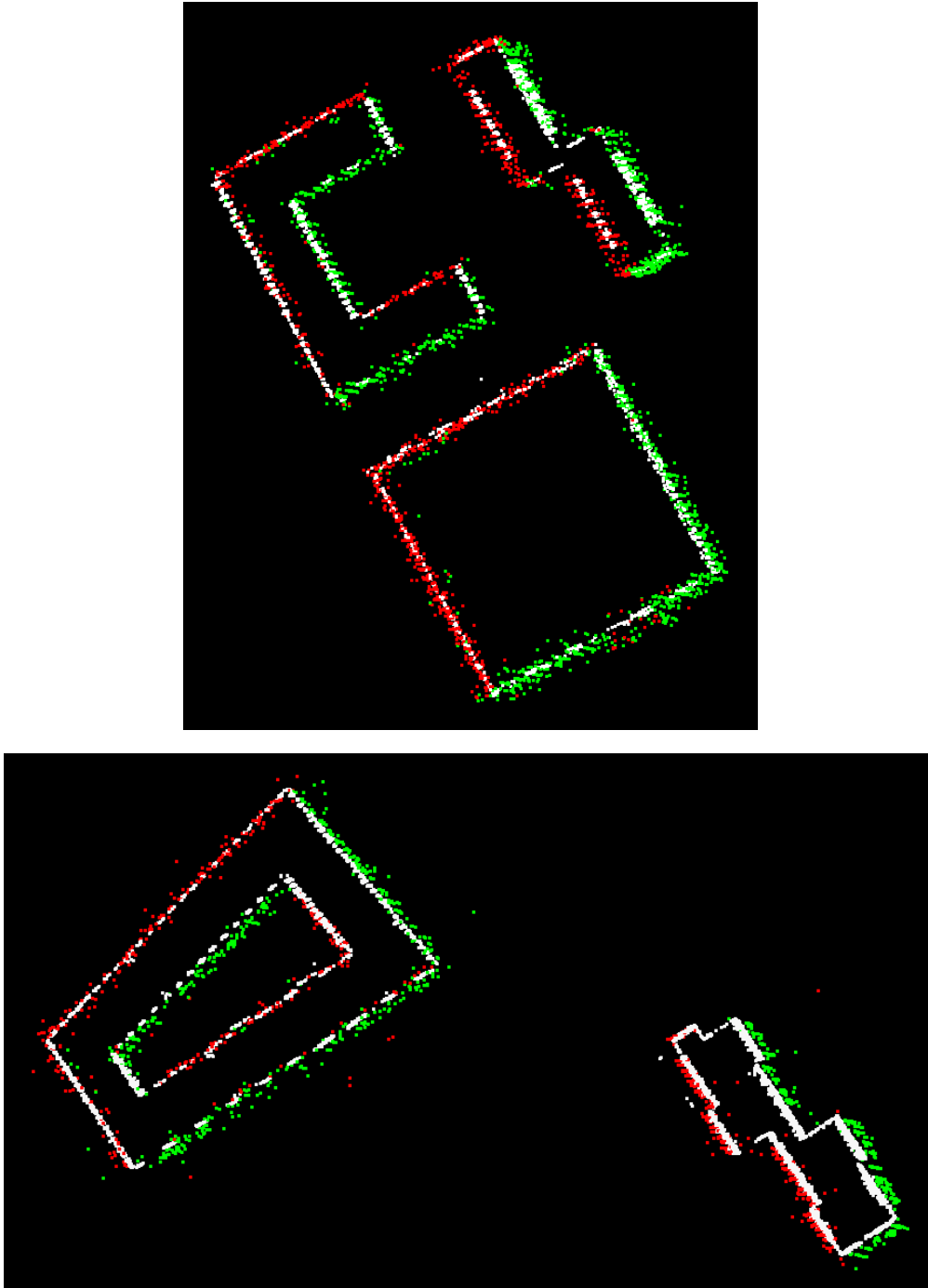
Figure 77. Top view on PS positions after fusion of ascending stack A42 (red dots) and descending stack D36 (green dots). The white dots represent the reference data of the LIDAR point cloud. All data is clipped to the parts corresponding to facades of the buildings. Two examples of different location of Berlin test site are given. The deviations of a mean plane obtained from the PS and one calculated from the reference LIDAR point cloud are investigated.

the parallel of the y-axis (south-north) for ascending as well as descending tracks. Hence, the functional model is restricted to the two mentioned components and the unity LOS vector has to be adapted by a restriction to components in the xz-plane including normalization to length one:

$$\vec{e}_{LOS} = \begin{bmatrix} \cos(t_{Az}) \cdot \sin(\theta_{inc}) \\ -\cos(\theta_{inc}) \end{bmatrix} \cdot \frac{1}{\sqrt{\cos^2(t_{Az}) \cdot \sin^2(\theta_{inc}) + \cos^2(\theta_{inc})}} \tag{87}$$

The fractions of estimated LOS deformation originating from motion in direction of the y-axis are assumed negligible. The mathematical model for a least-squares solution based on equation 85 can be formulated as follows:

$$\cos(t_{Az}) \cdot \sin(\theta_{inc}) \cdot \alpha_x - \cos(\theta_{inc}) \cdot \alpha_z - \alpha \cdot \sqrt{\cos^2(t_{Az}) \cdot \sin^2(\theta_{inc}) + \cos^2(\theta_{inc})} = 0 \qquad (88)$$

The unknowns to be determined are the components of displacement α_x and α_z, whereas the observations are given by the estimated amplitudes of deformation α obtained by PSI. For the determination of the unknowns at least two observations of different viewing directions are needed. The inclusion of several points leads to redundancy that allows for a solution in a (least-squares) adjustment. Therefore, the equation system at hand is solved in the exact same manner as the LSA presented in Section 5.2.3, because the equation system represents again a Gauß-Helmert model. Besides the unknown parameters, the respective accuracies are obtained from the adjustment, that show the precision of the estimated motion components.

For the test sites at hand, the following approach is used; for Berlin the fusion result of 2 ascending and 2 descending stacks is used, whereas for Munich the observations are obtained from a fusion of two cross-heading tracks only. For each PS within the fused point clouds the two motion components are estimated as mentioned above. To this end, all PS within a volume of 5 m by 5 m by 5 m around the point of interest are included, whereas each observation – the estimated amplitude of displacement – is weighted additionally by its distance to the central point besides the available variance information of PSI. This approach will limit the influence of the observations at larger distances that could bias the result. For each PS the respective LOS vector is used, given by the acquisition geometry and the range position of the point. The preceding fusion of stacks provides the variances of the angles t_{Az} and θ_{inc}, therefore, these angles are treated as observations in the adjustment model.

The results are depicted in Figures 78 to 87, whereas all estimated motion components showing an estimated standard deviation of larger than 1 mm (for periodic motion) or 1 mm/y (for linear motion) are discarded. However, the large majority of estimates show a standard deviation of approximately 0.25 mm and 0.25 mm/y respectively. The first two figures provide an overview of the seasonal motion components in west-eastern and vertical directions. Obviously, there exist some buildings affected by large amplitudes of horizontal as well as vertical deformation, indicated by blue or red colors. Especially Berlin central train station shows intense colors. This building is also included in a zoom to area 1 (cf. Figures 80, 81), that has already been investigated in Section 4.4.2 for motion analysis of single stacks.

From Figures 80 and 81 the apparent deformation is clearly visible. The rail tracks near central train station are mainly affected by horizontal dilation in direction of the tracks. Due to the alignment of these parts of the rail tracks in west-eastern direction, this kind of displacement can be easily observed by PSI. From the decomposition of motion components, the interpretation of PSI results of different stacks is validated. The main buildings and the tower are moving in vertical direction and the rail tracks as well as the halls show major components of displacement in horizontal directions. In addition, a periodic uplift of the halls and the bridge to the right can be recovered from the motion decomposition. Again, the gaps at the rail tracks can be identified by the abrupt color reversal from blue to red/yellow or vice versa. In this area, all bridges are affected by motion mainly in horizontal or vertical directions, possibly depending on the mounting. In addition, large horizontal and medium vertical seasonal motion components are present at the second train station to the east. Certainly several other buildings are affected by seasonal motion of medium or low amplitudes, that can be identified by slightly blue or red colors.

In area 2 mainly horizontal seasonal deformation can be derived from an interpretation of PSI results of different stacks. Again, this is validated numerically by the motion decomposition results (cf. Figure 82), whereas the large hall is only slightly affected by vertical motion, as
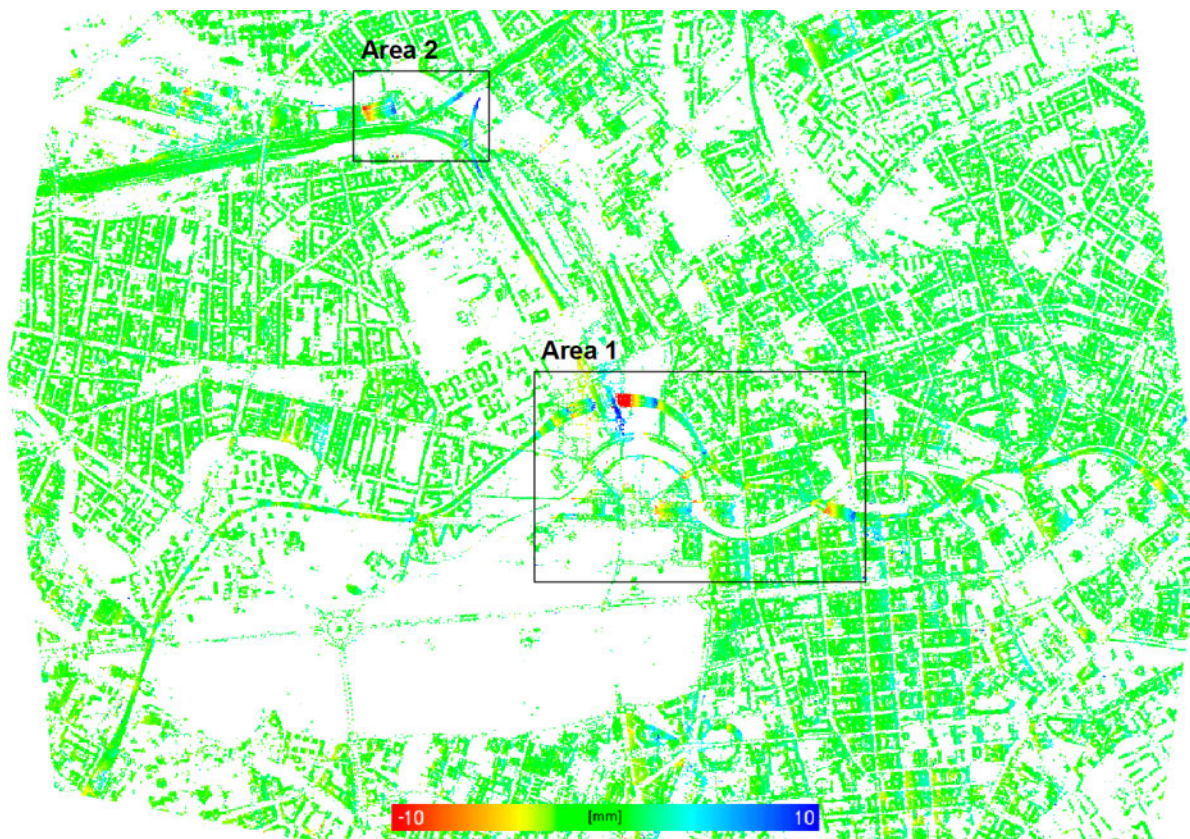
Figure 78. Top view on PS of Berlin test site colorcoded by the estimated seasonal components in west-eastern direction in the interval [-10, +10] mm.
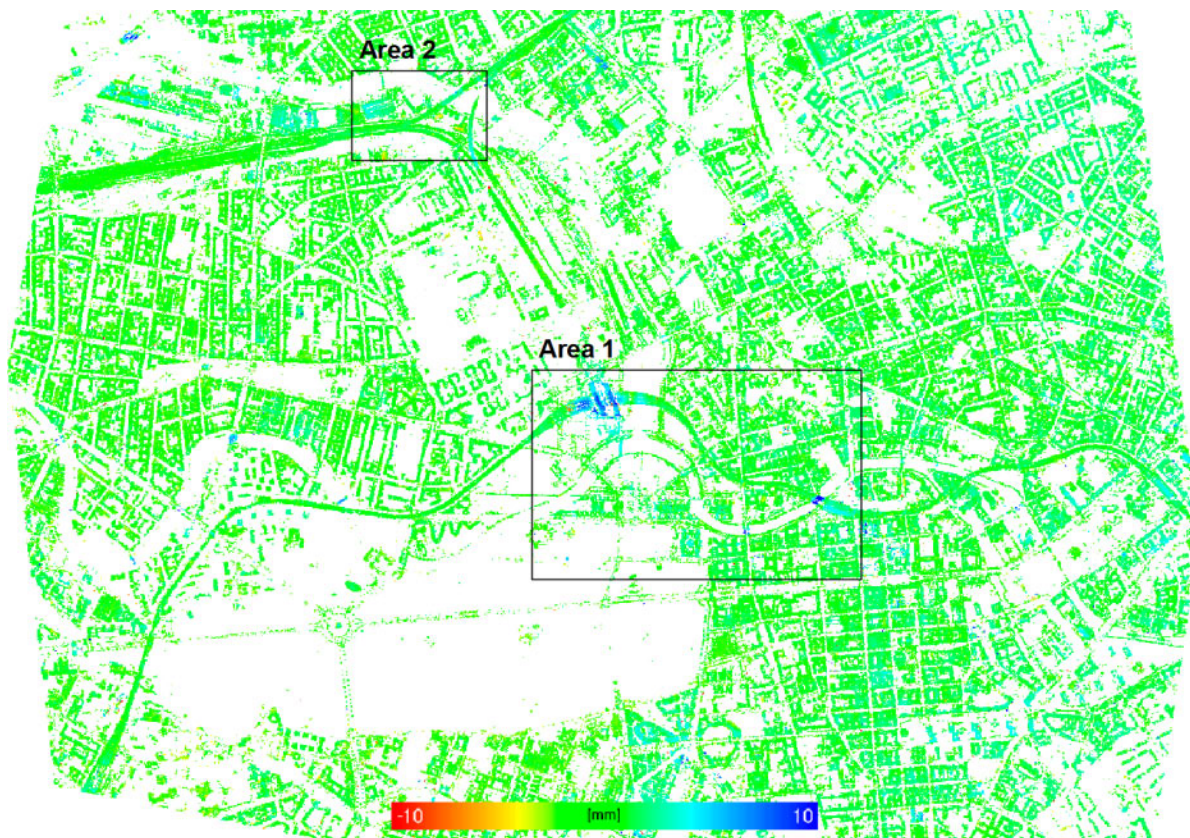
Figure 79. Top view on PS of Berlin test site colorcoded by the estimated seasonal components in vertical direction in the interval [-10, +10] mm.
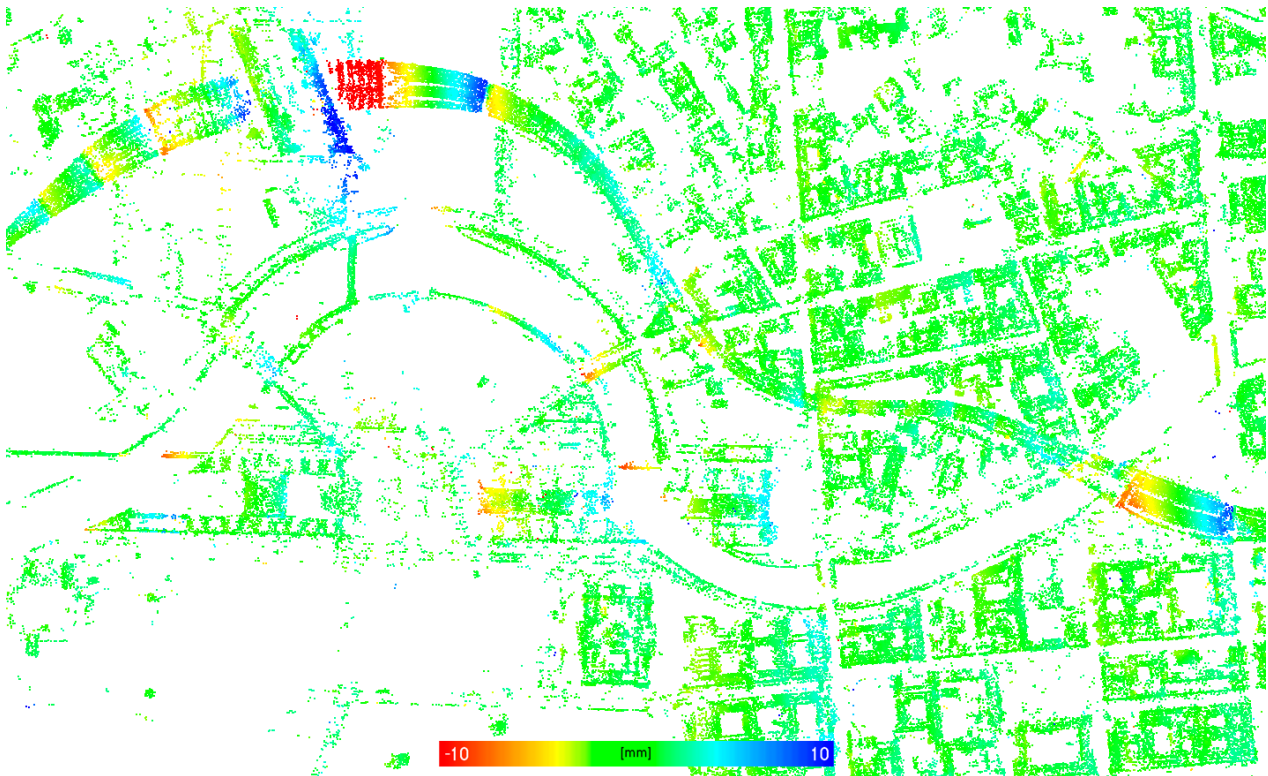
Figure 80. Top view on PS of area 1 in Berlin (cf. Section 4.4.2) colorcoded by the estimated seasonal components in west-eastern direction in the interval [-10, +10] mm.
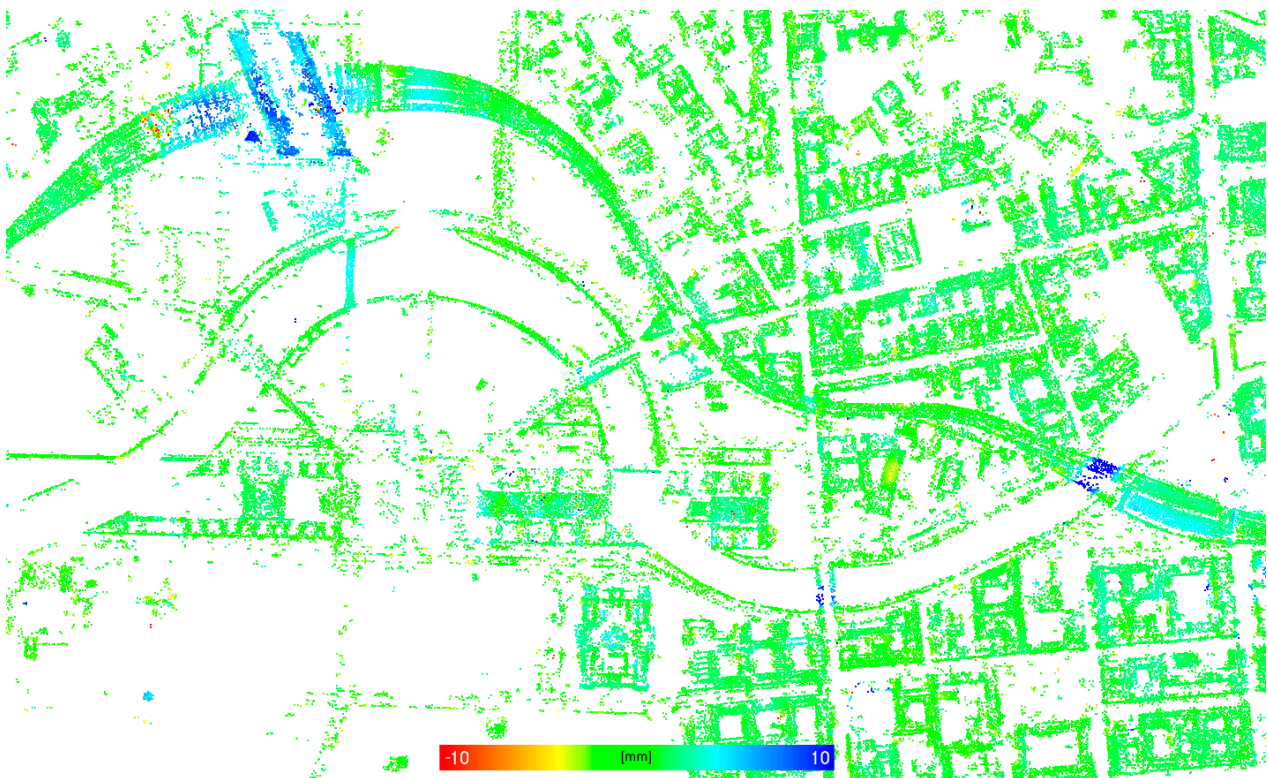
Figure 81. Top view on PS of area 1 in Berlin (cf. Section 4.4.2) colorcoded by the estimated seasonal components in vertical direction in the interval [-10, +10] mm.
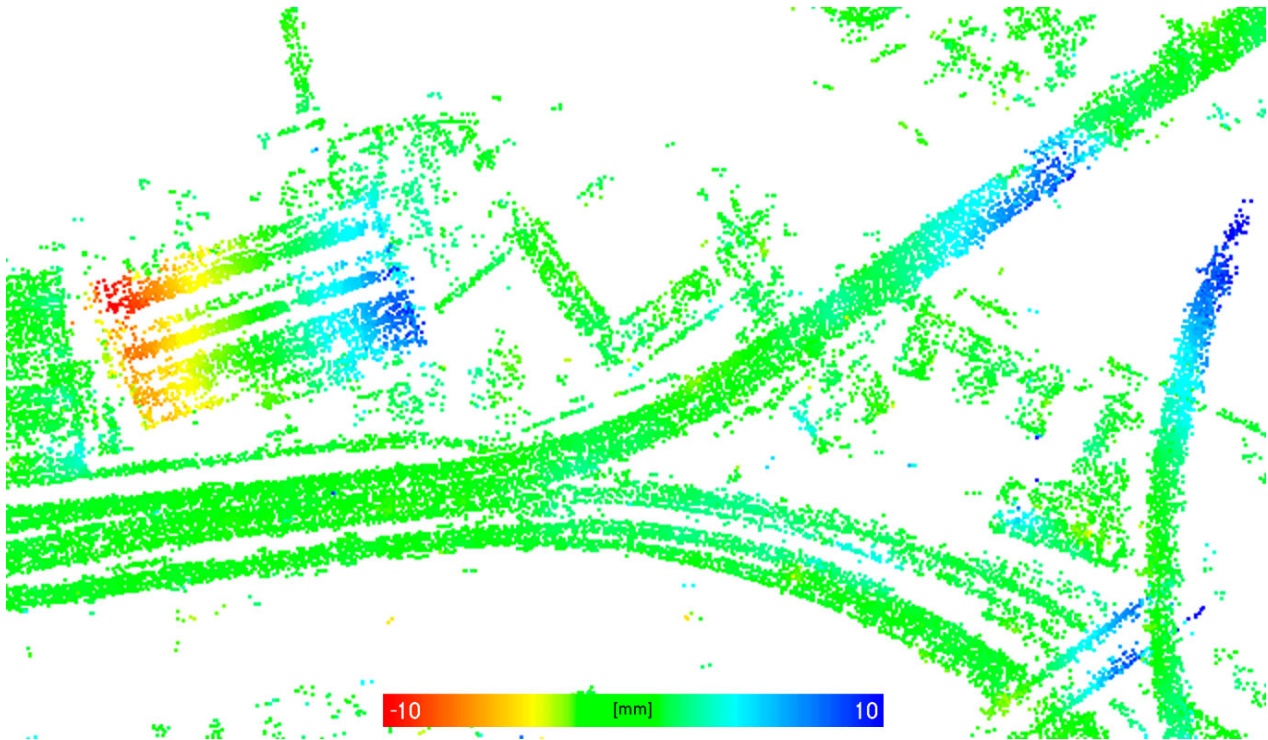
Figure 82. Top view on PS of area 2 in Berlin (cf. Section 4.4.2) colorcoded by the estimated seasonal components in west-eastern direction in the interval [-10, +10] mm.
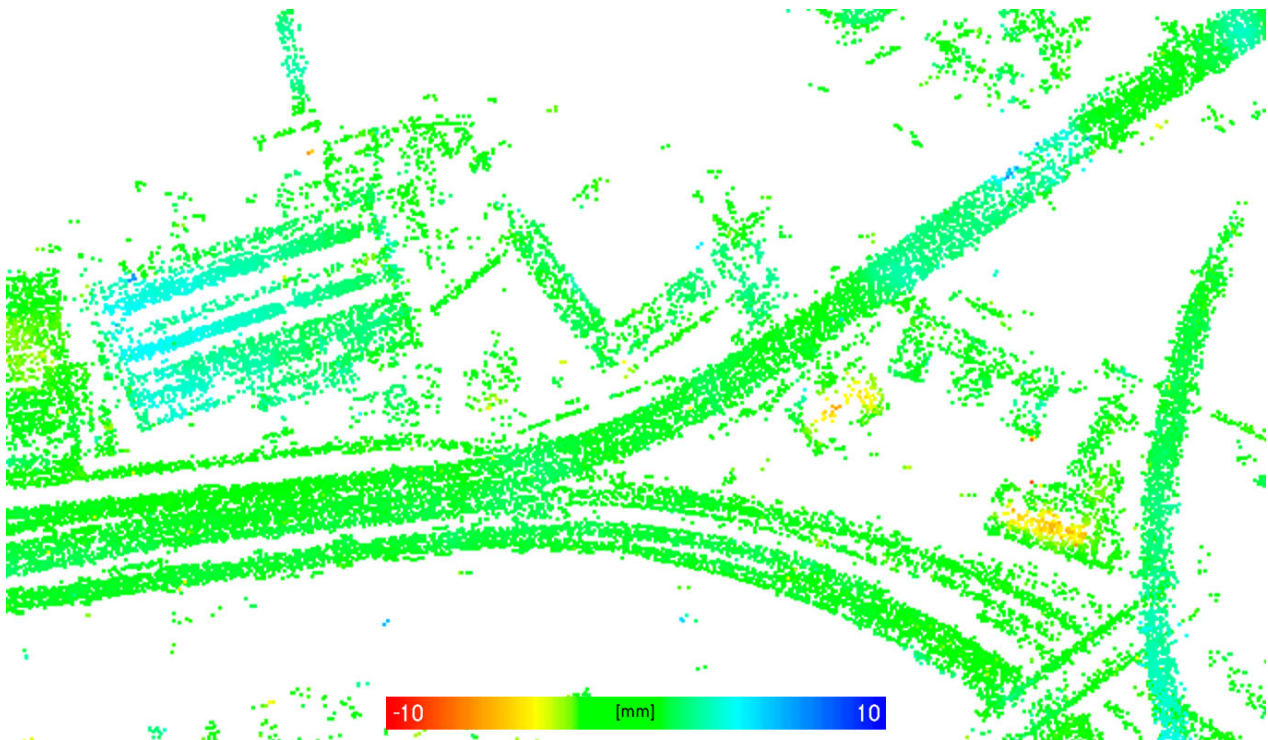
Figure 83. Top view on PS of area 2 in Berlin (cf. Section 4.4.2) colorcoded by the estimated seasonal components in vertical direction in the interval [-10, +10] mm.

can be seen in Figure 83. In addition, parts of the rail track to the right and a bridge in the lower right corner show large components of horizontal deformation. The explanation is easy; these rail tracks are located on a bridge, hence, the thermal expansion during summer times is observed. Interestingly, two buildings show negative seasonal amplitudes on parts of the roof. From optical images the gable roof construction can be identified, whereas the slope of the roof is very small but the area of the roof is quite large. Hence, the effect of subsidence during

summer times may be related to a thermal expansion of horizontally aligned steel girders that are fixed at the walls. Therefore, the sag is exaggerated in the middle of the building and the roof is pulled downwards. However, this is speculation only. Nevertheless, two additional buildings are discovered in Berlin, that show a comparable color distribution. They also hold the same type of gable roof construction.

Finally, the overviews on the test site of Berlin are shown again in Figures 84 and 85, but the range of amplitudes for the colorcoding is reduced to the intervall -5 mm to +5 mm. Consequently, the number of buildings rises that visually can be detected to be affected by medium seasonal displacement. This visualization shows, that thermal expansion in horizontal as well as vertical direction does have significant influence on a large majority of objects in urban areas. Hence, seasonal deformation always has to be considered within PSI, especially when using meter-resolution SAR data. The motion decomposition algorithm is limited to surfaces that contain PS from different viewing directions, hence, most likely the components can be separated for roofs and ground surface areas only. Nevertheless, monitoring of single objects is facilitated because a subsidence or uplift of the whole building will also be observable from PS of the roof, which additionally may be affected by seasonal motion.

In addition to seasonal motion, linear components are available from the decomposition. However, no conspicuous linear motion in west-eastern directions is present. In contrast, several areas within the Berlin test site are affected by significant linear vertical displacement (cf. Figure 86). Figure 87 shows a detailed view on two examples. The amplitudes of displacement are colorcoded in the interval of -10 mm/y to $+10$ mm/y. Two locally limited areas of subsidence are visible. Unfortunately, the origin of the subsidence is not known at the moment. One possible source of linear subsidence in urban areas may be the load of recently built houses, like observed in the Munich test site. Supplementary, the high level of ground water in Berlin may influence the stability of ground below buildings.

However, the reliability of linear estimates may still be slightly restricted due to the low number of acquisitions in the last 6 months for most of the stacks (cf. Section 4.1.2). Consequently, single isolated phase observations at a larger temporal distance to the majority of observations may bias the estimation. In Figure 88 two examples of phase histories are shown, that are reduced by the estimated seasonal motion. In the first case linear vertical subsidence of Berlin central train station is investigated. The amplitude of the estimated linear motion most probably is slightly biased by the last phase observations, because a line of less slope may fit better to the majority of observations. Nevertheless, a subsidence is present for several points, only the magnitude may be different. In the second case the analysis covers the two areas of subsidence shown in Figure 87. Within both areas the estimated linear trend is apparent for the whole distribution of observations, as the deviations from the line are very small and regularly distributed. Anyhow, the last two phase observations again can be considered as so called leverage points, which may bias the estimation due to a larger distance to the majority of observations. However, the influence is obviously negligible in this case.

At the moment, the temporal baseline only covers approximately two years. Hence, the continuity of subsidence will only be revealed by an extension of the stacks within the next years. The linear evolutions could be slowed down or even stop, but a prediction is not possible. Nevertheless, piecewise linear functions can be introduced into the motion estimation process (cf. Kampes (2006)). Consequently, it is possible to estimate magnitudes of linear motion within different intervals of the temporal baseline separately, but only if a priori data about the temporal intervals is available in order to define the breakpoints.
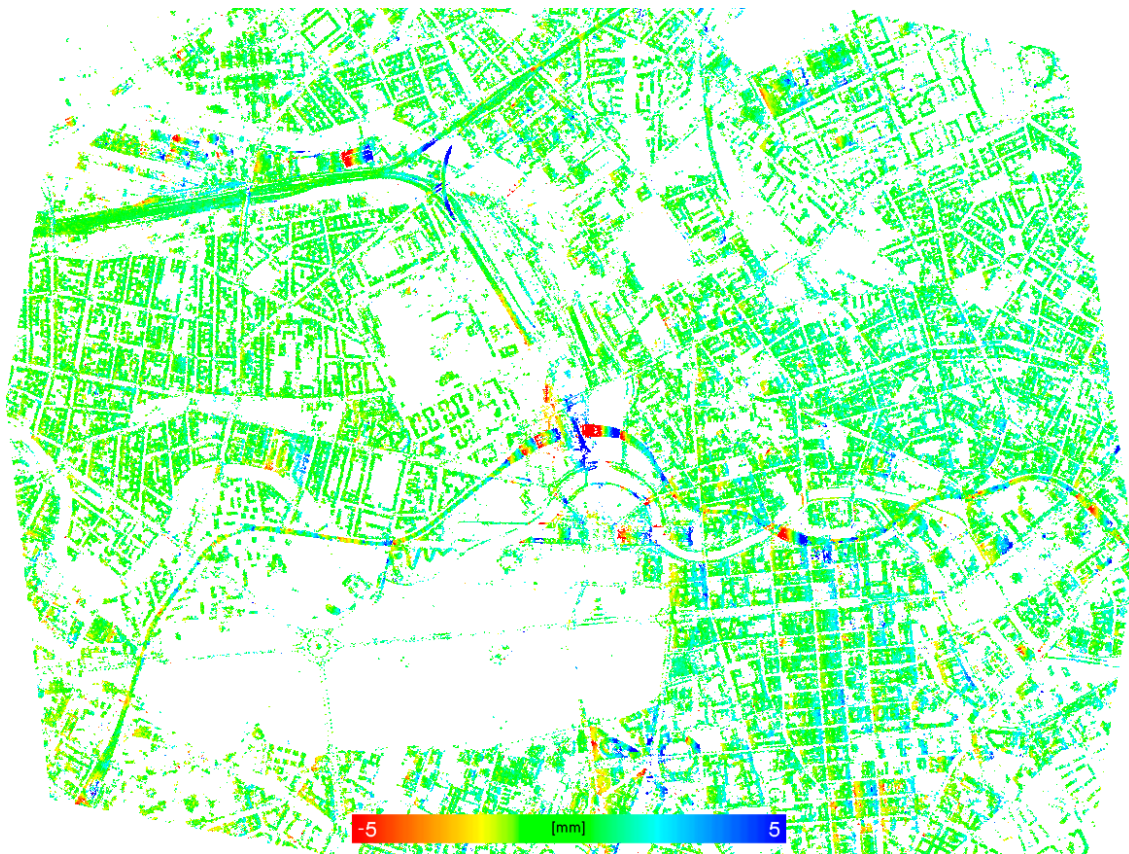
Figure 84. Top view on PS of Berlin test site colorcoded by the estimated seasonal components in west-eastern direction in the interval [-5, +5] mm.
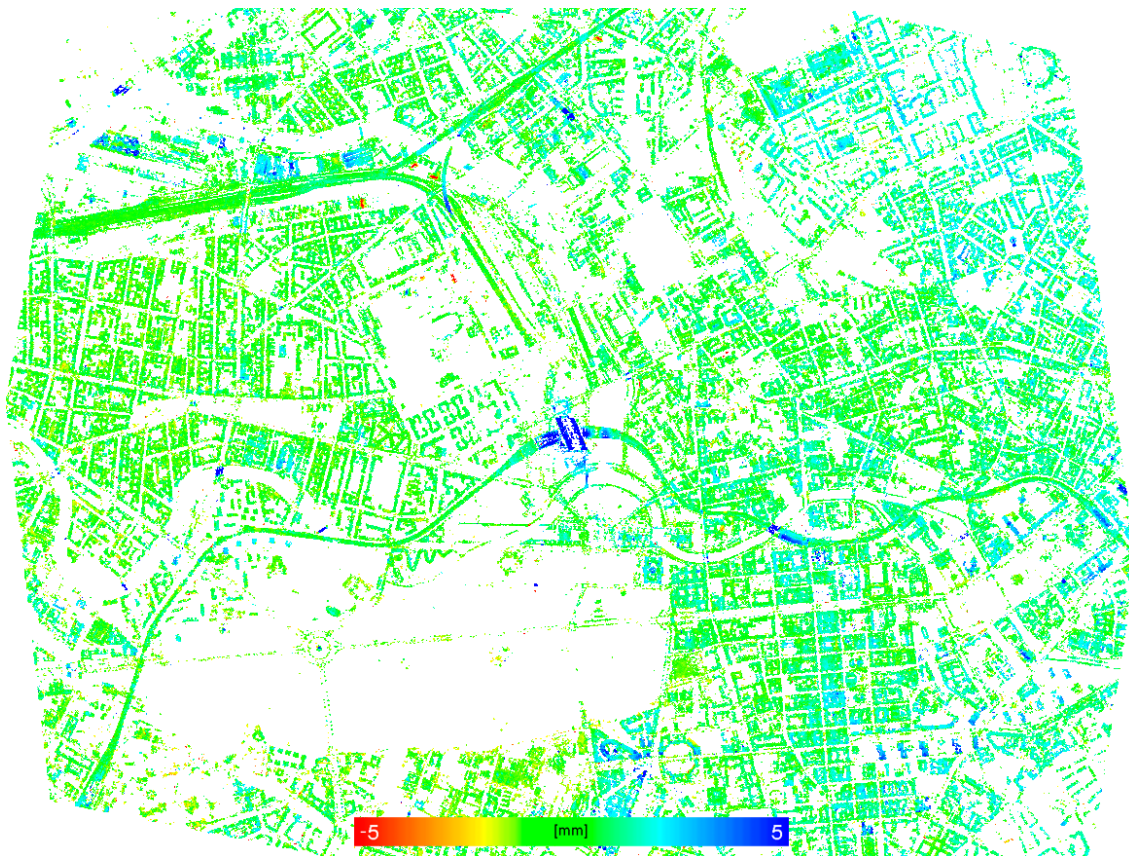
Figure 85. Top view on PS of Berlin test site colorcoded by the estimated seasonal components in vertical direction in the interval [-5, +5] mm.
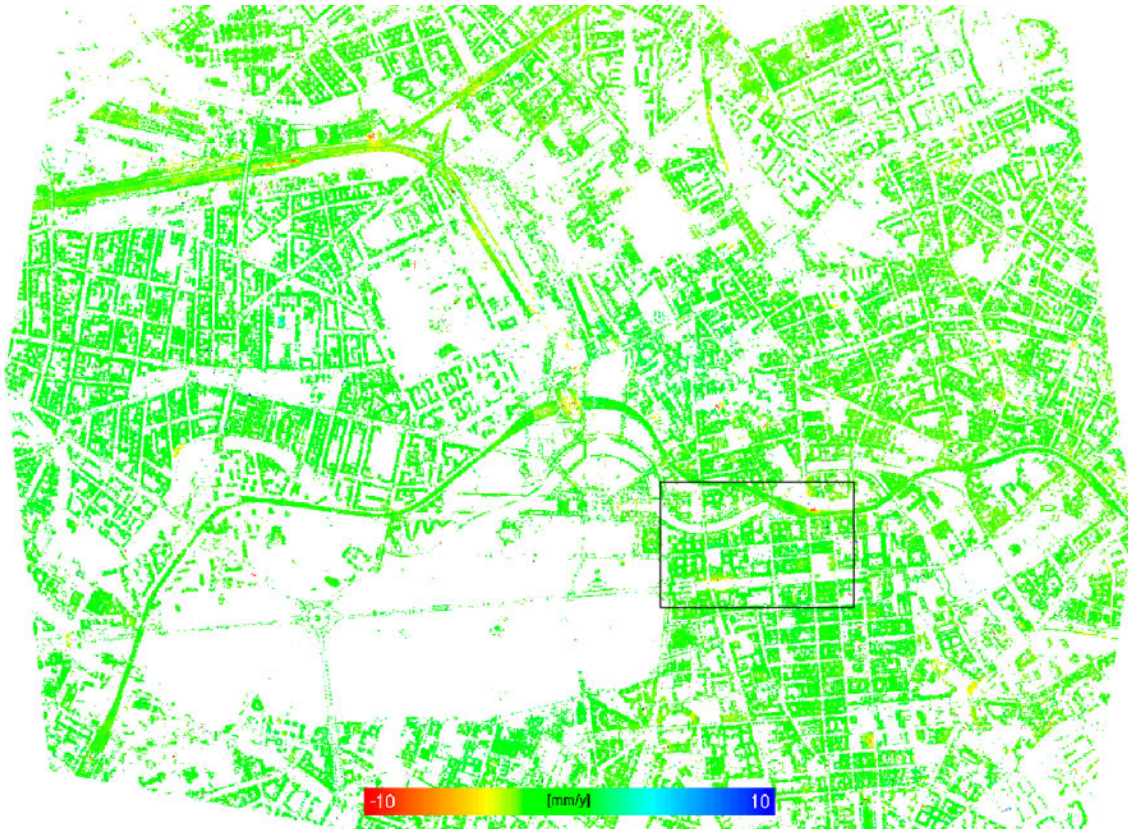
Figure 86. Top view on PS of Berlin test site colorcoded by the estimated linear components in vertical direction in the interval [-10, +10] mm/y. Significant subsidence is visible for some locally limited areas. Area of Figure 87 indicated by black rectangle.
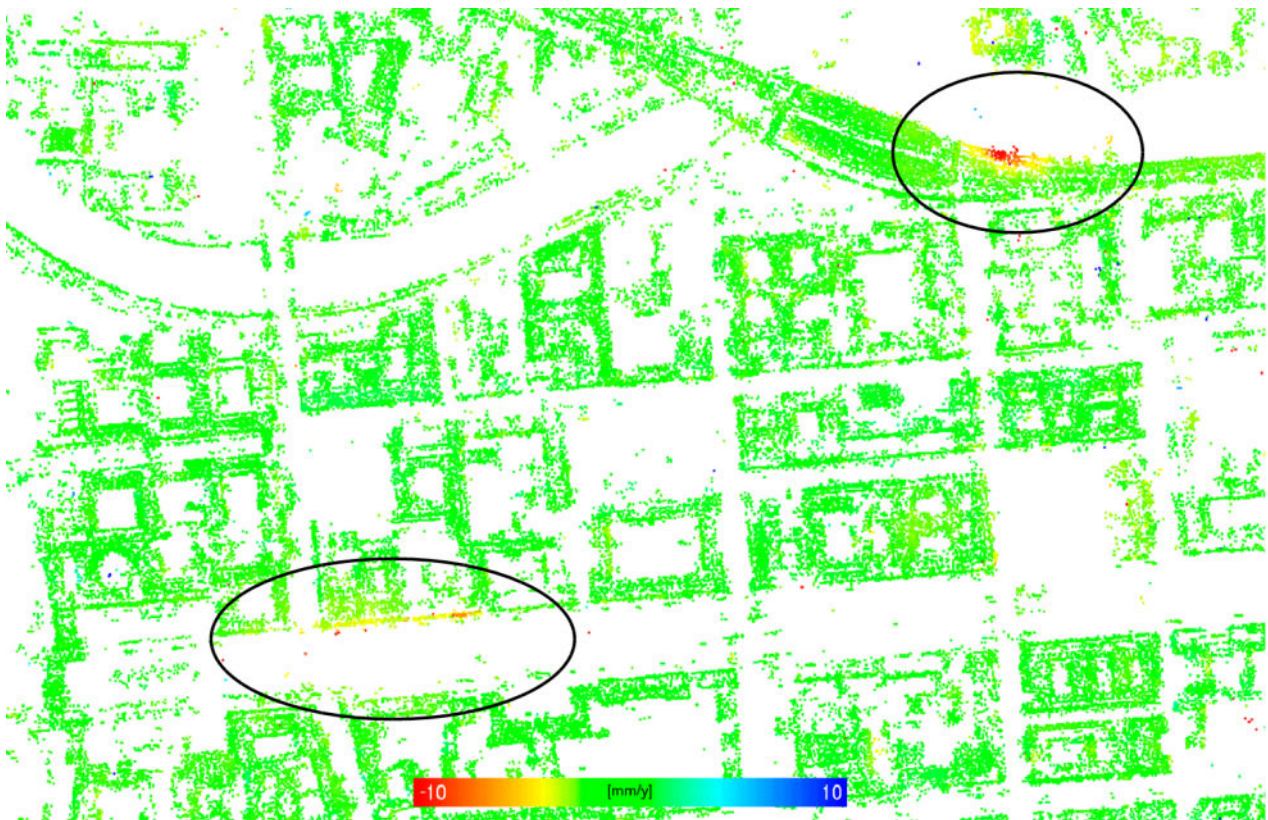
Figure 87. Top view on PS of Berlin test site colorcoded by the estimated linear components in vertical direction in the interval [-10, +10] mm/y. Significant subsidence is visible for two areas, highlighted by black ellipsis.
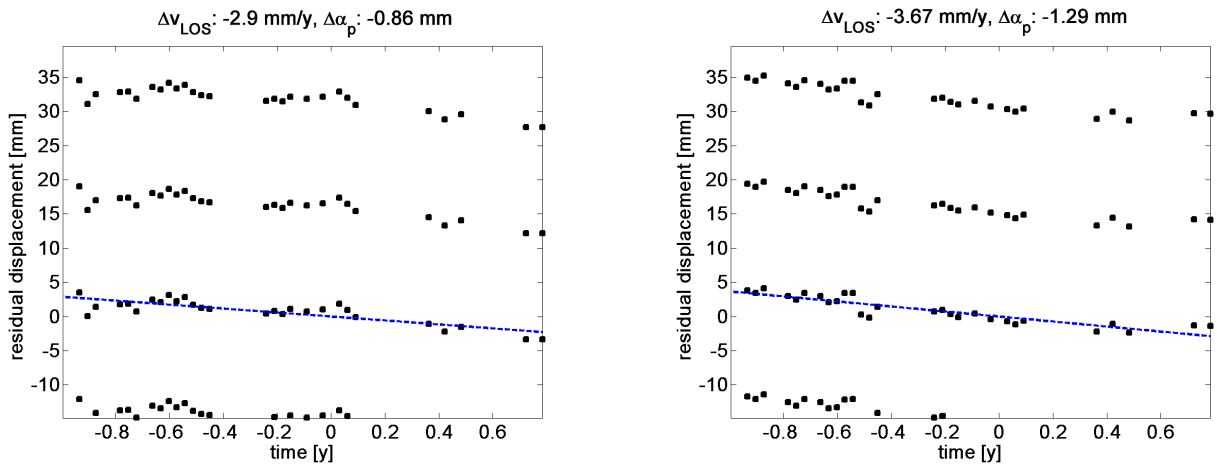
(a) Residual phase history for two PS at Berlin central train station.

(b) Residual phase history for two PS within the area shown in Figure 87.

Figure 88. Phase history (including $\pm 2\pi$ ambiguities) showing residual relative deformation rate between two PS after removal of estimated seasonal motion. Black dots represent remaining relative deformation signal. Blue line indicates estimated linear deformation. First number in title corresponds to estimated linear, second to amplitude of periodic deformation.

6 Conclusions and Outlook

6.1 Evaluation of Results Regarding a Geodetic Monitoring of Buildings

The availability of six large stacks for the Berlin test site consisting of high resolution spotlight SAR data of TerraSAR-X covering the same area and including different types of polarization (at least 6 small stacks of HH data) can be considered unique. Therefore, the major advantages of meter-resolution SAR data for PSI can be investigated and evaluated based on a comparison of results between different stacks. In addition, conclusions for a geodetic utilization of PSI for monitoring of single buildings can be drawn.

At first, the high density of PS throughout urban areas enormously facilitates monitoring tasks at small scales, because in comparison to medium resolution SAR data, the opportunistic character of PS almost vanished. Certainly, ridges and edges at a minimum extent of several centimeters are necessary in order to provide appropriate reflection surfaces for PS to appear in radar images. However, the analysis of the two test sites of Berlin and Munich already proved that modern buildings do not lack of several tens of PS. Solely, the presence of rows of windows already guarantees the availability of PS at a very high probability. Hence, the analysis of structural details of the objects of interest allows for a better choice of acquisition parameters prior to data ordering, depending on the demands of deformation monitoring.

Secondly, precise linear as well as seasonal motion estimates are provided by PSI. If applied to meter-resolution SAR data of TerraSAR-X, this method reveal variations of deformation within single buildings, which may be helpful for investigations on structural stress. However, the introduction of a seasonal deformation model seems to be mandatory, because many buildings are affected by thermal dilation, as shown by results of the Berlin test site. A restriction to a certain temporal offset of the periodic function seems to be counterproductive, because several PS may be lost due to deviations from a smooth temperature evolution within one year. One limitation for deformation monitoring using single stacks is the direction of motion estimates in LOS, that prevents to conclude the major direction of deformation without any further knowledge. Nevertheless, the availability of at least one ascending and one descending stack allows for discrimination between vertical and horizontal components of motion. Hence, a detailed deformation analysis on single buildings is feasible.

The positions of the deformation estimates are available at an accuracy of some centimeters in range and azimuth. Unfortunately, the precision in elevation direction influences a 3D localization of the PS within a range of approximately 0.5 m to 1 m. In addition, some PS positions deviate significantly by reason of two or more scatterers in the same resolution cell that are not separated within PSI at the moment. Hence, in order to improve the localization performance multiple dominating scatterers have to be separated. Nevertheless, the precision of PS at hand already enables to detect the source of scattering, i.e., PS can be assigned to certain regions on building facades. Consequently, dangerous variations of deformation can be located at building facades or roofs. In addition, the spatial distribution of PS provides 3D object information, that may be useful for long term change detection, for example.

Finally, an automatic fusion of independently geocoded PS obtained from meter-resolution SAR data of TerraSAR-X is accomplished for the first time. After the fusion precise monitoring of single buildings is feasible, because PS are available from all facades and the roof for the large majority of buildings. Therefore, 4D city information is provided; 3D object information is available from the distribution of PS in 3D space including temporal displacement estimates for each of these points. Furthermore, deformation components in west-eastern and vertical

directions can be separated, if cross-heading tracks are combined. Consequently, PSI can be considered suitable for a precise geodetic monitoring of single objects. In other words, single object observation is feasible after a fusion of cross-heading track results based on data of this new class of meter-resolution SAR sensors.

6.2 Future Developments

From the gained experience of applying PSI to meter-resolution SAR data, some potential improvements and future topics are briefly outlined in this section.

The fusion methodology may be improved at the step of creating appropriate point correspondences, that are substantial for a successful combination of different stacks. Especially for cross-heading tracks, the registration procedure may be supported by a matching of simple features, like borderlines of rivers or rail tracks. Another possibility may be the derivation of parts of building outlines from the PS situated at facades. However, a robust approach to combine two opposing fractions of building outlines has to be integrated. Both approaches could improve the final results.

An enhancement of parameter estimation within PSI may be implemented by an exploitation of spatial relationships between adjacent PS. From the phase histories showing large amplitudes it is evident, that a reliable estimation becomes more and more difficult due to the ambiguous phase. Especially phase noise may prevent a successful resolution of the underlying deformation signal. However, an inclusion of spatial correlation between single independent estimations could possibly help in these cases. Potentials to enhance the estimation based on common, non-destructive deformation models as well as preliminary simulation results are provided by Gernhardt and Hinz (2008). In this study, an increase in accuracy of about 15% to 20% is reported. However, an initial grouping of PS is necessary for this task. Suitable information could be provided by a DSM of the area, by cadastral maps or by SAR simulation (Auer et al., 2008).

Further improvements for PSI could include a supplementary processing chain if multiple adjacent stacks are available by applying a radargrammetric approach on corresponding points. Consequently, a joint and more robust estimation of PS heights and deformation including a decomposition of motion components is accomplished for a subset of points. This information could be used to strengthen individual stack estimations. Initial investigations and results are shown by (Adam et al., 2010).

PSI may also be supported by absolute phase determination approaches based on delta-k algorithms that are capable of providing absolute phase differences between pixels. Hence, aliases in the phase history by reason of large phase gradients can be resolved. This would enable the usage of larger temporal or spatial baselines, because error propagation effects by reason of single phase unwrapping errors can be reduced (Brcic et al., 2009a,b).

However, one of the largest problems in urban areas is layover. As a consequence the assumption of a single dominating scatterer within one resolution cell could be violated. Only tomographic approaches allow for a detection of multiple scatterers within one resolution cell (Zhu and Bamler, 2010c). The basic principle is the reconstruction of the reflectivity profile along elevation direction. Hence, the "aperture" in elevation direction is evaluated for a separation of dominating PS within the same resolution cell. Recent works based on meter-resolution SAR data are presented by Zhu and Bamler (2010b) and Zhu and Bamler (2010a). The successful resolution of layover areas is shown and multiple scatterers are separated, expecting a limited number of typically 1-3 PS. The number of PS is mentioned to be increased by 30%, whereas most of the additional points are at low height with respect to a horizontal surface in front of the building facade. Hence, the super-resolution capability of tomographic SAR is a major advantage that

should be combined with PSI. However, PSI is an important method that can be regarded as a special case of SAR tomography, because the estimation is limited to the assumed best points including only one single dominating scatterer. The residuals of phase values of PS after the successful estimation of the reference network hold important information on the atmospheric fractions. This data is needed for a subtraction of these fractions from the interferograms before SAR tomography can be applied. Furthermore, the robust network approach of PSI will deliver very reliable estimates for displacement and PS heights, that already enable detailed analyses on deformation of single buildings at reasonable computational costs.

Although, results of PSI using meter-resolution data may be improved at several stages, the investigations at hand reveal the potential of this new class of radar data for PSI. Especially the monitoring of single buildings from space at a precision in the sub-millimeter domain is facilitated by a fusion of different stacks. The general approach of the algorithm certainly allows for an application to results of sophisticated 3D imaging methods like tomographic SAR. Based on the achievements of fundamental research in this scientific field, the request for high resolution 4D monitoring in urban areas by means of tomographic methods may increase significantly in the near future. Nevertheless, the evaluation processes have to be enhanced for an economic and commercial utilization.

References

Adam, N., Bamler, R., Eineder, M., Kampes, B., 2005. Parametric estimation and model selection based on amplitude-only data in ps-interferometry. In: Proceedings of FRINGE Workshop, on CD.

Adam, N., Eineder, M., Yague-Martinez, N., Bamler, R., 2008a. High resolution interferometric stacking with TerraSAR-X. In: Proceedings of IEEE International Geoscience and Remote Sensing Symposium, Vol. 2, 117–120.

Adam, N., Eineder, M., Yague-Martinez, N., Bamler, R., 2008b. TerraSAR-X high resolution SAR-interferometry. In: Proceedings of European Conference on Synthetic Aperture Radar, on CD.

Adam, N., Gernhardt, S., Eineder, M., Bamler, R., 2010. Multi beam joined estimation for persistent scatterer interferometry. In: Proceedings of IEEE International Geoscience and Remote Sensing Symposium, 4403–4406.

Adam, N., Kampes, B., Eineder, M., 2004. Developement of a scientific permanent scatterer system: Modifications for mixed ERS/ENVISAT time series. In: Proceedings of Envisat & ERS Symposium, on CD.

Adam, N., Kampes, B., Eineder, M., Worawattanamateekul, J., Kircher, M., 2003. The developement of a scientific permanent scatterer system. In: Proceedings of ISPRS Workshop High Resolution Mapping from Space, Hannover, Germany, on CD.

Adam, N., Parizzi, A., Eineder, M., Crosetto, M., 2009. Practical persistent scatterer processing validation in the course of the terrafirma project. Journal of Applied Geophysics 69 (1): 59–65.

Auer, S., 2011. 3D synthetic aperture radar simulation for interpreting complex urban reflection scenarios. Ph.D. thesis, Deutsche Geodätische Kommission, Reihe C, Heft 660, 126 pages.

Auer, S., Balz, T., Becker, S., Bamler, R., 2010a. 3D SAR simulation of urban areas based on detailed building models. Photogrammetric Engineering & Remote Sensing, Journal of the American Society of Photogrammetry and Remote Sensing 76 (12): 1373–1384.

Auer, S., Gernhardt, S., Bamler, R., 2011a. Ghost persistent scatterers related to multiple signal reflections. Geoscience and Remote Sensing Letters 8 (5): 919–923.

Auer, S., Gernhardt, S., Bamler, R., 2011b. Ghost persistent scatterers related to signal reflections between adjacent buildings. In: Proceedings of IEEE International Geoscience and Remote Sensing Symposium, 919–923.

Auer, S., Gernhardt, S., Bamler, R., 2011c. Investigations on the nature of persistent scatterers based on simulation methods. In: Proceedings of Joint Urban Remote Sensing Event, 61–64.

Auer, S., Gernhardt, S., Hinz, S., Bamler, R., 2008. Simulation of radar reflection at man-made objects and its benefits for persistent scatterer interferometry. In: Proceedings of European Conference on Synthetic Aperture Radar, on CD.

Auer, S., Hinz, S., Bamler, R., 2010b. Ray-tracing simulation techniques for understanding high-resolution SAR images. IEEE Transactions on Geoscience and Remote Sensing 48 (3): 1445–1456.

Auer, S., Zhu, X., Hinz, S., Bamler, R., 2009. 3D analysis of scattering effects based on ray tracing techniques. In: Proceedings of IEEE International Geoscience and Remote Sensing Symposium, Vol. 3, 17–20.

Bamler, R., Eineder, M., 2005. Accuracy of differential shift estimation by correlation and split-bandwidth interferometry for wideband and delta-k SAR systems. Geoscience and Remote Sensing Letters 2 (2): 151–155.

Bamler, R., Eineder, M., Adam, N., Zhu, X., Gernhardt, S., 2009. Interferometric potential of high resolution spaceborne SAR. Photogrammetrie Fernerkundung Geoinformation 5: 407–419.

Bamler, R., Hartl, P., 1998. Synthetic aperture radar interferometry. Inverse Problems 14 (4): R1–R54.

Berardino, P., Casu, F., Fornaro, G., Lanari, R., Manunta, M., Manzo, M., Pepe, A., Pepe, S., Sansosti, E., Serafino, F., Solaro, G., Tizzani, P., Zeni, G., 2007. The sbas-dinsar technique as a tool for the observation of active volcanic areas: Results and future perspectives. In: Proceedings of IEEE International Geoscience and Remote Sensing Symposium, 10 –13.

Berardino, P., Casu, F., Fornaro, G., Lanari, R., Manunta, M., Manzo, M., Pepe, A., Sansosti, E., 2003. Small baseline DIFSAR techniques for earth surface deformation analysis. In: Proceedings of FRINGE Workshop, on CD.

Berardino, P., Fornaro, G., Lanari, R., Sansosti, E., 2002. A new algorithm for surface deformation monitoring based on small baseline differential sar interferograms. IEEE Transactions on Geoscience and Remote Sensing 40 (11): 2375–2383.

Blanco, P., Mallorqui, J., Duque, S., Navarrete, D., 2006. Advances on dinsar with ers and envisat data using the coherent pixels technique (cpt). In: Proceedings of IEEE International Geoscience and Remote Sensing Symposium, 1898 –1901.

Blanco-Sanchez, P., Mallorqui, J., Duque, S., Monells, D., 2008. The coherent pixels technique (CPT): An advanced DInSAR technique for nonlinear deformation monitoring. Pure and Applied Geophysics 165: 1167–1193.

Brcic, R., Eineder, M., Bamler, R., 2009a. Interferometric absolute phase determination with TerraSAR-X wideband SAR data. In: Proceedings of IEEE Radar Conference, on CD.

Brcic, R., Eineder, M., Bamler, R., Steinbrecher, U., Schulze, D., Methig, R., Papathanassiou, K., 2009b. Delta-k wideband SAR interferometry for DEM generation ans persistent scatterers using TerraSAR-X. In: Proceedings of FRINGE Workshop, on CD.

Breit, H., Fritz, T., Balss, U., Lachaise, M., Niedermeier, A., Vonavka, M., 2010. Terrasar-x sar processing and products. IEEE Transactions on Geoscience and Remote Sensing 48 (2): 727–740.

Breit, H., Schattler, B., Fritz, T., Damerow, H., Schwarz, E., Balss, U., 2008. Terrasar-x payload data processing: Results from commissioning and early operational phase. In: Proceedings of IEEE International Geoscience and Remote Sensing Symposium, Vol. 2, 209–212.

Colesanti, C., Ferretti, A., Novali, F., Prati, C., Rocca, F., 2003. SAR monitoring of progressive and seasonal ground deformation using the permanent scatterers technique. IEEE Transactions on Geoscience and Remote Sensing 41 (7): 1685–1700.

Colesanti, C., Ferretti, A., Prati, C., Rocca, F., 2002. Full exploitation of the ERS archive: Multi data set permanent scatterers analysis. In: Proceedings of IEEE International Geoscience and Remote Sensing Symposium, Vol. 2, 1234–1236.

Costantini, M., Falco, S., Malvarosa, F., Minati, F., Trillo, F., 2009. Method of persistent scatterer pairs (psp) and high resolution sar interferometry. In: Proceedings of IEEE International Geoscience and Remote Sensing Symposium, Vol. 3, 904–907.

Costantini, M., S., F., Malvarosa, F., Minati, F., 2008. A new method for identification and analysis of persistent scatterers in series of SAR images. In: Proceedings of IEEE International Geoscience and Remote Sensing Symposium, Vol. 2, 449–452.

Cumming, I., Wong, F., 2005. Digital Processing of Synthetic Aperture Radar Data: Algorithms and Imple-

mentation. Artech House Publishers.

de Jonge, P., Tiberius, C., 1996. The lambda method for integer ambiguity estimation: Implementation aspects. LGR-Series 12, Delft Geodetic Computing Centre, Delft, The Netherlands, 59 pages.

de Jonge, P., Tiberius, C., Teunissen, P., 1996. Computational aspects of the lambda method for gps ambiguity resolution. In: Proceedings of International Technical Meeting of the Satellite Division of the Institute of Naviagtion, USA, 935–944.

Duque, S., Mallorqui, J., Blanco, P., Monells, D., 2007. Application of the coherent pixels technique (cpt) to urban monitoring. In: Proceedings of Joint Urban Remote Sensing Event, 1–7.

Eineder, M., Adam, N., 2005. A maximum-likelihood estimator to simultaneously unwrap, geocode, and fuse SAR interferograms from different viewing geometries into one digital elevation model. IEEE Transactions on Geoscience and Remote Sensing 43 (1): 24–36.

Eineder, M., Adam, N., Bamler, R., Yague-Martinez, N., Breit, H., 2009. Spaceborne spotlight SAR interferometry with TerraSAR-X. IEEE Transactions on Geoscience and Remote Sensing 47 (5): 1524–1535.

Eineder, M., Adam, N., Brcic, R., Yague-Martinez, N., Fritz, T., 2008. High bandwidth spotlight SAR interferometry with TerraSAR-X. In: Proceedings of IEEE International Geoscience and Remote Sensing Symposium, Vol. 2, 113–116.

Esfahany, S., van Leijen, F., Marinkovic, P., Ketelaar, G., R., H., 2007. Lessons learned from PSIC4: Improving PSI results for a constrained test site. In: Proceedings of FRINGE Workshop, on CD.

Ferretti, A., Bianchi, M., Prati, C., Rocca, F., 2005. Higher-order permanent scatterers analysis. EURASIP Journal on Applied Signal Processing 20 (20): 3231–3242.

Ferretti, A., Fumagalli, A., Novali, F., Prati, C., Rocca, F., Ruc, 2010. Exploitation of coherence matrices in multi-temporal SAR datasets: the SqueeSAR approach. In: Proceedings of IEEE International Geoscience and Remote Sensing Symposium, Vol. 3, 1319–1322.

Ferretti, A., Novali, F., De Zan, F., Prati, C., Rocca, F., 2008. Moving from PS to slowly decorrelating targets: A prospective view. In: Proceedings of European Conference on Synthetic Aperture Radar, on CD.

Ferretti, A., Prati, C., Rocca, F., 2000. Nonlinear subsidence rate estimation using permanent scatterers in differential SAR interferometry. IEEE Transactions on Geoscience and Remote Sensing 38 (5): 2202–2212.

Ferretti, A., Prati, C., Rocca, F., 2001. Permanent scatterers in SAR interferometry. IEEE Transactions on Geoscience and Remote Sensing 39 (1): 8–20.

Ferretti, A., Savio, G., Barzaghi, R., Borghi, A., Musazzi, S., Novali, F., Prati, C., Rocca, F., 2007. Submillimeter accuracy of InSAR time series: Experimental validation. IEEE Transactions on Geoscience and Remote Sensing 45 (5): 1142–1153.

Fischler, M., Bolles, R., 1981. Random sample consensus: A paradigm for model fitting with apphcatlons to image analysis and automated cartography. Communications of the ACM 24 (6): 381–395.

Fornaro, G., Serafino, F., 2006. Imaging of single and double scatterers in urban areas via SAR. IEEE Transactions on Geoscience and Remote Sensing 44 (12): 3497–3505.

Fornaro, G., Serafino, F., Lombardini, F., 2005. Three-dimensional multipass SAR focusing: Experiments with long-term spaceborne data. IEEE Transactions on Geoscience and Remote Sensing 43 (4): 702–714.

Gernhardt, S., Hinz, S., 2008. Advanced displacement estimation for PSI using high resolution SAR data. In: Proceedings of IEEE International Geoscience and Remote Sensing Symposium, Vol. 3, 1276–1279.

Gernhardt, S., Meyer, F., Bamler, R., Adam, N., 2007. A stability analysis of the lambda estimator for solving the ambiguity problem in persistent scatterer interferometry. In: Proceedings of IEEE International Geoscience and Remote Sensing Symposium, 2082–2085.

Hajnsek, I., 2006. SAR polarimetry i/ii, CCG lecture notes on SAR Principles and Application.

Hanssen, R., 2001. Radar Interferometry - Data Interpretation and Error Analysis. Kluwer Academic Publishers.

Hellwich, O., Ebner, H., 2000. Geocoding SAR interferograms by least lquares adjustment. ISPRS Journal of Photogrammetry and Remote Sensing 55: 277–288.

Henderson, F., Lewis, A. (Ed.), 1998. Principles & Applications of Imaging Radar. Wiley.

Herrera, G., Tomás, R., Lopez-Sanchez, J., Delgado, J., Vicente, F., Mulas, J., Cooksley, G., Sanchez, M., Duro, J., Arnaud, A., Blanco, P., Duque, S., Mallorqui, J., De la Vega-Panizo, R., Monserrat, O., 2009. Validation and comparison of advanced differential interferometry techniques: Murcia metropolitan area case study. ISPRS Journal of Photogrammetry and Remote Sensing 64: 501–512.

Hooper, A., 2007. A combined multi-temporal InSAR method incorporationg persistent scatterer and small baseline approaches. In: Proceedings of FRINGE Workshop, on CD.

Hooper, A., 2008. A multi-temporal InSAR method incorporating both persistent scatterer and small baseline approaches. Geophysical Research Letters 35: 5 PP.

Hooper, A., Segall, P., Zebker, H., 2007. Persistent scatterer interferometric synthetic aperture radar for crustal deformation analysis, with application to volcan alcedo, galapagos. Journal of Geophysical Research 112: 21 PP.

Hooper, A., Zebker, H., Segall, P., Kampes, B., 2004. A new method for measuring deformation on volcanoes and other natural terrains using InSAR persistent scatterers. Geophysical Research Letters 31: 5 PP.

Kampes, B., 2006. Radar Interferometry - Persistent Scatterer Technique. Springer.

Kampes, B., Hanssen, R., 2004. Ambiguity resolution for permanent scatterer interferometry. IEEE Transactions on Geoscience and Remote Sensing 42 (11): 2446–2453.

Ketelaar, G., van Leijen, F., Marinkovic, P., R., H., 2007. Multi-track PS-InSAR datum connection. In: Proceedings of IEEE International Geoscience and Remote Sensing Symposium, 2481–2484.

Klausing, H., Holpp, W. (Ed.), 2000. Radar mit Realer und Synthetischer Apertur. Oldenbourg.

Kovesi, P., 2006. MATLAB implementation of RANSAC. Copyright (c) 2003-2006 Peter Kovesi, School of Computer Science & Software Engineering, The University of Western Australia, pk at csse uwa edu au, http://www.csse.uwa.edu.au/~pk, checked: June 2010.

Lanari, R., Mora, O., Manunta, M., Mallorqui, J., Berardino, P., Sansosti, E., 2004. A small-baseline approach for investigating deformations on full-resolution differential SAR interferograms. IEEE Transactions on Geoscience and Remote Sensing 42 (7): 1377–1386.

Lee, J.-S., 1981. Speckle analysis and smoothing of synthetic aperture radar images. Computer Graphics and Image Processing 17 (1): 24–32.

Liebhart, W., Adam, N., Parizzi, A., 2010. Least squares estimation of PSI networks for large scenes with multithreaded singular value decomposition. In: Proceedings of European Conference on Synthetic Aperture Radar, on CD.

Lombardini, F., 2003. Differential tomography: A new framework for SAR interferometry. In: Proceedings of IEEE International Geoscience and Remote Sensing Symposium, Vol. 2, 1206–1208.

Marinkovic, P., Hanssen, R., 2007. Dynamic persistent scatterers interferometry. In: Proceedings of IEEE International Geoscience and Remote Sensing Symposium, 4894–4897.

Marinkovic, P., van Leijen, F., Ketelaar, G., R., H., 2005. Recursive persistent scatterer interferometry. In: Proceedings of FRINGE Workshop, on CD.

Massonnet, D., Feigl, K., 1998. Radar interferometry and its application to changes in the earth's surface. Reviews of Geophysics 36 (4): 441–500.

Mikhail, E., Ackermann, F., 1983. Observations and Least Squares. University Press of America.

Mora, O., Mallorqui, J., Broquetas, A., 2003. Linear and nonlinear terrain deformation maps from a reduced set of interferometric sar images. IEEE Transactions on Geoscience and Remote Sensing 41 (10): 2243–2253.

Neitzel, F., Petrovic, S., 2008. Total least squares (TLS) im kontext der ausgleichung nach kleinsten quadranten am beispiel der ausgleichenden geraden. ZfV : Zeitschrift für Geodäsie, Geoinformation und Landmanagement 133 (3): 141–148.

Niemeier, W., 2002. Ausgleichungsrechnung. Walter de Gruyter.

Pepe, A., Lanari, R., 2006. On the extension of the minimum cost flow algorithm for phase unwrapping of multitemporal differential SAR interferograms. IEEE Transactions on Geoscience and Remote Sensing 44 (9): 2374–2383.

Perissin, D., Ferretti, A., 2007. Urban-target recognition by means of repeated spaceborne sar images. IEEE Transactions on Geoscience and Remote Sensing 45 (12): 4043–4058.

Perissin, D., Ferretti, A., Piantanida, R., Piccagli, D., Prati, C., Rocca, F., Rucci, A., de Zan, F., 2007. Repeat-pass SAR interferometry with partially coherent targets. In: Proceedings of FRINGE Workshop, Frascati, Italy, on CD.

Perissin, D., Rocca, F., 2006. High-accuracy urban dem using permanent scatterers. IEEE Transactions on Geoscience and Remote Sensing 44 (11): 3338–3347.

Pitz, W., Miller, D., 2010. The terrasar-x satellite. IEEE Transactions on Geoscience and Remote Sensing 48 (2): 615–622.

Shannon, C., 1949. Communication in the presence of noise. Proceedings of IRE 37 (1): 10–21.

Skolnik, M. (Ed.), 1990. Radar Handbook. McGraw-Hill Professional.

Teunissen, P., 1993. A new method for fast carrier phase ambiguity estimation. LGR-Series 6, Delft Geodetic Computing Centre, Delft, The Netherlands, 59 pages.

Teunissen, P., 1995. The least-squares ambiguity decorrelation adjustment: A method for fast GPS integer ambiguity estimation. Journal of Geodesy 70: 65–82.

Teunissen, P., de Jonge, P., Tiberius, C., 1996. The volume of the GPS ambiguity search space and its relevance for integer ambiguity resolution. In: International Technical Meeting of the Satellite Division of the Institute of Naviagtion, Kansas City, USA, on CD.

Teunissen, P. J. G., Jonge, P. J. D., Tiberius, C., 1995. The lambda-method for fast GPS surveying. In: Proceedings of International Symposium GPS technology applications, Romania, 26–29.

van Leijen, F., Hanssen, R., 2007. Persistent scatterer density improvement using adaptive deformation models. In: Proceedings of IEEE International Geoscience and Remote Sensing Symposium, 2102–2105.

Verhagen, S., 2005. The gnss integer ambiguities: Estimation and validation. Ph.D. thesis, Delft University of Technology, 196 pages.

Wang, Y., Zhu, X., Bamler, R., 2011. Advanced coherence stacking technique using high resolution terraSAR-x spotlight data. In: Proceedings of Joint Urban Remote Sensing Event, 233–236.

Werninghaus, R., Buckreuss, S., 2010. The terrasar-x mission and system design. IEEE Transactions on Geoscience and Remote Sensing 48 (2): 606–614.

Yoon, Y., Eineder, M., Yague-Martinez, N., Montenbruck, O., 2009. TerraSAR-X precise trajectory estimation and quality assessment. IEEE Transactions on Geoscience and Remote Sensing 47 (6): 1859–1868.

Zebker, H., Shankar, P., Hooper, A., 2007. InSAR remote sensing over decorrelating terrains: Persistent scattering methods. In: Proceedings of IEEE Radar Conference, on CD.

Zhu, X., Adam, N., Bamler, R., 2008. First demonstration of space-borne high resolution SAR tomography in urban environment using TerraSAR-X data. In: Proceedings of CEOS SAR Workshop on Calibration and Validation, on CD.

Zhu, X., Bamler, R., 2010a. Let's do the time warp: Multi-component nonlinear motion estimation in differential SAR tomography. Geoscience and Remote Sensing Letters 8 (4): 735–739.

Zhu, X., Bamler, R., 2010b. Super-resolution for 4-D SAR tomography via compressive sensing. In: Proceedings of European Conference on Synthetic Aperture Radar, on CD.

Zhu, X., Bamler, R., 2010c. Very high resolution spaceborne SAR tomography in urban environment. IEEE Transactions on Geoscience and Remote Sensing 48 (12): 4296–4308.